IMPROVED FINITE ELEMENT MODELING AND DYNAMIC ANALYSIS OF ROTATING MACHINERY AND A DRILLSTRING WITH IMPACT DAMPERS

A Dissertation

by

LINGNAN HU

Submitted to the Office of Graduate and Professional Studies of
Texas A&M University
in partial fulfillment of the requirements for the degree of

DOCTOR OF PHILOSOPHY

Chair of Committee,	Alan Palazzolo
Committee Members,	Chii-Der Suh
	Shima Hajimirza
	Stefan Hurlebaus
Head of Department,	Andreas A. Polycarpou

December 2018

Major Subject: Mechanical Engineering

ABSTRACT

Accurate modeling and analysis approaches have long been important concerns for designers of rotating machinery. This work is focused on the improvement of high-fidelity finite element (FE) modeling approaches and software algorithms for analysis of a rotor dynamic system that is comprised of rotors, bearings, and support structures.

First, improved formulations for the axisymmetric solid harmonic FE method are developed, which account for the centrifugal stress-stiffening effects and spin-softening effects. A thorough comparison of beam-type FE and axisymmetric solid FE is conducted based on various non-dimensional rotor topologies. In addition to the simulation of rotors, an improved modeling approach is developed to simulate coupled rotor-support systems. This modeling approach utilizes multiple-input and multiple-output (MIMO) transfer functions (TFs) to represent a flexible support structure. The TFs are derived by curve-fitting the frequency response functions of the support model at bearing locations, and then transform into a state-space model to perform general rotor dynamic analyses. Moreover, improvements are made in modeling a rotor system that undergoes large support motion. The shaft continuum is discretized with beam FEs and connected to the support structure via hydrodynamic journal bearings. The bearing forces acting on the rotor are determined by solving the Reynold's equation for lubricant film pressure utilizing a two-dimensional (2D) FE fluid film model. The influences of the time-varying parameters and unloaded bearings on the dynamic behavior of the rotor system are investigated.

This work also contributes to the development of novel centralized impact and torsional dampers for suppression of lateral and torsional stick-slip vibrations of drillstrings. The rotor model of the drillstring utilizes the beam FEs that account for the gravity and axial loading effects on the transverse string stiffness and includes the radial and tangential contact forces that occur when the impactors contact the drill collar or sub. An improved contact force model containing nonlinear Hertzian contact restoring forces and nonlinear, viscous contact damping force is developed, in place of the conventional coefficient of restitution (COR) model that cannot provide the required normal and tangential contact forces.

DEDICATION

To my parents who love me and never gave up on me.

ACKNOWLEDGEMENTS

I would first like to express my sincere gratitude to my advisor Dr. Palazzolo for his guidance and continuous support of my study and research. His understanding and patience were invaluable throughout this effort. I could not have imagined having a better mentor for my Ph.D. study.

I would also like to thank the rest of my dissertation committee, Dr. Suh, Dr. Hurlebaus, and Dr. Hajimirza, for their encouragement and insightful advice which widen my field of vision from various perspectives.

My sincere thanks also go to Dr. Goenezen, who kindly agreed to attend my dissertation defense despite his busy schedule. His help was greatly appreciated.

I thank my labmates, faculty and staff members of the Department of Mechanical Engineering for their assistance.

Appreciation is also acknowledged to the Turbomachinery Research Consortium who funded my research work.

Last but not the least, I would like to thank my family and friends for supporting me along the way.

CONTRIBUTORS AND FUNDING SOURCES

Contributors

This work was supervised by a dissertation committee consisting of Professors Alan Palazzolo, Chii-Der Suh and Shima Hajimirza of the Department of Mechanical Engineering and Professor Stefan Hurlebaus of the Department of Civil Engineering.

All the work conducted for the dissertation was completed by the student independently.

Funding Sources

Graduate study was supported by a fellowship and a graduate assistantship from the Department of Mechanical Engineering at Texas A&M University.

This work was also made possible in part by the Turbomachinery Research Consortium (TRC) at Texas A&M University.

NOMENCLATURE

A_1, A_2	Attachment nodes of bearing 1 and 2
A^e	Element area (m^2)
A_s	Area of a shaft segment (m^2)
$[B_{\mathrm{RB}}]$, $[B_{\mathrm{RU}}]$	Matrices transforming bearing force and unbalanced force acted on the rotor from Cartesian coordinates into polar coordinates, respectively
BHA	Bottom Hole Assembly
BRSSM	Beam FE rotor with a solid FE support model
BW	Backward whirl
$[C]$	Damping matrix
$[C_R]$	Resultant damping matrix of the rotor system
$[C_V]$	Structural damping matrix
COR	Coefficient of Restitution
CSRSM	Complete Solid FE Rotor-Support Model
c	Damping coefficient ($N \cdot s/m$)
D_{ol}, D_{or}	Outer diameter of the left and right ends of a step-like shaft, respectively
DA	Drilling-Ahead
DB	Drill Bit
DC	Drill Collar

DOF	Degree of Freedom
DP	Drill Pipe
E	Modulus of elasticity (N/m)
e	Base of natural logarithm
e_{COR}	Coefficient of restitution
F	External force (N)
$\tilde{F}$	Deformation gradient
F_{BY}, F_{BZ}	Bearing forces in Y and Z direction, respectively (N)
F_c	Contact force acting on the drill collar (N)
F_r^y, F_r^z	Components in Y, Z directions of the radial bearing forces translated from the cylindrical coordinates to Cartesian coordinates, respectively (N)
F_V	Force per unit volume (N)
F_y, F_z	Bearing forces in Y, Z directions in the Cartesian coordinate system, respectively (N)
F_z^+, F_z^-	Bearing forces in the circumferential direction and the opposite direction in the cylindrical coordinate system, respectively (N)
FE	Finite element
FEM	Finite element method
FRF	Frequency response function
FW	Forward whirl
$\{f\}$	External load vector (N)

$\{f_B\}$	Bearing force vector (N)
$\{f_R\}$	External force vector of the rotor
$\{f_U\}$	Unbalanced force vector (N)
$[G]$	Gyroscopics matrix
G_{AiBj}	Frequency response function corresponding to the force acted on bearing j in B direction and the response at bearing i in A direction
$[G_R]$	Gyroscopics matrix of the rotor system
$[G(s)]$	MIMO transfer function matrix
h	Fluid film thickness
I	Second moment of inertia
I_{pd}	Polar moment of inertia of a disk
I_{ps}	Polar moment of inertia of a shaft segment
I_{td}	Second moment of inertia of a disk
I_{ts}	Second moment of inertia of a shaft segment
ID	Inner diameter
i^{th}/j^{th}	i^{th}-order numerator divided by j^{th}-order denominator
j	Imaginary component
K	Stiffness (N/m)
$[K]$	Stiffness matrix
$[K_R]$	Resultant stiffness matrix of the rotor system
$[K_S]$	Structural stiffness matrix of the rotor

$[K_\sigma]$	Centrifugal stress-stiffening matrix of the rotor
$[K_\Omega]$	Spin-softening matrix of the rotor
L	Shape function of the three-node triangular finite element
M	Mass (kg)
$[M]$	Mass matrix
$[M_R]$	Resultant mass matrix of the rotor system
MIMO	Multi-input and multi-output
m	Harmonics number
m_d	Mass of the disk
$[N]$	Shape function matrix
N_e	Number of nodes within an element
$N_{m,j}$	Shape functions
OD	Outer diameter
PDC	Polycrystalline diamond compact
p	Pressure
p-p	Peak-to-peak
Q_V	External load per unit volume
q	Node displacement/DOF or state variable
$\{q\}$	Displacement/DOF vector
$\{q_\sigma\}$	Displacement/DOF vector due to initial stress (including the stress induced by centrifugal forces)
R_F	Reference frame with respect to the foundation/support structure

R_G	Reference frame with respect to the ground
R_{outer}, R_{inner}	Outer and inner radius of the rotor, respectively
R_R	Reference frame with respect to the shaft segment or disk
RAM	Random-Access Memory
ROB	Rotating-Off-Bottom
RSSM	Reduced State-Space Model
r	Radius
rpm	Revolutions per minute
SISO	Single-input and single-output
SRSSM	Solid FE rotor with a super-element support model
s	Complex variable
TF	Transfer Function
TOB	Torque-On-Bit
TRC	Turbomachinery Research Consortium
U	Strain energy
U_A	Antisymmetric component of displacement
$\{U_R\}$	Displacement vector of the rotor
U_S	Symmetric component of displacement
u	Displacement
u_{mr}	Radial displacement when the harmonics are m
u_{mz}	Axial displacement when the harmonics are m
$u_{m\theta}$	Circumferential displacement when the harmonics are m

u_r	Radial displacement (m)
u_z	Axial displacement (m)
u_θ	Circumferential displacement (m)
u_0	Displacement in X direction
V	Volume
V^e	Element volume
v_i	Input impact velocity
v_0	Displacement in Y direction
WOB	Weight-On-Bit
w_0	Displacement in Z direction
X, Y, Z	Cartesian coordinates
XLTRC^2	Rotor dynamics software developed by the Turbomachinery Lab of Texax A&M University
x_F, y_F, z_F	Displacements of the support structure in x, y, and z directions with respect to R_G and projected in R_F
x_R, y_R, z_R	displacements of the disk in x, y, and z directions with respect to R_F and projected in R_F
x_S, y_S, z_S	displacements of the shaft segment in x, y, and z directions with respect to R_F and projected in R_F
$\{y\}$	Displacement vector in the Cartesian coordinates (m)
α	Coefficient for the input impact velocity

$\alpha_F, \beta_F, \gamma_F$	Rotation angle of the support structure about x, y, and z axes with respect to R_G and projected in R_F
$\alpha_R, \beta_R, \gamma_R$	Rotation angle of the disk about x, y, and z axes with respect to R_F and projected in R_F
$\alpha_S, \beta_S, \gamma_S$	Rotation angle of the shaft segment about x, y, and z axes with respect to R_F and projected in R_F
δ	Interference in impact
$\tilde{\delta}_{ij}$	Kronecker delta
$\tilde{\varepsilon}$	Tensor-based strain
ε_2	Second order strain
θ	Circumferential angle
υ	Poisson's ratio
ρ	Mass density (kg/m^3)
ρ_s	Mass density of a shaft (kg/m^3)
σ_0	Initial stress such as centrifugal forces induced stress
ϕ	Rotational angle
Ω	Spin speed of the rotor (rad/s)
ω	Rotating speed or excitation frequency of the unbalanced force (rad/s)
$\omega_{Fx}, \omega_{Fy}, \omega_{Fz}$	Rotation speed of the support structure about x, y, and z axes with respect to R_G and projected in R_F

ω_{Rx}, ω_{Ry}, ω_{Rz}	Rotation speed of the disk about x, y, and z axes with respect to R_F and projected in R_F
ω_{Sx}, ω_{Sy}, ω_{Sz}	Rotation speed of the shaft segment about x, y, and z axes with respect to R_F and projected in R_F
1D	One-Dimensional
2D	Two-Dimensional
3D	Three-Dimensional

Subscripts

A	Torsional damper
B	Bearing
$B1$, $B2$	Bearing 1 and 2
e	Eccentricity
I, D	Impactor and DC, respectively
i	Node i of an axisymmetric element
m	Harmonic number
mS, mA	Symmetric and anti-symmetric components in mth harmonics, respectively
P, Q	Contact point of the impactor and DC, respectively
R	Rotor
R, C	Retained and condensed DOFs, respectively
r, z, θ	Radial, axial and circumferential directions, respectively
S	Support structure

S, A	Symmetric and antisymmetric components, respectively
T	The entire state-space model of the rotor-support system
t	Tangential direction
U	Unbalance
V	Volume
XX, YY, ZZ, ZY	Refer to YZ
X, Y, Z	X, Y and Z directions in the Cartesian coordinates, respectively
xx, yy, zz, zy	Refer to yz
YZ	Force in Y direction due to the displacement in Z direction in the Cartesian coordinates
y, z, φ	Y, Z, and torsional directions, respectively
yz	Force in Y direction due to the displacement in Z direction in the Cartesian coordinates
σ	Stress stiffness matrix

Superscripts

A_1, A_2, B	Nodes A_1, A_2 and B on the rotor, respectively
e	Elemental matrix/vector/variable
P	Surface node P in the journal section mesh
$\cdot$	Derivative of time
^	In the complex form
$\vec{\ }$	Vector

TABLE OF CONTENTS

Page

LIST OF FIGURES

Page

LIST OF TABLES

Page

1. INTRODUCTION

1.1. Background

Rotor dynamics is a specialized subject dealing with the machinery that has rotating structures. These machines are known as rotating machinery. The rotating components are defined as rotors, and the stationary parts are referred to as stators. Physical dynamic systems like rotating machines are continuous both spatially and temporally. The closed-form solutions to the dynamic problems in relation to continuous systems are not feasible in many practical applications. Therefore, modeling of the dynamic systems like rotating machinery requires good approximations, such as discretization in space or transformation from time domain to frequency domain.

The finite element method (FEM) is a good numerical modeling technique that is widely used in many dynamics modeling and analysis areas. But general-purpose FEM programs are not adequate for rotor dynamic analysis because the rotor rotates with significant angular momentum and complex interactions between the shaft and bearing. In order to resolve this problem, a variety of specialized finite element (FE) models are developed and applied in the dedicated dynamics software for modeling and analysis of various rotating machines.

The expensive cost of manufacture and maintenance for the high-speed rotating machines like gas turbines makes it essential that early-stage designs function as intended. This requires the FE models to be more accurate not only in the rotor modeling but also in the whole machine system modeling. In recent years, this requirement is

becoming feasible owing to the rapid advance in computer techniques and software algorithms and continuously improved FE modeling approaches for rotor systems.

1.1.1. Rotating Machinery

Rotating machinery is a general term that describes the machines with rotating components. In this work, they are referred to as turbomachines that transfer energy between fluid and rotor and drillstrings (which will be introduced in Section 1.1.2). The applications of turbomachines include steam turbines and compressors in the oil and gas industry, gas turbines in the aerospace industry, turbochargers in automobiles, centrifuges in medical equipment, etc.

Modern turbomachines that were manufactured in significant numbers dates back to the late nineteenth century. The basic structure of turbomachines consists of shafts, disks, blades, bearings, seals, and bearing housing support structures (or foundations). Generally speaking, a shaft with disks and blades (also called blisks) is considered to be a rotor and is supported by the bearings that are mounted in the support structures or foundations. In regard to turbines, the fluids like pressurized gas or steam move through the blades and drive the shaft to rotate, transforming thermal energy into mechanical energy. As for compressors, the shaft rotates and pressurizes the fluids.

The clearance between the rotor and fluid film bearing is extremely small (on a scale of several mils) for achieving high bearing capacity. The gaps between the blade tip or impeller edge and the casing are also small compared to the dimensions of the shaft. Hence, large vibrations are one of the major causes for machine failure. To avoid the human injury caused by the failure and enormous cost on the machine repair,

engineers should design rotating machinery based on an in-depth understanding of rotor dynamics and better use software to model and analyze the dynamic behaviors of the machines. The modeling approaches for rotating machinery are being improved concurrently with the enhancement of computer performance. The latest improvements of rotor dynamic modeling and analysis are presented in this work.

1.1.2. Drillstring

As mentioned in Section 1.1.1, drillstrings can be categorized as low-speed rotating machines. As shown in Figure 1, a conventional drillstring is basically a long rotating pipe hoisted by a vertical drilling rig. The drillstring is usually composed of a drill bit (DB), and several drill pipes (DPs) and drill collars (DCs). The DB normally consists of a steel body and three rotating parts with steel or carbide inserts teeth that can break up rocks. Some new types of DBs like the one with polycrystalline diamond compact (PDC) bits do not have the rotating components but are more capable of crushing rocks by using artificial diamond cutters. The DPs are basically slender tubes with joints at the end to connect two tubular sections. The DCs are made up of the steel tubes of larger thickness than the DP, in order to apply more weight on the DB for achieving a higher rate of penetration (ROP). The bottom hole assembly (BHA), which consists of the DCs including subs like stabilizers, DB, motors and some measurement equipment, is the lowest part of the drillstring in a well and helps to control the drilling direction and borehole shape.

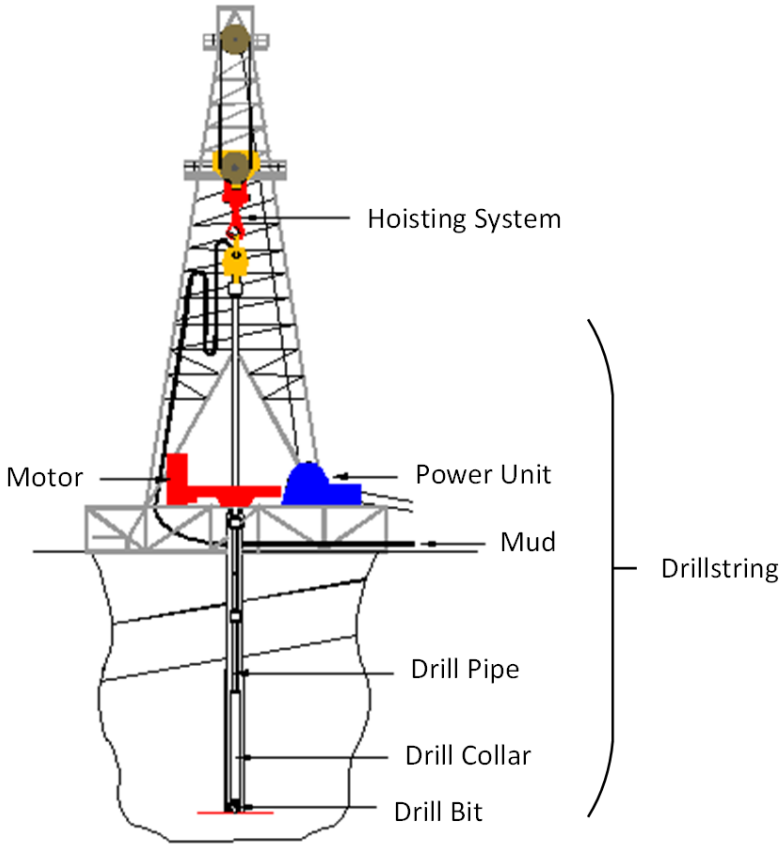

Figure 1. Drilling rig. Adapted from Ref. [1].

Although many dynamic characteristics of drillstrings are different from those of turbomachines, many principles and analysis approaches in rotor dynamics can be used to study drillstring vibrations. Violent drillstring vibrations in a well, including torsional stick slip and lateral whirl vibrations, may cause premature failure of tubulars and DBs and damage to the borehole wall. In addition, these vibrations may result in an inefficient drilling process with excessive trips to replace worn DBs.

Some approaches that utilize an elastomer and viscous fluid-based damper have been applied to mitigate lateral vibrations. However, typical fluid dampers vary viscosity

radically with working temperature, which may lead to inefficient damping in higher temperatures (>120°C). But this is not the primary concern in industry since there are very few high-temperature wells currently being drilled. In the harsh deep well environment exposed to oil and water (or moisture), the combined effects of oxidization, swelling and degradation due to age and chemical reactants on the elastomer may result in the premature ineffectiveness of the elastomer damper. Therefore, novel centralized impact dampers and torsional vibration dampers, which will function well in the harsh environment in the well due to their all-metal construction, are developed for suppression of lateral and torsional stick-slip vibrations.

1.2. Literature Review

1.2.1. Rotor modeling

Accurate prediction of resonant critical speeds in rotating machinery has long been an important concern for designers of turbomachinery. Historically, multi-station rotors were originally modeled with transfer matric methods [2, 3]. This approach has been for the most part replaced with the use of the FEM due to the increased speed of computers and development of highly efficient algorithms for solving FE equations. FE modelling approaches for rotor dynamic response have used both Euler-Bernoulli and Timoshenko beam elements.

McVaugh and Nelson [4] have developed a general cylindrical rotating shaft model using beam elements and including gyroscopic effects, rotary inertia and axial loads. This was subsequently extended by Nelson [5] to include the shear deformation and torque effects. Thomas, et al. [6] considered conical shaft sections and utilized two

additional coordinates at the element ends to improve the modelling of shear deformation. On the basis of their work, Rouch and Kao [7] developed linearly tapered beam elements by applying numerical integration to derive element matrices. In order to use closed form expressions rather than numerical integration, Greenhill et al. [8] employed the kinematic representation of Thomas, et al. [6] and derived closed form polynomial expressions for element matrices. A shear deflection factor is employed in their work to assess the effect of cross-section shape on shear deformation.

The basic beam assumption that plane sections remain plane after deformation is made for any beam element formulation. The deformations that violate this assumption are considered as non-beam deformations. In most cases, shafts have small bending displacements compared to the length, and the plane sections after deformation may be approximated to be plane. Hence, it has been generally believed that the aforementioned beam FE models are sophisticated and are able to yield acceptable results. However, a rising number of shafts with complex shapes are designed for modern turbomachinery, and as such, the beam assumption may be violated at sections with large diameter changes, which has been verified by Stephenson *et al.* [9]. Besides, a shaft that is composed of hollow conical segments may not be precisely modeled with beam elements due to distortions occurring at the hollow conical sections. Vest and Darlow [10] came up with correction factors to include the effect of distortions on the beam stiffness. However, this approach is limited to certain cases and is unable to precisely predict a wide range of natural frequencies.

An alternative approach, which differs from applying various correction factors to beam FE formulations, has been developed by Stephenson *et al.* [11]. They utilized solid harmonic elements to model axisymmetric shafts and extended the formulations to include gyroscopic effects based on the work of Cook [12] and Geradin and Kill [13]. Greenhill and Lease [14] investigated the influences of disk flexibility and locations on the rotor system by using axisymmetric solid harmonic elements, but they did not consider the centrifugal stress-stiffening and spin-softening effects. With regard to support boundary conditions, Stephenson *et al.* [11] mentioned that it is reasonable to apply bearing stiffness and damping to the outer surface node of a shaft, but they neither specified how to include these coefficients in the shaft matrices nor validated this point of view.

As disks in modern design of some high-speed turbomachines are becoming thinner and more flexible, additional attention may be required for both centrifugal stress-stiffening and spin-softening effects. Cook et al. [12] derived equations in the Cartesian coordinate system to interpret initial stress phenomena. However, their method cannot be directly applied in the axisymmetric FE rotor model on account of rotor rotation and the different definition of the Cartesian and cylindrical coordinate systems. The centrifugal stress-stiffening and spin-softening effects have not been adequately addressed in the rotor dynamics literature. Combescure and Lazarus [15] provided an axisymmetric FE model in the rotating frame to study the centrifugal stress-stiffening effects. Although they presented a general equation of motion including the centrifugal stress-stiffening and spin-softening effects, they did not provide detailed FE matrices

and a procedure to implement their formulation. In addition, their axisymmetric FE model is in the rotating frame, which has limited applications.

A solid FE model may produce thousands more of DOFs than a beam FE model, and it is thus required that the matrices should be reduced for the purpose of saving computational resources. Stephenson *et al.* [11] have successfully applied the Guyan reduction method [16] to the shaft axisymmetric FE model, but they mentioned that it was up to the analyst how to select master DOFs. Three-dimensional (3D) solid FE models have been presented in [17-19]. However, either the rotor was modeled with respect to the rotating reference frame or the bearing stiffness and damping coefficients was treated as symmetric in horizontal and vertical directions. An automatic master DOFs selection algorithm that utilizes main diagonal terms of stiffness and mass matrices to retain DOFs was provided in [20].

1.2.2. Support structure modeling

In addition to shafts and disks, support structures may be flexible as well due to lightweight design of rotating machinery. The effect of the flexible support on the rotor system may be significant per the investigation results reported in Refs. [21-24]. Except for the beam frame structures that can be modeled with 3D beam FEs, most flexible support structures are modeled with 3D solid elements. Although it is viable to use a complete solid FE model including the rotor and support structures to perform rotor dynamic analysis, especially at the design stage, it may require a large amount of computational resources and simulation time. A remedy for this is to model the support structures with super-elements, which condenses the internal degrees of freedom (DOFs)

but retains the DOFs of the attachment nodes that connect the rotor and support substructures through the bearings [12, 25].

In comparison with the solid FE and super-element models, an experimental approach is to obtain the frequency-dependent stiffness and damping of the support structure by measuring the frequency response functions (FRFs) at the bearings, and then include this equivalent physical model of the support structure in the analysis of the rotor system [26]. Vázquez and Barrett [27], and Vázquez *et al.* [28, 29] extracted a series of rational TFs from the measured FRFs of the support structure by using identification techniques. Both unbalance response and stability analyses of the rotor and support structure were accomplished with the TFs in the s-plane. Moore, et al. [30] applied the 1D beam FE and 3D solid FE in modeling the rotor and housing of a large industrial turbocompressor, respectively, and developed point TFs to investigate the effects of the housing on the rotor system. In the work by De Santiago and Abraham [31], the power turbine that is commonly used in the oil and gas industries as a mechanical driver is modeled with solid elements, and the comparison with the complete rotor-support FE model shows that the simplified structure model utilizing the support TFs is applicable in the rotor dynamic analysis.

1.2.3. Support motion

In the conventional rotor dynamic analysis, the foundation or support structure is normally assumed to be fixed to the ground. However, turbomachines like compressors and gas turbines may be installed in maneuvering aircrafts and ships encountering rough seas. In these scenarios, the on-board rotor is subject to large time-varying motions of its

support structure. A few researchers [32-36] studied the influences of support motions on the rotor system by using the simplified flexible rotor models similar to the Föppl-Jeffcott rotor model [37, 38]. To provide more accurate modeling approaches, some researchers [39-43] presented beam FE based rotor models that account for support motion. However, none of these models utilize hydrodynamic fluid film bearing models to simulate the interaction between the rotor and the support structure.

In the aforementioned models that account for support motion, the rotor is either assumed to be rigidly connected to the support or connected to the support via a short journal bearing model. The former assumption indicates there is no relative motion between the rotor and the support. The latter utilizes the short length bearing solutions [44, 45] to simulate the bearing forces acting on the rotor. However, the short journal bearing model is not accurate in many cases [37, 46, 47]. Most of the hydrodynamic fluid film bearings that are widely used in the rotating machinery are fixed-pad and tilting-pad journal bearings. Regarding the fixed-pad bearings, a simplified model with an extremely thin fluid film between two plane journal segments [37, 48] was utilized to apply the Reynolds equation. A specific fluid film 2D FE modeling approach was presented in [49].

1.2.4. Drillstring vibrations

Torsional and lateral drillstring vibrations have been investigated by many researchers. They borrowed ideas from the fundamentals of the rotor dynamics in order to explain the vibration phenomena of the slender beam-like drillstring. As far as torsional vibration is concerned, a viable way to avoid deep well environment problems

was reported by Jansen and van den Steen [50]. They proposed an active damping system above the rotary table and reduced the threshold value for stick-slip by using feedback control. Sowers *et al.* [51] found that a violent whirl occurring at the bit or in the BHA may result in large side forces at stabilizers, thereby generating high friction torques that lead to stick-slip vibrations. In such situations, they replaced the stabilizers with roller reamers to reduce the frictional drag acting at the BHA and eventually mitigate the bit whirl.

Kyllingstad and Halsey [52] used a pendulum model with a single degree-of-freedom (DOF), in which the drillstring is assumed to be suspended at the hoist/rotary table, and applied a constant Coulomb friction torque to the DB during rotation-off-bottom (ROB) or drilling-ahead (DA) to analyze its stick-slip motion. Jansen and van den Steen [50] employed a static-sliding torque model, which is similar to the Coulomb friction torque model, and divided the torque-on-bit (TOB) into static and sliding torque by assuming that the DB never rotates backwards (i.e., no rolling occurs), and that the DP does not come to a complete standstill. Their assumptions are helpful to understanding how the stick-slip vibration occurs though the observations in the drilling field demonstrate three different types of stick-slip vibrations, i.e., simple speed oscillation, full stick, and backward rotation. More comprehensive drillstring models that account for multiple types of stick-slip vibrations were investigated in Refs. [53] and [54].

Although the classic Coulomb (static-sliding) torque model has provided a good estimation of torsional vibrations in many cases, Dawson et al. [55] came up with a

hypothesis that the torque acting on the DB undergoes a continuous and mild reduction with an increasing spin speed. Brett [56] proved by experiment that the PDC bit has the characteristic described in Dawson's et al. hypothesis [55] and is thereby prone to causing torsional vibrations. Moreover, the lab measurements presented in his work indicated that other types of bits may have the same characteristic (torque reduction with an increase in spin speed) as the PDC bit. This velocity-dependent friction torque is analogous to the Stribeck friction model in physics. Leine et al. [57] utilized a similar torque model, in which the dry friction torque drops with a rising rotary speed, to investigate the coupled stick-slip and whirl vibrations. In accordance with Ref. [56], the Stribeck torque model is sensitive to the type of DB, the weight-on-bit (WOB), the drilling condition, and even the wear of the bit.

With regard to the lateral whirl of a drillstring, a simplified 2DOFs lateral dynamic model of a drillstring has been presented by Jansen [58]. As stated in his paper, the lower part of a drillstring (i.e. the DC) is essential for the analysis of whirl motion, and the DC section between two stabilizers is analogous to a rotor supported by two bearings. Bailey et al. [59] used the transfer function matrices based on the Euler-Bernoulli beam bending equations to model the DC span (DC section between two nearby stabilizers). The boundary conditions were defined in two ways. One is that the DC span is pinned at both ends (stabilizers), and the other is that the span has one end built-in and the other end free. The same lateral dynamic model of a drillstring and boundary conditions was applied in Ref. [60], and the region of parameters for a DC

span that contains common spin speeds, span lengths and natural frequencies was also provided. The DC used in this work is modeled based on this region of parameters.

1.2.5. Impact damper

Impact dampers have long been used to dampen out structural vibrations in traffic light poles, turbomachinery blades, machine tools, etc. Moore et al. [61] employed a single-DOF impacting model characterized by the COR to simulate the collision between an impact damper and an impact housing and then utilized a high speed cryogenic rotor-bearing test rig with a multiple-impactor set that consists of impact dampers and housings to verify the simulation result that the lateral vibration was suppressed by impact dampers. McElhaney et al. [62] presented the mitigation effects of cylindrical impact dampers on lateral vibrations at resonances of a rotating shaft. The cylindrical impactor was assumed to have planar motions and impact with the housing that was connected to the shaft, but the tangential friction between the impactor and housing was neglected. The rotating shaft was modeled with multi-DOF (multiple nodes with six DOFs per node) beam FEs. The dissipated kinetic energy was characterized by the COR.

The COR is defined as the ratio of relative translational speeds of two bodies after and before an impact. According to the earlier measured data that has been published in Refs. [63] and [64], the COR of inelastic impact is mainly dependent upon the conditions like collision velocity, mass ratio, material properties, and geometry of the impactors. In order to account for the velocity-dependent characteristic of inelastic

impact, Hunt and Crossley [65] developed a nonlinear damping model based on the Kelvin-Voigt viscoelastic model to interpret the COR in vibro-impact.

1.3. Statement of the Problem

As discussed in Section 1.1, modern designs of high-speed rotating machinery require more accurate models and less simulation time. In regard to a drillstring, which is a low-speed rotating machine, innovative solutions are demanded for suppressing vibrations in a harsh environment like a deep well. In summary, the problems to resolve in the present work are stated below.

(a) High-fidelity rotor dynamic modeling and analysis approaches are in demand for accurate prediction of resonance and critical speed, rotor instability, and unbalanced force response of a flexible, spinning rotor with thin-walled shafts or flexible disks. When modeling such a rotor, limitations of the commonly used beam FE models must be identified in order to avoid significant errors.

(b) For maneuvering aircrafts and ships, the on-board rotors are subject to large time-varying support structure motions. Such motions may have a great impact on the performance of the hydrodynamic journal bearings, such as inducing large rotor vibrations or invoking rotor instability.

(c) The computation speed of the simulation needs to be enhanced as a high-fidelity model requires much more computational resources to solve large matrices than a beam FE model.

(d) New vibration control devices are needed to suppress drillstring vibrations in deep-well drilling, in place of the fluid and elastomer dampers that might become ineffective due to a harsh deep-well environment.

1.4. Contributions

The contributions of this work aim to:

(a) Develop an enhanced axisymmetric FE formulation of the centrifugal stress-stiffening and spin-softening effects and integrate the formulation into the axisymmetric solid FE modeling of a flexible, spinning rotor. Then compare beam FE and axisymmetric FE natural frequencies, mode shapes and critical speeds and identify rotor geometries where the beam model yields significant error. Finally, provide limitations of beam FE models and guidance for utilizing axisymmetric solid FE models in rotor dynamic simulations.

(b) Improve the accuracy of the beam FE model of a rotor undergoing large support structure motions by integrating a high-fidelity hydrodynamic journal bearing FE model, and then provide analysis and solutions for the instability problem of an on-board rotor system.

(c) Develop a MIMO transfer-function modeling approach for simulating a complete rotor-bearing-support system with a lower cost of computational resources (less computation time, RAM, and overall simulation time).

(d) Develop novel centralized impact dampers and torsional dampers for suppressing drillstring vibrations, and provide modeling approaches and design guidelines.

In addition to the theoretical formulation and analysis, a stand-alone rotor dynamics software, in which the unique formulations and software algorithms developed in the work are built in, is developed for research and industry applications.

The contributions summarized above are further explained below.

1.4.1. Improved axisymmetric FE modeling of flexible rotor

The axisymmetric solid harmonic FE formulation of a flexible, spinning rotor with thin-walled shafts or flexible disks is improved by including both centrifugal stress-stiffening and spin-softening effects. Furthermore, a new way of bearing attachment is developed especially for a thin-walled shaft FE model, which is more accurate than the conventional way in the regard of resonance prediction. This is the first time that detailed FE matrices of the centrifugal stress-stiffening and spin-softening effects and novel bearing attachment fit for a thin-walled shaft are presented. The development of rotor dynamics software for academic research and industry applications can greatly benefit from the formulations and matrices. The influences of thin-walled shafts and flexible disks on the rotor system are investigated. The conclusions drawn from numerous simulation results and analyses provide designers and engineers with guidelines on when and how to use an axisymmetric FE model instead of a beam FE model for rotor dynamic analysis.

1.4.2. Improved modeling of rotor undergoing support motion

An improved modeling approach utilizing the Timoshenko beam FE is developed to simulate a rotor system with flexible shafts on hydrodynamic journal bearings undergoing large support motion. This is the first time that a hydrodynamic fluid film

journal bearing 2D FE model, instead of a short journal bearing model or linear bearing coefficients, has been integrated into a flexible rotor system under large support motion. The influences of support motions on the rotor stability are studied. The conclusions based on numerous nonlinear transient analyses not only address the rotor instability problem but also provide remedies for the on-board rotor instability caused by support motions.

1.4.3. Improved MIMO transfer-function modeling of support structure

An alternative modeling approach for a complete rotor-support system is developed. The approach takes advantage of both axisymmetric solid FE rotor model (accurate prediction of the dynamics of a rotor with complex shapes) and simplified support structure model utilizing the MIMO support TFs (reduction of the computation time and requirement for computational resources). The shaft with multiple flexible disks is modeled using the improved axisymmetric solid harmonic FE method. The flexible support structure, including the bearing housing and foundation is represented by the MIMO TFs. The TF matrix is further transformed into a state-space support model that connects the rotor FE model via bearing forces. Guidance is provided for selecting an adequate polynomial degree of the TFs.

The previous work completed by other researchers did not include the state-space form that represents the complete rotor-bearing-support system. They either did not conduct stability analysis [27] or utilized the s-plane to perform stability analysis. However, none of them provided detailed approaches to calculate the real components of the complex eigenvalues of the rotor system [27-29].

To validate the proposed approach, a comprehensive comparison between the complete solid FE rotor-support model (CSRSM) and the reduced state-space model (RSSM) is presented. Additionally, the modes up to 100,000 cpm are compared among the super-element, beam element, and RSSM.

1.4.4. Development of impact and torsional dampers for drillstrings

In addition to the improved FE modeling of rotating machinery, the novelty of this work includes the development of the centralized impact dampers and torsional dampers. These dampers, when properly designed and installed, are able to attenuate lateral vibration of the drillstring that operates close to the bending critical speeds and the stick-slip torsional vibration within the operating speed range.

A Timoshenko beam FE model, which accounts for gyroscopics, rotary inertia and shear deformations, is employed, though the shear deformations may be negligible due to a large ratio of beam length to diameter. Additionally, the stress-stiffening effects are included to account for the influences of gravity and axial loading on transverse string stiffness. As previously stated, stick-slip is too complex to perfectly describe by using a single model, and thereby, both Coulomb and Stribeck torque models are employed to validate the mitigation effects of the impact and torsional dampers. The vibro-impact model developed in Ref. [65] is employed to simulate the translational collision between the DC and impactor, and the tangential friction in between is also taken into account. In order to provide guidance for acquiring stronger suppression effects on the drillstring vibration, various design parameters of the impactors and torsional damper are analyzed and compared.

1.5. Dissertation Outline

Chapter 2 presents various FE modeling approaches that are applicable in the rotating machinery modeling, including the beam FE, axisymmetric solid FE, 3D solid FE, and fluid film 2D FE methods. A specific formulation of both centrifugal stress-stiffening and spin-softening effects and noval bearing attachment approach are developed, in order to enhance the accuracy of the axisymmetric FE method for flexible rotors with thin-walled shafts and flexible disks. The chapter also clarifies how to use these FE methods to model hydrodynamic journal bearings and flexible support structures. Moreover, a new modeling approach that utilizes the MIMO TFs and state space to represent flexible support structures are developed. In regard to support motion, a systematic modeling approach based on the Timoshenko beam element is presented.

Chapter 3 shows the beam FE modeling of a rotating drillstring with the centralized impact dampers and torsional dampers that are installed in the DC. Nonlinear Hertzian contact restoring forces and nonlinear, viscous contact damping force are included in the impact model, and both Coulomb torque and Stribeck torque models are considered.

In Chapter 4, the modeling approach proposed in Chapter 2, i.e. utilizing MIMO TFs and state space to represent the support structure, is validated by a comprehensive comparison with the complete solid FE rotor system. Comparisons are made between critical speeds, logarithmic decrements, unbalanced responses, computation speeds, and high-frequency modes.

Chapter 5 conducts parametric studies using the axisymmetric solid harmonic FE modeling approach proposed in Chapter 2, and investigates not only the individual influences of either thin-walled shafts or flexible disks but also the combined influences of both shafts and disks on the rotor system. A discussion and guidance are provided on proper attachment of the bearing stiffness and damping to a thin-walled shaft mode. Various combinations of thin-walled shafts and flexible disks are modeled, and the influences of the flexibility of the shaft and disk on the accuracy of the resonance prediction are investigated.

Chapter 6 is focused on the nonlinear dynamic analysis of rotor-bearing systems under large support motion. The beam FE modeling approach presented in Chapter 2 is utilized to model a flexible rotor on hydrodynamic journal bearings and a moving support structure. Pitch motions of a support structure with different types of hydrodynamic journal bearings are studied. The impact of the support pitch on rotor stability and relavant remedies for rotor instability induced by the support motion are studied.

Chapter 7 presents a dynamic model of a drillstring with the centralized impact dampers and torsional dampers that are developed in Chapter 3. A thorough investigation of the suppression effects of these dampers on lateral and stick-slip vibrations of the drillstring is conducted in both ROB and DA conditions.

Chapter 8 firstly summarizes the modeling approaches that are developed or improved in this work, then draws conclusions from numerous simulations and analyses,

and finally proposes future work for the continuous development of the FE modeling approaches for rotating machinery.

The specific matrices and equations that are derived to improve the rotating machinery modeling are provided in the appendices.

2. IMPROVED FINITE ELEMENT MODELING OF ROTATING MACHINERY

In this chapter, a few FE methods that are widely used for rotating machinery modeling are presented. Improvements on those FE methods are proposed.

2.1. Beam Element Modeling of Rotors

The Timoshenko beam element model developed by Nelson [5] is specialized for slender beam-like shafts. The specialty of the rotor dynamic beam model that differs from the general beam model in structural dynamics lies in that the gyroscopic effects are included. However, Nelson's model [5] only contains eight DOFs for each element, namely u_{y1}, u_{z1}, θ_{y1}, θ_{z1}, u_{y2}, u_{z2}, θ_{y2}, and θ_{z2}. To extend that model, two rotational and two axial DOFs are added, with the final DOF vector $\{u\}$ written as,

$$\{u\} = [u_{x1},\ u_{y1},\ u_{z1},\ \theta_{x1},\ \theta_{y1},\ \theta_{z1},\ u_{x2},\ u_{y2},\ u_{z2},\ \theta_{x2},\ \theta_{y2},\ \theta_{z2}]^T \quad (1)$$

where u and θ represent the translational and rotational displacements, respectively, and the subscripts x, y, z indicate the X, Y, and Z directions, respectively. Figure 2 shows the beam element model employed in this work.

* Part of this chapter is reprinted with permission from "Solid Element Rotordynamic Modeling of a Rotor on a Flexible Support Structure Utilizing Multiple-Input and Multiple-Output Support Transfer Functions" by Hu, L., and Palazzolo, A., 2016, Journal of Engineering for Gas Turbines and Power, 139(1), 012503, Copyright 2016 by ASME.

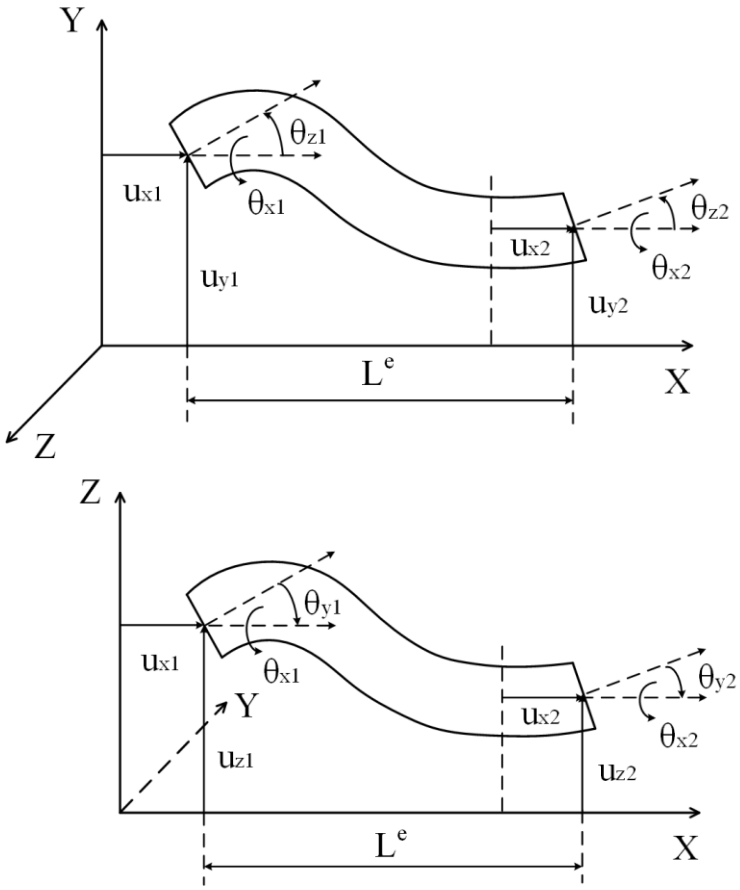

Figure 2. Timoshenko beam element model.

The kinetic energy including torsional and axial motions may be expressed as,

$$T^e = \frac{1}{2}\int_0^{L^e}\left(\rho A^e\left(\dot{u}_x^2 + \dot{u}_y^2 + \dot{u}_z^2\right) + I_t\left(\dot{\theta}_y^2 + \dot{\theta}_z^2\right)\right)dx - \frac{1}{2}\int_0^{L^e}\Big(I_p\left(\omega + \dot{\theta}_x\right)\left(\theta_y\dot{\theta}_z - \theta_z\dot{\theta}_y\right) - I_p\left(\omega + \dot{\theta}_x\right)^2\Big)dx \quad (2)$$

where L^e, A^e, I_t, I_p, u and θ represent the length, cross-section area, moment of inertia, polar moment of inertia, translational displacements and rotational displacements per unit length of an element, respectively.

The elastic potential energy including torsional and axial displacements may be written as,

$$U^e = \frac{1}{2}\int_0^{L^e} EI\left(\left(\frac{\partial\theta_y}{\partial x}\right)^2 + \left(\frac{\partial\theta_z}{\partial x}\right)^2\right)dx + \frac{1}{2}\int_0^{L^e} EA^e\left(\frac{\partial u_x}{\partial x}\right)dx + \frac{1}{2}\int_0^{L^e} \kappa GA^e\left(\left(\frac{\partial u_y}{\partial x} - \theta_z\right)^2 + \left(\frac{\partial u_z}{\partial x} + \theta_y\right)^2\right)dx + \frac{1}{2}\int_0^{L^e} GI_p\left(\frac{\partial\theta_x}{\partial x}\right)^2 dx \quad (3)$$

where E is the elastic modulus, I the area moment of inertia, G the shear modulus, and κ the shear form factor.

In order to derive the equation of motion for the shaft element, the Lagrange's equation is applied to T^e and U^e. Specific matrices for the Timoshenko bean element can be found in [5, 66].

2.2. Axisymmetric Solid Element Modeling of Rotors

Extreme performance and efficiency requirements demand modern rotor designs to be lighter-weight and operate at increasingly higher speeds. This may require shafts to have complex thin-wall and thin-disk designs and to operate through more resonant speeds. Active magnetic bearing mounted machinery is also increasing, which requires careful design of modes well above the operating speed to maintain stable levitation control. Those evolving requirements may not be adequately met by beam FE models and instead require more general solid FE models. The axisymmetric solid harmonic FE model is a good replacement of beam FE models. Generally speaking, the axisymmetric element is one type of the solid elements that can fill a 3D space. The only limitation is that the 3D space must be axisymmetric. Shaft warping and flexural disk modes, which cannot be modeled with beam elements due to violation of the beam assumption, can be

modeled using axisymmetric elements. This yields higher accuracy for rotor dynamic response prediction. The present paper provides theoretical development and numerical examples for an extended axisymmetric solid harmonic element especially useful for high-fidelity modeling of flexible rotors with shafts, disks, and general bearings.

2.2.1. Theory and basic formulation

As pointed out in [12, 67, 68], a 3D axisymmetric structure can be formed by rotating the longitudinal semi-section plane about the axis of symmetry. Furthermore, the rotor displacements of the longitudinal semi-section plane can be expanded circumferentially using the Fourier series in the angle taken about the axis of symmetry. That being said, a 2D plane mesh filled with axisymmetric elements can represent a 3D rotor. More details are given in [12, 67].

In the present work, the longitudinal semi-section region of a rotor is filled with linear triangle elements in order to cover irregularly shaped areas. Just to clarify, the methodology of the axisymmetric FE formulation presented here is applicable not only to the triangle element type but also to other axisymmetric element types. As is shown in Figure 3, the shaded area with nodes 1, 2 and 3 represents the three-node triangular element. The displacements of each element are attained through the superposition of both symmetric and antisymmetric components at all harmonics, which may be expressed as,

$$\{U_R^e\} = \begin{bmatrix} u_r \\ u_z \\ u_\theta \end{bmatrix} = \begin{bmatrix} \sum_{m=0}^{\infty}(U_{mrS}\, cos(m\theta) + U_{mrA}\, sin(m\theta)) \\ \sum_{m=0}^{\infty}(U_{mzS}\, cos(m\theta) + U_{mzA}\, sin(m\theta)) \\ \sum_{m=0}^{\infty}(U_{m\theta S}\, sin(m\theta) - U_{m\theta A}\, cos(m\theta)) \end{bmatrix} \quad (4)$$

where u_r, u_z and u_θ represent the radial, axial and circumferential displacements, respectively. U_{mij} with $i= r, z, \theta$ representing the radial, axial, or circumferential displacement component and $j= S, A$ representing the symmetric or antisymmetric displacement component is the node degree-of-freedom (DOF) of an element for the mth harmonics.

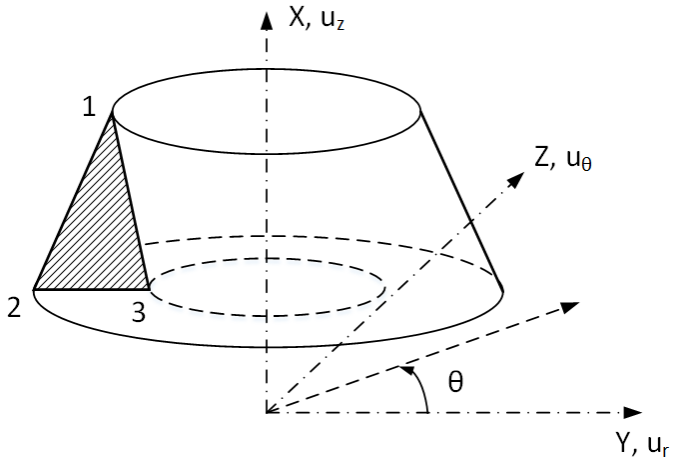

Figure 3. Solid of revolution based on three-node triangular axisymmetric elements. Reprinted from Ref. [69].

Then element displacements $\{U_R^e\}$ can be further approximated by,

$$\{U_R^e\} = [N]\{q^e\} \tag{5}$$

where the node DOF vector of the element, $\{q^e\}$, and the corresponding shape function, $[N]$, can be found in [11, 14].

The harmonics of interest in this work are m=0, 1, 2. The zeroth order harmonics contribute to a radial expansion u_0, an axial displacement v_0, and a torsional rotation w_0. Both first and second order harmonics describe the displacements in the YZ plane and

the rotations about the X. axis of the finite element. Below are the two reasons to set m=0, 1, 2. Firstly, extensive numerical tests have shown that including higher harmonics, above 2, significantly increases computation time, but yields little in terms of increased accuracy of rotor dynamic analysis [9, 12, 25]. Secondly, although the first order harmonics are the only harmonics of interest for a shaft in purely lateral bending scenarios [9, 14], this may be insufficient in the case of thin-walled shafts as thin-walled structures are prone to warping. A flexible disk may have local flexural modes below the critical speeds, which requires an axisymmetric FE model with higher harmonics. Therefore, the second order harmonics representing the local modes that are uncoupled from the lateral modes of the shaft are employed. In addition, the zeroth order harmonics are included in order to account for the centrifugal stress-stiffening effects.

The axisymmetric FE rotor model can be obtained by assembling the equations of motion of all elements. The equation of motion for an individual axisymmetric element may be expressed as,

$$[M_R^e]\{\ddot{U}_R^e\} + [C_R^e]\{\dot{U}_R^e\} + [K_R^e]\{U_R^e\} = \{f_R^e\} \tag{6}$$

where $[M_R^e]$, $[C_R^e]$ and $[K_R^e]$ represent the total mass, damping and stiffness matrices of the rotor element, respectively. $\{f_R^e\}$ is the external force vector. $\{U_R^e\}$ is obtained by assembling the displacements at all harmonics.

In regard to Eq. (6), the total damping matrix $[C_R^e]$ contains gyroscopic matrix and viscous structural damping matrix (neglectable for most rotors). The total stiffness matrix $[K_R^e]$ contains the elastic stiffness, centrifugal stress-stiffening, and spin-softening matrices. $\{f_R^e\}$ contains unbalanced forces and bearing forces. The damping and stiffness

matrices derived from bearing forces will be integrated into $[C_R^e]$ and $[K_R^e]$, respectively. The formulations of the mass, gyroscopic and elastic stiffness matrices have been provided in [9, 14]. However, other important contributions to the rotating system element matrices were not included in those references, such as bearing forces, centrifugal stress-stiffening, and spin-softening. These matrices will be derived and presented in this work.

2.2.2. Mesh generation tools

In regard to the axisymmetric element model, an appropriate mesh model is desirable. Mesh2D [70] is a good mesh generation tool, which is able to tune the mesh size and generate an 2D triangle mesh. The well-established Delaunay triangulation and refinement algorithms are implemented in the Mesh2D code. High-quality constrained triangulations are automatically generated.

In addition, SolidWorks is capable of generating both 2D triangular element mesh and 3D tetrahedral element mesh. The mesh models of the rotor or support structures can be exported as TXT files and extracted by our in-house rotor dynamics software.

2.2.3. Bearing attachment

One of the key factors that affect the prediction of critical speeds is the approach of attaching linear force coefficients of transient bearing forces to the shaft model. Bearing coefficients or forces are connected at a node corresponding to the bearing centerline in a shaft beam FE model, regardless of whether the shaft is solid or hollow. In contrast, there are many nodes at the bearing centerline position in an axisymmetric

FE model, but none on the shaft axis if the shaft is hollow. One approach is to connect the bearing coefficients or force to a single surface node of the journal. However, this may be inadequate for a thin-walled shaft that may distort locally or a bearing with a large longitudinal length. Therefore, an improved approach is presented in Figure 4.

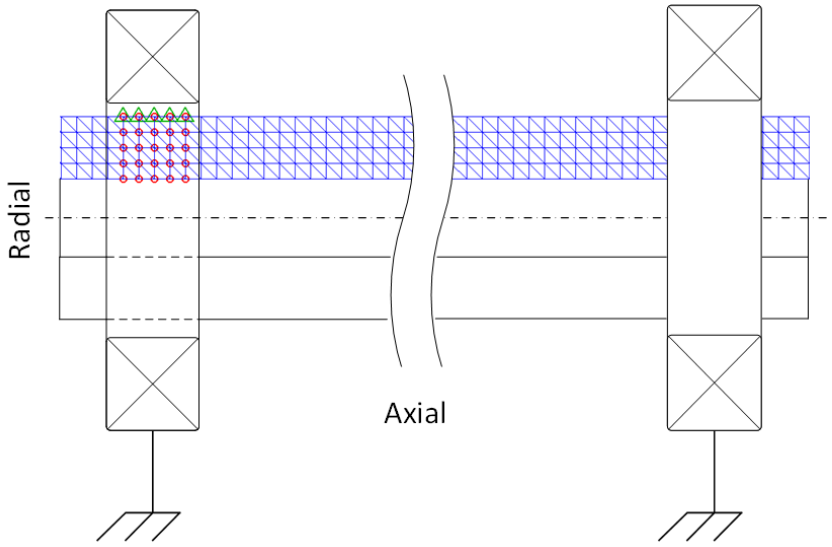

Figure 4. Mesh model of a hollow shaft supported by two bearings: green triangles represent the surface nodes to which the bearing forces are distributed, and red circles denote the nodes of the stiffened elements. Reprinted from Ref. [69].

The damping and stiffness dynamic force coefficients of fluid film bearings and seals are generally measured or obtained by numerically solving Reynold's equation for pressure and integrating to obtain force. The Y and Z reaction forces exerted by the bearing on the journal are represented by the general linearized forces,

$$F_y = -K_{yy}w_y - K_{yz}w_z - C_{yy}\dot{w}_y - C_{yz}\dot{w}_z$$
$$F_z = -K_{zy}w_y - K_{zz}w_z - C_{zy}\dot{w}_y - C_{zz}\dot{w}_z \quad (7)$$

where w_y, w_z, $\dot{w}_y$ and $\dot{w}_z$ represent the Y and Z transverse displacements, and Y and Z velocities at the bearing centerline and at the center of the shaft, respectively. The challenge is how to "distribute" the dynamic coefficients, K_{yy}, K_{yz}, K_{zy}, K_{zz} (also called linear stiffness coefficients) and C_{yy}, C_{yz}, C_{zy}, C_{zz} (also called linear damping coefficients) over the axisymmetric FE journal surface nodes in a manner that yields the same forces as defined in Eq. (7). The following procedure and analysis are employed to fit the dynamic coefficients of a bearing in the rotor axisymmetric FE model.

As can be seen from Figure 5, the bearing forces F_y and F_z, which act on node P, translate from the cylindrical coordinates to the Cartesian coordinates as,

$$w_y^P = u_r^P \cos(\theta) - u_\theta^P \sin(\theta)$$

$$w_z^P = u_r^P \sin(\theta) + u_\theta^P \cos(\theta) \tag{8}$$

where the superscript represents node P. u_r^P and u_θ^P are scalar displacements of node P corresponding to the unit vectors e_r and e_θ in the cylindrical coordinates, respectively. u_r^P and u_θ^P can be decomposed into different harmonics by using Fourier series, which is similar to Eq. (4).

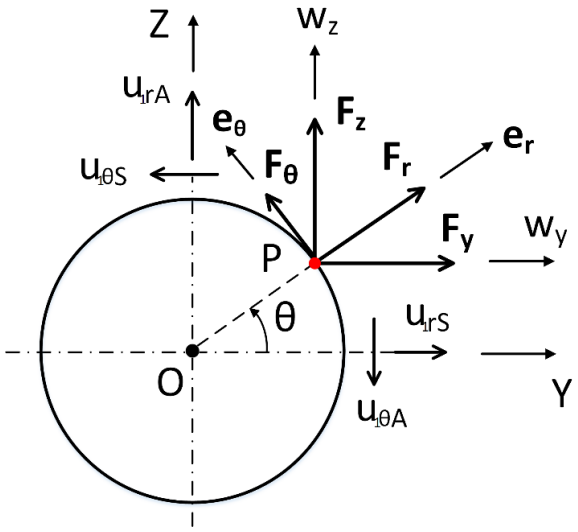

Figure 5. Bearing forces on the node of an axisymmetric element. Reprinted from Ref. [69].

Before applying stiffness and damping coefficients of a linear bearing model to an axisymmetric FE rotor, three prerequisites are clarified as follows. First of all, bearing forces act on the outer circumferential surface of a journal. Secondly, most rotating machines operate far below the critical speed for the local journal deformation modes. This factor leads to a practically appropriate assumption that the node circumferential circle at P may be assumed a rigid node circle moving with a constant displacement for all the nodes on the circle (also called rigid node circle). Finally, the expansion or shrink of the journal is generally negligible in comparison with lateral displacements caused by shaft bending. However, there are a few thermal expansion cases in which the expanding journal may have an impact on the rotor stability [71, 72]. Accordingly, an asymmetric journal model and probably transient analysis are required to investigate those minority cases. Based on the above three prerequisites, the first order harmonics, which contribute

to the lateral displacement, are used to approximate the total displacement of node P in the cylindrical coordinates, u_r^P and u_θ^P, as,

$$u_r^P = U_{1rS}^P cos(\theta) + U_{1rA}^P sin(\theta)$$

$$u_\theta^P = U_{1\theta S}^P sin(\theta) - U_{1\theta A}^P cos(\theta) \quad (9)$$

Substituting Eq. (9) into Eq. (8) yields,

$$w_y^P = U_{1rS}^P cos^2(\theta) - U_{1\theta S}^P sin^2(\theta) + \left(U_{1rA}^P + U_{1\theta A}^P\right) sin(\theta) cos(\theta)$$

$$w_z^P = U_{1rA}^P sin^2(\theta) - U_{1\theta A}^P cos^2(\theta) + \left(U_{1rS}^P + U_{1\theta S}^P\right) sin(\theta) cos(\theta) \quad (10)$$

Per the rigid node circle assumption, the lateral displacements w_y and w_z are constant for all nodes (i.e. all θ) on the rigid circle. This implies that w_y and w_z shown in Eq. (10) are constant regardless of θ. As a result, the relationship between displacement components can be obtained as,

$$U_{1\theta S}^P = -U_{1rS}^P$$

$$U_{1\theta A}^P = -U_{1rA}^P \quad (11)$$

The bearing force acting on node P is expressed as,

$$dF_y^P = \frac{K_{yy} w_y^P + K_{yz} w_z^P}{2\pi} d\theta$$

$$dF_z^P = \frac{K_{zy} w_y^P + K_{zz} w_z^P}{2\pi} d\theta \quad (12)$$

As shown in Figure 5, the bearing forces, F_y and F_z translate from Cartesian coordinates to the cylindrical coordinates. Then applying the forces circumferentially to the rigid circle yields,

$$Q_j^P = \int_0^{2\pi} dF_r^P \, \vec{e}_r \cdot \frac{\partial u_r^P}{\partial q_j} \vec{e}_r + \int_0^{2\pi} dF_\theta^P \, \vec{e}_\theta \cdot \frac{\partial u_\theta^P}{\partial q_j} \vec{e}_\theta \quad (13)$$

where $\vec{e}_r$ and $\vec{e}_\theta$ (equivalent to bold $\boldsymbol{e_r}$ and $\boldsymbol{e_\theta}$ shown in Figure 5) represent unit vectors in the radial and tangential directions, respectively. The generalized bearing force Q_j^P, which corresponds to the jth DOF q_j, contains bearing stiffness coefficients and displacement DOF terms. Substituting Eqs. (4), (10), (11) and (12) in Eq. (13) yields Q_j^P, the formulation of which is provided in Appendix A. By adding Q_j^P into $\{f_R^e\}$ of Eq. (6) and rearranging the DOF related terms, the bearing stiffness coefficients are integrated into $[K_R^e]$. The damping coefficients of the bearing can be obtained by simply replacing the stiffness coefficients K with C as the derivation for the damping coefficients follows the same path as the stiffness coefficients.

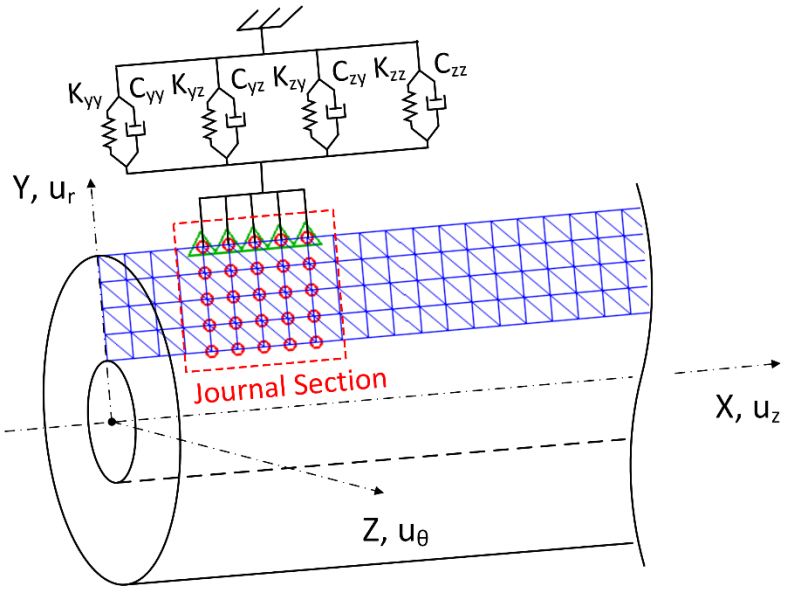

Figure 6. Add stiffness and damping coefficients of a bearing to the nodes in the longitudinal semi-section of a shaft: green triangles and red circles represent the surface nodes and the stiffened element nodes, respectively. Reprinted from Ref. [69].

As depicted by Figure 6, the stiffness coefficients, K_{yy}, K_{yz}, K_{zy}, K_{zz} and the damping coefficients, C_{yy}, C_{yz}, C_{zy}, C_{zz} of a bearing are equally divided by five, which equals the number of surface nodes, and are added to each surface node on the journal. Bearing lubricant induced forces occur on the longitudinal length of the shaft inside the bearing, which is also called the journal. The bearing forces are assumed to be equally distributed (the distribution proportion is adjustable) on the surface nodes of the journal in the axisymmetric element model. A thin-walled journal model may also be artificially stiffened for certain types of bearings. The degree of artificial stiffening (an increase in modulus of elasticity) can be varied by the analyst to balance excessive journal deformation vs. the increased numerical integration time that may result from artificial stiffening [25] (Book section 4.8.17).

The bearing forces are applied to the journal in a distributed manner because applying the forces or linearized force coefficients (stiffness, damping, and inertia) at a single node may result in excessive local deformation at the point of application especially when the journal is thin-walled and the bearing forces or dynamic coefficients are large. The simulation results presented in Section 5.2 will illustrate this by an example.

2.3. Centrifugal Stress-Stiffening

In this section, the prior axisymmetric solid harmonic FE formulation of a flexible rotor [11, 14, 73] is improved by including the centrifugal stress-stiffening effects.

2.3.1. Phenomenon and problem overview

Centrifugal stress-stiffening may have a significant effect on rotor dynamic response especially at high spin rates and for highly flexible disks and shafts. Consider the rotating shaft-disk system shown in Figure 7. The disk bends with an axial displacement u. The radial displacement Δr and the displacement along the resultant deformation direction ΔL are related by,

$$\Delta L = \Delta r\sqrt{1+\left(\frac{\partial u}{\partial r}\right)^2} \simeq \Delta r\left(1+\frac{1}{2}\left(\frac{\partial u}{\partial r}\right)^2\right) \tag{14}$$

The disk is radially under tensile load due to the centrifugal forces, which creates a restoring force for axial deflection and hence raises the disk's bending stiffness and natural frequencies for disk flexural and axial modes. As the tensile load causes radial strain expansion, only the component of the zeroth order harmonics is associated with the centrifugal stress-stiffening.

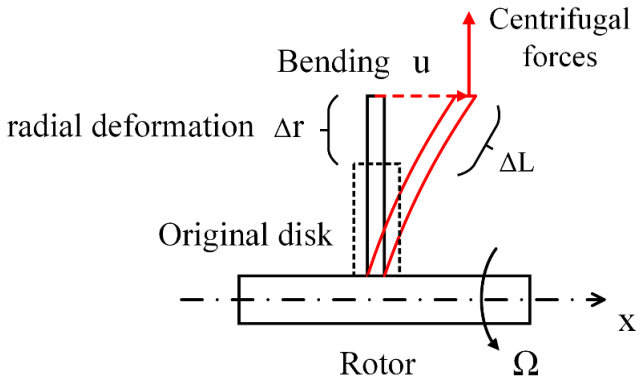

Figure 7. Disk stress-stiffening effect caused by centrifugal forces.

2.3.2. Strain energy due to centrifugal forces

To include the centrifugal stress-stiffening effects, an improved formulation of the axisymmetric FE rotor model in the cylindrical coordinate system is presented in this section, as an extension to Cook et al.'s work [12]. The centrifugal forces cause the initial strain ε_0 and the initial stress σ_0 prior to the bending of the rotor, as is shown in Figure 8.

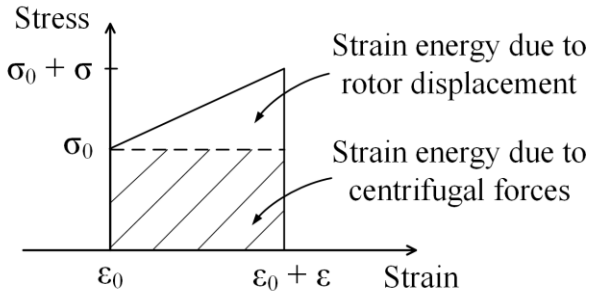

Figure 8. Strain energy due to centrifugal forces. Reprinted from Ref. [69].

As the rotor has further deformations on the basis of the initial strain, the strain energy U that excludes the elastic potential energy caused by centrifugal forces prior to rotor bending consists of two parts: one caused by centrifugal forces (represented by the shaded area in Figure 8), and the other resulting from rotor displacement (represented by the blank area in Figure 8). The strain energy of the spinning rotor when bending, U, may be expressed as,

$$U = \frac{1}{2}\int_V \{\varepsilon\}^T \{\sigma\} dV + \int_V \{\varepsilon\}^T \{\sigma_0\} dV \tag{15}$$

where the first and second components represent the two parts of the elastic potential energy shown in Figure 8, respectively. $\{\sigma\}$ and $\{\varepsilon\}$ are stress and strain vectors that exclude the initial stress and strain prior to rotor bending, respectively. $\{\sigma_0\}$ are the initial stress induced by centrifugal forces.

The linear small strain (also called infinitesimal strain) model that is widely used in engineering (including rotor dynamics) may not be an appropriate model for rotors with highly flexible disks or blades. This is because the small rotation assumption for the small strain model may be violated when the amount of rotation (such as for bending of a flexible disk) becomes large. A remedy is to employ the Green strain model in mechanics.

Consider the deformation gradient $\tilde{F}$ in the cylindrical coordinate system. $\tilde{F}$can be separated into rigid body translations and rotations from deformations and may be expressed as,

$$\tilde{F}_{ij} = \tilde{\delta}_{ij} + \tilde{u}_{i,j} \tag{16}$$

where $\tilde{\delta}_{ij}$ is Kronecker delta, i, j=r, z, or θ, and $\tilde{u}_{i,j}$ is the derivative of each component of the displacement $\tilde{u}_i$ after deformation with respect to each component of the cylindrical coordinates vector j. The corresponding matrix form may be written as,

$$[\tilde{F}] = [\tilde{I}] + [\nabla\tilde{u}] = \begin{bmatrix} \left(1+\frac{\partial u_r}{\partial r}\right) & \frac{\partial u_r}{\partial z} & \left(\frac{1}{r}\frac{\partial u_r}{\partial \theta} - \frac{u_\theta}{r}\right) \\ \frac{\partial u_z}{\partial r} & \left(1+\frac{\partial u_z}{\partial z}\right) & \frac{1}{r}\frac{\partial u_z}{\partial \theta} \\ \frac{\partial u_\theta}{\partial r} & \frac{\partial u_\theta}{\partial z} & \left(1+\frac{1}{r}\frac{\partial u_\theta}{\partial \theta}+\frac{u_r}{r}\right) \end{bmatrix} \tag{17}$$

where $[\tilde{I}]$ and $[\nabla\tilde{u}]$ are the matrix form of $\tilde{\delta}_{ij}$ and $\tilde{u}_{i,j}$, respectively. The strain matrix of the Green strain model is defined as,

$$[\tilde{\varepsilon}] = \frac{1}{2}\left([\tilde{F}]^T[\tilde{F}] - [\tilde{I}]\right) \tag{18}$$

Substituting Eq. (17) in Eq. (18) yields,

$$[\tilde{\varepsilon}] = \begin{bmatrix} \tilde{\varepsilon}_{rr} & \tilde{\varepsilon}_{rz} & \tilde{\varepsilon}_{r\theta} \\ \tilde{\varepsilon}_{zr} & \tilde{\varepsilon}_{zz} & \tilde{\varepsilon}_{z\theta} \\ \tilde{\varepsilon}_{\theta r} & \tilde{\varepsilon}_{\theta z} & \tilde{\varepsilon}_{\theta\theta} \end{bmatrix} \tag{19}$$

where the components of the tensor strain $\tilde{\varepsilon}_{ij}$ represent the deformation in i direction with respect to the coordinates vector j. The tensor-based strain $\tilde{\varepsilon}_{ij}$ are expanded for clarification of first and second order strain components as,

$$\tilde{\varepsilon}_{rr} = \frac{\partial u_r}{\partial r} + \frac{1}{2}\left[\left(\frac{\partial u_r}{\partial r}\right)^2 + \left(\frac{\partial u_z}{\partial r}\right)^2 + \left(\frac{\partial u_\theta}{\partial r}\right)^2\right]$$

$$\tilde{\varepsilon}_{zz} = \frac{\partial u_z}{\partial z} + \frac{1}{2}\left[\left(\frac{\partial u_r}{\partial z}\right)^2 + \left(\frac{\partial u_z}{\partial z}\right)^2 + \left(\frac{\partial u_\theta}{\partial z}\right)^2\right]$$

$$\tilde{\varepsilon}_{\theta\theta} = \frac{u_r}{r} + \frac{1}{r}\frac{\partial u_\theta}{\partial \theta} + \frac{1}{2r^2}\left[\left(u_r + \frac{\partial u_\theta}{\partial \theta}\right)^2 + \left(u_\theta - \frac{\partial u_r}{\partial \theta}\right)^2 + \left(\frac{\partial u_z}{\partial \theta}\right)^2\right] \tag{20}$$

$$\tilde{\varepsilon}_{rz} = \frac{1}{2}\left(\frac{\partial u_r}{\partial z} + \frac{\partial u_z}{\partial r}\right) + \frac{1}{2}\left(\frac{\partial u_r}{\partial r}\frac{\partial u_r}{\partial z} + \frac{\partial u_z}{\partial r}\frac{\partial u_z}{\partial z} + \frac{\partial u_\theta}{\partial r}\frac{\partial u_\theta}{\partial z}\right)$$

$$\tilde{\varepsilon}_{z\theta} = \frac{1}{2}\left(\frac{1}{r}\frac{\partial u_z}{\partial \theta} + \frac{\partial u_\theta}{\partial z}\right) + \frac{1}{2r}\left[\frac{\partial u_\theta}{\partial z}\left(u_r + \frac{\partial u_\theta}{\partial \theta}\right) + \frac{\partial u_r}{\partial z}\left(-u_\theta + \frac{\partial u_r}{\partial \theta}\right) + \frac{\partial u_z}{\partial z}\frac{\partial u_z}{\partial \theta}\right]$$

$$\tilde{\varepsilon}_{r\theta} = \frac{1}{2}\left(\frac{1}{r}\frac{\partial u_r}{\partial \theta} - \frac{u_\theta}{r} + \frac{\partial u_\theta}{\partial r}\right) + \frac{1}{2r}\left[\frac{\partial u_\theta}{\partial r}\left(u_r + \frac{\partial u_\theta}{\partial \theta}\right) + \frac{\partial u_r}{\partial r}\left(-u_\theta + \frac{\partial u_r}{\partial \theta}\right) + \frac{\partial u_z}{\partial r}\frac{\partial u_z}{\partial \theta}\right] \tag{21}$$

The tensor-based shear terms in Eq. (21) may be replaced by engineering shear strains by doubling the strains. Only the second order terms of $\tilde{\varepsilon}$ are related to the centrifugal forces induced strains in rotor bending [12]. Replacing tensor-based shear terms in $\tilde{\varepsilon}$ with engineering shear strains yields the second order strains as,

$$\varepsilon_{2r} = \frac{1}{2}\left[\left(\frac{\partial u_r}{\partial r}\right)^2 + \left(\frac{\partial u_z}{\partial r}\right)^2 + \left(\frac{\partial u_\theta}{\partial r}\right)^2\right]$$

$$\varepsilon_{2z} = \frac{1}{2}\left[\left(\frac{\partial u_r}{\partial z}\right)^2 + \left(\frac{\partial u_z}{\partial z}\right)^2 + \left(\frac{\partial u_\theta}{\partial z}\right)^2\right]$$

$$\varepsilon_{2\theta} = \frac{1}{2r^2}\left[\left(u_r + \frac{\partial u_\theta}{\partial \theta}\right)^2 + \left(u_\theta - \frac{\partial u_r}{\partial \theta}\right)^2 + \left(\frac{\partial u_z}{\partial \theta}\right)^2\right]$$

$$\gamma_{2rz} = \frac{\partial u_r}{\partial r}\frac{\partial u_r}{\partial z} + \frac{\partial u_z}{\partial r}\frac{\partial u_z}{\partial z} + \frac{\partial u_\theta}{\partial r}\frac{\partial u_\theta}{\partial z}$$

$$\gamma_{2z\theta} = \frac{1}{r}\left[\frac{\partial u_\theta}{\partial z}\left(u_r + \frac{\partial u_\theta}{\partial \theta}\right) + \frac{\partial u_r}{\partial z}\left(-u_\theta + \frac{\partial u_r}{\partial \theta}\right) + \frac{\partial u_z}{\partial z}\frac{\partial u_z}{\partial \theta}\right]$$

$$\gamma_{2r\theta} = \frac{1}{r}\left[\frac{\partial u_\theta}{\partial r}\left(u_r + \frac{\partial u_\theta}{\partial \theta}\right) + \frac{\partial u_r}{\partial r}\left(-u_\theta + \frac{\partial u_r}{\partial \theta}\right) + \frac{\partial u_z}{\partial r}\frac{\partial u_z}{\partial \theta}\right] \quad (22)$$

where the subscript 2 represents the second order strain. ε_{2r}, ε_{2z} and $\varepsilon_{2\theta}$ correspond to the second order normal strain terms $\tilde{\varepsilon}_{rr}$, $\tilde{\varepsilon}_{zz}$ and $\tilde{\varepsilon}_{\theta\theta}$, respectively. γ_{2rz}, $\gamma_{2z\theta}$ and $\gamma_{2r\theta}$ correspond to the second order shear strain terms $\tilde{\varepsilon}_{rz}$, $\tilde{\varepsilon}_{z\theta}$ and $\tilde{\varepsilon}_{r\theta}$, respectively.

The strain energy due to the bending of the rotor that undergoes centrifugal forces may be expressed as,

$$U_\sigma^e = \int_{V^e} \{\varepsilon_2^{\mathrm{e}}\}^T \{\sigma_0^{\mathrm{e}}\} dV \quad (23)$$

where V is the bounded volume region, and the superscript e represents the element. The strain vector $\{\varepsilon_2\}$ and stress vector $\{\sigma_0\}$ for isotropic homogeneous elastic materials are of the following vector form,

$$\{\varepsilon_2^{\mathrm{e}}\} = [\varepsilon_{2r},\ \varepsilon_{2z},\ \varepsilon_{2\theta},\ \gamma_{2rz},\ \gamma_{2z\theta},\ \gamma_{2r\theta}]^T$$

$$\{\sigma_0^{\mathrm{e}}\} = [\sigma_{0r},\ \sigma_{0z},\ \sigma_{0\theta},\ \tau_{0rz},\ \tau_{0z\theta},\ \tau_{0r\theta}]^T \quad (24)$$

The elastic potential energy shown in Eq. (23) is derived from Eq. (15) by excluding the first order strain terms.

2.3.3. Formulation of stress-stiffening effects

The strain energy due to the centrifugal stress-stiffening effects will ultimately lead to the stress-stiffening stiffness matrix that differs from the structural stiffness matrix in the equation of motion for the rotor. The way to derive this stiffness matrix is presented below. Although the derivation is based on the axisymmetric harmonic element, the approach can be applied to other solid element methods.

The centrifugal forces corresponding to the jth node DOF may be expressed as,

$$Q_{Vj}^{e} = \int_{V^e} \left(dF_{Vr} \vec{e}_r \cdot \frac{\partial u_r}{\partial q_j^e} \vec{e}_r \right)$$

$$= \int_0^{2\pi} \int_{A^e} \rho \Omega^2 r \sum_{m=0}^{N} \left(\frac{\partial U_{mrS}}{\partial q_j^e} cos(m\theta) + \frac{\partial U_{mrA}}{\partial q_j^e} sin(m\theta) \right) dA d\theta \quad (25)$$

where dF_{Vr} is centrifugal forces per unit volume and can be expressed as $dF_{Vr} = \rho \Omega^2 r$. q_j^e is the jth node DOF of the element. U_{mrS} and U_{mrA} are defined in Eq. (4). It can be seen from Eq. (25) that the integral over the circumferential angle $\theta = 0 \sim 2\pi$ eliminates the first and second order harmonics. That said, only the zeroth harmonics contribute to the initial stress and strain caused by centrifugal forces.

Applying the Lagrange's equations to the strain energy caused by centrifugal forces yields,

$$\frac{\partial U_0^e}{\partial q_j^e} = Q_{Vj}^e \text{ with } U_0^e = \frac{1}{2} \int_{V^e} \{\varepsilon_0^e\}^T \{\sigma_0^e\} dV \quad (26)$$

where U_0^e represents the elastic strain energy of the element caused by centrifugal forces prior to the bending of the rotor. σ_0^e and ε_0^e are initial stress and strain caused by centrifugal forces, respectively. The node displacements induced by centrifugal forces,

$\{U_R^e\}$, can be solved for based on Eq. (26). For isotropic homogeneous elastic materials, the initial stress, $\{\sigma_0^e\}$, can be obtained from,

$$\{\sigma_0^e\} = [D][\partial]\{U_R^e\} \tag{27}$$

where the linear stress-strain constitutive matrix $[D]$and partial derivative matrix $[\partial]$ are provided in Appendix A.

Substituting Eqs. (22), (24) and (27) in Eq. (23) yields the strain energy due to centrifugal forces, U_σ^e, as,

$$U_\sigma^e = \frac{1}{2}\int_{V^e}\{\delta_\sigma^e\}^T[S_\sigma^e]\{\delta_\sigma^e\}dV \tag{28}$$

where $[S_\sigma^e]$ represents the centrifugal stress matrix. $\{\delta_\sigma^e\}$ is the expanded strain vector derived from Eq. (22) by re-arranging the second order strain terms. Both are specified in Appendix A. $\{\delta_\sigma^e\}$ can be decomposed into,

$$\{\delta_\sigma^e\} = [\partial_\sigma]\{U_R^e\} = [\partial_\sigma](\sum_{m=0}^{N}[N_m]\{q_m^e\}) \tag{29}$$

By using the shape functions and node DOF shown in Eq. (5), U_σ^e can be further re-arranged as,

$$U_\sigma^e = \sum_{m=0}^{N}\frac{1}{2}\{q_m^e\}^T\left(\int_{V^e}[G_{\sigma m}^e]^T[S_\sigma^e][G_{\sigma m}^e]dV\right)\{q_m^e\} \tag{30}$$

The final form of U_σ^e shows that different harmonics are not coupled. This is expected from the statement made by [12] that different harmonics are uncoupled. From a mathematic perspective, the orthogonality of the harmonic contributions may be explained by,

$$q_m q_n \int_0^{2\pi} cos(m\theta)\, cos(n\theta)\, d\theta = 0$$

$$q_m q_n \int_0^{2\pi} cos(m\theta)\, sin(n\theta)\, d\theta = 0$$

$$q_m q_n \int_0^{2\pi} sin(m\theta)\, sin(n\theta)\, d\theta = 0 \tag{31}$$

where the harmonics numbers $m \neq n$. By expanding U_σ^e, it can be found that every coupling term containing $q_m q_n$ comes with the trigonometrical series as shown in Eq. (31). That being said, the coupling terms $q_m q_n$ eventually become zero, implying that the harmonics are uncoupled.

Applying Lagrange's equations to Eq. (30) yields the elemental centrifugal stress-stiffening matrix for the m th harmonics, $[K_{\sigma m}^e]$, as,

$$\frac{\partial U_\sigma^e}{\partial \{q_m^e\}} = [K_{\sigma m}^e] = \int_{V^e} [G_{\sigma m}^e]^T [S_{\sigma 0}^e][G_{\sigma m}^e] dV \tag{32}$$

where $\{q_m^e\}$ represents the DOF vector for the m th harmonics. The total DOFs q_j^e contain the DOF for all harmonics and thereby include $\{q_m^e\}$. $[K_{\sigma m}^e]$ is given in Appendix A. Although only the zeroth modes contribute to the initial centrifugal stress, the strain energy due to centrifugal forces for the bending rotor is contributed by all harmonics. $[K_{\sigma m}^e]$ is the final centrifugal stress-stiffening matrix that will be used in the equation of motion for the axisymmetric solid element model.

2.4. Spin-Softening Effects

In addition to the stress-stiffening effects, rotor spin induces so called spin-softening effects. The effects are most pronounced for flexible disks or large-diameter, thin-walled shafts.

2.4.1. Phenomenon and problem overview

For sake of illustration consider the simplified shaft-disk-mass system shown in Figure 9, which includes a concentrated mass at the tip of the disk and a massless-disk body oriented radially with respect to the axis of rotation.

The deflection of the disk, u may be expressed as,

$$\underbrace{(K_0 - \Omega^2 M)}_{K_1} u = \Omega^2 M r \tag{33}$$

where K_1 is the equivalent disk stiffness in the radial direction at the spin speed of $\Omega = 0\ rpm$. It can be seen from Eq. (33) that the equivalent disk stiffness changes from K_0 to K_1, implying a decrease in the effective stiffness of the attachment point of the mass, with increasing spin rate.

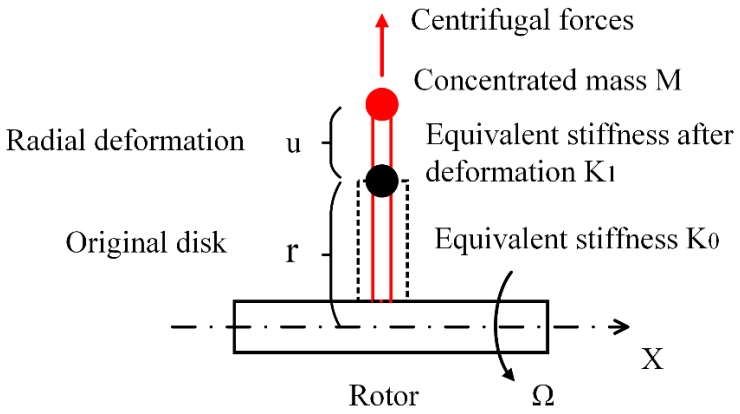

Figure 9. Rotating mass-spring system.

In this work, the spin-softening effects are formulated for the axisymmetric harmonic element. The modeling details will be presented in the next section.

2.4.2. Formulation of spin-softening effects

Prior publications [12, 15] provided qualitative discussions of this phenomenon, but did not develop a formal FE treatment for the spin-softening effects utilizing axisymmetric elements.

The additional body force ΔF_r results from the extension of the element beyond the initial element radius (distance between the element and the center line of the rotor), which is caused by centrifugal forces. However, unlike the centrifugal forces discussed in Eq. (25), ΔF_r is independent of the element radius r. This can be explained by,

$$F_r = \Omega^2 \int_{V^e} \rho(r + u_r) dV \Rightarrow \Delta F_r = \Omega^2 \int_{V^e} \rho u_r dV \tag{34}$$

where u_r are radial displacement of the element with respect to the axis of symmetry. Then the generalized external load Q_S^e may be written as,

$$Q_{Sj}^e = \int_{V_e} d(\Delta F_r)\vec{e}_r \cdot \frac{\partial u_r}{\partial q_j^e}\vec{e}_r = \int_0^{2\pi} \int_{A^e} \rho\Omega^2 u_r \frac{\partial u_r}{\partial q_j^e} dA d\theta \tag{35}$$

where the subscript j indicates jth node DOF of the element.

Transforming Eq. (35) to the following matrix form,

$$\underset{18\times1}{\{Q_S^e\}} = \int_0^{2\pi} \int_{A^e} \underset{3\times18}{[N]^T} \begin{bmatrix} \rho\Omega^2 & 0 & 0 \\ 0 & 0 & 0 \\ 0 & 0 & 0 \end{bmatrix} \underset{3\times1}{\{U_R^e\}} dA d\theta \tag{36}$$

where $[N]$ is a shape function. $\{U_R^e\}$ is defined in Eq. (5) as the displacement DOF of a rotor element. In regard to the Lagrange's equations, $\{Q_S^e\}$ shown in Eq. (36) may be included as external load, leading to the elemental spin-softening matrix for the mth harmonics, $[K_{\Omega m}^e]$, as,

$$[K_{\Omega m}^{e}] = \frac{\partial\{Q_S^e\}}{\partial\{q_m^e\}} = \int_{V_e}[N_m]^T \begin{bmatrix} \rho\Omega^2 & 0 & 0 \\ 0 & 0 & 0 \\ 0 & 0 & 0 \end{bmatrix} [N_m] dV \quad (37)$$

Extra attention needs be given to the zeroth harmonics, which have a different formulation. $[K_{\Omega m}^{e}]$ is given in Appendix A.

By utilizting the improved axisymmetric FE model, a specialized rotor dynamic software program is developed. Various rotor systems that are comprised of thin-walled shafts and flexible disks will be investigated in Chapter 5. The conclusions drawn from the simulation results should provide designers with guidelines for when and how to use a solid FE rotor model instead of a beam FE rotor mode.

2.5. Hydrodynamic Fluid Film Bearings

Hydrodynamic fluid film bearings, such as fixed-pad and tilting-pad bearings, are widely used on heavy duty rotating machines.

In linear rotor dynamics, a hydrodynamic fluid film bearing is greatly simplified to be an eight-coefficient bearing model [37], which includes four stiffness coefficients, K_{YY}, K_{YZ}, K_{ZY}, and K_{ZZ}, and four damping coefficients, C_{YY}, C_{YZ}, C_{ZY}, and C_{ZZ}. The eight coefficients are added to the stiffness and damping matrices corresponding to the node in the rotor FE mesh that the bearing is attached to.

Although the eight coefficients vary in a linear manner with the spin speed of the rotor, bearing forces are nonlinear in nature and may have strong nonlinearity in the special situations such as under large support structure motion. A short bearing approximation [74] was used to approximate bearing nonlinearity. However, the approximation only applies for bearings having the ratio of length vs. diameter < 0.5

[37] or even less than 0.25 [47] and an eccentricity ratio < 0.7 [37]. In fact, a ratio of bearing length vs. diameter larger than 0.25 or even 0.5 is commonly seen in industry.

A nonlinear hydrodynamic journal bearing FE model, as a remedy for the eight-coefficient bearing model and short bearing approximation, will be introduced in this section.

2.5.1. Introduction to lubrication theory

As shown in Figure 10, the principle of the hydrodynamic lubrication can be characterized in brief as lubrication fluids flowing into a wedge-shaped narrow gap between the upper surface (journal surface) and lower surface (bearing pad surface). The gap (also called pad clearance) is extremely small in comparison with the bearing diameter. More details can be found in [75, 76].

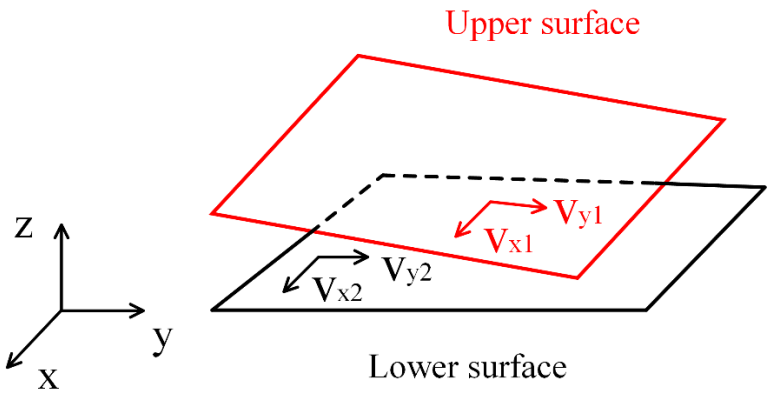

Figure 10. Lubrication between two surfaces.

The fluid (lubricant) film with high pressure supports the rotor and lubricates the rotating journal. The pressure of the fluid film can be derived from the Reynolds equations with the following assumptions:

(a) iso-viscous Newtonian fluid,

(b) ignoring inertial forces,

(c) incompressible lubricant,

(d) viscosity independent of fluid film height (z direction),

(e) spatially independent slider velocities in x and y directions.

The Reynold's equation applied in rotor dynamics may be written as,

$$\frac{\partial}{\partial y}\left(\frac{h^3}{12\mu}\cdot\frac{\partial p}{\partial y}\right)+\frac{\partial}{\partial x}\left(\frac{h^3}{12\mu}\cdot\frac{\partial p}{\partial x}\right)=\bar{v}_y\frac{\partial h}{\partial y}+\bar{v}_x\frac{\partial h}{\partial x}+\frac{\partial h}{\partial t} \tag{38}$$

where p is lubricant pressure, h the fluid film thickness, μ the absolute/dynamic viscosity. $\bar{v}_x$ and $\bar{v}_y$ are the mean values of the velocities of the upper and lower surfaces and can be expressed as,

$$\bar{v}_x=\frac{v_{x1}+v_{x2}}{2} \tag{39}$$

$$\bar{v}_y=\frac{v_{y1}+v_{y2}}{2} \tag{40}$$

where v_{x1}, v_{x2}, v_{y1} and v_{y2} are the velocities of the surfaces shown in Figure 10.

2.5.2. Finite element modeling of hydrodynamic journal bearing

A brief introduction to a nonlinear FE fluid film model is given in this section. More details are provided in [77]. As is shown in Figure 11, the beginning angle θ_{Bi} and the ending angle θ_{Ei} for pad i indicate the circumferential region of the lubricant film.

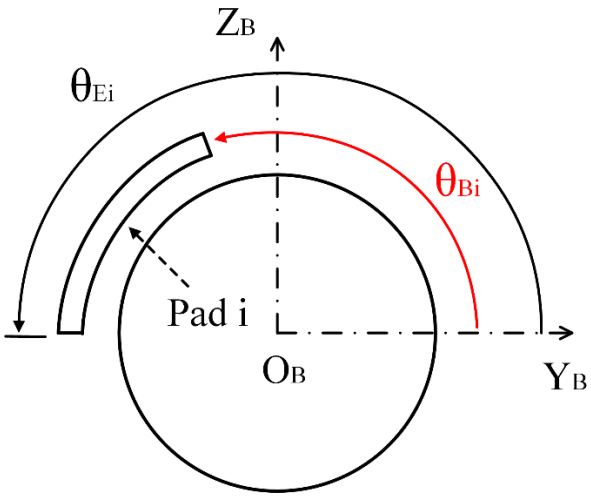

Figure 11. Beginning and ending angles of pad *i*.

The lubricant film thickness h_B is correlated with the pad clearance C_P, the preload factor M_P, the axial position x_B, the circumferential position y_B (position in Y direction after unfolding the fluid film circumferentially), and the fluid element circumferential angle θ. h_B may be expressed as,

$$h_B = C_P - x_B\, cos(\theta) - y_B\, sin(\theta) - C_P M_P\, cos(\theta - \theta_C) \tag{41}$$

where

$$M_p = 1 - \frac{C_B}{C_P} \tag{42}$$

C_B is the bearing clearance. θ_C is the center angle of the fluid film on the pad. If there is zero offset, θ_C is equal to the mean value of θ_{Bi} and θ_{Ei}.

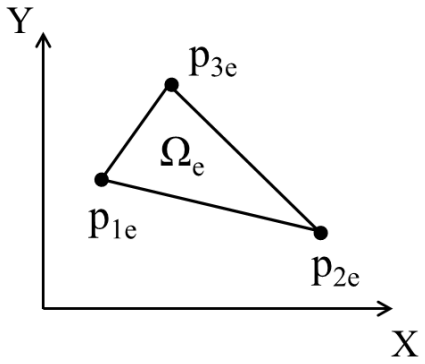

Figure 12. Three-node triangle element for fluid pressure interpolation.

For a linear 2D three-node triangle element shown in Figure 12, the governing equation of the bearing FE model is given as,

$$[K_b^e]\{p_b^e\} = \{B_b^e\} + \{S_b^e\} + \{L_b^e\} \tag{43}$$

where

$$[K_b^e] = \frac{h_e^3}{12\mu_e}\int_{\Omega_e}\left(\frac{\partial[N]^T}{\partial x}\frac{\partial[N]}{\partial x} + \frac{\partial[N]^T}{\partial y}\frac{\partial[N]}{\partial y}\right)dxdy \tag{44}$$

wedge effect: $$\{B_b^e\} = h_e\int_{\Omega_e}\left(\bar{u}\frac{\partial[N]}{\partial x} + \bar{v}\frac{\partial[N]}{\partial y}\right)dxdy \tag{45}$$

squeeze effect: $$\{S_b^e\} = -\frac{\partial h_e}{\partial t}\int_{\Omega_e}[N]\,dxdy \tag{46}$$

imposed boundary flow effect: $$\{L_b^e\} = -\int_{\Gamma_e} q_n[N]\,d\Gamma_q \tag{47}$$

shape function: $$[N] = [N_1 \quad N_2 \quad N_3] \tag{48}$$

where p_b^e represents the bearing pressure within the element. The viscosity μ_e is assumed constant within the element e. h_e denotes the film thickness. Ω_e is the lubricant domain. q_n is the volumetric flow rate per unit length along the boundry Γ_e.

Integrating the pressure of the fluid film yields the lubricant forces acting on the journal in Y and Z directions as,

$$F_{by} = -2\sum_{i=1}^{N_{pad}}\sum_{e=1}^{N_{ei}}\frac{1}{3}(p_{1ei}+p_{2ei}+p_{3ei})\Omega_{ei}\cdot cos\left(\theta_{Bi}+\frac{Y_{ei}}{R_j}\right) \quad (49)$$

$$F_{bz} = -2\sum_{i=1}^{N_{pad}}\sum_{e=1}^{N_{ei}}\frac{1}{3}(p_{1ei}+p_{2ei}+p_{3ei})\Omega_{ei}\cdot sin\left(\theta_{Bi}+\frac{Y_{ei}}{R_j}\right) \quad (50)$$

where Y_{ei} represent Y coordinate of the centroid of element e in pad i. N_{pad} is the number of pads. N_{ei} is the number of elements in pad i. p_{1ei}, p_{2ei} and p_{3ei} represent the 3 nodal pressures of element e in pad i. Ω_{ei} is the area of element e in pad i.

Eqs. (49) and (50) can be used to calculate lubricant forces for a single pad. The total bearing forces are a sum of the lubricant forces of all pads. Note that the pressure of the fluid film is a nonlinear function of journal displacements though the pressure itself is linear in Reynolds equation. This can be explained by substituting Eq. (38) in Eq. (41) (substituting h_B for h). The fluid film thickness h is a nonlinear function of journal displacements x and y.

2.6. Support Structure

As a part of a rotating system, support structures such as a casing, foundation and base are usually considered as rigid bodies and fixed to the ground. However, the skyrocketing amount of light-weight structure applications raises the concern of the rotor dynamics community. The influences of flexible support structures on the dynamic behavior of a rotor system can be investigated by using special support structure modeling approaches. This section will present two support structure models, namely 3D solid element model and MIMO transfer function model.

2.6.1. 3D solid element model

Most support structures of rotating machines have complex geometries, for which a solid element model will be a good fit. In this work, linear tetrahedral elements shown in Figure 13 are employed to model support structures. Just to be clear, there are a few other solid elements that are superior to tetrahedral elements in terms of mesh size. For the same support structure, the tetrahedral element model generally requires more elements than the other solid element models such as the hexahedral element model. However, tetrahedral elements are friendly to most automatic mesh generation software algorithms in comparison with the hexahedral elements.

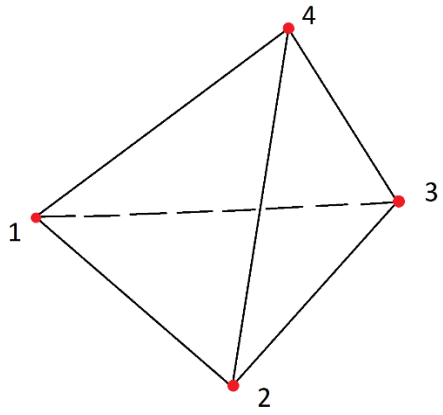

Figure 13. Linear tetrahedral element for support structure model.

The finite-element equation of motion is derived based on [67, 78, 79]. As shown in Figure 13, the four-node solid tetrahedron element is employed to fill 3D volume of the stator. For simplicity, the equation of motion for the support structure model is provided as,

$$[M_S]\{\ddot{q}\} + [C_S]\{\dot{q}\} + [K_S]\{q\} = \{f\} \tag{51}$$

where the DOFs of each element are given as,

$$\{q^e\} = \{u_{x1},\ u_{y1},\ u_{z1},\ u_{x2},\ u_{y2},\ u_{z2},\ u_{x3},\ u_{y3},\ u_{z3},\ u_{x4},\ u_{y4},\ u_{z4}\}^T \tag{52}$$

The detailed matrices can be found in [67, 78, 79].

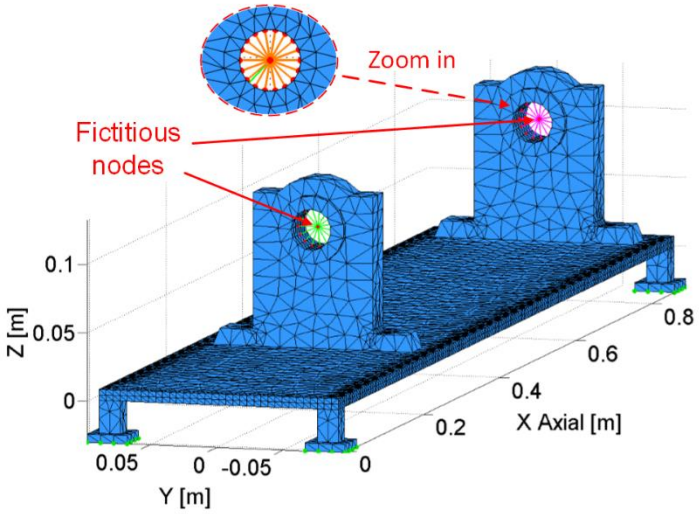

Figure 14. Solid tetrahedron element mesh model of the support structure with two fictitious nodes. Reprinted from Ref. [80].

The support structure including the bearing pedestal is first modeled with solid tetrahedron elements. Then, the fictitious node, which corresponds to the attachment point of each bearing, is created to connect the rotor and support structure. As can be seen from Figure 14, each fictitious node is connected by the rigid and massless beams (a fictitious beam web) with the nodes that are circumferentially around the bearing center. In calculation, these rigid beams can be treated as the ones with the stiffness coefficients that are much higher than the modulus of elasticity of the support structure. The governing equation of the support FE model may be written as,

$$[M_S]\{\ddot{U}_S\} + [C_S]\{\dot{U}_S\} + [K_S]\{U_S\} = \{f_S\} \quad (53)$$

where $[C_S]$ denotes the proportional damping matrix of the support structure.

2.6.2. MIMO transfer function model

This section presents an alternative modeling approach for support structures. The support structure is simplified by utilizing the multi-input and multi-output (MIMO) support TFs (reduction of the computation time and requirement for computational resources).

Concerning the type of solid elements, the model with the hexahedron elements normally has a smaller size than that with the tetrahedron elements, thereby requiring less computation time. However, this may not be true if the shape of support structure is complex or the time for meshing is counted in the total simulation time, in which case it usually takes more time to generate the hexahedral mesh than the tetrahedral mesh, particularly at the boundaries. Hence, the influences of the solid element types are not quantified in the present work.

The FRFs are obtained by using the support FE model instead of experimental measurement. First of all, we apply a virtual point force (in a sinusoidal form) at one fictitious node, which is representative of the bearing center. Then Eq. (6) is solved for forced responses at all bearing locations and in all directions. Take the support model shown in Figure 14, for instance. One point force, F, is acted at one bearing location in one direction (indicated by the subscript Y or Z) and yields four responses, U_{Y_1}, U_{Z_1}, U_{Y_2}, and U_{Z_2} (one response for one bearing location and one direction). The responses can be finally correlated with the forces by the following equation,

$$\begin{bmatrix} U_{Y1} \\ U_{Z1} \\ U_{Y2} \\ U_{Z2} \end{bmatrix} = \begin{bmatrix} G_{Y1Y1} & G_{Y1Z1} & G_{Y1Y2} & G_{Y1Z2} \\ G_{Z1Y1} & G_{Z1Z1} & G_{Z1Y2} & G_{Z1Z2} \\ G_{Y2Y1} & G_{Y2Z1} & G_{Y2Y2} & G_{Y2Z2} \\ G_{Z2Y1} & G_{Z2Z1} & G_{Z2Y2} & G_{Z2Z2} \end{bmatrix} \cdot \begin{bmatrix} F_{Y1} \\ F_{Z1} \\ F_{Y2} \\ F_{Z2} \end{bmatrix} \tag{54}$$

where G is the FRF, and the subscripts 1 and 2 represent the first (left) and second (right) bearing locations shown in Figure 14, respectively.

By utilizing the complex curve-fitting algorithm [81], we are able to obtain from the FRFs the rational TF that corresponds to the location and direction of each force-response pair. The optimal polynomial coefficients of the TF are obtained by minimizing the weighted sum of the squares of the amplitude errors between the frequency-dependent functions and polynomial ratios. The minimization of the errors depends on both sampling quality and polynomial degree of the TF. Two guidelines for acquiring an effective set of sampling frequencies are provided. The first is that the number of excitation frequencies should be sufficient to retain the dynamic information (amplitudes and phases) of the response in the neighborhood of the frequencies with a dramatic amplitude or phase change. Second, the final frequency sample should be the union of the frequencies of all the sixteen FRFs. A general rule for the selection of the polynomial degree is to ensure that the curve fit retains the peaks and shifts of the TF amplitude or phase while avoiding a higher polynomial degree than needed. This is because high-degree polynomials can be highly oscillatory, which may include undesired information, such as noises in modal testing. The derived TFs in the s-plane may be expressed as,

$$G_{AiBj}(s) = \frac{b_1 s^m + b_2 s^{m-1} + \cdots + b_{m+1}}{s^n + a_1 s^{n-1} + \cdots + a_n} \tag{55}$$

where the subscripts A, B indicate Y or Z, and i, j =1 or 2. For simplicity, the TF matrix in Eq. (54) is written as $[G(s)]$.

It can be clearly seen that $[G(s)]$ is a MIMO system. We may derive each single-input and single-output (SISO) state space from the individual TF, $G_{AiBj}(s)$, and stack the state-space matrix into the corresponding block of the MIMO state space. There is the possibility that the final MIMO system is not a minimal state-space realization, leading to extra states and eigen-solutions. Several theoretical approaches [82-84] may help to resolve this problem. A practical approach is to identify repeated modes by inspection of the mode shapes and frequencies. The final state-space support model can be expressed as,

$$\{\dot{q}_S\} = [A_S]\{q_S\} + [B_S]\{f_S\} \tag{56}$$

$$\{y_S\} = [C_S]\{q_S\} \tag{57}$$

where $\{f_S\}$ is the bearing force vector, $\{y_S\}$ are the displacements of the support at the bearing attachment points. $[A_S]$, $[B_S]$ and $[C_S]$ represent the system matrix, input matrix and output matrix, respectively, and these three matrices can be obtained by transforming $[G(s)]$ into a state-space form. The detailed composition of these matrices is given in the appendix. $\{q_S\}$ is the state variable vector that consists of purely mathematical variables without physical meanings. It can be seen from the Eqs. (56) and (57) that the support model is substantially reduced by utilizing the TFs and state-space model as the number of state variables is considerably smaller than the DOF number of the support structure.

2.7. Rotor-Bearing System on Stationary Support Structure

The rotor-bearing system used in the linear rotor dynamics is commonly comprised of beam FE rotor model and eight-coefficient bearing model. In this section, however, more options are presented to assemble the rotor, bearing, and support structure. Beam elements, axisymmetric elements, and 3D solid elements are employed in the rotor system modeling and assembling.

2.7.1. Beam element rotor and solid element support structure

Beam element rotor is associated with the support structure by adding the stiffness and damping coefficients of the linear bearing model to the nodes of the rotor to which the bearing is attached. The special attachment method presented in Section 2.2.3 is not applicable for the 1D beam element model.

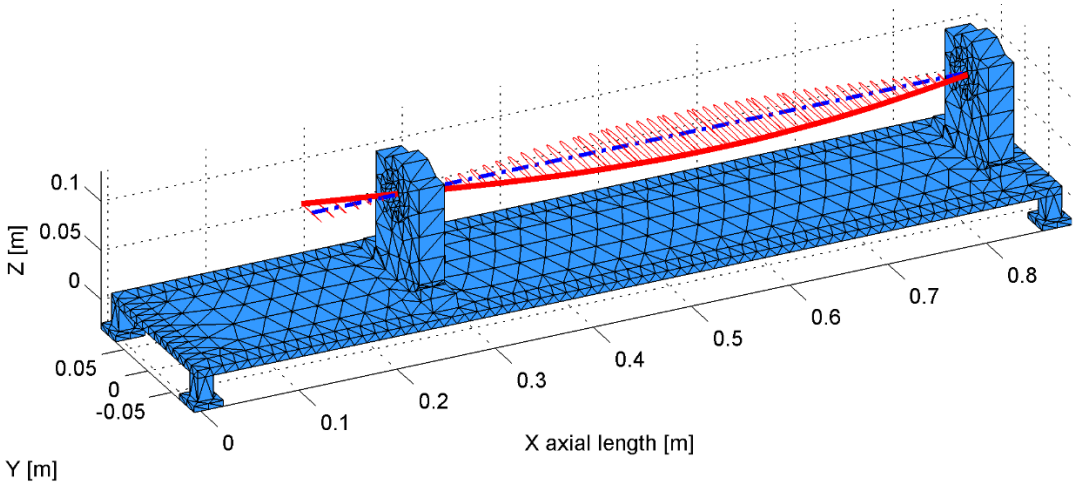

Figure 15. First bending mode of a beam element rotor and solid element support model.

The support structure is first modeled with solid tetrahedron elements. Then, the fictitious node, which corresponds to the attachment point of each bearing, is created to connect the rotor and support. Each fictitious node is connected by the rigid and massless beams with the nodes that are circumferentially around the bearing center. The linear bearing model is attached to the node of the rotor beam element. An example is shown in Figure 15. The 1D beam element rotor has no radial dimensions.

2.7.2. Axisymmetric element rotor and solid element support structure

Similar to the assembling method for beam element rotor and solid element support models, linear bearing models are attached to fictitious node of the massless beam web. Figure 16 shows the basic idea how to assemble the rotor, bearing, and support structure. The difference lies in that the bearing coefficients are associated with the surface nodes of the axisymmetric element rotor in a special way. It has been introduced in Section 2.2.3 how to connect bearings with the axisymmetric element rotor.

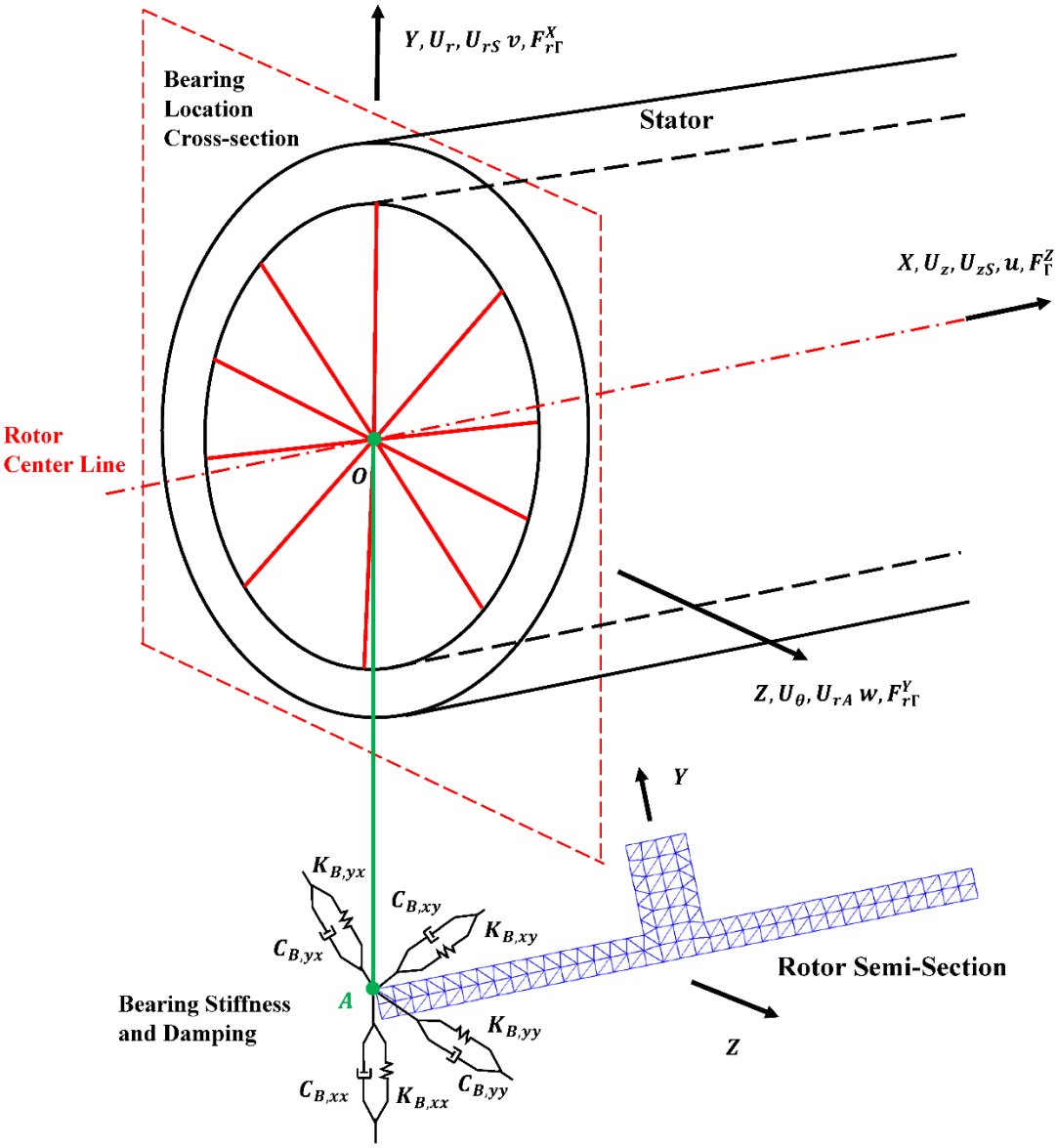

Figure 16. Connection of axisymmetric element rotor and solid element support by linear bearing model.

Table 1. Nomenclature for Figure 16.

Notation	Unit	Description
X, Y, Z	m	The horizontal, vertical and Z direction for rotor and stator in Cartesian coordinate system
U_r, U_θ, U_z	m	The radial, circumferential and axial direction for axisymmetric rotor in Polar coordinate system
u, v, w	m	The horizontal, vertical and Z direction for stator in Cartesian coordinate system
U_{rS}	m	Symmetric direction in axisymmetric element approach
U_{rA}	m	Anti-symmetric direction in axisymmetric element approach
$F_{\mathrm{r}\Gamma}^{X}$	N	External force in Y direction at the stator inner surface node P
$F_{\mathrm{r}\Gamma}^{Y}$	N	External force in Z direction at the stator inner surface node Q
F_{Γ}^{Z}	N	External force in X direction at the stator inner surface node P
O	$-$	Origin point
A	$-$	Axisymmetric rotor surface node
P	$-$	Stator inner surface node in Y direction
Q	$-$	Stator inner surface node in Z direction

Table 1. Continued.

Notation	Unit	Description
$K_{B,xx}$	N/m	Direct bearing stiffness coefficients (force acted in Y direction at a distance in Y direction)
$K_{B,yy}$	N/m	Direct bearing stiffness coefficients (force acted in Z direction at a distance in Z direction)
$K_{B,xy}$	N/m	Cross-coupled bearing stiffness coefficients (force acted in Y direction at a distance in Z direction)
$K_{B,yx}$	N/m	Cross-coupled bearing stiffness coefficients (force acted in Z direction at a distance in Y direction)
$C_{B,xx}$	$N \cdot s/m$	Direct bearing damping coefficients (force acted in Y direction at a velocity in Y direction)
$C_{B,yy}$	$N \cdot s/m$	Direct bearing damping coefficients (force acted in Z direction at a velocity in Z direction)
$C_{B,xy}$	$N \cdot s/m$	Cross-coupled damping stiffness coefficients (force acted in Y direction at a velocity in Z direction)
$C_{B,yx}$	$N \cdot s/m$	Cross-coupled damping stiffness coefficients (force acted in Z direction at a velocity in Y direction)
q_j	m	Axisymmetric element DOF j
Q_j^A	$N \; or \; N \cdot m$	External load at the rotor node A for axisymmetric element DOF j

Table 1. Continued.

Notation	Unit	Description
U_{irS}^{A}	m	Displacement of axisymmetric element node A in the symmetric radial direction for ith harmonics in Polar coordinate system
U_{irA}^{A}	m	Displacement of axisymmetric element node A in the anti-symmetric radial direction for ith harmonics in Polar coordinate system
$U_{i\theta S}^{A}$	m	Displacement of axisymmetric element node A in the symmetric circumferential direction for ith harmonics in Polar coordinate system
$U_{i\theta A}^{A}$	m	Displacement of axisymmetric element node A in the anti-symmetric circumferential direction for ith harmonics in Polar coordinate system
U_{izS}^{A}	m	Displacement of axisymmetric element node A in the symmetric axial direction for ith harmonics in Polar coordinate system
U_{izA}^{A}	m	Displacement of axisymmetric element node A in the anti-symmetric axial direction for ith harmonics in Polar coordinate system

Table 1. Continued.

Notation	Unit	Description
X, Y, Z	m	The horizontal, vertical and Z direction for rotor and stator in Cartesian coordinate system
U_r, U_θ, U_z	m	The radial, circumferential and axial direction for axisymmetric rotor in Polar coordinate system
u, v, w	m	The horizontal, vertical and Z direction for stator in Cartesian coordinate system
U_{rS}	m	Symmetric direction in axisymmetric element approach
U_{rA}	m	Anti-symmetric direction in axisymmetric element approach
$F_{\mathrm{r}\Gamma}^{X}$	N	External force in Y direction at the stator inner surface node P
$F_{\mathrm{r}\Gamma}^{Y}$	N	External force in Z direction at the stator inner surface node Q
F_{Γ}^{Z}	N	External force in X direction at the stator inner surface node P

2.7.3. Axisymmetric element rotor and MIMO support TF

This section presents an improved modeling approach for a complete rotor-bearing-support system, which takes advantage of both axisymmetric solid FE rotor

model (accurate prediction of the dynamics of a rotor with complex shapes) and simplified support structure model utilizing the MIMO support TFs (reduction of the computation time and requirement for computational resources).

A thin-walled shaft with multiple flexible disks is modeled using the axisymmetric solid harmonic FE method. The flexible structure supporting the rotor is first modeled with solid elements, and then the bearing location FRFs are determined by calculating the corresponding receptances over the frequency range of interest. Subsequently, the corresponding FRFs of the support structure are obtained by using the curve-fitting technique [81]. Guidance is provided for selecting an adequate polynomial degree of the TFs of the support structure. The TFs representing the support structure are rearranged to constitute a TF matrix, which contains the necessary information for unbalance response and stability analysis of the entire rotor system. The TF matrix is further transformed into a state-space form. In general, however, the support TF model is MIMO, implying that the way of transforming the TF into the state-space form for a SISO system [85] needs modifications. Finally, the state-space support model is connected with the rotor FE model by bearing forces.

The rotor model described by Eq. (6) in Section 2.2 is employed and combined with MIMO support TF model to be a complete rotor system. The Guyan reduction method [16] is used to reduce the rotor FE model and enhance the computational speed. Regarding the selection of retained DOFs for the Guyan reduction, a general rule is to retain the DOFs with large inertia, damping, or external load. The dynamic model described by Eq. (6) can then be rearranged to yield the following state-space form,

$$\{\dot{q}_R\} = [A_R]\{q_R\} + [B_{\mathrm{RB}}]\{f_B\} + [B_{\mathrm{RU}}]\{f_U\} \tag{58}$$

$$\{y_R\} = [C_R]\{q_R\} \tag{59}$$

where $\{f_B\}$ and $\{f_U\}$ represent the bearing force vector and unbalanced force vector (any external load including unbalanced force), respectively. $\{q_R\}$ is the state variable vector, and $\{y_R\}$ are the displacements of the rotor at the bearing attachment points. All matrices and vectors in Eqs. (58) and (59) are given in the appendix.

The state-space support model has been given in Section 2.6.2. The rotor and support structure are connected by bearings, or more precisely, by bearing forces. The different forms of bearing forces that are written in Eqs. (56) and (58) can be correlated by,

$$\{f_S\} = -\{f_B\} \tag{60}$$

With regard to most of the fluid film bearings, the bearing forces at a certain rotating speed may be applied to the rotor in the form of

$$F_B = c_B \cdot \dot{U}_B + k_B \cdot U_B \tag{61}$$

where U_B are the relative displacements between the rotor and support structure. Therefore, the general bearing forces can be derived from

$$\{f_B\} = -[C_B](\{\dot{y}_R\} - \{\dot{y}_S\}) - [K_B](\{y_R\} - \{y_S\}) \tag{62}$$

Substituting Eqs. (60) and (62) into Eqs. (58), (59), (56) and (57) yields,

$$[A_T]\{\dot{q}\} = [B_T]\{q\} + [B_{\mathrm{UT}}]\{f_U\} \tag{63}$$

With the benefit of this state-space form, controllers, actuators and AMBs may be integrated in the rotor system. The detailed matrices for the state-space form are provided in Appendix B.

With Eq. (63) representing the entire state-space model of the rotor-support system, stability analysis of the system can be conducted by using the characteristic equation,

$$\phi(s) = |s[I] - [A_T]| = 0 \tag{64}$$

If there are positive real eigenvalues or negative log dec, the rotor system is unstable. Additionally, unbalance response of the rotor can be obtained by substituting $\{\hat{f}_U\}e^{j\omega t}$ for $\{f_U\}$ into Eq. (63), which yields,

$$(j\omega[A_T] - [B_T])\{\hat{q}\} = [B_{\mathrm{UT}}]\{\hat{f}_U\} \tag{65}$$

where $\{\hat{q}\}$ represents the complex state vector in the state-space model, $\{\hat{f}_U\}$ is the complex unbalanced force vector, and ω is the frequency of the unbalanced force.

A specific example will be provided in Chapter 4.

2.8. Rotor-Bearing System on Moving Support Structure

Generally, rotor dynamic modeling and analysis assume that the rotor support structure is fixed to the ground in industrial applications. However, rotating machines like compressors and gas turbines may be installed in maneuvering aircrafts and ships encountering rough seas. In these scenarios, the on-board rotor is subject to large time-varying motions of its support structure, during which the support fixed frame direction of the gravity force on the rotor varies with the moving support structure, causing considerable change in bearing load components. Such changes may have a great impact on the performance of the hydrodynamic journal bearings that are widely used in rotating machinery, such as inducing large rotor vibrations or invoking rotor instability.

A few beam element rotor models with the eight-coefficient bearing attachment [39, 40] have been developed to investigate the dynamics of a rotor under support motion or base excitation. Some reseachers replaced the eight-coefficient bearing model with a nonlinear short bearing approximation [35, 36, 42]. This section corrects the erroneous Timoshenko beam element formulation presented in [39] and provides an improved systematic modeling approach for a rotor system by including hydrodynamic journal bearings, Timoshenko beam element shaft model and a moving support structure with arbitrary motions, such as heave, sway, surge, roll, pitch and yaw.

The shaft continuum is discretized with Timoshenko beam finite elements that account for gyroscopic moments, shear deformation and rotary inertia and is connected to the support structure via hydrodynamic journal bearings. The disk is added to the shaft as a rigid body with concentrated mass and moments of inertia. The bearing forces acting on the rotor, are determined by solving the Reynold's equation for lubricant film pressure utilizing a fluid film 2D FE model shown in Section 2.5. Finally, the equations of motion of the flexible rotor with hydrodynamic journal bearings and a moving support structure are derived by using the Lagrange's equation and expressed with respect to a non-inertial reference frame representing the moving support structure.

The rigid support model containing three translational and three rotational motions introduces time-varying parameters into the rotor system. Due to these time-varying parametric terms, the rotor may become unstable within the operating speed range. Therefore, the influences of the support pitch motion on the dynamic behavior of the rotor system are investigated using the derived rotor system model. In addition,

fixed-pad and tilting-pad bearings, the two types of hydrodynamic journal bearings that are commonly used in rotating machinery, are separately included as bearings in the rotor system. The influences of these two types of bearings on the rotor vibration are studied and compared in terms of general rotor dynamic characteristics, such as rotor orbit, unbalanced response, and stability.

2.8.1. Kinetic energy of a disk

The disk on the rotor is assumed rigid body. Hence, no strain energy is considered.

The relative motion of the rotor with respect to the support structure is essential to rotor dynamic analysis. The first step is to derive the transformation relationships among the rotor reference frame, support reference frame, and the ground reference frame (also called the absolute reference frame). These three reference frames are defined as,

(a) R_G represents the reference frame with respect to the ground (fixed to the center of mass of the support before moving), i.e. $O_G X_G Y_G Z_G$ in Figure 17;

(b) $R_F$represents the reference frame with respect to the foundation/support structure (fixed to the journal center of the left bearing pedestal), i.e. $O_F X_F Y_F Z_F$ in Figure 17;

(c) R_R represents the reference frame with respect to the shaft segment or disk (fixed to the center of mass of the shaft segment), i.e. $O_R X_R Y_R Z_R$ in Figure 17.

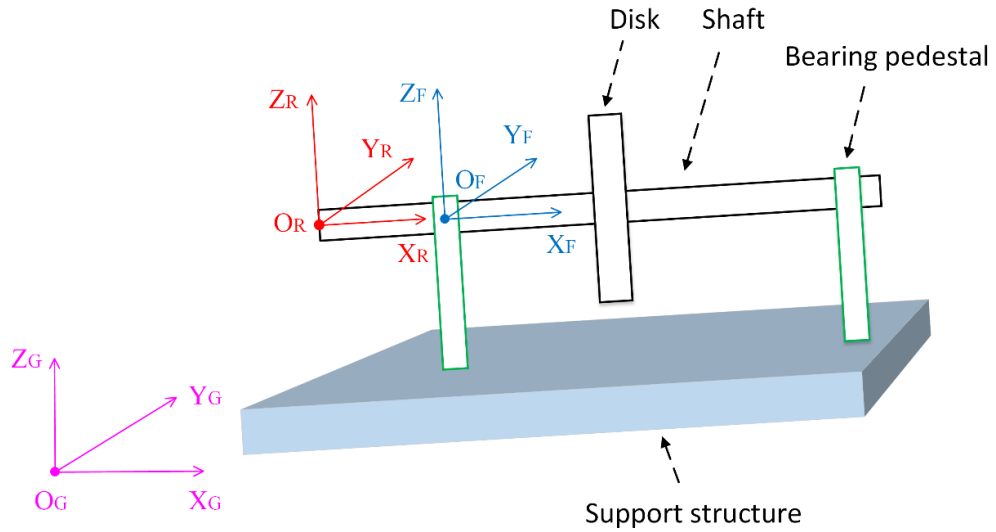

Figure 17. Maneuvering rotor-bearing-support system with three reference frames (ground frame $O_G X_G Y_G Z_G$, support frame $O_F X_F Y_F Z_F$, and rotor frame $O_R X_R Y_R Z_R$).

The relationship between the vectors $\vec{r}$ that is expressed in the reference frame R_F and in the reference frame R_R may be described by,

$$\vec{r}|_{R_R} = [T_{R_F \to R_R}] \cdot \vec{r}|_{R_F} \tag{66}$$

where $|_{R_R}$ indicates that the vector is expressed or projected in the reference frame R_R. $[T]$ represents the transformation matrix. The subscript $R_F \to R_R$ indicates that the reference frame where the vector is projected transforms from R_F to R_R. The transformation matrix $[T_{R_F \to R_R}]$ can be obtained by following the way shown in Eqs. (67) to (70).

Transform the vector projected in the frame R_F into the one projected in the frame R_R by means of Euler angles. The transformation matrix may be expressed as,

$$[T_{R_F \to R_R}] = [T_{Rx}][T_{Ry}][T_{Rz}] \tag{67}$$

where

$$[T_{Rx}] = \begin{bmatrix} 1 & 0 & 0 \\ 0 & cos(\alpha_R) & sin(\alpha_R) \\ 0 & -sin(\alpha_R) & cos(\alpha_R) \end{bmatrix} \tag{68}$$

$$[T_{Ry}] = \begin{bmatrix} cos(\beta_R) & 0 & -sin(\beta_R) \\ 0 & 1 & 0 \\ sin(\beta_R) & 0 & cos(\beta_R) \end{bmatrix} \tag{69}$$

$$[T_{Rz}] = \begin{bmatrix} cos(\gamma_R) & sin(\gamma_R) & 0 \\ -sin(\gamma_R) & cos(\gamma_R) & 0 \\ 0 & 0 & 1 \end{bmatrix} \tag{70}$$

The vectors representing the rotational angle and angular velocity can transform in the following way (Figure 18).

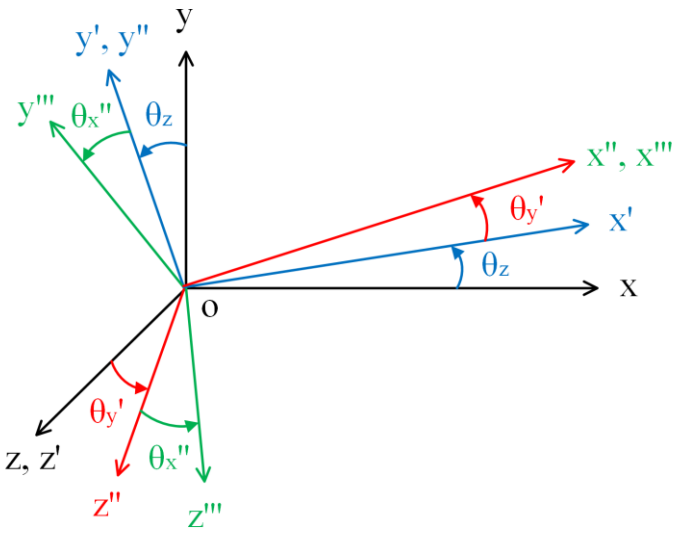

Figure 18. Coordinate system rotation for an angular vector.

First, rotate θ_z about z axis, which generates the coordinate system $ox'y'z'$. Then, rotate $\theta_{y'}$ about y' axis, generating the coordinate system $ox''y''z''$. Finally, rotate

$\theta_{x''}$ about x'' axis, leading to the coordinate system $ox'''y'''z'''$. The angular velocity vector may be written as,

$$\vec{\omega}_r = \dot{\theta}_z \vec{e}_z + \dot{\theta}_{y'} \vec{e}_{y'} + \dot{\theta}_{x''} \vec{e}_{x''} \tag{71}$$

where $\vec{e}_z$, $\vec{e}_{y'}$ and $\vec{e}_{x''}$ represent the unit vector in z direction of the coordinate systems $oxyz$, the one in y' direction of $ox'y'z'$ and the one in z'' direction of $ox''y''z''$, respectively.

$\vec{\omega}_r$ can be obtained by using a similar Euler angle transformation to Eqs. (67) to (70). As the rotor rotation angles θ_z and $\theta_{y'}$ are very small (because the deformation due to bending is small), the rotor rotations are approximately collinear with y and z axes. In regard to the rotor with respect to the reference frame R_F, this approximation yields,

$$\vec{\omega}_{R_R/R_F}\big|_{R_R} = \begin{bmatrix} \dot{\alpha}_R - \dot{\gamma}_R \sin(\beta_R) \\ \dot{\beta}_R \cos(\alpha_R) - \dot{\gamma}_R \sin(\alpha_R)\cos(\beta_R) \\ -\dot{\beta}_R \sin(\alpha_R) + \dot{\gamma}_R \cos(\alpha_R)\cos(\beta_R) \end{bmatrix}_{R_R} \tag{72}$$

where $\vec{\omega}_{R_R}$ represents the angular velocity vector of the reference frame R_R, and the subscript $/R_F$ denotes a vector with respect to the reference frame R_F. Both $\big|_{R_R}$ and $[\ ]_{R_R}$ indicate that the vector is expressed or projected in the reference frame R_R. Additionally, α_R, β_R and γ_R represent the rotation angles of the shaft segment or disk about x, y, and z axes with respect to R_F and prejected in R_F, respectively. The remaining of the chapter will use the same naming rules for formulation of support motion. The assumption that β_R and γ_R are very small for small bending deformations of the rotor is made for simplifying the kinetic energy of the rotor or disk.

Similar to Eq. (72), the angular velocity vector of the frame R_F with respect to R_G may be written as,

$$\vec{\omega}_{R_F/R_G}\big|_{R_F} = \begin{bmatrix} \dot{\alpha}_F - \dot{\gamma}_F \, sin(\beta_F) \\ \dot{\beta}_F \, cos(\alpha_F) - \dot{\gamma}_F \, sin(\alpha_F) \, cos(\beta_F) \\ -\dot{\beta}_F \, sin(\alpha_F) + \dot{\gamma}_F \, cos(\alpha_F) \, cos(\beta_F) \end{bmatrix}_{R_F} \tag{73}$$

where α_F, β_F and γ_F represent the rotation angles of the support structure about x, y, and z axes with respect to R_G and prejected in R_G, respectively. Note that α_F, β_F and γ_F are arbitrary angles, unlike the previous assumption that β_R and γ_R are very small.

Then the angular velocity vector of the shaft segment or disk with respect to R_G and projected in R_R is expressed as,

$$\vec{\omega}_{R_R/R_G}\big|_{R_R} = \vec{\omega}_{R_R/R_F}\big|_{R_R} + \left[T_{R_F \to R_R}\right] \cdot \vec{\omega}_{R_F/R_G}\big|_{R_F} \tag{74}$$

Therefore, the rotational kinetic energy of the disk can be written as,

$$T_{rot} = \frac{1}{2}\left(\vec{\omega}_{R_R/R_G}\big|_{R_R}\right)^T [I_d] \left(\vec{\omega}_{R_R/R_G}\big|_{R_R}\right) \tag{75}$$

where $[I_d]$ denotes the matrix representing the moment of inertia of the disk and may be written as,

$$[I_d] = \begin{bmatrix} I_{pd} & 0 & 0 \\ 0 & I_{td} & 0 \\ 0 & 0 & I_{td} \end{bmatrix} \tag{76}$$

where I_{pd} and I_{td} represent the moment of inertia of the disk about the axial axis (x axis) and non-axial axis (y or z axis), respectively.

After obtaining the rotational kinetic energy, we start deriving the translational kinetic energy of the disk. The absolute position vector of the origin O_F of the reference

frame R_F, which is expressed or projected in the frame R_G, is defined as $\overrightarrow{O_G O_F}\big|_{R_G}$. $\big|_{R_G}$ indicates that the vector is projected in the frame R_G. By using Euler angles, the position vector projected in the frame R_G is transformed into the one projected in the frame R_F, which yields,

$$\overrightarrow{O_G O_F}\big|_{R_F} = \left[T_{R_G \to R_F}\right] \cdot \overrightarrow{O_G O_F}\big|_{R_G} = \begin{bmatrix} x_F \\ y_F \\ z_F \end{bmatrix}_{R_F} \tag{77}$$

where

$$[T_{R_G \to R_F}] = [T_{Fx}]\left[T_{Fy}\right][T_{Fz}] \tag{78}$$

$$[T_{Fx}] = \begin{bmatrix} 1 & 0 & 0 \\ 0 & cos(\alpha_F) & sin(\alpha_F) \\ 0 & -sin(\alpha_F) & cos(\alpha_F) \end{bmatrix} \tag{79}$$

$$\left[T_{Fy}\right] = \begin{bmatrix} cos(\beta_F) & 0 & -sin(\beta_F) \\ 0 & 1 & 0 \\ sin(\beta_F) & 0 & cos(\beta_F) \end{bmatrix} \tag{80}$$

$$[T_{Fz}] = \begin{bmatrix} cos(\gamma_F) & sin(\gamma_F) & 0 \\ -sin(\gamma_F) & cos(\gamma_F) & 0 \\ 0 & 0 & 1 \end{bmatrix} \tag{81}$$

The position vector of the center of mass of the shaft segment or disk with respect to the frame R_F and projected in the frame R_F is expressed as,

$$\overrightarrow{O_F O_R}\big|_{R_F} = \begin{bmatrix} x_R \\ y_R \\ z_R \end{bmatrix}_{R_F} \tag{82}$$

where x_R, y_R, and z_R represent the displacement of the disk in x, y, and z directions with respect to R_F and projected in R_F as well, respectively.

The absolute position vector of the mass center of the shaft segment or disk with respect to the frame R_G and projected in the frame R_F is given by,

$$\overrightarrow{O_G O_R}\big|_{R_F} = \overrightarrow{O_G O_F}\big|_{R_F} + \overrightarrow{O_F O_R}\big|_{R_F} = \begin{bmatrix} x_F + x_R \\ y_F + y_R \\ z_F + z_R \end{bmatrix}_{R_F} \tag{83}$$

where x_F, y_F, and z_F represent the displacement of the rigid support in x, y, and z directions with respect to R_G and projected in R_F, respectively.

Applying the transport theorem, which relates the time derivative of the position vector $\overrightarrow{O_G O_R}$ measured from the frame R_G to that of the same vector but measured from the moving frame R_F, yields,

$$\begin{aligned} \vec{v}_{R_R/R_G}\big|_{R_F} &= \frac{d\overrightarrow{O_G O_R}}{dt}\bigg|_{R_F}^{R_G} = \frac{d\overrightarrow{O_G O_R}}{dt}\bigg|_{R_F}^{R_F} + \vec{\omega}_{R_F/R_G}\big|_{R_F} \times \overrightarrow{O_G O_R}\big|_{R_F} \\ &= \begin{bmatrix} \dot{x}_F + \dot{x}_R \\ \dot{y}_F + \dot{y}_R \\ \dot{z}_F + \dot{z}_R \end{bmatrix} + \begin{bmatrix} \omega_{Fx} \\ \omega_{Fy} \\ \omega_{Fz} \end{bmatrix} \times \begin{bmatrix} x_F + x_R \\ y_F + y_R \\ z_F + z_R \end{bmatrix} \end{aligned} \tag{84}$$

where $\big|_{R_F}^{R_G}$ indicates that the vector is projected in the frame R_F and the time derivative operation is sensed in the frame R_G. ω_{Fx}, ω_{Fy} and ω_{Fz} represent the components of the angular velocity vector of the support with respect to the ground R_G and projected in the frame R_F, i.e. $\vec{\omega}_{R_F/R_G}\big|_{R_F}$, which correspond to x, y and z directions, respectively.

The translational kinetic energy of the disk may be expressed as,

$$T_{trs} = \frac{1}{2}\left(\vec{v}_{R_R/R_G}\big|_{R_F}\right)^T [M_d] \left(\vec{v}_{R_R/R_G}\big|_{R_F}\right) \tag{85}$$

where $[M_d]$ denotes the matrix representing the mass of the disk and is written as,

$$[M_d] = \begin{bmatrix} m_d & 0 & 0 \\ 0 & m_d & 0 \\ 0 & 0 & m_d \end{bmatrix} \tag{86}$$

where m_d represents the mass of the disk.

The total kinetic energy of a disk T_d consists of the rotational energy shown in Eq. (75) and the translational kinetic energy shown in Eq. (85) and may be expressed as,

$$T_d = T_{rot} + T_{trs} \tag{87}$$

2.8.2. Kinetic energy of a shaft segment

The derivation of the kinetic energy of the shaft is the same as that of the disk except that the integral operations are applied through the length of the shaft or shaft segment. We define,

$$\vec{\omega}_{R_R/R_G}\big|_{R_R} = \begin{bmatrix} \dot{\alpha}_{R_R/R_G} \\ \dot{\beta}_{R_R/R_G} \\ \dot{\gamma}_{R_R/R_G} \end{bmatrix}_{R_R} \tag{88}$$

$$\vec{v}_{R_R/R_G}\big|_{R_F} = \begin{bmatrix} \dot{x}_{R_R/R_G} \\ \dot{y}_{R_R/R_G} \\ \dot{z}_{R_R/R_G} \end{bmatrix}_{R_F} \tag{89}$$

The expanded formulation of $\dot{\alpha}_{R_R/R_G}$, $\dot{\beta}_{R_R/R_G}$, $\dot{\gamma}_{R_R/R_G}$, $\dot{x}_{R_R/R_G}$, $\dot{y}_{R_R/R_G}$ and $\dot{z}_{R_R/R_G}$ can be obtained by following the same approach as shown from Eqs. (72) to (84) except that x_R, y_R, z_R, $\dot{x}_R$, $\dot{y}_R$, $\dot{z}_R$, α_R, β_R, γ_R, $\dot{\alpha}_R$, $\dot{\beta}_R$ and $\dot{\gamma}_R$ are replaced with x_S, y_S, z_S, $\dot{x}_S$, $\dot{y}_S$, $\dot{z}_S$, α_S, β_S, γ_S, $\dot{\alpha}_S$, $\dot{\beta}_S$ and $\dot{\gamma}_S$, respectively.

Thus, the kinetic energy of the shaft segment may be expressed as,

$$T_s = \frac{1}{2}\rho_s A_s \int_{x_1}^{x_2} \left(\dot{x}^2_{R_R/R_G} + \dot{y}^2_{R_R/R_G} + \dot{z}^2_{R_R/R_G}\right) dx$$

$$+\frac{1}{2}\left(I_{ps}\int_{x_1}^{x_2}\dot{\alpha}_{R_R/R_G}^2 dx + I_{ts}\int_{x_1}^{x_2}\dot{\beta}_{R_R/R_G}^2 dx + I_{ts}\int_{x_1}^{x_2}\dot{\gamma}_{R_R/R_G}^2 dx\right) \quad (90)$$

where ρ_s is the density of the shaft. A_s is the area of the shaft cross-section. I_{ps} is the moment of inertia of the shaft about the axial axis (x axis). I_{ts} is the moment of inertia of the shaft about the non-axial axis (y or z axis). x_1 is the beginning position of the axial length of the shaft segment. x_2 is the ending position of the axial length of the shaft segment.

2.8.3. Strain energy of a shaft segment

A Timoshenko element model for a rotor with a rigid support structure fixed to the ground has been developed in [5]. The formulation of the elastic strain energy for a rotor with a support fixed to the ground is the same as for a rotor under support motion except that the displacements are replaced with the ones with respect to the support reference frame. For simplicity, only the final formulation of elastic strain energy is given as,

$$U_s = \frac{1}{2}EI\int_{x_1}^{x_2}\left(\left(\frac{\partial\beta_r}{\partial x}\right)^2 + \left(\frac{\partial\gamma_r}{\partial x}\right)^2\right)dx + \frac{1}{2}G\kappa A_s\int_{x_1}^{x_2}\left(\left(\frac{\partial y_r}{\partial x} - \gamma_r\right)^2 + \left(\frac{\partial z_r}{\partial x} + \beta_r\right)^2\right)dx \quad (91)$$

where E is the elastic modulus of the shaft. I is the second moment of inertia of the shaft. G is the shear modulus of the shaft. κ is the shear form factor of the shaft. A_s is the cross-section area of the shaft.

2.8.4. Gravitational potential energy

Since the fluid film bearing in the rotor-bearing-support system is modeled as nonlinear forces acted on the journal, the assumption that the gravity of the rotor is balanced at the equilibrium position in the steady-state analysis is invalid. As a result,

the potential energy due to gravity of the rotor (shaft and disk) should be taken into consideration.

The position vector with respect to the frame R_G and projected in the frame R_G can be written as,

$$\overrightarrow{O_G O_R}\big|_{R_G} = \left[T_{R_F \to R_G}\right] \cdot \overrightarrow{O_G O_R}\big|_{R_F} = \begin{bmatrix} x_G \\ y_G \\ z_G \end{bmatrix}_{R_G} \tag{92}$$

where $\left[T_{R_F \to R_G}\right]$ is the inverse matrix of $\left[T_{R_G \to R_F}\right]$.

The vertical distance relative to the datum of the ground, i.e. z_G leads to the potential energy due to gravity of the disk, which can be written as,

$$P_d = m_d \cdot g \cdot z_G \tag{93}$$

where g is the coefficient representing the gravity of earth and m_d is the mass of the disk.

The potential energy due to gravity of the shaft segment may be expressed as,

$$P_s = \rho_s \cdot A_s \cdot g \cdot \int_{x_1}^{x_2} z_G dx \tag{94}$$

2.8.5. Mass imbalance

As shown in Figure 19, we place a concentrated mass m_u at point P_u with a distance r_u from the geometric center of the cross-section of the rotor segment (shaft segment or disk). The initial angle about the $\overrightarrow{O_F X_F}$ axis of the frame R_F at rest is set as φ_u. When the rotor rotates, the angle becomes θ_u. $\theta_u$may be correlated with φ_u, rotor spin speed Ω and time t by,

$$\theta_u = \Omega t + \varphi_u \tag{95}$$

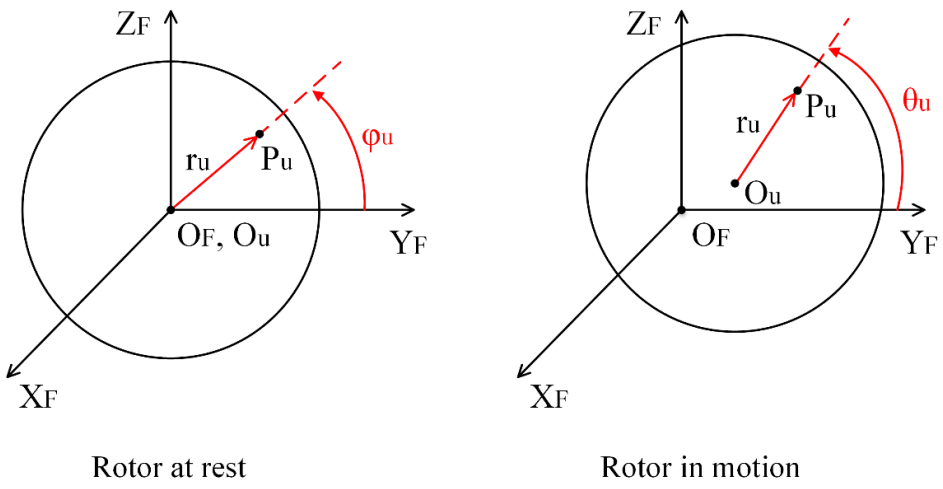

Figure 19. Mass unbalance of the rotor segment.

The absolute position vector of the mass unbalance is defined as $\overrightarrow{O_G P_u}$, which may be obtained from,

$$\overrightarrow{O_G P_u}\big|_{R_F} = \overrightarrow{O_G O_F}\big|_{R_F} + \overrightarrow{O_F O_u}\big|_{R_F} + \overrightarrow{O_u P_u}\big|_{R_F} = \begin{bmatrix} x_F \\ y_F \\ z_F \end{bmatrix} + \begin{bmatrix} x_u \\ y_u \\ z_u \end{bmatrix} + \begin{bmatrix} 0 \\ r_u\, cos(\theta_u) \\ r_u\, sin(\theta_u) \end{bmatrix} \tag{96}$$

Applying the transport theorem to Eq. (96) yields,

$$\vec{v}_{P_u/R_G}\big|_{R_F} = \frac{d\overrightarrow{O_G P_u}}{dt}\Big|_{R_F}^{R_G} = \frac{d\overrightarrow{O_G P_u}}{dt}\Big|_{R_F}^{R_F} + \vec{\omega}_{R_F/R_G}\big|_{R_F} \times \overrightarrow{O_G O_u}\big|_{R_F} = \begin{bmatrix} \dot{x}_{P_u/R_G} \\ \dot{y}_{P_u/R_G} \\ \dot{z}_{P_u/R_G} \end{bmatrix}_{R_F} \tag{97}$$

where $\frac{d}{dt}\Big|_{R_F}^{R_G}$ represents the time derivative of the vector with respect to the reference frame R_G (sensed in R_G) and projected in the reference frame R_F.

After obtaining the velocity of the unbalance mass from Eq. (97), the kinetic energy of the mass unbalance can be written as,

$$T_u = \frac{1}{2} m_u \left(\dot{x}^2_{P_u/R_G} + \dot{y}^2_{P_u/R_G} + \dot{z}^2_{P_u/R_G} \right) \tag{98}$$

2.8.6. Equation of motion

The beam element rotor model presented in Section 2.8 and the nonlinear fluid film bearing introduced in Section 2.5 are combined together to simulate a rotor-bearing system under large support motions.

The displacements of the journal with respect to the support structure are included to derive the lubricant thickness between the journal and bearing pad. In the meantime, the lubricant forces (pressure) are calculated based on the thickness of the lubricant film and included in the equilibrium equations for the entire rotor-bearing-support system.

Due to the nonlinearity of the rotor system, transient analysis is employed. An iterative computation approach [77] is applied in order to obtain the equilibrium point of the journal in the bearing.

The virtual work done by bearing forces can be expressed as,

$$\delta W_b = \left(F_{by} \vec{e}_y + F_{bz} \vec{e}_z \right) \cdot \delta \vec{u}_b \tag{99}$$

where δW_b and $\delta \vec{u}_b$ represents the virtal work and displacement vector per infinitesimal displacement. $\vec{e}_y$ and $\vec{e}_z$ are unit vectors in Y and Z directions, respectively. F_{by} and F_{bz} are the same bearing forces as defined in Eq. (49) and (50).

The Lagrange's equations are applied to Eqs. (75), (85), (90), (91), (93), (94), (98) and (99) to derive the equation of motion of the rotor-bearing system under support motion. The erroneous formulation of kinetic energy presented in [39] is corrected by

using the formulations derived in this work. The corrected formulations of kinetic energy for a rigid disk and shaft segment, T_d and T_s, are provided in Appendix A.

2.9. Guyan Reduction Method

A solid element model may involve thousands of DOFs more than a beam element model. As a result, the solid element model requires more computation time and a large RAM. In other words, a solid element model is more accurate that beam element model at the sacrifice of computational resources. A remedy for this is to use model reduction methods to condense the DOFs of the solid element model. The Guyan reduction method [16] has been successfully applied to the shaft axisymmetric FE model in [11], and thereby, is used in the present work to reduce the FE model size and enhance the computation speed. The master DOFs for the Guyan reduction are selected in such a way that the DOFs with large damping, inertia, or external load are retained [25]. A software algorithm that automates the retaining process has been provided in [20]

The equation of motion for a rotor or support solid element model may be described as,

$$[M]\{\ddot{q}\} + [C]\{\dot{q}\} + [K]\{q\} = \{f\} \tag{100}$$

where the DOF vector $\{q\}$ can be separated into two groups, namely retained DOF vector $\{q_R\}$ and condensed DOF vector $\{q_C\}$. The retained vector contains N_R DOFs. The condensed vector has N_C DOFs. It is clear that the DOF number is reduced from the original N to N_R. Accordingly, the mass or inertia matrix $[M]$, damping matrix $[C]$, stiffness matrix $[K]$ and external load vector $\{f\}$ are rearranged to be,

$$\begin{bmatrix}[M_{RR}] & [M_{RC}] \\ [M_{CR}] & [M_{CC}]\end{bmatrix}\begin{bmatrix}\{\ddot{q}_R\} \\ \{\ddot{q}_C\}\end{bmatrix}+\begin{bmatrix}[C_{RR}] & [C_{RC}] \\ [C_{CR}] & [C_{CC}]\end{bmatrix}\begin{bmatrix}\{\dot{q}_R\} \\ \{\dot{q}_C\}\end{bmatrix}+\begin{bmatrix}[K_{RR}] & [K_{RC}] \\ [K_{CR}] & [K_{CC}]\end{bmatrix}\begin{bmatrix}\{q_R\} \\ \{q_C\}\end{bmatrix}=\begin{bmatrix}\{f_R\} \\ \{f_C\}\end{bmatrix} \tag{101}$$

where the subscripts R and C indicate the retained and condensed DOFs, respectively. The condensed inertia, damping and external load terms are assumed to be negligible. Regarding the selection of retained DOFs for the Guyan reduction, a general rule is to retain the DOFs with large inertia, damping, or external load.

The displacements of the rotor system can be obtained by following the equation

$$\begin{bmatrix}\{q_R\} \\ \{q_C\}\end{bmatrix}=[T_G]\{q_R\} \tag{102}$$

where the Guyan transformation matrix $[T_G]$ is defined as,

$$[T_G]=\begin{bmatrix}[I_{RR}] \\ -[K_{CC}]^{-1}[K_{CR}]\end{bmatrix} \tag{103}$$

Substituting Eqs. (102) and (103) into Eq. (101) yields,

$$[M_G]\{\ddot{q}_R\}+[C_G]\{\dot{q}_R\}+[K_G]\{q_R\}=\{f_G\} \tag{104}$$

where

$$[M_G]=[T_G]^T[M][T_G] \tag{105}$$

$$[C_G]=[T_G]^T[C][T_G] \tag{106}$$

$$[K_G]=[T_G]^T[K][T_G] \tag{107}$$

$$\{f_G\}=[T_G]^T\{f\} \tag{108}$$

It can be seen from Eqs. (104)-(108) that the dimension of the equation of motion has been reduced from $(N \times N)$ in Eq. (100) to $(N_R \times N_R)$ in Eq. (104). More detailed derivations can be found in Ref. [25].

2.10. Summary of Modeling Approaches

This chapter presented improved formulations of the axisymmetric solid harmonic element rotor model and a systematic modeling approach for analysis of a rotor system with hydrodynamic fluid film bearings undergoing large support motion.

The improvements made on the rotor axisymmetric FE modeling include (1) developing an axisymmetric FE formulation of the centrifugal stress-stiffening effects that is implementable as a software algorithm, and (2) developing an axisymmetric FE formulation of the spin-softening effects that is implementable as a software algorithm. This is the first time that the centrifugal stress-stiffening and spin-softening effects are formulated for the axisymmetric solid harmonic element rotor modeling.

An improved MIMO TF modeling approach is presented for modeling a support structure. MIMO TFs representing a support structure are transformed into a state-space form and then integrated in the rotor axisymmetric FE model. The rotor-bearing-support model constructed based on a rotor axisymmetric FE model and support MIMO TFs consumes much less computation time than a complete solid FE rotor-bearing-support model.

In addition, an improved systematic modeling approach that utilizes Timoshenko beam elements and accounts for support motion is presented. This approach is for modeling a rotor system with flexible shafts on hydrodynamic journal bearings undergoing large support motion. This is the first time that the hydrodynamic fluid film journal bearing model, instead of the linear eight-coefficient bearing model and short journal bearing model, is integrated into a rotor-bearing system undergoing support

motion. The bearing forces acting on the rotor are determined by solving the Reynold's equation for lubricant film pressure utilizing a 2D finite element fluid film model.

Finally, Guyan reduction method is introduced and applied in order to reduce the simulation time and save computer resources.

3. MODELING OF A DRILLSTRING WITH IMPACT AND TORSIONAL DAMPERS

This chapter presents a FE modeling approach for simulation of a drillstring with impactors and torsional dampers. The drillstring model is shown in Figure 20.

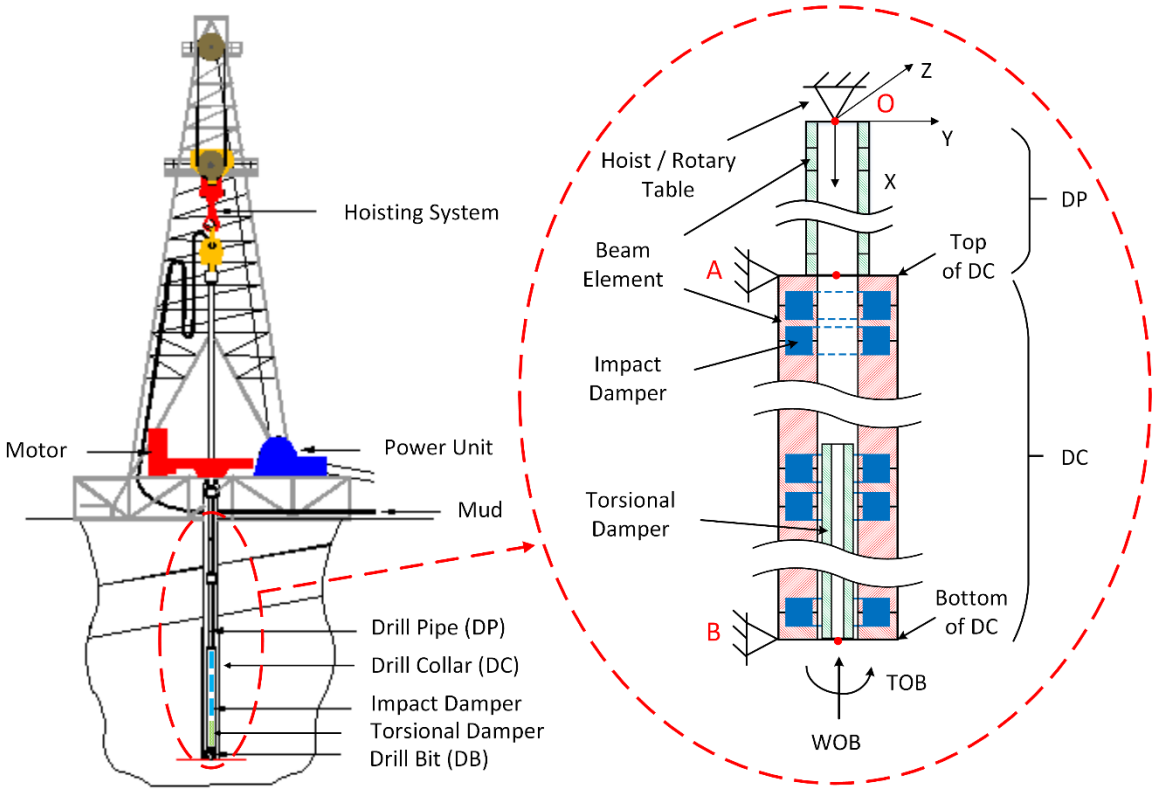

Figure 20. Drilling rig (left) and cross section of the drillstring (right) with impact dampers and a torsional damper. Reprinted from Ref. [1].

* Reprinted with permission from "Suppression of Lateral and Torsional Stick–Slip Vibrations of DrillstringsWith Impact and Torsional Dampers" by Hu, L., Palazzolo, A., and Karkoub, M., 2016, ASME J. Vib. Acoust. 138(5), 051013, Copyright 2016 by ASME.

By resorting to the modeling approach proposed in this chapter, novel centralized impact dampers and torsional dampers are developed for suppressing drillstring vibrations, and various design parameters of the dampers are compared. Finally, guidance of the damper design is provided for acquiring stronger suppression effects on drillstring vibration.

3.1. Impact Damper

Impact dampers, also known as impactors, are able to dissipate kinetic energy in impact. Due to the complex drilling conditions underneath, prediction of drillstring resonance might be inaccurate and hence result in violent vibrations that cause damage to the tubulars and borehole wall.

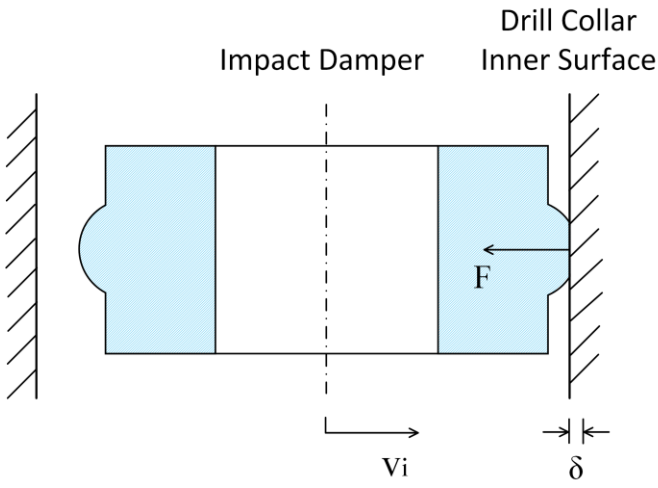

Figure 21. Cross section of the impact damper and DC at moment of impact. Reprinted from Ref. [1].

The impactors are made of metals like steel or iron and are installed in the DC. As is shown in Figure 21, the hollow cylinder shape enables drilling fluids to pass

through, and the spherical bump is designed for impact. The novel centralized impact dampers presented here are explained by analysis and demonstrated by simulations, with an underlying assumption that the physical implementations are feasible.

3.1.1. Coefficient of restitution model

The COR model is widely used to measure the restitution of an impact between two objects. The kinetic energy of two bodies after one-dimensional impact of pure translation can be measured by,

$$v_1^+ = \frac{1}{1+\mu_m}[(\mu_m - e_{COR})v_1^- + (1 + e_{COR})v_2^-] \tag{109}$$

$$v_2^+ = \frac{1}{1+\mu_m}[\mu_m(1 + e_{COR})v_1^- + (1 - \mu_m \cdot e_{COR})v_2^-] \tag{110}$$

where v_1^+ and v_1^- represent the velocities of body 1 before and after impact, respectively, and v_2^+ and v_2^- represent the velocities of body 2 before and after impact, respectively. The mass ratio μ_m is defined as,

$$\mu_m = \frac{m_1}{m_2} \tag{111}$$

where m_1 and m_2 are the mass of body 1 and body 2, respectively. The COR here is defined as,

$$e_{COR} = \frac{v_2^+ - v_1^+}{v_1^- - v_2^-} \tag{112}$$

By referring to Ref. [65], the COR e_{COR} for most materials within a linear elastic range and below the input impact velocity of $0.5\ m/sec$ can also be written as,

$$e_{COR} = 1 - \alpha \cdot v_i \tag{113}$$

where α ranges between 0.1 and 0.6 sec/m for steel and iron according to [63], v_i refers to the relative velocity of body 1 and body 2 before impact (e.g. the input impact velocity shown in Figure 21).

3.1.2. Nonlinear dynamic contact model

The COR of inelastic impact is dependent on material properties, collision velocity, and geometry of the impactors. In order to include the latter two characteristics, a nonlinear dynamic contact model is developed based on the nonlinear damping model proposed in [65]. This improved dynamic contact model includes not only a nonlinear Hertzian contact restoring force and a nonlinear, viscous contact damping force but also a dry friction tangential contact force induced by the relative rotation between the impactor and the DC.

As can be found in [65], it is a prerequisite for the nonlinear damping model to be valid that $\alpha^2 v_i^2$ is negligible in comparison with $2\alpha v_i$. Therefore, in this work, the COR model is not used for simulation of impact, but determines whether this prerequisite is valid.

In accordance with the Hertz law of contact, impact forces can be formulated by the force-interference relations (Figure 21),

$$F = k\delta^{\frac{3}{2}} \tag{114}$$

where F and δ denote the force and interference in contact, respectively, and k is interpreted in the Appendix C. As noted in Ref. [65], this formula is only applicable if the dimensions of the impact area are relatively small compared to the radii of curvature of the contact bodies. The size of the impacting bodies in the present paper meets this

requirement. The shape of the impact damper and DC at the moment of impact can be approximated as sphere and cylindrical cup, respectively.

The force-interference law yields the final equation of motion during impacting [65] as,

$$m_I\ddot{\delta} + c\dot{\delta} + k\delta^{\frac{3}{2}} = 0 \tag{115}$$

where $c = \frac{3}{2}\alpha k\delta^{\frac{3}{2}}$. Consequently, the contact forces reacting on the DC are equal to $c\dot{\delta} + k\delta^{\frac{3}{2}}$.

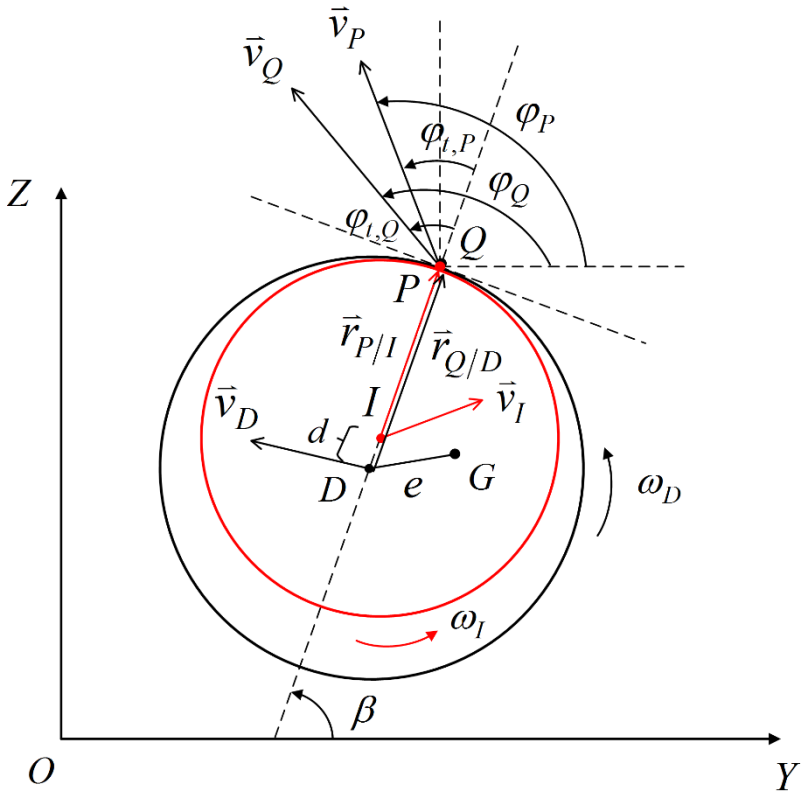

Figure 22. Planar impacting model for impactor-DC collision. Reprinted from Ref. [1].

For each pair of impactor and DC section that come into collision, the total transverse loads acting on the DC section are included in the planar impacting model, which is depicted in Figure 22. The dash line connecting the DC center D and the impactor center I is extended across the contact point Q of the DC and the point P of the impactor. The impactor collides with the DC wall when the distance between D and I, d, exceeds the clearance C_0, and the collision is approximated to occur in the YZ plane. During collision, the restoring forces due to the elastic deformation will induce friction forces in the tangential direction, and it is assumed here that only sliding frictions exist between the two impacting surfaces. As shown in Figure 22, the velocity vectors of the DC and impactor centers are defined as $\vec{v}_D$ and $\vec{v}_I$, respectively. The edge velocity vectors $\vec{v}_P$ and $\vec{v}_Q$ of the contact points P and Q are derived from,

$$\vec{v}_P = \vec{v}_I + \vec{\omega}_I \times \vec{r}_{\frac{P}{I}} \tag{116}$$

$$\vec{v}_Q = \vec{v}_D + \vec{\omega}_D \times \vec{r}_{\frac{Q}{D}} \tag{117}$$

where $\vec{\omega}_D$ and $\vec{\omega}_I$ are the rotation speed vectors of the DC and impactor, respectively, $\vec{r}_{P/I}$ represents the radius vector starting from I and ending at P, and it is similar with $\vec{r}_{Q/D}$. The velocity vector angle φ_P can be derived from $\vec{v}_P$, and then, the tangential angle $\varphi_{t,P}$ is obtained from $\varphi_{t,P} = \varphi_P - \beta$ where $\beta = tan^{-1}\left(\frac{z_I - z_D}{y_I - y_D}\right)$. $\varphi_{t,Q}$ can be derived in the same way. Finally, the tangential velocities of the contact points P and Q are given as,

$$v_{t,P} = v_P \, sin\left(\varphi_{t,P}\right) \tag{118}$$

$$v_{t,Q} = v_Q \, sin\left(\varphi_{t,Q}\right) \tag{119}$$

The interference in Eq. (115), δ, is related to C_0 by,

$$\delta = \sqrt{(y_I - y_D)^2 + (z_I - z_D)^2} - C_0 \tag{120}$$

and the corresponding velocity vector is written as,

$$\dot{\vec{\delta}} = (\dot{y}_I - \dot{y}_D)\vec{\imath} + (\dot{z}_I - \dot{z}_D)\vec{\jmath} \tag{121}$$

where $\vec{\imath}$ and $\vec{\jmath}$ represent the unit vector in Y and Z directions, respectively, and the vector angle of $\dot{\vec{\delta}}$ can be subsequently expressed as,

$$\beta_c = tan^{-1}\left(\frac{\dot{z}_I - \dot{z}_D}{\dot{y}_I - \dot{y}_D}\right) \tag{122}$$

An imbalance mass is located in the middle of the DC (Figure 21) with an eccentric distance e. The drillstring rotation creates centrifugal forces that can be decomposed into two components in Y and Z directions as,

$$F_{e,y} = m_D e \omega_D^2 \, cos(\omega_D t) \tag{123}$$

$$F_{e,z} = m_D e \omega_D^2 \, sin(\omega_D t) \tag{124}$$

The final equations for the impact forces and moments acting on the DC and impactor are given as,

$$F_{D,y} = F_{e,y} + k\delta^{\frac{3}{2}} cos(\beta) + c\dot{\delta} \, cos(\beta_c) - \left[k\delta^{\frac{3}{2}} + c\dot{\delta} \, cos(\beta - \beta_c)\right] \mu \, cos\left(\beta + \frac{\pi}{2}\right) \cdot sign\left(v_{t,Q} - v_{t,P}\right) \tag{125}$$

$$F_{D,z} = F_{e,z} + k\delta^{\frac{3}{2}} sin(\beta) + c\dot{\delta} \, sin(\beta_c) - \left[k\delta^{\frac{3}{2}} + c\dot{\delta} \, cos(\beta - \beta_c)\right] \mu \, sin\left(\beta + \frac{\pi}{2}\right) \cdot sign\left(v_{t,Q} - v_{t,P}\right) \tag{126}$$

$$T_{D,\varphi} = -r_D \mu \left[k\delta^{\frac{3}{2}} + c\dot{\delta}\, cos(\beta - \beta_c) \right] \cdot sign\left(v_{t,Q} - v_{t,P}\right) \tag{127}$$

$$F_{I,y} = -k\delta^{\frac{3}{2}} cos(\beta) - c\dot{\delta}\, cos(\beta_c) + \left[k\delta^{\frac{3}{2}} + c\dot{\delta}\, cos(\beta - \beta_c) \right] \mu\, cos\left(\beta + \frac{\pi}{2}\right) \cdot sign\left(v_{t,Q} - v_{t,P}\right) \tag{128}$$

$$F_{I,z} = -k\delta^{\frac{3}{2}} sin(\beta) - c\dot{\delta}\, sin(\beta_c) + \left[k\delta^{\frac{3}{2}} + c\dot{\delta}\, cos(\beta - \beta_c) \right] \mu\, sin\left(\beta + \frac{\pi}{2}\right) \cdot sign\left(v_{t,Q} - v_{t,P}\right) \tag{129}$$

$$T_{I,\varphi} = r_I \mu \left[k\delta^{\frac{3}{2}} + c\dot{\delta}\, cos(\beta - \beta_c) \right] \cdot sign\left(v_{t,Q} - v_{t,P}\right) \tag{130}$$

The equations of motion for the impactor may be written as,

$$m_I \ddot{y}_I = F_{I,y} \tag{131}$$

$$m_I \ddot{z}_I = F_{I,z} \tag{132}$$

$$J_I \ddot{\varphi}_I = T_{I,\varphi} \tag{133}$$

3.2. Torsional Damper

As demonstrated in Figure 20, a torsional damper of a cylindrical shape is installed inside the DC. Damping forces may be induced by the drilling mud passing through the outer surface of the torsional damper that has a relative rotational speed with respect to the DC. Larger damping forces can be obtained by encasing the torsional damper surrounded by high-viscosity fluid. Another way to increase the torsional damping is to reduce the clearance between the surfaces of the torsional damper and the DC wall.

The torsional damper can be placed on an angular contact thrust ball bearing at the bottom of the DC (shown in Figure 23) or on a grooved baseplate fixed to the bottom

of the DC (shown in Figure 24). The relative rotation of the torsional damper with respect to the DC causes the drag torque of the high-viscosity fluid and tends to dampen out the rotational vibration of the DC.

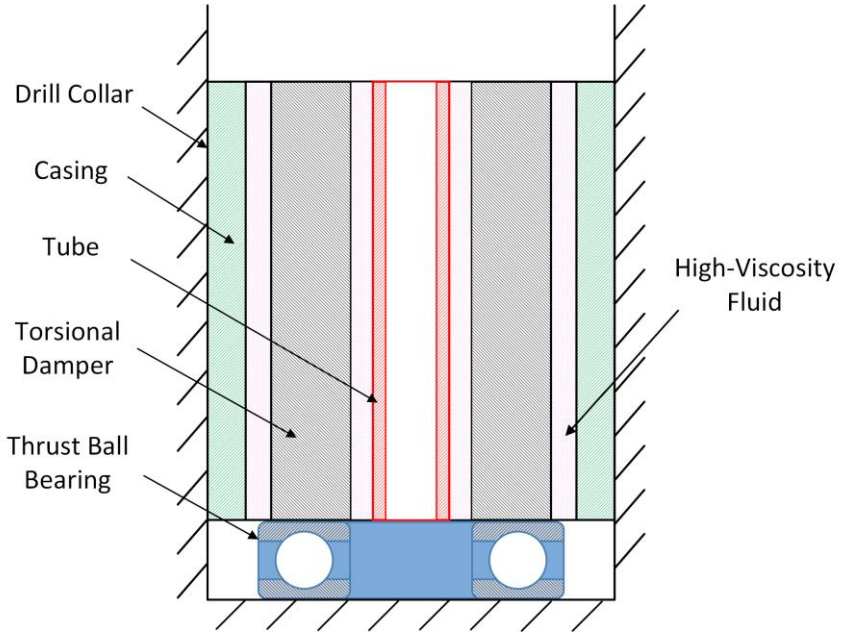

Figure 23. Torsional damper on an angular contact thrust ball bearing.

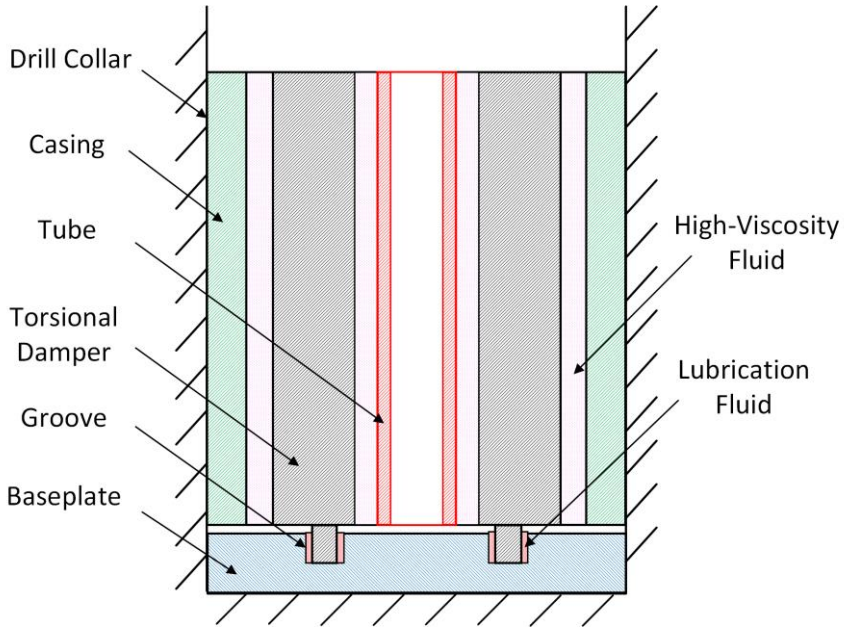

Figure 24. Torsional damper on a grooved baseplate.

The damping forces act as torque on the torsional damper. The total angular motion can be described by,

$$J_A\ddot{\varphi}_A + c_M(\dot{\varphi}_A - \dot{\varphi}_B) + T_A \cdot sign(\dot{\varphi}_A - \dot{\varphi}_B) = 0 \quad (134)$$

where c_M denotes the coefficient of the mud damping, and the torque T_A is induced by sliding frictions between the torsional damper A and inner base of the DC B.

3.3. Beam Element Modeling of Drillstrings

The Timoshenko beam element model shown in Section 2.1 is applied in simulation of the rotor dynamic behaviors of the DP and DC.

3.3.1. Drillstring rotor model

The dynamic formulation based on the Timoshenko beam FEs for the model of a drillstring either in or out of impacting is given as,

$$[M^e]\{\ddot{q}^e\} + ([C^e] + [G^e])\{\dot{q}^e\} + ([K_S^e] + [K_\sigma^e])\{q^e\} = \{f^e\} \quad (135)$$

where $[G^e]$ represents the gyroscopic matrix, and $[K_S^e]$ the stiffness matrix. The stress-stiffening matrix $[K_\sigma^e]$ is representative of the influences of gravity and axial loading on transverse stiffness of the drillstring. The weight of the drillstring with the impactors and torsional damper and the WOB are accounted for as axial load in the external load vector $\{f^e\}$. Stress stiffening acts to increase lateral bending stiffness under tensile load or reduce it under compressive load. The specific matrices can be found in [5, 66].

3.3.2. Coulomb and Stribeck friction torque

In the previous study of stick-slip vibration, either Coulomb [50, 52] or Stribeck [56, 57] torque models has been applied, but it highly depends on the type of DBs and drilling conditions to decide which torque model is adequate. Therefore, we apply both Coulomb torque T_C and Stribeck torque T_S as TOB to the DB node (the bottom node of the drillstring beam FE model shown in Figure 20). As illustrated in Figure 25, the torque T_C equals T_{stt} when the angular velocity of the bit $\omega_B = 0$ while turns into T_{sld} when the bit starts rotating.

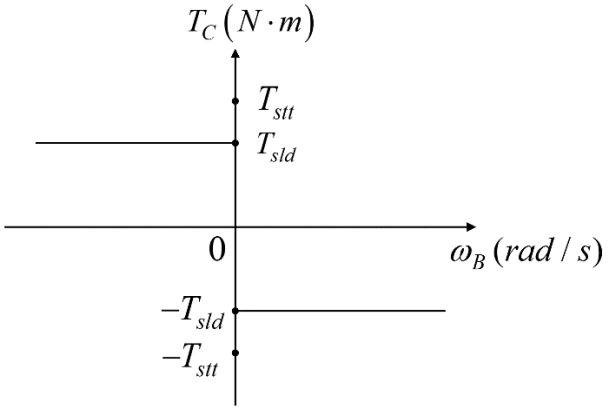

Figure 25. Coulomb torque model: sliding torque T_{sld} and static torque T_{stt}. Reprinted from Ref. [1].

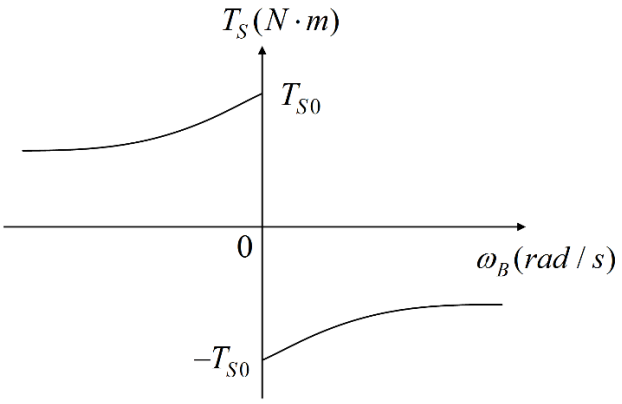

Figure 26. Stribeck torque model. Reprinted from Ref. [1].

In contrast, the Stribeck torque model shown in Figure 26 allows a continuous change of the TOB with the angular velocity of the bit, which can be described by,

$$T_S = -\frac{T_{S0}}{1+\lambda|\omega_B|}\cdot sign(\omega_B) \tag{136}$$

where a small λ indicates a moderately declining torque curve.

3.3.3. Integration of impact and torsional dampers

In impacting, the external load $\{f^e\}$ in Eq. (135) consists of the weight of the drillstring with the impactors and torsional damper and the WOB F_W, the TOB T_{TOB}, the impact-induced forces $F_{D,y}$ and $F_{D,z}$ and the torque $T_{D,\varphi}$ (refer to Eqs. (125)-(130)), and the torque resulting from the mud damping $c_M(\dot{\varphi}_A - \dot{\varphi}_B)$ and sliding friction $T_A \cdot sign(\dot{\varphi}_A - \dot{\varphi}_B)$ (refer to in Eq. (134)). The resultant external load vector for the element node n may be written as,

$$\{\mathrm{f_n}^{\mathrm{e}}\} = [F_W, F_{D,y}, F\left(T_{D,\varphi} + T_{TOB} + c_M(\dot{\varphi}_A - \dot{\varphi}_B) + T_A \cdot sign(\dot{\varphi}_A - \dot{\varphi}_B)\right)^T_{D,z} \quad (137)$$

The specific load to be added into Eq. (137) depends upon the load condition, and thereby, not all the external loads need to be included. The novel impact and torsional dampers presented here are explained by analysis and demonstrated by simulations, with an underlying assumption that the physical implementations are feasible.

3.4. Summary

The chapter presented an approach to model a drillstring equipped with centralized impact dampers and torsional dampers. This novel damper design is aimed at suppressing lateral vibrations of the drillstring that operates close to the bending critical speeds and stick-slip torsional vibration within the operating speed range. The simulation of the collision between the impactor and DC utilized a vibro-impact model, which included a nonlinear Hertzian contact restoring force and a viscous contact

damping force as the radial impacting forces and considers the sliding frictions in between as tangential forces.

The drillstring was modeled with the Timoshenko beam FEs. The stress-stiffening effect was introduced into the drillstring FE model in order to include the influences of drillstring weight and axial loading on transverse string stiffness. Both Coulomb torque and Stribeck torque models were applied when modeling the external forces contributing to the drillstring vibration.

4. VALIDATION OF MIMO TRANSFER FUNCTION MODELING

This chapter aims to validate the MIMO support TF modeling approach that was proposed in Sections 2.6 and 2.7. A rotor system that is composed of a rotor, two bearings and a solid support structure is utilized for validation.

The proposed RSSM that consists of a solid FE rotor model and a state-space support model is compared with the CSRSM. General rotor dynamic analyses, such as natural frequencies, critical speeds, unbalanced response, and logarithmic decrement (log dec) are compared in order to demonstrate the accuracy of using the RSSM in lieu of the CSRSM. In the meanwhile, the computation time is provided to show whether the proposed modeling approach is effective in model reduction. Furthermore, a thorough comparison of the rotor-support modes up to 100,000 cpm (~1667 Hz) is conducted among the RSSM, the solid FE rotor with a super-element support model (SRSSM), and the beam FE rotor with a solid FE support model (BRSSM).

In addition, the modes up to 100,000 cpm are compared among the super-element, beam element, and RSSM. Further, the proposed RSSM is useful for applications in vibration control and active magnetic bearing systems.

---

* Reprinted with permission from "Solid Element Rotordynamic Modeling of a Rotor on a Flexible Support Structure Utilizing Multiple-Input and Multiple-Output Support Transfer Functions" by Hu, L., and Palazzolo, A., 2016, Journal of Engineering for Gas Turbines and Power, 139(1), 012503, Copyright 2016 by ASME.

4.1. Rotor System Model and Grid Sensitivity

A scaled-down rotor-support system, which is modeled with either the solid elements or both solid elements and TFs, is presented for investigation and comparison. The rotor consists of a thin-walled shaft and three disks and is supported by two tilting pad bearings. The axisymmetric harmonic FE method is used to model the thin-walled rotor, which is depicted in Figure 27. The material properties of the rotor are set as $\rho = 7800kg/m^3$, $\nu = 0.3$, $E = 2.1 \times 10^{11}N/m^2$. The stiffness and damping of the bearings are obtained from a specialized bearing coefficient-prediction program and are given in Figure 28 and Figure 29. The structure supporting the rotor is composed of a bearing pedestal and a baseplate with four feet fixed to ground. The material properties of the support structure are given as $\rho = 2700kg/m^3$, $\nu = 0.33$, $E = 6.9 \times 10^{10}N/m^2$. Tetrahedron elements are used to model the support structure. The CSRSM is demonstrated in Figure 30.

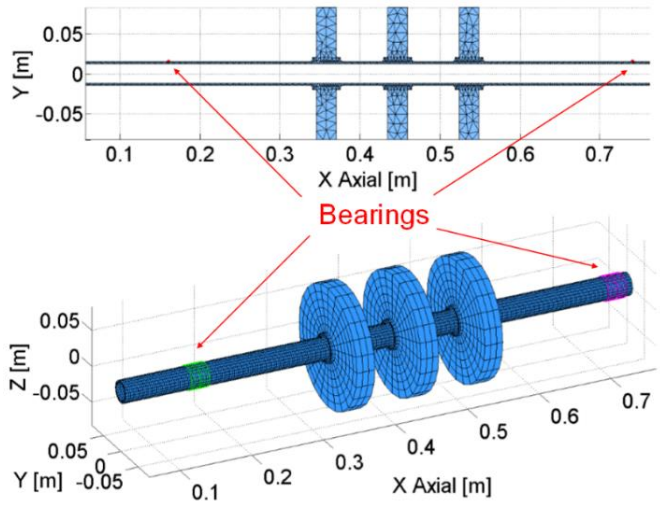

Figure 27. Cross-section (top) and 3D solid (bottom) FE mesh models of the rotor supported by two tilting-pad bearings. Reprinted from Ref. [80].

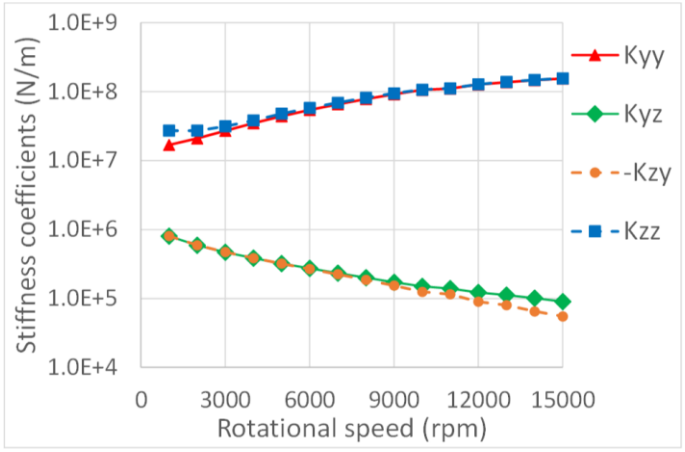

Figure 28. Stiffness coefficients of the bearing. Reprinted from Ref. [80].

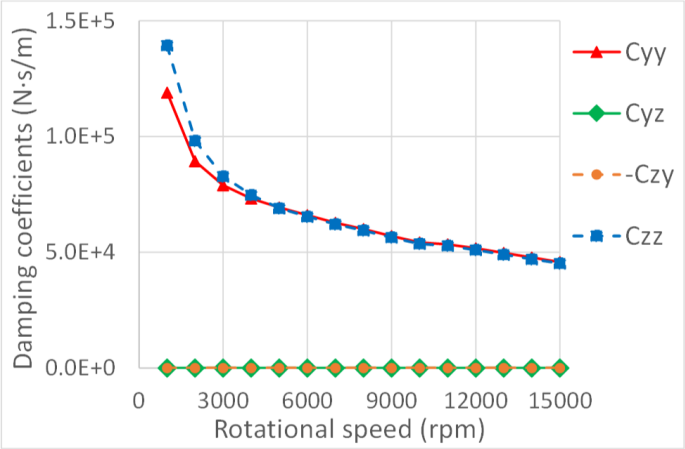

Figure 29. Damping coefficients of the bearing. Reprinted from Ref. [80].

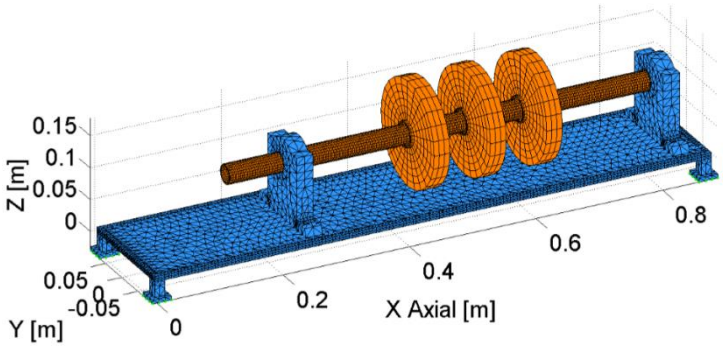

Figure 30. Solid FE mesh model of the rotor-support system. Reprinted from Ref. [80].

Before the FE simulation results can be used for comparison, a grid sensitivity test on the CSRSM is conducted in order to validate the solid FE modeling. The damped natural frequencies of the third mode of the rotor-support system are calculated for comparison and are presented in Figure 31. It can be seen that the percentage difference of the natural frequencies, compared to the natural frequencies obtained from the finest mesh, varies from 36.3% to 1.2%, which indicates that the natural frequencies converge with the refinement of mesh of the rotor and support. Therefore, the FE model with a

1.2% difference can be used as a benchmark in evaluation of the proposed modeling approach.

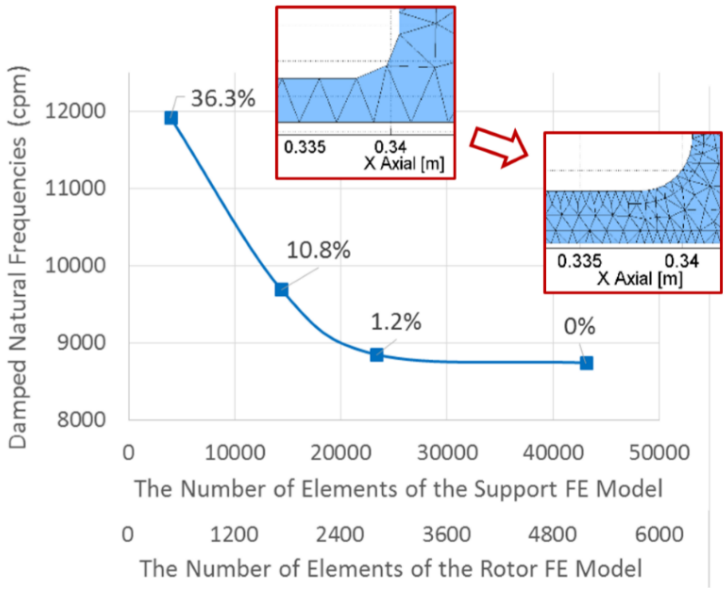

Figure 31. Grid sensitivity test for the third mode of the CSRSM at the rotational speed of 5000 rpm. Reprinted from Ref. [80].

4.2. Significance of Curve-Fitting

The FRF data is obtained by applying frequency-dependent load (sinusoidal forces) on the fictitious bearing attachment points of the support FE model. The TFs are subsequently obtained by curve-fitting the FRF data with polynomials, where extra attention needs be given to the polynomial order selection. Consider curve-fitting with the lower degree TFs like the second-order numerator divided by third-order denominator (second/third or written as $2^{th}/3^{th}$ in Figure 32) polynomials. It is found that not all the sixteen TFs in Eq. (54) are well fitted. Take G_{Z2Z2}, for example. The curve fit shown in Figure 32 fails to capture the exact frequency (150 Hz) of the amplitude peak, where the rotor and support structure vibrate vertically (refer to the bottom figure shown

in Figure 35). Since G_{Z2Z2} represents the TF between the excitation force and response in the vertical direction at the right bearing location, the shifting of the critical frequency of G_{Z2Z2} probably leads to shifted vibration peaks or extra peaks. In order to solve this problem, a higher polynomial degree with the fifth-order numerator divided by sixth-order denominator (fifth/sixth or written as $5^{th}/6^{th}$ in Figure 32) is employed. As Figure 32 shows, the fifth/sixth TF perfectly fits the original FRF curve.

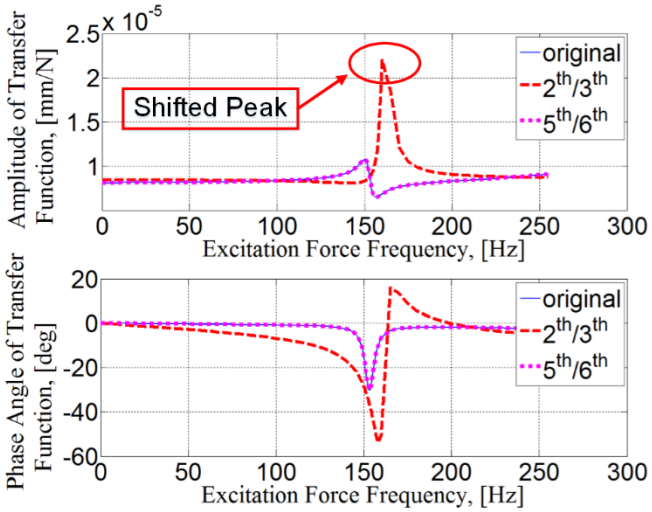

Figure 32. Transfer function G_{Z2Z2} with the second/third and fifth/sixth polynomials. Reprinted from Ref. [80].

For simplicity, the detailed TF matrices are not provided. After converting the TF matrices into a state space, the matrix formulas provided in the preceding sections are employed to combine the state-space model of the support structure with the rotor FE model.

4.3. Comparison of Rotor Dynamic Analyses

Simulation results of commonly applied rotor dynamic analyses, such as the critical speed map, unbalance response, and log dec, are presented in Figure 33 through Figure 43.

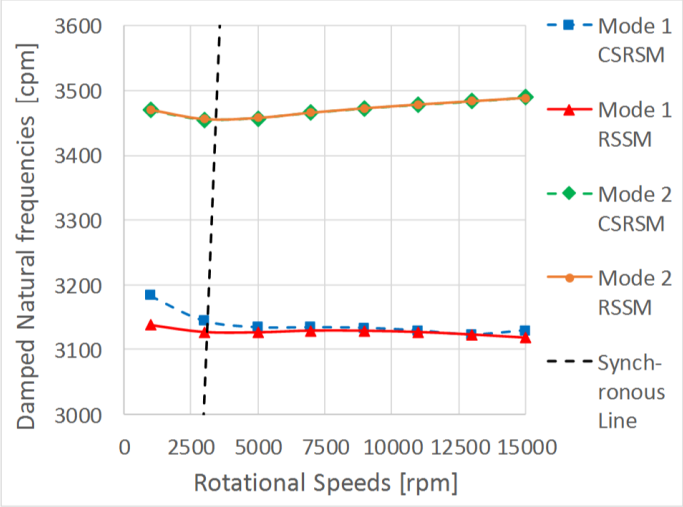

Figure 33. Critical speeds for the first and second modes. Reprinted from Ref. [80].

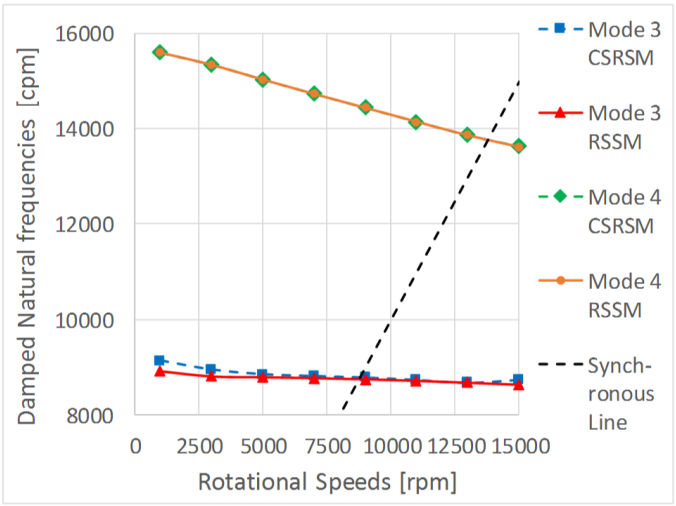

Figure 34. Critical speeds for the third and fourth modes. Reprinted from Ref. [80].

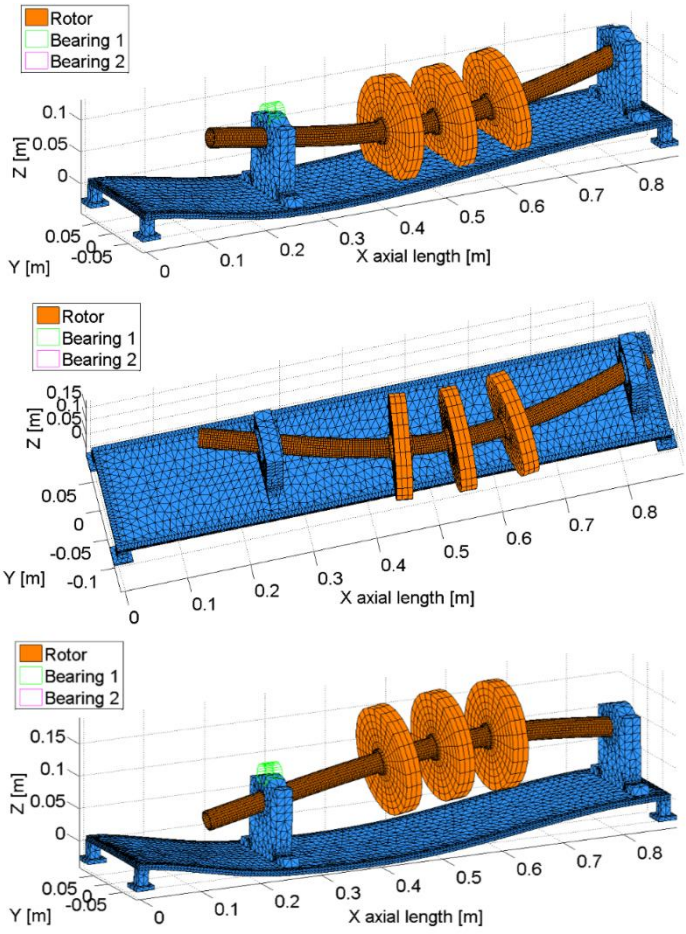

Figure 35. Mode shapes for the first (top), second (middle) and third (bottom) critical speeds of the rotor-support system. Reprinted from Ref. [80].

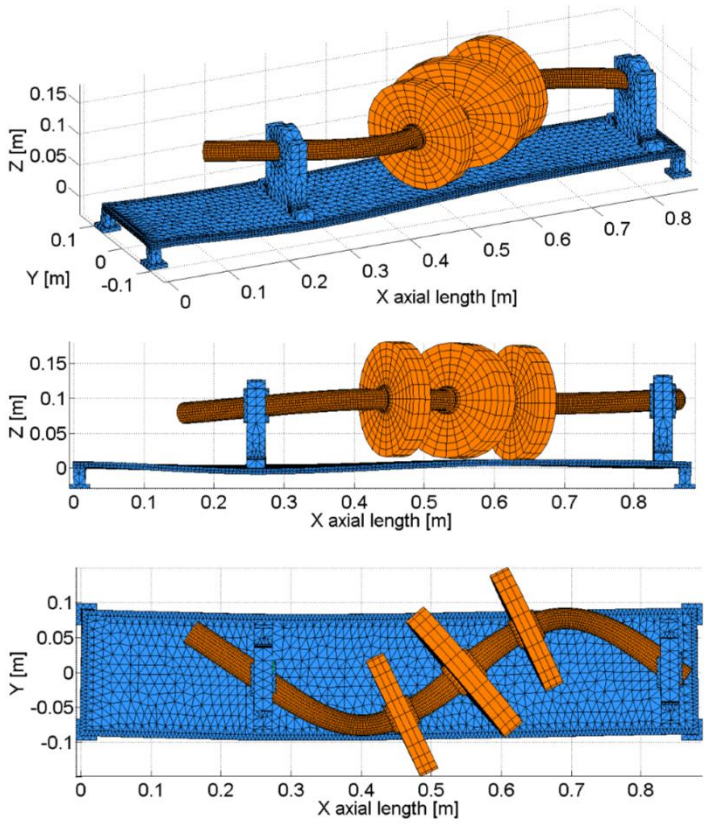

Figure 36. Mode shape (top: orthographic projection, middle: front view, bottom: top view) for the fourth critical speed of the rotor-support system. Reprinted from Ref. [80].

In regard to the rotor-support system, the first four critical speeds to appear within the rotating speed range of 0-15,000 rpm are presented in Figure 33 and Figure 34, with the corresponding mode shapes shown in Figure 35 and Figure 36. As can be seen from Figure 33, the first critical speed is 3140 rpm for the CSRSM and 3125 rpm for the RSSM. That is to say, the percentage difference of the first critical speeds between these two models is less than 0.5%. The second and fourth critical speeds obtained from the proposed RSSM are 3455 rpm and 13,769 rpm, respectively. For the CSRSM, they are 3455 rpm and 13,771 rpm, respectively. As demonstrated in Figure 33

and Figure 34, the natural frequency lines for these two modes nearly coincide with each other. The third critical speed of the RSSM is 8748 rpm with a 0.6% difference from 8805 rpm of the CSRSM. The close agreement confirms the accuracy of the proposed modeling approach compared with the complete solid FE modeling approach, in terms of the natural frequency prediction.

To further validate the RSSM, unbalance response analysis is performed. The unbalanced mass distance of $25g \cdot mm$ is attached to the center of the middle disk. The peak-to-peak (p-p) unbalance response of the rotor at the middle disk and two bearing locations is demonstrated in Figure 37 to Figure 42. It can be clearly observed that the vibration amplitudes of the RSSM agree with those of the CSRSM. The highest vibration peaks at each of those three locations all occur at the speed of 3125 rpm (the first critical speed) or 3450 rpm (near the second critical speed). At the speed of 8830 rpm (close to the third critical speed), violent vibrations appear in the vertical direction, whereas the horizontal vibrations are much milder. This may be attributed to the mode coupling in the vertical direction between the rotor and support structure, as can be seen from the bottom mode shape depicted in Figure 35. At 13,800 rpm (near the fourth critical speed), however, vibrations peak in both vertical and horizontal directions. This can be explained by the mode shapes shown in Figure 36, where the rotor and support structure are not only coupled in the vertical direction but in horizontal direction as well, thereby leading to both vertical and horizontal vibration peaks.

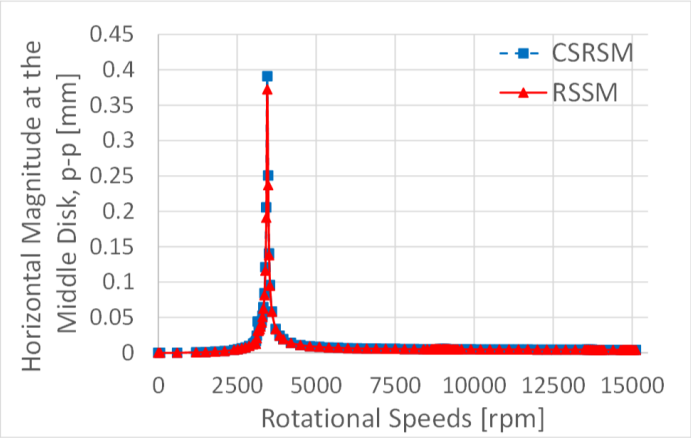

Figure 37. Horizontal magnitude of the unbalance response at the center of the middle disk. Reprinted from Ref. [80].

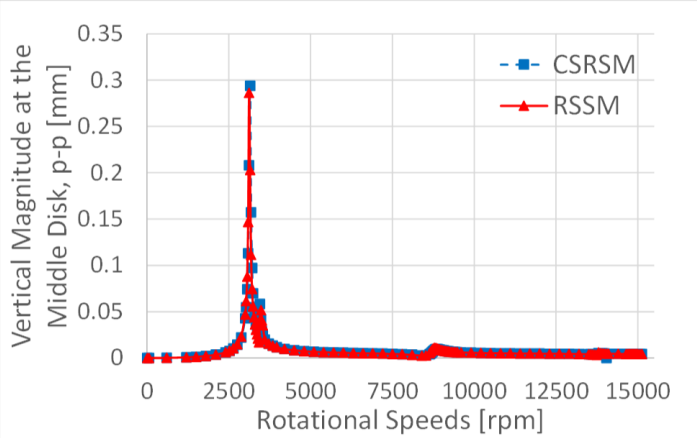

Figure 38. Vertical magnitude of the unbalance response at the center of the middle disk. Reprinted from Ref. [80].

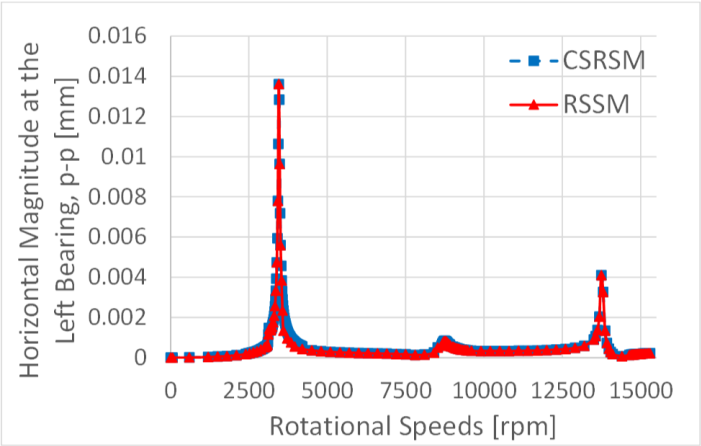

Figure 39. Horizontal magnitude of the unbalance response at the left bearing location. Reprinted from Ref. [80].

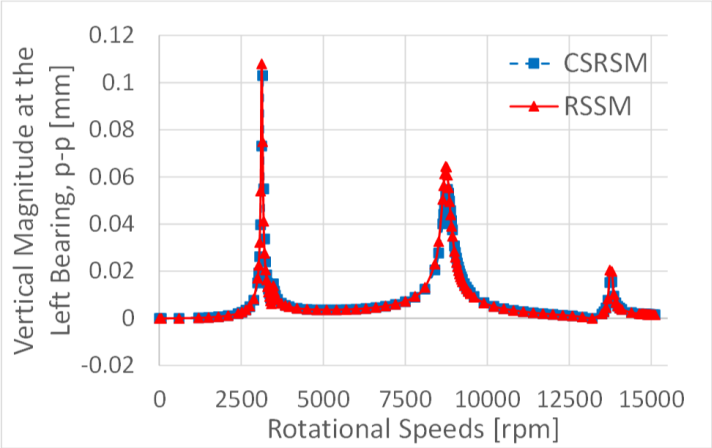

Figure 40. Vertical magnitude of the unbalance response at the left bearing location. Reprinted from Ref. [80].

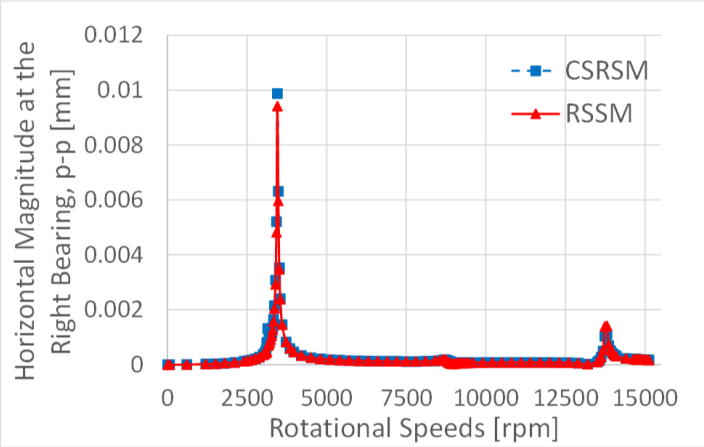

Figure 41. Horizontal magnitude of the unbalance response at the right bearing location/ Reprinted from Ref. [80].

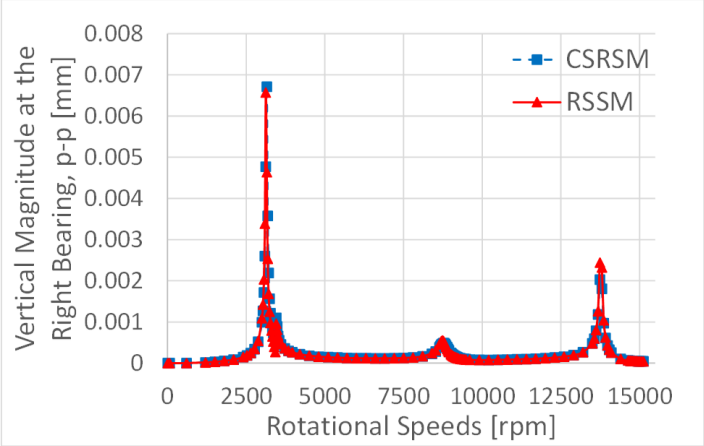

Figure 42. Vertical magnitude of the unbalance response at the right bearing location. Reprinted from Ref. [80].

Apart from the unbalance analysis, stability of the rotor system is always one of the primary concerns in rotor dynamic analyses. The log dec of the rotor system, which is commonly used in the turbomachinery industry to determine the dynamic stability, is calculated and compared in Figure 43. For the first, third and fourth modes, the percentage difference of the log dec between the RSSM and the CSRSM is within 3%.

With regard to the second mode within the operating speed range, the largest difference is 15%, which occurs at the speed of 15,000 rpm. In general, the RSSM shows good agreement with the CSRSM.

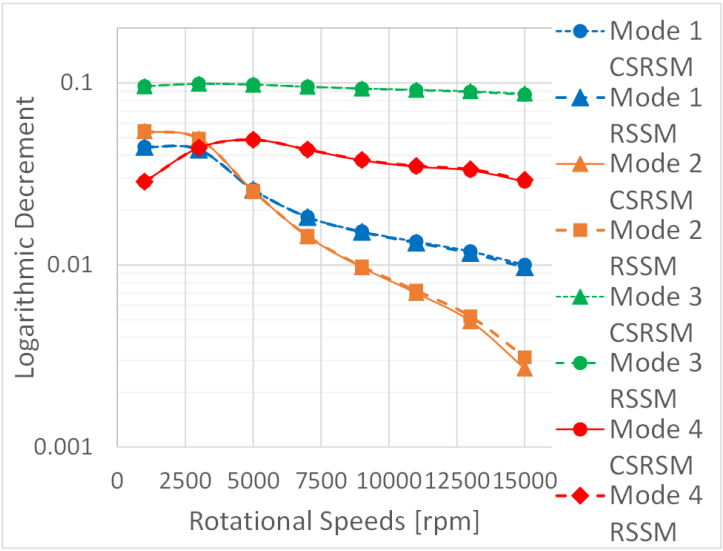

Figure 43. Stability analysis of the rotor-support system. Reprinted from Ref. [80].

4.4. Comparison of Computation Time

In order to demonstrate the computational efficiency of the proposed approach, the computation time is compared among the CSRSM, RSSM, SRSSM, and BRSSM. Before comparison, the Guyan reduction method [16] is applied to all the FE models, retaining 10% DOFs of each model. The comparison, as illustrated in Table 2, is made between the simulation time required for obtaining the eigenvalues of the lowest 100 modes of the rotor-support system. The simulation is performed on the HP Z420 workstation with a 3.7 GHz Quad-core Intel Xeon CPU and 48 GB RAM.

Table 2. Simulation time for obtaining the eigenvalues of the lowest 100 modes of the rotor-support system with 10% DOFs retained. Reprinted from Ref. [80].

	CSRSM	RSSM	SRSSM	BRSSM
Rotor model	2050 DOFs	2050 DOFs	2050 DOFs	38 DOFs
Support model	2537 DOFs	96×96 state-space matrix (96 DOFs)	6 DOFs	2537 DOFs
Total DOFs	4587	2146	2056	2575
Time for meshing	2 min	2 min	2 min	1.5 min
Computation time per speed	14 min	2.5 min	2.5 min	3 min
Time for obtaining FRFs		5 min		

For the CSRSM, it takes 14 min to obtain the eigenvalues at each rotational speed. In contrast, the RSSM requires only 2.5 min. The reduction of the computation time benefits from the substantial reduction of the solid FE support structure model from 2537 DOFs to the 96×96 (96 DOFs) state-space model that corresponds to the 5th/6th TFs of the support structure. Generally, rotordynamic analyses will be conducted at

dozens of different rotational speeds, due to the gyroscopic effects, the change of the bearing or seal coefficients, etc. Also, both the mesh generation and the calculation of the FRFs are performed only once. Therefore, by counting the total simulation time, the RSSM is nearly five times faster than the CSRSM. This time reduction factor will increase with less DOFs of the rotor model and more DOFs of the support structure model as the RSSM mainly retains the DOFs of the rotor model.

In addition to the comparison with the solid FE model, the RSSM is compared with the SRSSM and BRSSM. As Table 2 shows, the computation time is 2.5 minutes for the RSSM vs. 3 minutes for the BRSSM. This can be explained by the larger total number of DOFs of the BRSSM, i.e. that the sum of DOFs of the beam FE rotor model (38 DOFs) and the solid FE support structure model (2537 DOFs) are more than the DOFs of the RSSM (2146 DOFs in total). In regard to the SRSSM, the reduced substructure (support structure) is assembled together with the rotor FE model via two bearing attachment points that are exterior to the super-element support model.

As illustrated in Table 2, either the computation time or the time for mesh generation is quite close between the RSSM and the SRSSM. Although the state-space support model seems to have many more DOFs (96 DOFs) than the super-element support model (6 DOFs), the computation difference between these two models is in practice less than three seconds on account of having nearly the same total number of DOFs (2146 DOFs vs. 2056 DOFs).

4.5. Comparison of Higher-Frequency Mode Predictions

In contrast with the slight advantage of the SRSSM in computation time, the predictions made by the SRSSM are probably less accurate than the RSSM for some higher-frequency modes. To prove this, both the RSSM and the SRSSM are compared with the CSRSM in terms of natural frequencies. The BRSSM is also included in this comparison in order to show that the proposed modeling approach is more accurate than the beam rotor model in higher-frequency modes.

For the rotor-support system with the rotor spinning at 10,000 rpm, the natural frequencies of the modes up to 100,000 cpm (~1667 Hz) are given in Table 3. It can be seen that nearly all the natural frequencies of the RSSM are in close agreement with those of the CSRSM except for a few higher modes such as modes 16 and 17. The inaccurate prediction is caused by the insufficiently accurate curve-fitting. The currently employed TFs with the fifth-order numerator divided by sixth-order denominator (fifth/sixth) is accurate for curve-fitting the FRF data for the lower modes (lower than mode 13) but may not be accurate enough for the higher modes. When the higher modes of the support structure become as complicated as shown in the bottom figure of Figure 44, the fifth/sixth order curve-fitting may cause prediction errors.

Table 3. Natural frequencies of the rotor-support system at the rotational speed of 10,000 rpm. Reprinted from Ref. [80].

Natural frequency (cpm)	**CSRSM**	**RSSM**	**SRSSM**	**BRSSM**
Mode 1	3091	3086 (0%)	3092 (0%)	3171 (3%)
Mode 2	3485	3485 (0%)	3490 (0%)	3586 (3%)
Mode 3	8719	8705 (0%)	8868 (2%)	8809 (1%)
Mode 4	14,323	14,315 (0%)	14,509 (1%)	14,660 (2%)
Mode 5	17,471	17,451 (0%)	17,818 (2%)	17,748 (2%)
Mode 6	19,081	19,081 (0%)	19,081 (0%)	19,484 (2%)
Mode 7	21,615	21,430 (-1%)	35,391 (64%)	21,672 (0%)
Mode 8	29,588	29,584 (0%)	29,609 (0%)	31,137 (5%)
Mode 9	33,037	33,037 (0%)	33,037 (0%)	33,812 (2%)
Mode 10	37,350	36,986 (-1%)	40,213 (8%)	37,615 (1%)
Mode 11	41,473	41,422 (0%)	41,836 (1%)	42,621 (3%)
Mode 12	42,392	42,407 (0%)	42,554 (0%)	47,608 (12%)
Mode 13	47,938	49,359 (3%)	63,414 (32%)	47,960 (0%)
Mode 14	60,550	60,560 (0%)	60,549 (0%)	67,418 (11%)
Mode 15	64,606	67,945 (5%)	N/A	64,717 (0%)
Mode 16	70,190	67,914 (-3%)	N/A	70,224 (0%)
Mode 17	76,890	90,004 (17%)	N/A	76,892 (0%)

Table 3. Continued.

Natural frequency (cpm)	CSRSM	RSSM	SRSSM	BRSSM
Mode 18	78,786	79,436 (1%)	93,125 (18%)	80,184 (2%)
Mode 19	85,458	85,458 (0%)	85,457 (0%)	95,523 (12%)
Mode 20	89,814	106,427 (18%)	N/A	104,394 (16%)
Mode 21	89,923	90,772 (1%)	91,865 (2%)	88,171 (-2%)
Mode 22	91,451	91,395 (0%)	91,349 (0%)	97,181 (6%)
Mode 23	98,168	98,495 (0%)	98,771 (1%)	104,318 (6%)
Mode 24	98865	98,958 (0%)	117,339 (19%)	100,618 (2%)
Mode 25	100,889	100,948 (0%)	101,033 (0%)	111,100 (10%)

As for the SRSSM, most of the modes are in accordance with those of the CSRSM, except that modes 7 and 13 are inaccurately predicted (64% and 32% differences, respectively) and modes 15, 16, 17 and 20 are missing. The reason for these inaccurate or missing modes can be found in Figure 44. As the top figure shows, the rotor and support are coupled in mode 7. It is likely that the support structure is over-reduced by using the super-element. As a result, the dynamic characteristics of the support structure modes that have a complex mode shape like mode 7 may not be perfectly represented by the support super-element model. In addition, the super-element support model fails to predict some of the high-frequency support structure modes like

mode 16 (bottom figure in Figure 44) when the mode shape is more complicated. This can be remedied by dividing the support structure into more than one substructure. For example, the bearing pedestal could be separated as a substructure, or even the baseplate could be divided into several segments. However, the selection of substructures greatly depends on people's experience and may sacrifice the modeling time for accuracy.

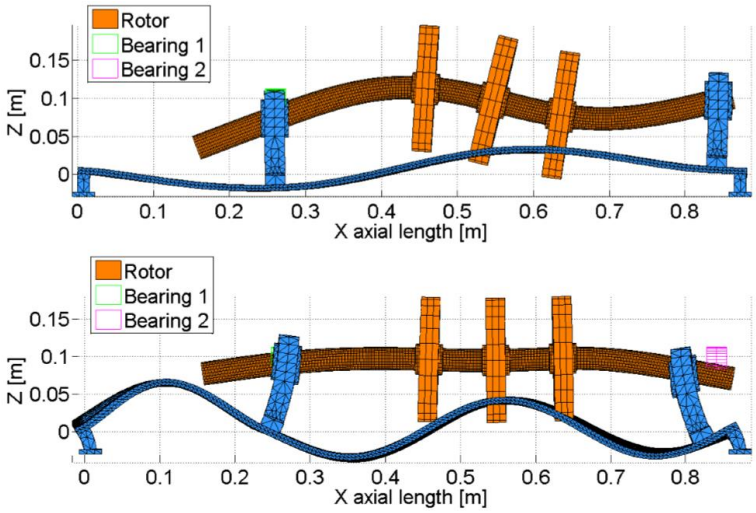

Figure 44. Mode shapes of the solid FE rotor-support model corresponding to modes 7 (top) and 16 (bottom) in Table 3. Reprinted from Ref. [80].

With regard to the BRSSM, the prediction is fairly accurate (within 10% difference) for the lower-frequency modes but slightly inaccurate (10-20% difference) for the higher-frequency modes. This may be caused by the violation of the assumption in the beam theory that the plane sections remain plane after deformation. As can be observed from Figure 45, the segments of the shaft between the disks are severely bending, which may result in the non-beam deformation (i.e., the shaft sections are not plane after deformation).

From the comparison of the modes well above the operating speed range, it can be briefly concluded that the RSSM is more accurate than the SRSSM and BRSSM for the higher-frequency modes. Since the practical bandwidth of interest for AMB controllers is above 1000 Hz, the RSSM would be a good replacement of the SRSSM or BRSSM for the AMB-mounted turbomachinery. Moreover, the AMB controller can be easily integrated into the RSSM.

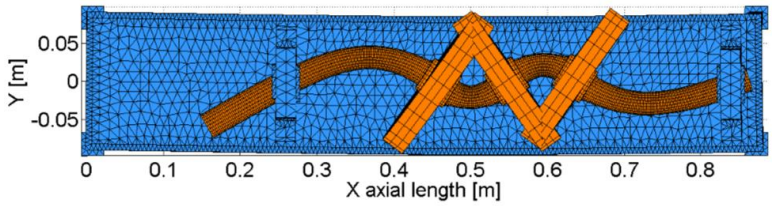

Figure 45. Mode shape of the solid FE rotor-support model corresponding to mode 12 in Table 3. Reprinted from Ref. [80].

4.6. Summary

This chapter validated the MIMO TF modeling approach proposed in Sections 2.6 and 2.7. A thin-walled shaft with multiple flexible disks on a flexible support structure was modeled using both the CSRSM and the RSSM.

In regard to the CSRSM, the rotor is modeled with the axisymmetric solid harmonic FEs, and the support structure is modeled with tetrahedral elements. The Guyan reduction method is applied to simplify both solid FE rotor and support models.

As for the RSSM, the structure supporting the rotor is represented by the TFs that are derived from the solid FE support model or measured FRFs of the substructure at the

bearing locations. The TF matrix is further transformed into a state-space form and integrated into the rotor FE model.

Firstly, the grid sensitivity test was conducted in order to validate the CSRSM.

Then, the RSSM was compared with the CSRSM in regard to the general rotor dynamic analyses. The metrics included natural frequency, critical speed, unbalance response, logarithm decrement, and computation speed. The simulation results show that the RSSM provides a dynamically accurate approximation of the solid FE model in terms of rotor dynamic analyses. Moreover, the computation time for the RSSM is reduced to less than 20% of the time required for the CSRSM.

At last, both the SRSSM and the BRSSM were included, along with the RSSM, in a comparison of the high-frequency modes of the rotor system. The results show that the RSSM is more accurate in predicting high-frequency modes than the other two approaches.

During the comparison, the way to find the curve fit for the FRFs of the support structure is also investigated. The frequency sampling and the polynomial degree of the TF are significant for the quality of curve-fitting. More specifically, a good excitation frequency sample should contain the response information in the neighborhood of the frequencies with a dramatic amplitude or phase change and should be the union of the frequencies of all the FRFs. In the meanwhile, the polynomial degree of the TF is better selected in such a way that the peaks and shifts of the TF amplitude or phase angle are retained by the curve fit with as a low polynomial degree as possible.

5. AXISYMMETRIC SOLID ELEMENT ROTORDYNAMIC ANALYSIS

This chapter will use the axisymmetric solid FE modeling approaches presented in Chapter 2 to investigate the dynamic behaviors of rotors with thin-walled shafts and flexible disks. A comprehensive comparison between the beam FE rotor model and the axisymmetric solid FE rotor model will be presented.

5.1. Verification of Rotor Dynamics Software

The axisymmetric FE formulation developed in the work is implemented in the in-house rotor dynamics software. Unless otherwise specified, the Guyan reduction method is applied to the solid FE models. Before comparison of beam FE and solid FE models, a three-disk rotor with tilting-pad bearing support [86, 87] has been used to validate the rotor dynamics code.

For the lowest five modes of the rotor system operating at 4000 rpm, the natural frequency differences between the axisymmetric FE model and experiment are no more than 5%. The results obtained from the axisymmetric FE model is more accurate than from the beam FE model. The maximum natural frequency difference is 7% (difference exceeds 10% if using the beam element model) for the sixth bending mode. As pointed out in [87], the maximum difference is due to the neglecting of the foundation structure. Overall, the improved axisymmetric FE model presented in this work is verified to be sufficiently accurate for the following comparisons with the beam element model.

5.2. Bearing Attachment

As mentioned in the previous bearing attachment section 2.2.3, excessive local distortions may occur if the bearing linear dynamic force coefficients (stiffness and damping) are not connected to the axisymmetric elements model in a manner that distributes the bearing forces. To illustrate this, consider the case of a cylindrical thin-walled shaft with $L/D_O = 4$ and $t = 0.025D_O$ (refer to Table 4 for definitions). As shown in Figure 46, the flexible shaft is supported by two identical symmetric bearings. The bearing damping is set zero. The bearing stiffness is set as $K_{yy} = K_{zz} = 5K_S$ (i.e. stiff bearing). K_S is defined as the bending stiffness of the shaft and can be expressed as $K_S = 48EI/L^3$. The physical meaning of K_S can be explained as the bending stiffness of a cylindrical shaft at the middle of which a lateral point force is imposed.

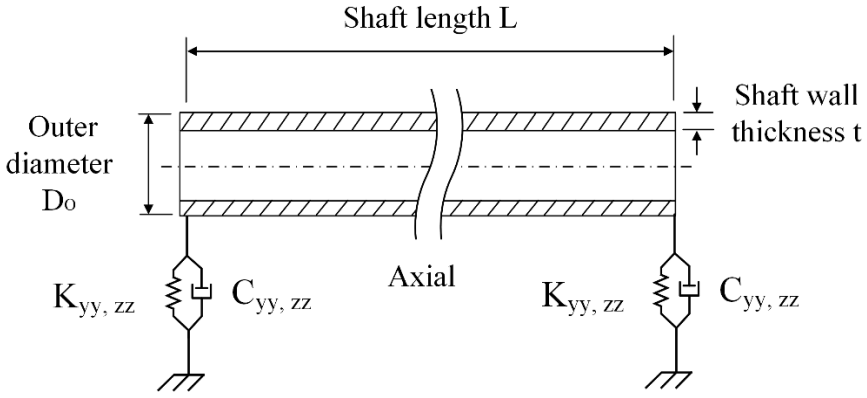

Figure 46. Straight hollow shaft supported by two bearings. Reprinted from Ref. [69].

Figure 47 (a) shows modal deformations with the bearing coefficients applied at a single surface node, leading to excessive local distortions of the journal. Figure 47 (b)

shows the same mode shape with the bearing attachment made in a distributed manner as described in the Bearing Attachment section. “Distributed” here implies that each bearing stiffness coefficient is equally (or adjustable) divided by the same number of surface nodes of the journal and then attached to the surface nodes. This may help to eliminate unrealistic local deformations and warping.

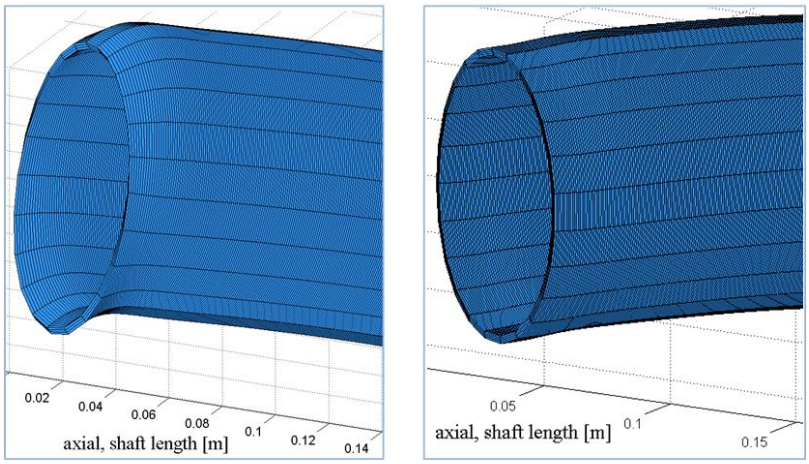

Figure 47. Deformation of a thin-walled journal with stiff bearing supports. (a) Point bearing attachment. (b) Distributed bearing attachment. Reprinted from Ref. [69].

5.3. Parametric Studies

Axisymmetric solid FE models will produce more accurate results than beam FE models when properly meshed as posited in [9]. In particular beam elements are not sufficiently accurate for modeling thin-walled shafts and flexible disks because of the violation of the beam assumption. The present work identifies specific design features of

a rotor system that are likely to cause inaccurate natural frequency predictions when using the beam FE model. Table 4 provides a list of related rotor parameters.

Table 4. Parameters of axisymmetric and beam FE rotor models. Reprinted from Ref. [69].

Variable	Definition
L/D_O	Ratio of the straight shaft length to the shaft outer diameter. Refer to Figure 46.
t/D_O	Ratio of the shaft wall thickness to the shaft outer diameter. Refer to Figure 46.
L_d/D_O	Ratio of the disk thickness to the straight shaft outer diameter. Refer to Figure 54 for L_d.
θ	Taper angle of the conical segment of a shaft. Refer to Figure 50 for θ.
t/D_{Or}	Ratio of conical segment wall thickness to shaft outer diameter at the right end. Refer to Figure 50 for D_{Or}.
K_B/K_S	Ratio of the bearing stiffness to the structural stiffness of the shaft. Refer to Section 5.3.1 for K_B and K_S.
1 or 2	The number of the disks and their locations.

5.3.1 Cylindrical thin-walled shaft

As depicted in Figure 46, a dimensionless straight hollow shaft supported by two identical bearings with symmetric stiffness (i.e. $K_{xx} = K_{yy} = K_B$) and zero damping. Various combinations of L/D_O , t/D_O , and K_B/K_S (K_S has been defined in Section 5.2)

have been investigated, and simulation results are demonstrated in Figure 48 and Figure 49. As can be seen from Figure 48, the difference of free-free natural frequencies between solid and beam FE models becomes larger as shaft wall thickness gets thinner (i.e. t/D_O decreases). when $t/D_O = 0.04$, the difference exceeds 10%. The dimensionless natural frequency, $\widehat{\omega}_n$, is defined as,

$$\widehat{\omega}_n = \omega_n \sqrt{\frac{M_S}{K_S}} \text{ with } M_S = \frac{\rho\pi}{4}(D_O^2 - D_I^2)L \tag{138}$$

where ω_n is the natural frequency of the shaft.

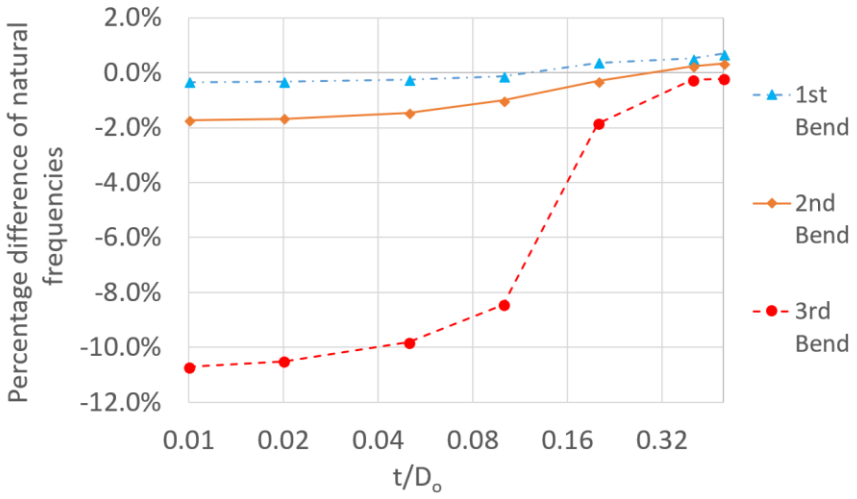

Figure 48. Percentage difference of natural frequencies between axisymmetric and beam FE models for a free-free straight thin-walled shaft with $L/D_O = 4$. Reprinted from Ref. [69].

Varying the bearing stiffness coefficients from 0.1 to 5 times the structural stiffness of the shaft shows the impact of bearing parameters on the prediction difference between axisymmetric FE and beam FE models. As can be seen from Figure 49, the

higher the bearing stiffness (i.e. K_B/K_S increases) is, the larger the difference is. In addition, a shorter shaft (i.e. L/D_O shown in the upper figures of Figure 49 are smaller than in the lower figures) or a thinner shaft wall (i.e. t/D_O shown in the left figures of Figure 49 are smaller than in the right figures) also results in a larger prediction difference of natural frequencies.

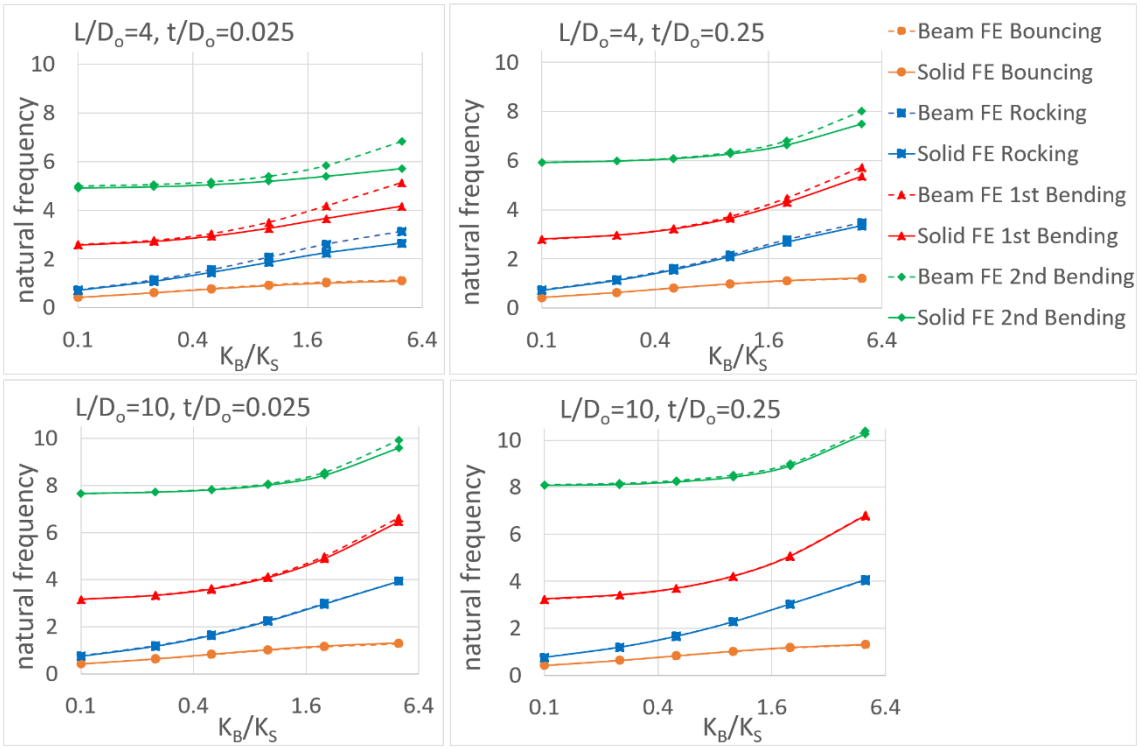

Figure 49. Dimensionless natural frequencies of the straight thin-walled shaft supported by two bearings with four different rotor configurations. Reprinted from Ref. [69].

5.3.2 Stepped, thin-walled shaft

This section investigates a thin-walled shaft composed of both straight and conical/stepped segments. The conical/stepped segment is modeled with conical beam

elements [8]. As Figure 50 shows, the shaft is divided into twenty elements (purely stepped shaft segment consists of one element, and the conical segment with $\theta = 11^{\circ}$ consists of five elements). A variety of thin-walled shafts with $t/D_{Or} = 0.025$ and the gradually decreasing taper angles from 90 to 11 degrees have been modeled with axisymmetric FEs, which are illustrated in Figure 51.

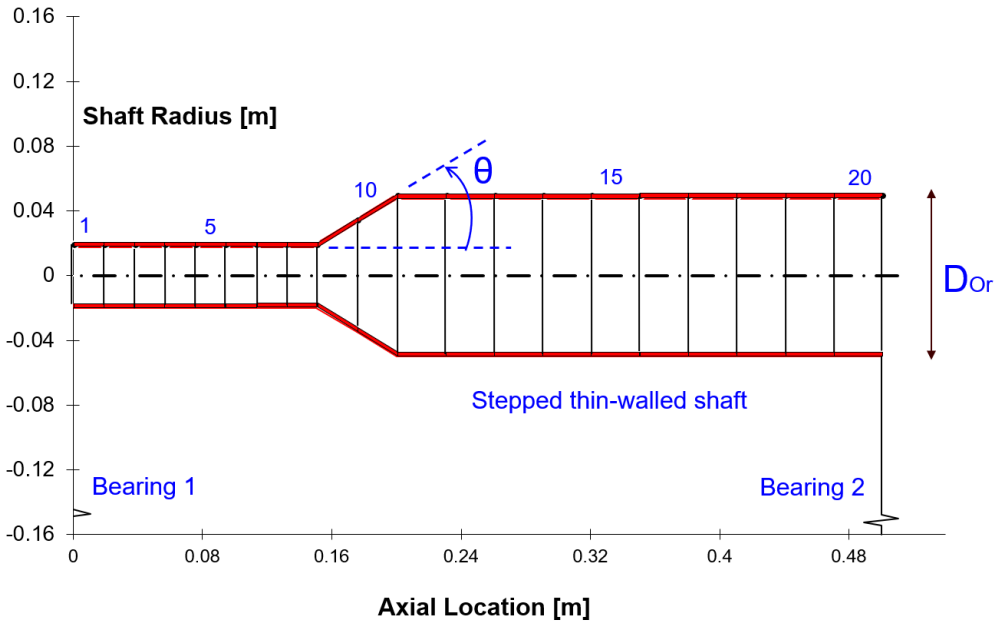

Figure 50. Beam element model for a stepped thin-walled shaft. Reprinted from Ref. [69].

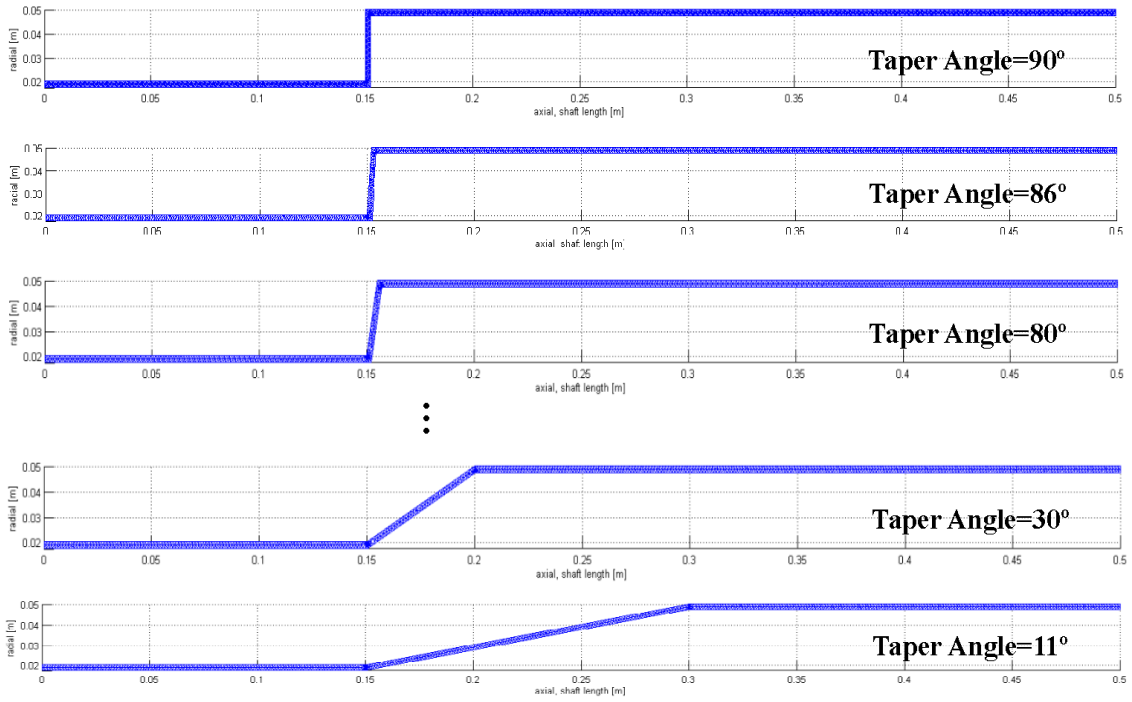

Figure 51. Axisymmetric element models of longitudinal semi-sections of the step shafts with different taper angles. Reprinted from Ref. [69].

It can be seen from the simulation results shown in Figure 52 that as the taper angle gets smaller, the natural frequencies for the first bending mode predicted by the axisymmetric FE model become closer to those predicted by the beam FE model. As shown in Figure 53, clearly non-beam deformations occur at the step location in the axisymmetric FE model, indicating that it may be inaccurate to use beam elements to model a stepped thin-walled shaft.

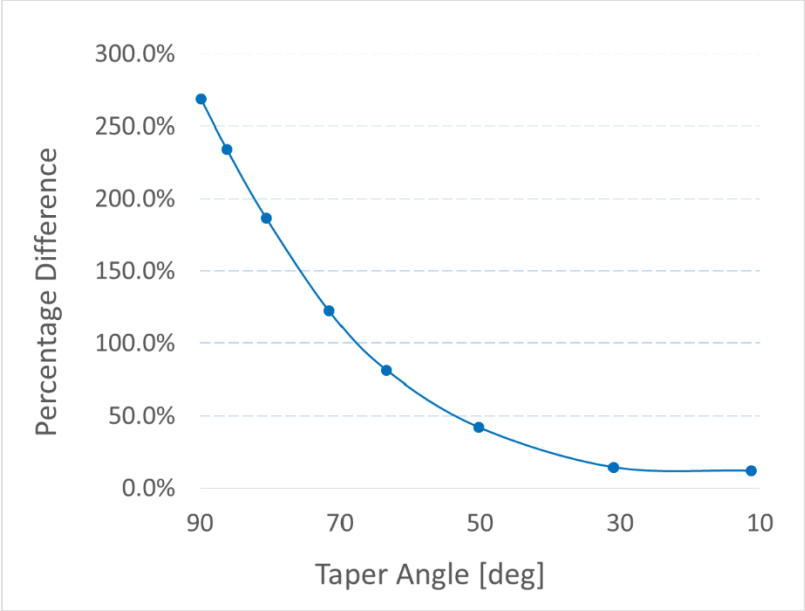

Figure 52. Percentage difference of natural frequencies for the first bending mode between axisymmetric FE and beam FE models for a free-free step-like thin-walled shaft. Reprinted from Ref. [69].

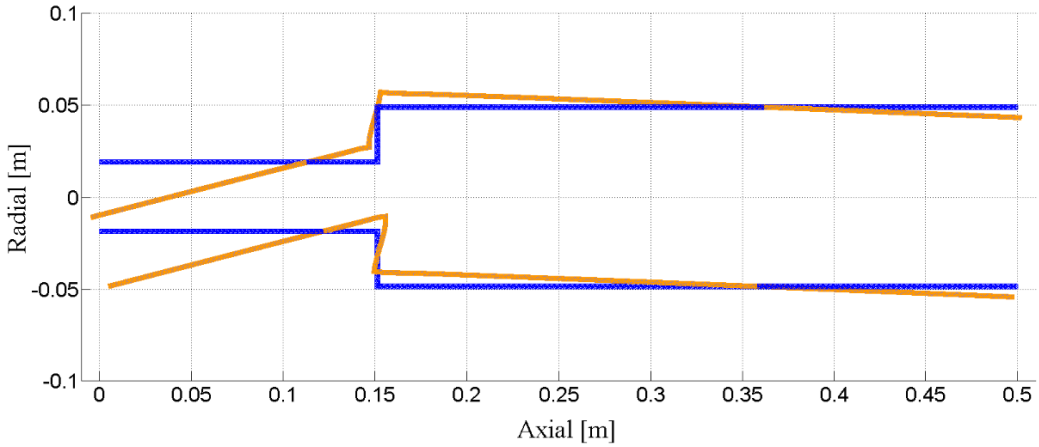

Figure 53. Non-beam-like deformations of the solid element's longitudinal section of the step shaft in the first bending mode. Reprinted from Ref. [69].

5.3.3 Thin-walled shaft with flexible disks

For a beam FE rotor model, a disk is typically represented by a rigid body with concentrated mass and inertia. However, its flexibility may become important as it gets relatively thin in comparison with the shaft diameter. Furthermore, if the first flexural modes of the disk appear within the operating speed range, the disk should not be treated as a rigid body. A rotor system composed of a thin-walled shaft and a flexible disk is utilized to investigate the influences of a disk flexibility on natural frequencies. The corresponding 2D triangle mesh of the longitudinal section of the rotor is shown in Figure 54 (the bottom semi-section is added just for visualization). The disk diameter is set as four times the outer diameter of the shaft. The stiffness of the two bearings that support the shaft at both ends varies from 0.1 to 5 times the structural stiffness of the shaft, K_S (the same definition as in the Bearing Attachment section). The other non-dimensional constants that characterize the model include L/D_O , t/D_O , and L_d/D_O .

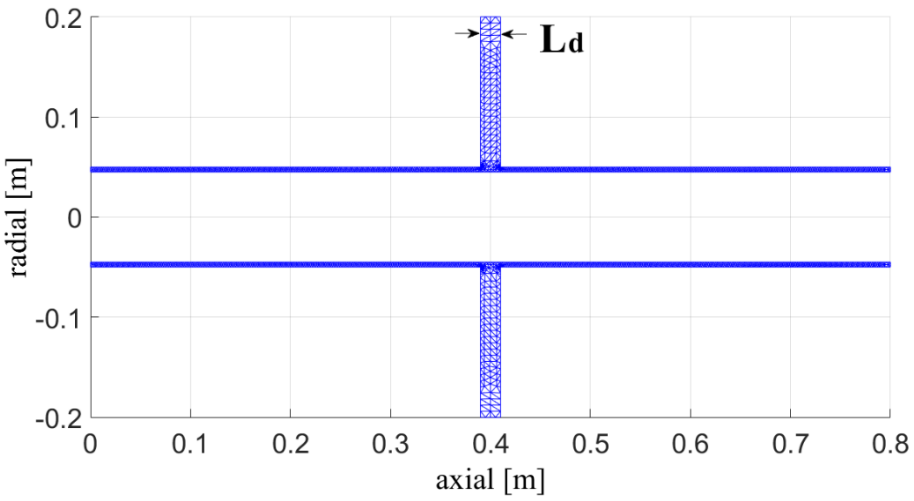

Figure 54. Longitudinal section mesh of a thin-walled shaft with a disk, shown here with $L/D_O = 8$, $t/D_O = 0.05$, $L_d/D_O = 0.2$. Reprinted from Ref. [69].

Simulation results are presented in Figure 55, which show increasing difference between axisymmetric FE and beam FE model natural frequency predictions in the rocking mode as either the bearings get stiffer (i.e. K_B/K_S increases) or the shaft wall gets thinner (i.e. t/D_O shown in the left figures of Figure 55 are smaller than in the right figures). This results from the greater amount of shaft deformation occurring as the bearings become stiffer and the wall thickness becomes smaller, which also effects the amount of shaft out of plane cross-sectional warping.

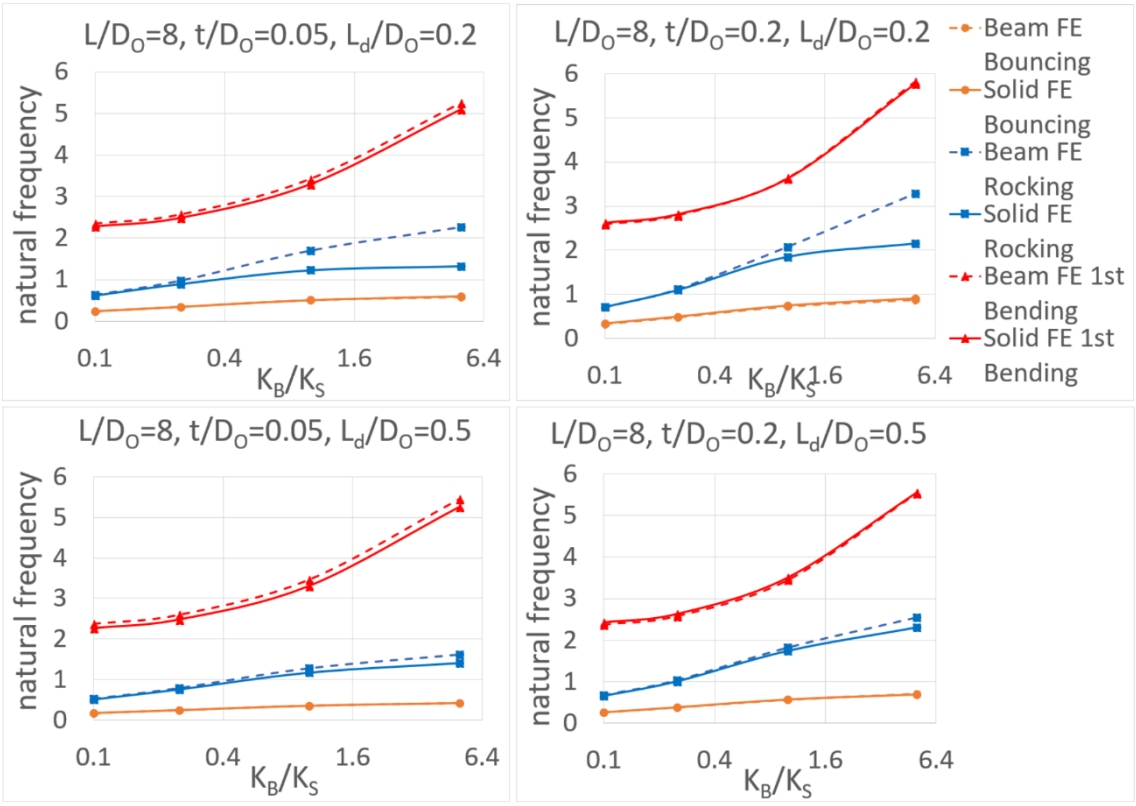

Figure 55. Dimensionless natural frequencies of a thin-walled shaft with a disk supported by two bearings with four different rotor configurations. Reprinted from Ref. [69].

For illustration, consider comparing the natural frequency differences between the axisymmetric FE and beam FE model predictions at $K_B/K_S = 5$ (i.e. stiff bearing). The percentage difference decreases only by 4.9% in the rocking mode when just the shaft wall thickness ratio t/D_O is increased from 0.05 to 0.2, and the disk is relatively thick with $L_d/D_O = 0.5$. In contrast, the percentage difference rises significantly by 55.8% with a decrease in the disk thickness L_d/D_O from 0.5 to 0.2. This indicates that in the rocking mode disk thickness changes contributes more to the natural frequency difference than shaft wall thickness. The thicker disk has only a slight effect on the

difference in the bouncing and first bending modes. This results from the cross-sections near the mid-span deforming heavily in the rocking mode while only slightly in the other two modes, which can be seen from Figure 56. Additionally, an axisymmetric FE model can predict the first disk diametral mode while a beam FE model cannot.

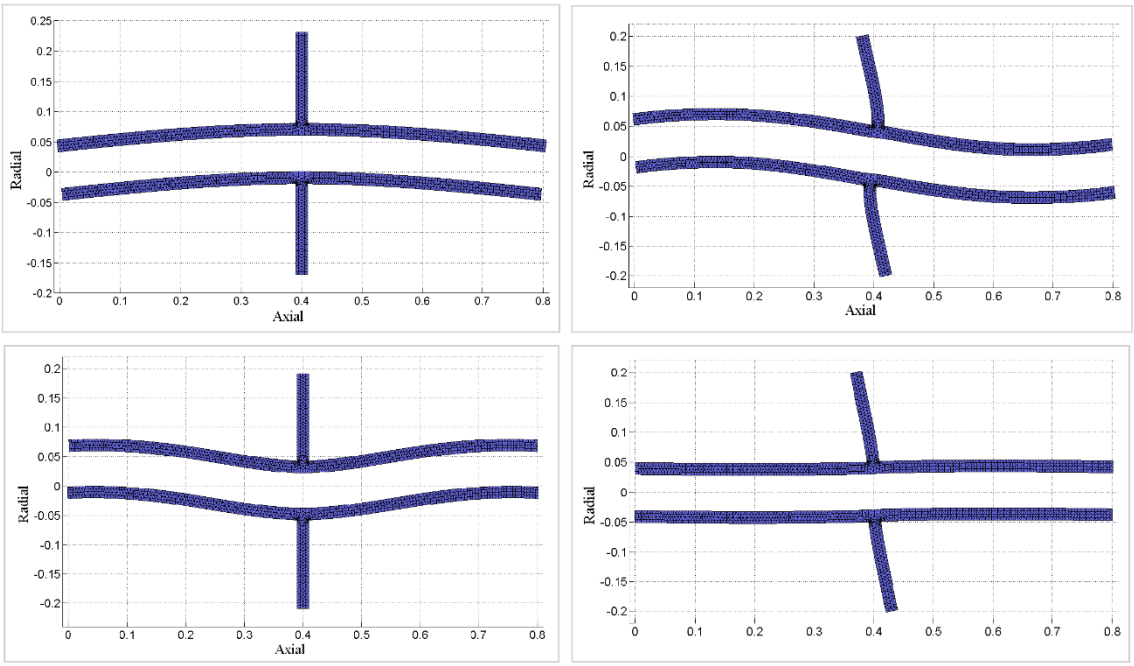

Figure 56. Lowest four modes of a hollow shaft with a disk supported by two stiff bearings: $L/D_O = 8$, $t/D_O = 0.2$, $L_d/D_O = 0.2$, shaft bouncing mode (top left), shaft rocking mode (top right), the first shaft bending mode (bottom left), the first disk diametral mode (bottom right). Reprinted from Ref. [69].

The next example considers a rotor with two flexible disks and a thin walled shaft. As shown in Figure 57, the shaft length is set as $L/D_O = 15$, and the disk diameter is four times the outer diameter of the shaft. Two disks are installed at $1/4$ and $3/4$ length along the shaft. The variables considered are shaft wall thickness, disk thickness,

and bearing stiffness. The three lowest mode shapes and their labels are provided in Figure 58.

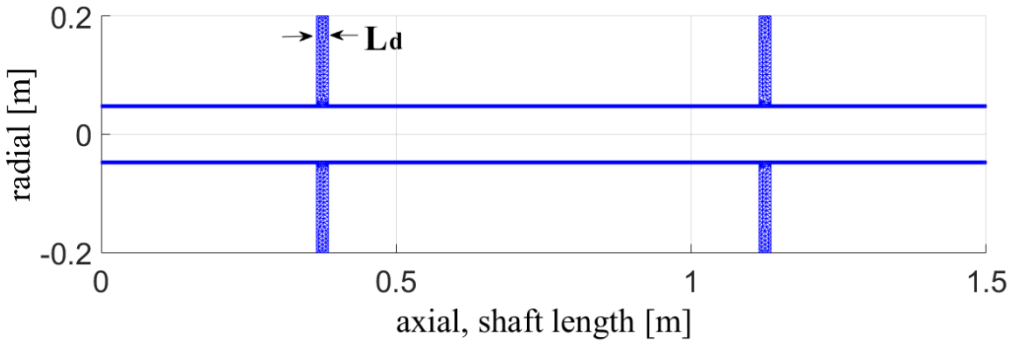

Figure 57. Longitudinal section mesh of a thin-walled shaft with two disks: $L/D_O = 15$, $t/D_O = 0.05$, $L_d/D_O = 0.2$. Reprinted from Ref. [69].

Figure 59 shows that for both bouncing and rocking modes, the predictions by the axisymmetric FE model are close to those by the beam FE model. This result can be explained the same way as in the straight thin-walled shaft case, i.e. the long shaft design with $L/D_O = 15$ helps reduce the difference. Non-beam deformations increase in the first bending mode as the bearings get stiffer (i.e. K_B/K_S increases). For this reason, the difference between the axisymmetric FE and beam FE models rises even with a long shaft and will get larger when the thickness of the shaft wall decreases (i.e. t/D_O shown in the upper left figure of Figure 59 are smaller than in the upper right figure) or the thickness of the disk decreases (i.e. L_d/D_O shown in the upper left figure of Figure 59 are smaller than in the lower left figure). However, it can be seen from the other figures of Figure 59 that the difference is not apparent when either the shaft or the disk is thick (i.e. when $t/D_O = 0.2$ or $L_d/D_O = 0.5$).

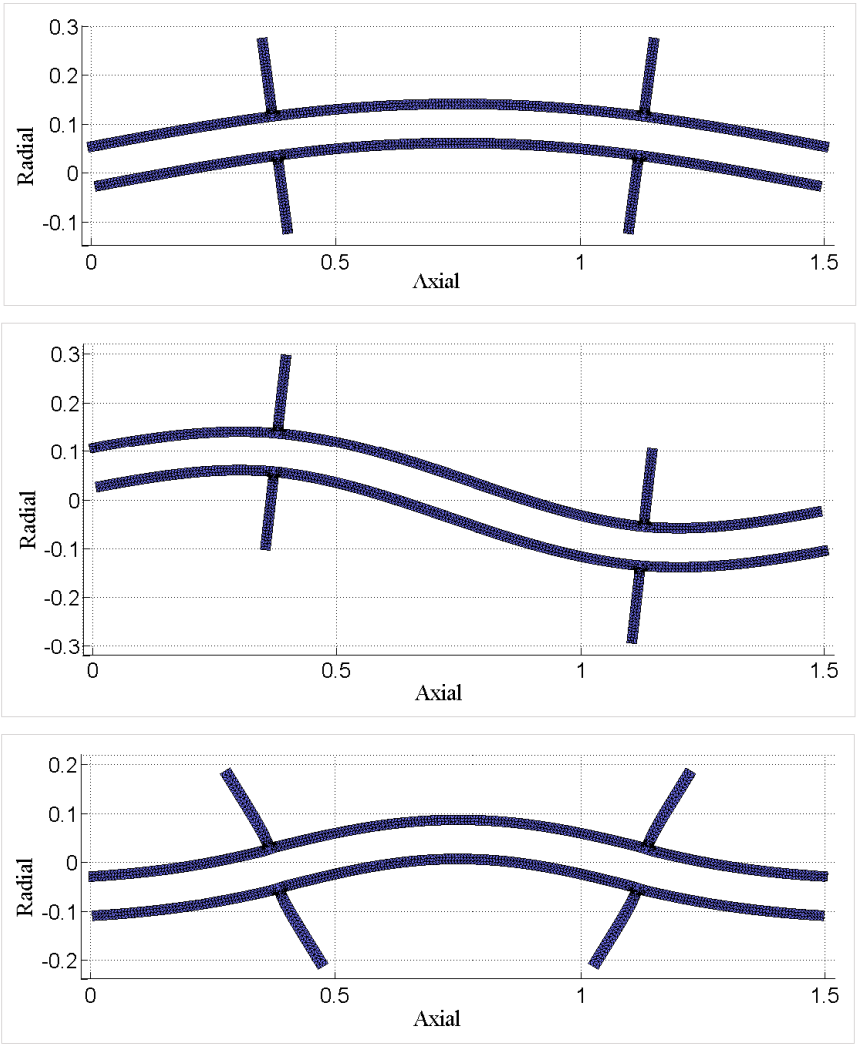

Figure 58. Lowest three modes of a thin-walled shaft with two disks, supported by two stiff bearings: $L/D_O = 15$, $t/D_O = 0.2$, $L_d/D_O = 0.2$; shaft bouncing mode (top), shaft rocking mode (middle), the first shaft bending mode (bottom). Reprinted from Ref. [69].

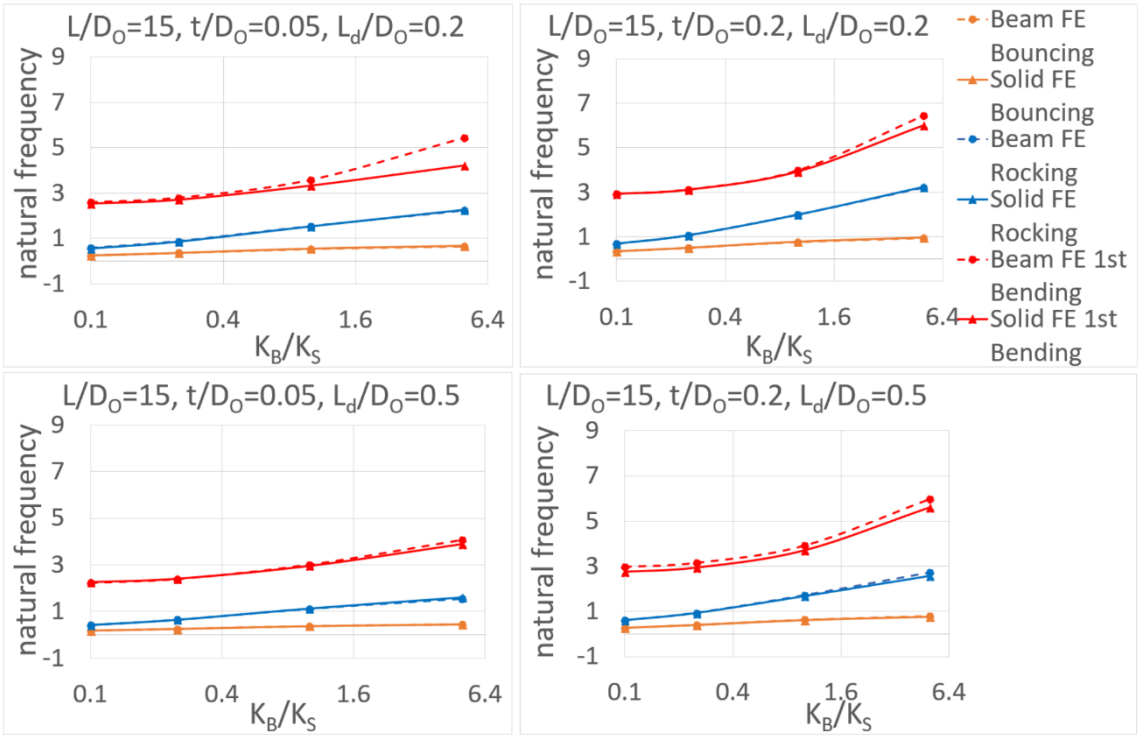

Figure 59. Dimensionless natural frequencies of a thin-walled shaft with two disks supported by two bearings with four different rotor configurations. Reprinted from Ref. [69].

5.4. Summary

An axisymmetric solid harmonic element approach with improved modeling capabilities for flexible rotor systems has been presented along with illustrative numerical examples and parametric studies. Improvements include the centrifugal stress-stiffening and spin-softening effects. More accurate simulations of thin-walled shaft and flexible disk rotor dynamic response can be attained by using the improved axisymmetric elements.

The implementation of the centrifugal stress-stiffening and spin-softening matrices enables an accurate prediction of the change of resonant frequencies and critical speeds caused by the rotation of the rotor.

Bearing forces are distributed to a number of nodes within the range of the longitudinal bearing length rather than a single surface node of the journal to prevent fictitious, excessive local distortions of the thin-walled journal.

Only the zeroth, first and second order harmonics are included in the axisymmetric FE model. The Guyan reduction method is employed to condense the matrices and significantly reduce computational time.

Both thin-walled shafts and flexible disks are prone to non-beam deformations. Natural frequency predictions using beam FE differs more from axisymmetric FE predictions when the shaft length gets shorter and wall gets thinner. Investigation of various thin-walled stepped shafts with straight and conical segments shows that the difference between the axisymmetric FE and beam FE predicted natural frequencies becomes larger with the increase in the taper angle of the conical segment.

Disk flexibility and locations have an impact on the prediction accuracy of the beam FE model compared with the axisymmetric element model. If a thin disk, implying more flexibility, is installed at the mid-span of a thin-walled shaft, then a large prediction difference tends to occur at the rocking or second bending mode due to large deformations of the disk. In contrast, a large difference of predicted natural frequencies between the axisymmetric and beam FE models may appear at the first bending mode if

two flexible disks are symmetrically placed away from the center of the shaft at quarter spans.

The comparison results can be used for guidance on choosing the axisymmetric solid or the beam FE models in the rotor design and rotor dynamic analysis.

6. ANALYSIS OF ROTOR-BEARING SYSTEM UNDERGOING SUPPORT MOTION

The chapter will study the influences of the support motion on the rotor stability. The beam element rotor model and hydrodynamic fluid film bearing model, which are presented in Chapter 2, will be applied in the investigation.

6.1. Validation of Finite Element Hydrodynamic Journal Bearing Model

Fixed-pad (or fixed-profile) bearings are commonly used in the rotating machinery. In comparison with tilting-pad bearings, fixed pad bearings are less expensive but have strong cross-coupling effects. The cross-coupling effects may cause severe instability of the rotor system. Therefore, the present investigations are focused on the rotor systems with fixed-pad bearings, in particular the four-axial groove and four-lobe journal bearings. The investigation results can be easily extended and applied to other fixed-pad bearings.

The bearing 2D FE model presented in Chapter 2 will be validated in this section before being used for the investigation of the impact of support motion on the rotor performance.

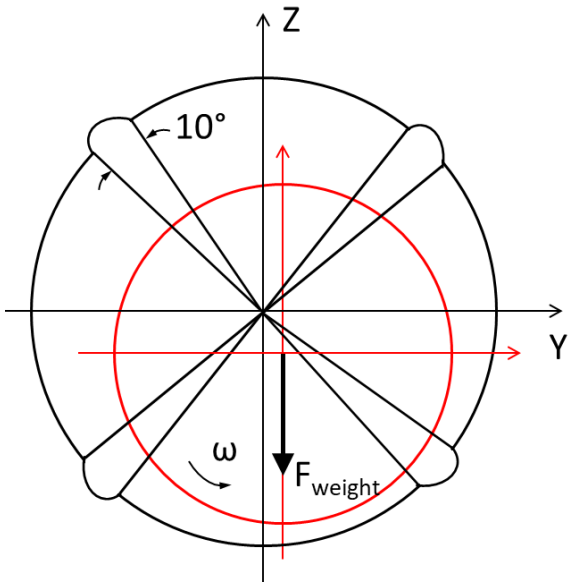

Figure 60. Four-lobe journal bearing.

As shown in Figure 60, the four-lobe journal bearing has four equally distributed grooves. The groove angle does not have to be 10° and can be adjustable. The dimensions and properties of the four-lobe bearing are given as follows.

Preload factor: $M_p = 0.5$

Radius of the bearing: $0.04\,m$

Length of the bearing: $0.04\,m$

Radial clearance of the bearing: $7\times10^{-5}\,m$ $(2.76\,mil)$

Lubricant viscosity: $0.02\,Pa\cdot s$

Lubricant density: $850\,kg/m^3$

The coefficients of the stiffness and damping are calculated by using a specialized bearing software (the relevant numerical algorithm has been implemented in

our in-house rotordynamics software). The bearing code is developed based on the 2D FE hydrodynamic bearing model presented in Section 2.5. The results are illustrated in Table 5.

Table 5. Coefficients of stiffness and damping of the four-lobe journal bearing with preload=0.5 predicted based on the bearing FE model presented in this work.

Sommer-feld Number	Eccen-tricity Ratio	Attitude Angle (deg)	Kyy	Kyz	Kzy	Kzz	Cyy	Cyz	Czy	Czz
1.17	0.203	-32.0	6.03	8.56	-9.18	6.32	17.96	-1.07	-0.98	18.72
0.719	0.304	-33.7	4.73	5.68	-6.70	5.39	12.17	-1.42	-1.37	13.57
0.478	0.404	-35.7	4.16	4.15	-5.68	5.38	9.17	-1.64	-1.63	11.41
0.323	0.505	-38.1	3.84	3.08	-5.25	5.84	7.12	-1.81	-1.82	10.46
0.215	0.603	-40.7	3.54	2.19	-5.07	6.63	5.49	-1.95	-1.95	10.04
0.137	0.702	-43.8	3.17	1.46	-5.08	7.97	4.17	-1.99	-2.00	10.03

Table 6. Coefficients of stiffness and damping of the four-lobe journal bearing with preload=0.5 in Someya table [88].

Somm-erfeld Number	Eccen-tricity Ratio	Attitud-e Angle (deg)	Kyy	Kyz	Kzy	Kzz	Cyy	Cyz	Czy	Czz
1.17	0.2	-31.6	6.03	8.65	-9.24	6.16	18.4	-1.14	-1.10	19.1
0.719	0.3	-33.4	4.63	5.82	-6.57	5.33	12.5	-1.30	-1.28	13.5
0.478	0.4	-35.5	4.08	4.01	-5.73	5.26	8.91	-1.64	-1.62	11.8

Table 6. Continued.

Somm-erfeld Number	Eccen-tricity Ratio	Attitud-e Angle (deg)	Kyy	Kyz	Kzy	Kzz	Cyy	Cyz	Czy	Czz
0.323	0.5	-37.8	3.74	3.21	-5.12	5.68	7.43	-1.82	-1.80	10.4
0.215	0.6	-40.6	3.41	2.18	-4.87	6.50	5.48	-1.85	-1.83	9.78
0.137	0.7	-43.6	3.00	1.26	-4.83	7.81	3.78	-1.78	-1.76	9.65

The coefficients of the same bearing can be looked up in the Someta table [88] and illustrated in Table 6. It can be seen that the results predicted by the hydrodynamic bearing FE model in this work match the data in Someya table.

6.2. Validation of Rotor System Model

A rotor system is built up by assembling the beam FE rotor model and the 2D FE hydrodynamic bearing model presented in Chapter 2.

Consider the rotor system shown in Figure 61 for the purpose of validation. A disk with an imbalance mass is mounted at the middle of a slender shaft. The whole rotor (shaft and disk) is supported by two hydrodynamic (here four-axial groove) journal bearings which are fixed to the ground (no support motion).

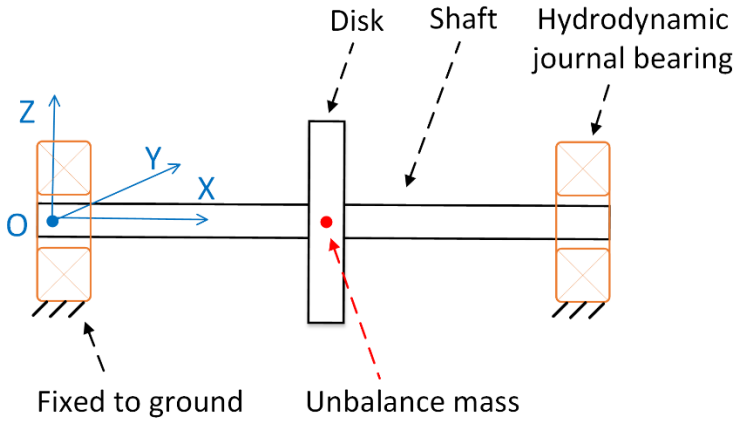

Figure 61. Rotor on two hydrodynamic journal bearings without support motion.

The dimensions and material properties of the rotor are given below.

Radius of the shaft: $0.04\ m$

Length of the shaft: $1.6\ m$

Radius of the disk: $0.15\ m$

Thickness (axial length) of the disk: $0.03\ m$

Density of the shaft and disk: $7800\ kg/m^3$

Elastic modulus of the shaft: $2\times10^{11}\ N/m^2$

Poisson's ratio: 0.3

Spin speed: $4000\ rpm$

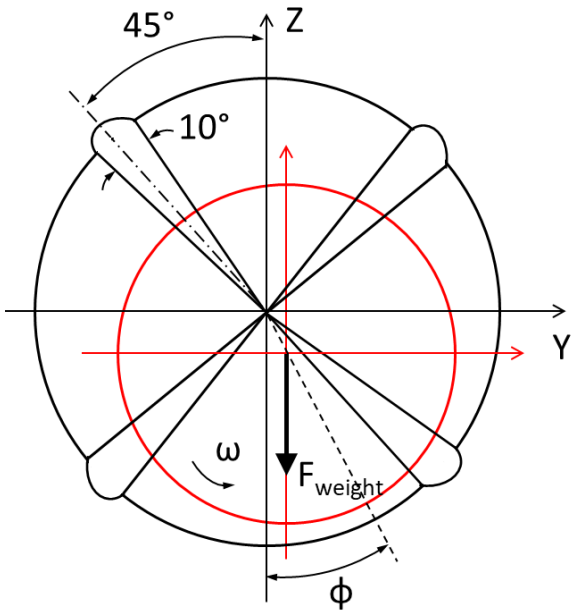

Figure 62. Four-axial groove journal bearing.

The dimensions and properties of the four-axial groove bearing dipicted in Figure 62 are given below.

Pad preload: $M_p = 0$

Pad offset: $\alpha_p = 0.5$

Length of the bearing: $0.04\,m$

Radial clearance of the bearing: $7\times10^{-5}\,m$ $(2.76\,mil)$

Lubricant viscosity: $0.02\,Pa\cdot s$

Lubricant density: $850\,kg/m^3$

The proposed rotor and hydrodynamic bearing FE models proposed in this work will be validated by comparison with the commercial rotor dynamics software XLTRC^2. XLTRC^2 is based on a beam element rotor model and linear coefficient bearing model.

The coefficients of the bearing are obtained from the in-house experimental dataset of the Turbomachinery lab of Texas A&M University.

The predicted amplitudes and orbits of the left journal based on the proposed rotor-bearing model are shown in Figure 63 and Figure 64. The amplitudes and orbits predicted by XLTRC^2 are shown in Figure 65. The displacements of the left journal are in good agreement.

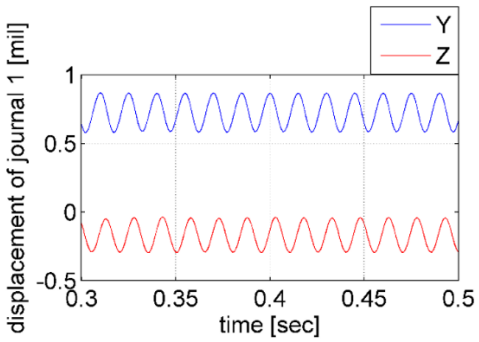

Figure 63. Displacements of the left journal predicted by the proposed rotor-bearing FE model at the rotor spin speed of 4000 *rpm*.

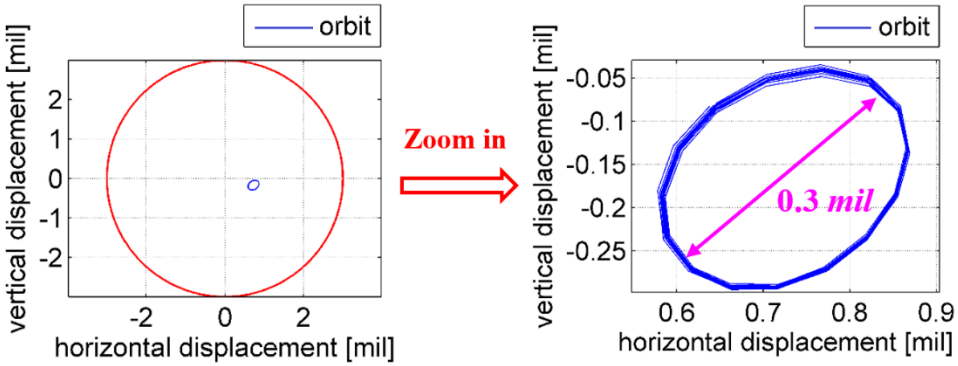

Figure 64. Orbits of the left journal (red circle is bearing clearance) predicted by the proposed rotor-bearing FE model at the rotor spin speed of 4000 *rpm*.

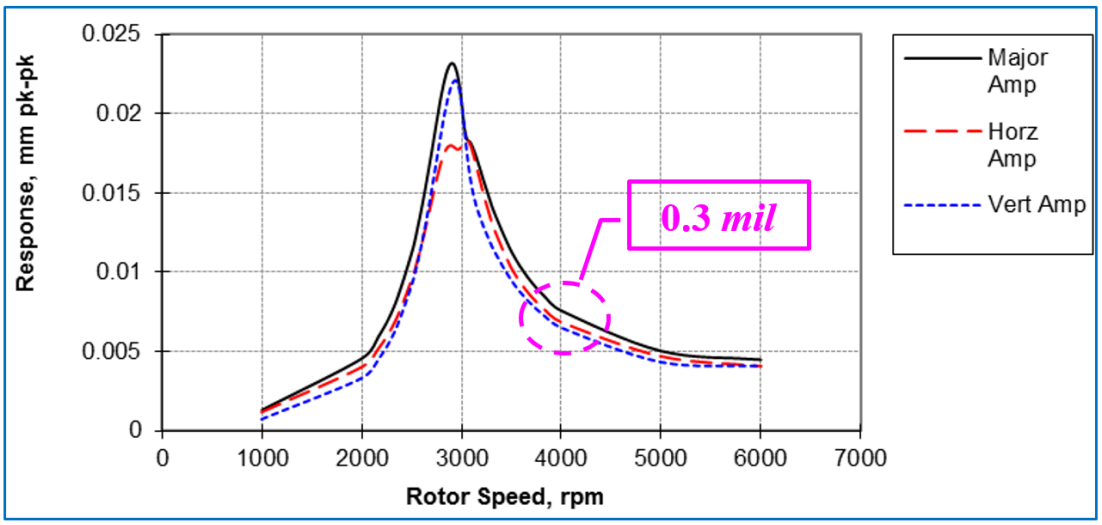

Figure 65. Response of the left journal predicted by XLTRC^2.

The predicted amplitudes and orbits of the right journal based on the proposed rotor-bearing model are shown in Figure 66 and Figure 67. The amplitudes and orbits predicted by XLTRC^2 are shown in Figure 68. The displacements of the right journal are in good agreement.

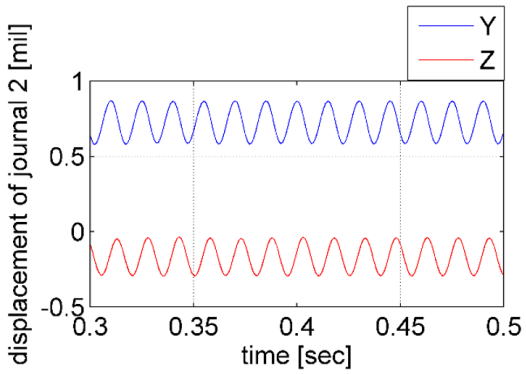

Figure 66. Displacements of the right journal predicted by the proposed rotor-bearing FE model at the rotor spin speed of 4000 *rpm*.

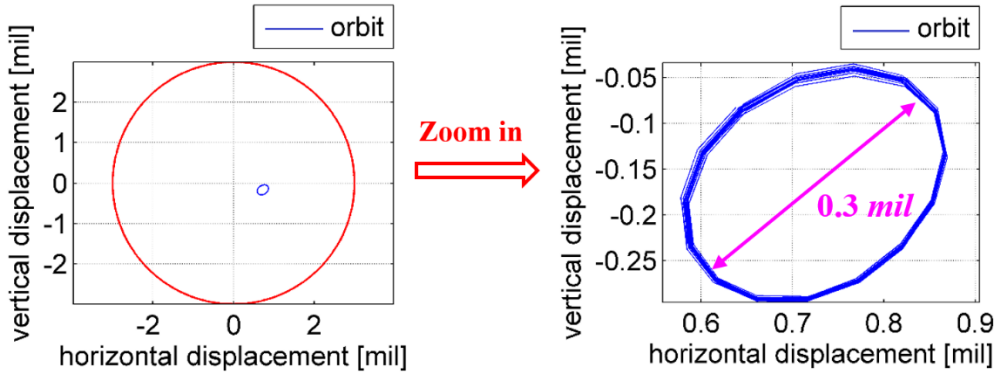

Figure 67. Orbits of the right journal (red circle is bearing clearance) predicted by the proposed rotor-bearing FE model at the rotor spin speed of 4000 *rpm*.

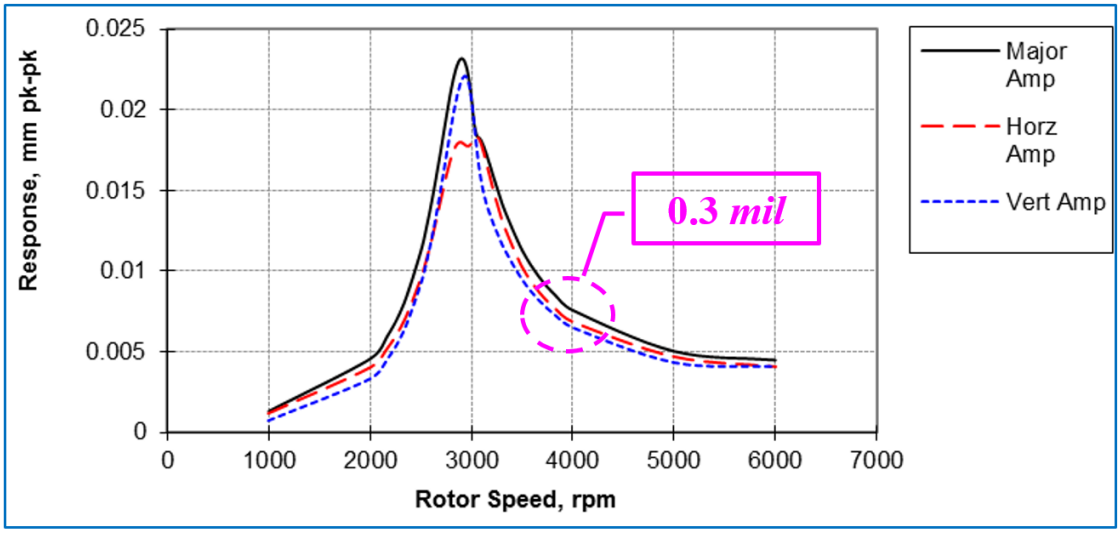

Figure 68. Response of the right journal predicted by XLTRC^2.

The predicted amplitudes and orbits of the disk based on the proposed rotor-bearing model are shown in Figure 69 and Figure 70. The amplitudes and orbits predicted by XLTRC^2 are shown in Figure 71. The displacements of the disk are in good agreement.

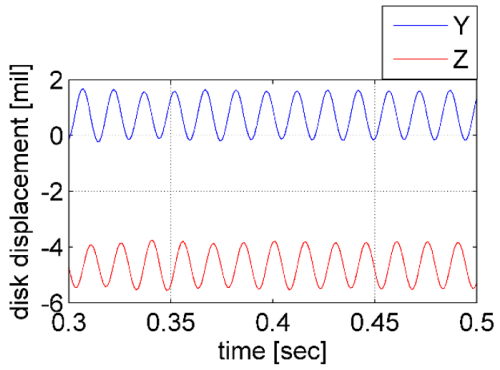

Figure 69. Displacements of the disk predicted by the proposed rotor-bearing FE model at the rotor spin speed of 4000 rpm.

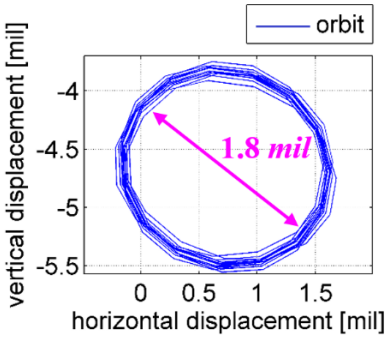

Figure 70. Orbits of the disk predicted by the proposed rotor-bearing FE model at the rotor spin speed of 4000 rpm.

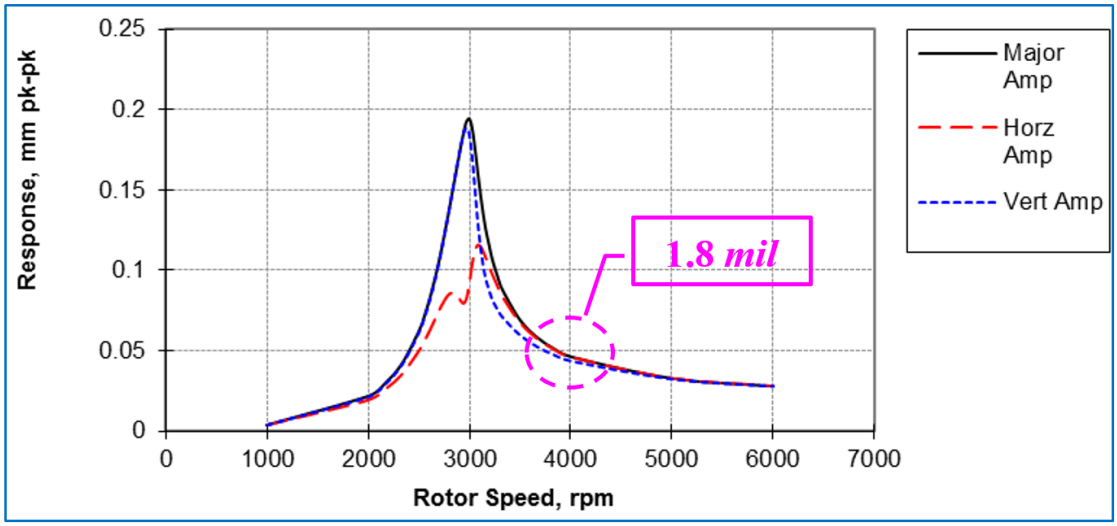

Figure 71. Response of the disk predicted by XLTRC^2.

It can be concluded from the validation presented in this section that the proposed beam element rotor model and hydrodynamic journal bearing 2D FE model are sufficiently accurate for investigation of the rotor behaviors under support motion.

6.3. Discretization of Rotor

The rotor consists of a flexible shaft and a rigid disk. The flexible shaft is discretized into 10 beam elements (utilizing the Timoshenko beam element model presented in Section 2.8), as is shown in Figure 72. A rigid disk that has the same dimensions as that shown in Figure 61 in Section 6.2 is mounted at the middle of the shaft. The rotor is supported by two identical four-axial journal bearings. The parameters of the bearing are provided in Section 6.2.

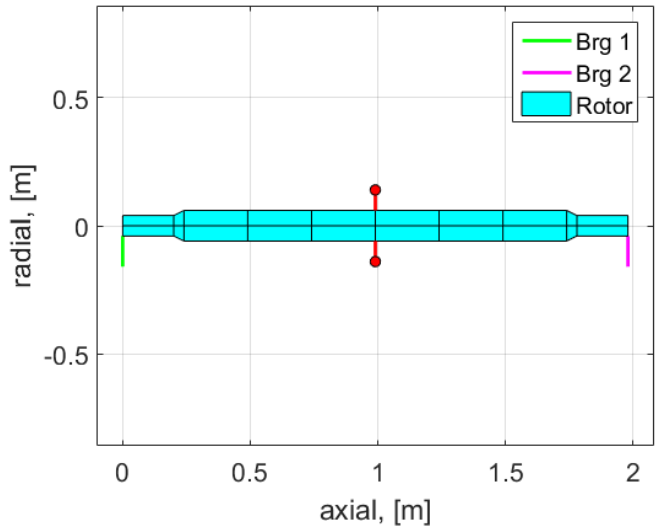

Figure 72. Cross-section of the beam FE rotor model (red circle represents rigid disk, and green and purple lines represent bearing attachment).

6.4. Influences of Support Pitch on Rotor Stability

The rotor-bearing system model presented in Chapter 2 is able to simulate six motion types: heave, sway, surge, roll, pitch, and yaw. This work is focused on investigation of the support pitch which is commonly seen in an on-board rotor system.

Consider a vessel (rigid support) that pitches about its body center, as is shown in Figure 73. Two identical four-axial groove journal bearings move with the support structure as they are rigidly connected to the support. The rotor and bearing parameters are the same as provided in Figure 61 in Section 6.2. The onset speed of instability of the rotor system is $5400\ rpm$. When the bearing load (equal to rotor weight here) is smaller, the onset speed of instability may be lower than than $5400\ rpm$. The rotor spin speed in this case is $5100\ rpm$, which is lower than the onset speed of instability of the

rotor-bearing system without support motion. In other words, the rotor is stable without support motion.

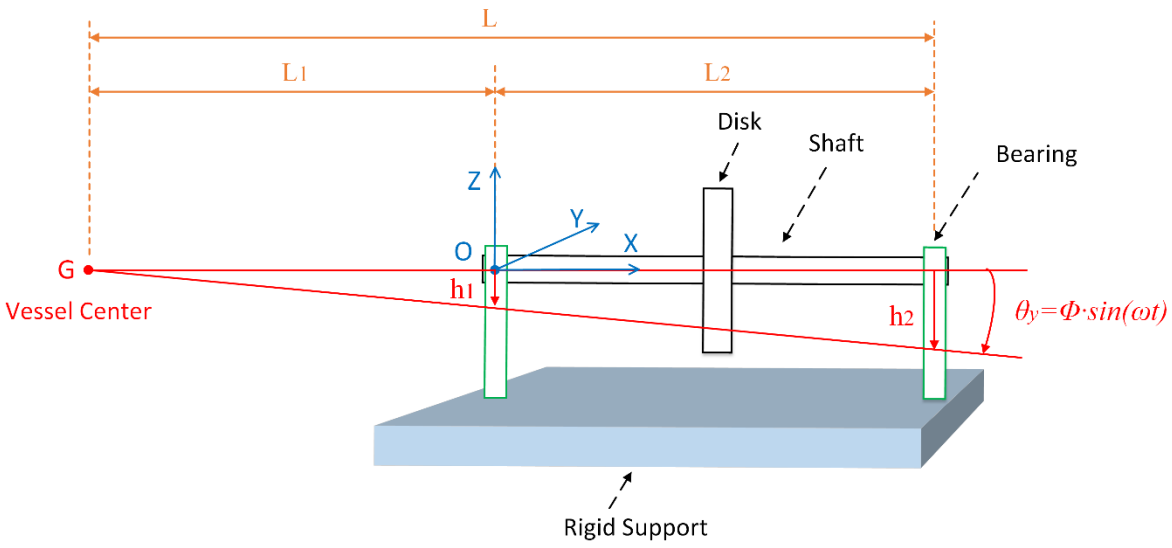

Figure 73. Rotor on two four-axial grooves journal bearings undergoing vessel pitch (θ_y represents the pitch angle about Y axis, L is equal to half the vessel length, L_1 is the distance of the center of gravity of the vessel from the left end of the rotor, and L_2 is the axial span of the two bearings).

The vessel pitch motion imposed on the rotor system is defined by,

$$\theta_y = \phi \cdot sin(\omega t) \tag{139}$$

where θ_y represents the support pitch angle. ϕ denotes the amplitude of the pitch motion and is set as $\phi = 10^\circ$ $(\simeq 0.175\ rad)$. ω represents the frequency of the pitch motion and is set as $\omega = 0.1\ Hz$, and t is time. $0.1\ Hz$ is a reasonable pitch frequency for small crafts. It is stated in [89] that the significant wave height can reach 2 m for 60% of the time in hostile seas. Wave heights may exceed 30 m. The mean wave period is normally

from 15 to 20 sec in severe weather situations and unlikely shorter than 4 sec. The peak acceleration defined here is also reasonable according to the practice reported in [89].

By assuming that the vessel body is rigid, the pitch angle θ_y is imposed on the foundation. As a result, the foundation not only pitches but heaves as well. The displacements of the left and right journals in the vertical direction are expressed as h_1 and h_2, respectively, which are shown in Figure 73.

First, consider the left journal under the support heave, which can be described as,

$$h_1 = -L_1 \cdot sin(\phi \cdot sin(\omega t)) \tag{140}$$

$$v_1 = -L_1 \cdot \phi \cdot \omega \cdot cos(\phi \cdot sin(\omega t)) \cdot cos(\omega t) \tag{141}$$

$$a_1 = L_1 \cdot \phi \cdot \omega^2 \cdot [\phi \cdot sin(\phi \cdot sin(\omega t)) \cdot cos^2(\omega t) + cos(\phi \cdot sin(\omega t)) \cdot sin(\omega t)] \tag{142}$$

where v_1 and a_1 represent the velocity and acceleration of the left bearing housing in the vertical direction, respectively.

Given that the vessel is 30 m in length, then $L = 15\ m$. As shown in Figure 73, point G, which represents the center of gravity of a vessel, is $13.02\ m$ away from the left bearing (i.e. $L_1 = 13.02\ m$). The axial span of the two bearings, which is also equal to the length of the shaft, is set as $L_2 = 1.98\ m$. As a result, the pitch motion of the support can be described by the curves shown in Figure 74 and Figure 75. It can be observed from Figure 75 that the decrease in vertical acceleration due to gravity may reach 40% , implying a 40% decrease in the rotor weight.

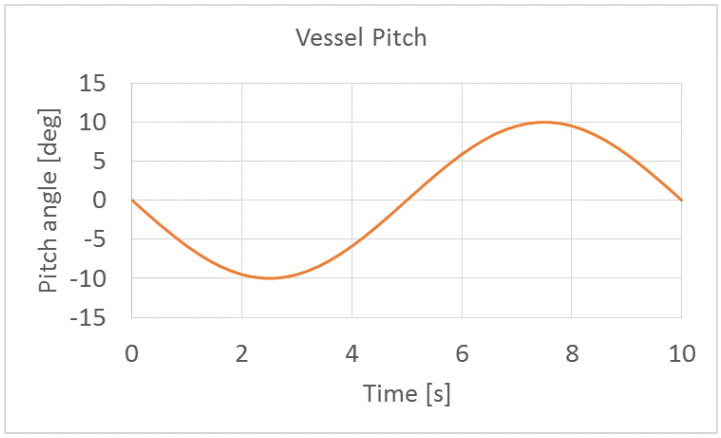

Figure 74. Pitch angle of the support with offset half bearings.

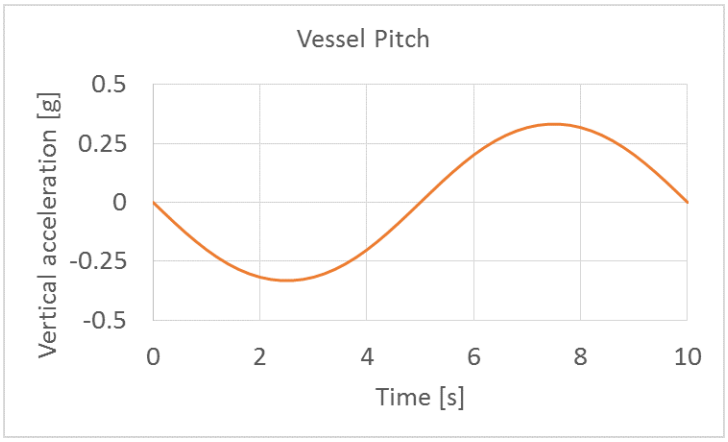

Figure 75. Vertical accelerations of the support (accelerations are expressed with the gravity of Earth g).

Simulation results of the vessel pitch are shown in Figure 76 and Figure 77. It can be seen that the rotor becomes unstable under support pitch. The root cause for the rotor instability is explained as follows. The pitching support imposes a tremendous acceleration on the rotor via bearing forces, leading to a decrease in the rotor gravity in the vertical direction. As can be seen from Figure 75, the vertical acceleration almost decreases by $0.4g$ at the valley point. The phenomenon is analogous to the so-called

weight loss effect. As the rotor weight on the bearing decreases, the threshold speed of instability goes down, causing the rotor instability.

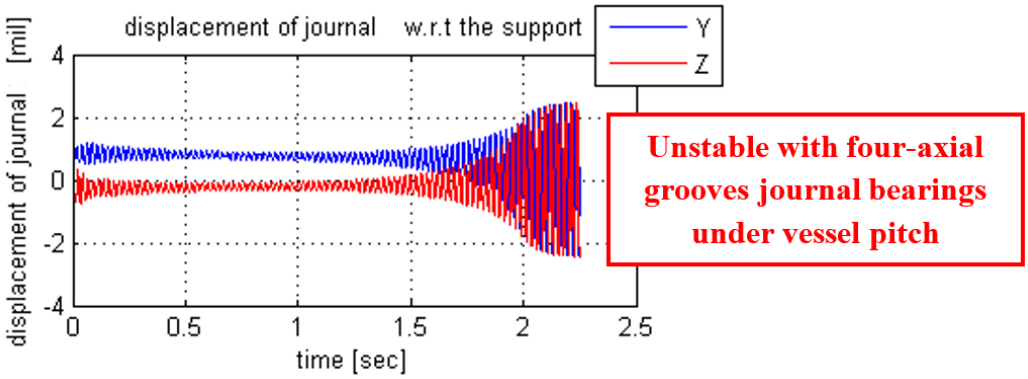

Figure 76. Displacements of the right journal with respect to the support under vessel pitch (supported by two four-axial groove bearings) at the rotor spin speed of 5100 rpm.

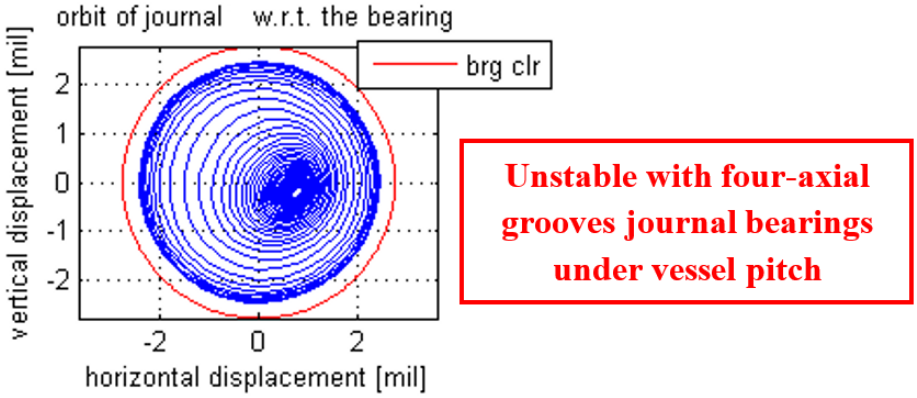

Figure 77. Orbits of the right journal with respect to the bearing under vessel pitch (supported by two four-axial groove bearings) at the rotor spin speed of 5100 rpm.

6.5. Remedy for Rotor Instability

This section aims at proving that an offset half bearing is a good replacement or remedy for a four-axial groove bearing.

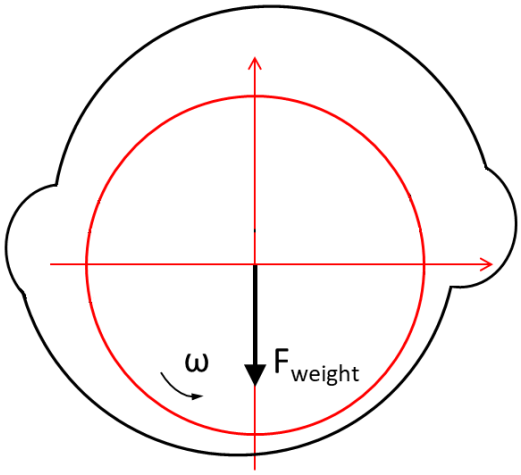

Figure 78. Offset half journal bearing.

Consider the same rotor and vessel shown in the last section for comparison. The dimensions and properties of a offset half journal bearing (Figure 78) is given below.

Ratio of bearing length to bearing diameter: 0.5

Pad preload: $M_p = 0.5$ for the offset half bearing

Pad offset: $\alpha_p = 1$ for the offset half bearing

Length of the bearing: 0.04 m

Radial clearance of the bearing: $7 \times 10^{-5} m$ $(2.76 mil)$

Lubricant viscosity: 0.02 $(Pa \cdot s)$

Lubricant density: 850 (kg/m^3)

To investigate the influences of the bearing offset on rotor stability, the four-axial groove bearing is compared with the offset half bearing. The same vessel pitch motion as shown in Figure 74 and Figure 75 is used in the comparison.

Figure 76 and Figure 77 show that the rotor on two four-axial groove bearings is unstable at the spin speed of 5100 rpm. But it can be seen from Figure 79 and Figure 80. that the rotor on two offset half bearings is stable.

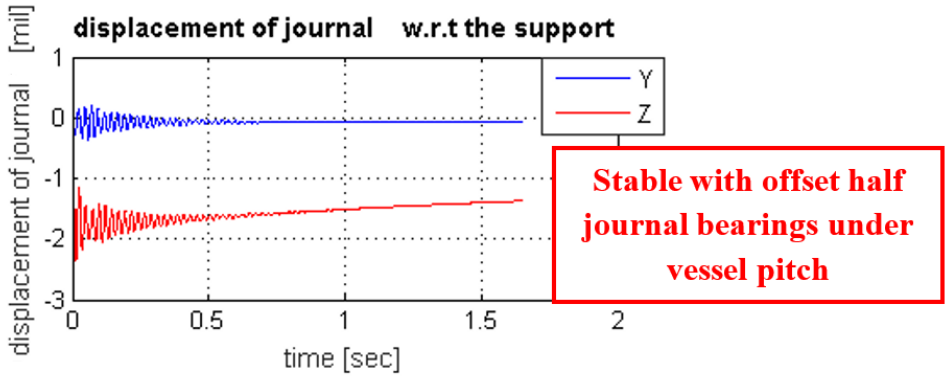

Figure 79. Displacements of the right journal with respect to the support under vessel pitch (supported by two offset half bearings) at the rotor spin speed of 5100 rpm.

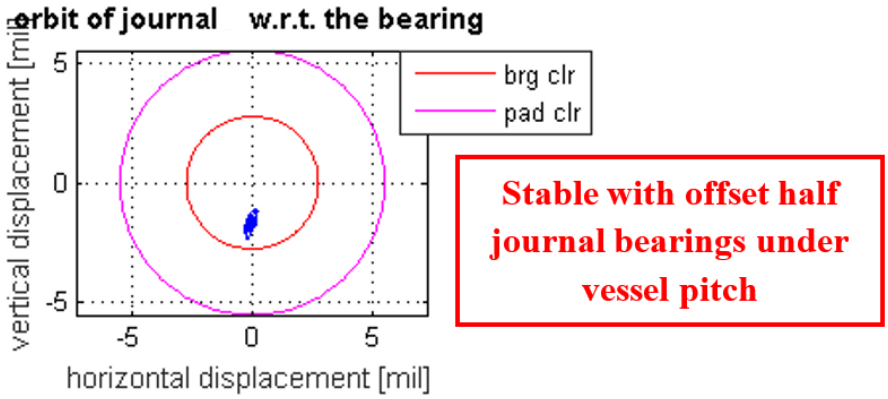

Figure 80. Orbits of the left journal with respect to the bearing under vessel pitch (supported by two offset half bearings) at the rotor spin speed of 5100 rpm.

It can be explained as the weight-loss effects that are induced by support motion. The preload and pad offset of the offset half bearing actually generate a rotor

eccentricity before being loaded. It could be argued that in brief, the higher rotor eccentricity compensates the weight loss effects (or bearing unloading in the rotor dynamics). In other words, the weight loss can be compensated by introducing pad preload and pad offset, which the offset half bearing has but the four-axial groove bearing does not.

6.6. Summary

The influences of the support motion on rotor stability are studied. The conclusions based on the nonlinear transient analysis addressed the nonlinear dynamic problems with rotor instability and provide remedies for the rotor instability caused by support motions.

Support pitch may cause rotor instability at the spin speed lower than the onset speed of instability. The root cause for this phenomenon is the weight-loss effects, also called unloaded bearing effects in the rotor dynamics perspective.

Finally, using offset half bearing is proposed as a remedy for the rotor instability caused by support pitch. The reason is that pad preload and pad offset of the offset half bearing can increase the journal eccentricity and compensate the weight loss of the rotor under support motion.

7. DEVELOPMENT OF IMPACT AND TORSIONAL DAMPERS FOR SUPPRESSION OF DRILLSTRING VIBRATIONS

The modeling approach for the drillstring rotor, impact damper and torsional damper have been clarified in Chapter 3. In this chapter, those components will be assembled to be a whole drillstring model for vibration analysis.

7.1. Drillstring Model

The conceptual design of the drillstring that is composed of a DP, a DC, a DB, and the impactors and torsional damper is demonstrated in Figure 20. The ROB and DA are the working conditions that are commonly seen in a drilling process. It is therefore necessary to ensure the effectiveness of the impactors and torsional damper in these conditions. The parameters of the drillstring system are illustrated in Table 7, and boundary conditions are specified for each working condition.

As the drillstring is fully suspended in the ROB condition and partially suspended in the DA condition, the weight of the impactors and torsional damper will increase the bending stiffness of the drillstring, thereby shifting the critical speeds. To exclude the influence of shifting critical speeds on the vibration amplitude, the weight of the impactors and torsional damper is always accounted for in the comparison of vibrations at the critical speed even if there are no dampers in the drillstring.

Table 7. Parameters of the drillstring. Reprinted from Ref. [1].

Component	Parameter	Value	Unit
DP	Length	80	m
	OD	100	mm
	ID	75	mm
	Number of beam FEs	40	-
	Density	8000	kg/m^3
	Mass	2199	kg
	Modulus of elasticity	2.1×10^{11}	N/m^2
	Poisson's ratio	0.3	-
	Transverse mud damping per axial length	50	$N \cdot s/m^2$
	Torsional mud damping per axial length	$0 - 2$	$N \cdot m \cdot s/rad$
DC	Length	15	m
	OD	150	mm
	ID	75	mm
	Number of beam FEs	10	-
	Density	8000	kg/m^3
	Mass	1590	kg
	Eccentricity	$1 - 8$	mm
	Modulus of elasticity	2.1×10^{11}	N/m^2

Table 7. Continued.

Component	Parameter	Value	Unit
DC	Poisson's ratio	0.3	-
	Transverse mud damping per axial length	300	$N \cdot s/m^2$
	Torsional mud damping per axial length	$0-6$	$N \cdot m \cdot s/rad$
Impact damper	Density	8000	kg/m^3
	Number	9	-
	Total mass	$143-286$	kg
	Modulus of elasticity	2.1×10^{11}	N/m^2
	Poisson's ratio	0.3	-
	Clearance between the impactor and DC	$10-30$	mm
	Sliding friction coefficient between the impactor and DC	0.4	-
Torsional Damper	Length	$2.5-6$	m
	Density	8000	kg/m^3
	Mass	$226-542$	kg
	Moment of inertia	$0.4-0.8$	$kg \cdot m^2$
	Number	1	-
	Sliding friction coefficient between the torsional damper and inner base of the DC	$0.002-0.35$	-

Table 7. Continued.

Component	Parameter	Value	Unit
Torsional Damper	Torsional damping	$0.25 - 8$	$N \cdot m \cdot s/rad$

The DC is usually $27 - 36m$ in length and is slender in terms of the ratio of length to diameter. Two or more stabilizers are installed on the DC, and the segment between two stabilizers (called DC span) is about $15m$ long. The DC may consist of several DC spans, and the total length of the DC is dependent on the BHA design. According to Refs. [59, 60], the lateral position of the stabilizer is assumed constrained to zero, and the first bending mode is most commonly seen within the rotating speed range of the drillstring. Therefore, it is acceptable for a conceptual design to use a DC span with two stabilizers located at both ends (see pinned points A and B shown in Figure 20) to investigate the lateral dynamics of the DC in impacting.

The length of the DP varies with the depth of the well and may even reach a few kilometers. In contrast, the diameter of the DP is normally less than $0.2m$, which makes the DP act more like a string than the DC. A pendulum drillstring model, in which case the top of the DP is pinned (the pinned node has zero displacement but is free to rotate), has been employed in [52, 58] to study lateral and torsional vibrations. As stated in [58], the DC is essential for the analysis of lateral whirl. This is understable because the DP is much slenderer (longer with a smaller diameter) than the DC and two ends of the DC span may experience a dramatic geomery change (the stabilizers which has a much

larger diameter than the DP are normally mounted at the ends of the DC). As a result, the bending mode shapes of the DP hardly affect that of the DC if the DP is very long. That being said, DP length may not have a significant impact on the DC lateral vibrations if the DP is enough long.

In this work, the length of the DP is set eighty meters. To verify that the DP is enough long, a forty meters long DP is constructed with the same drillstring beam elements (such as impactor dimension, density, etc.) and drilling conditions as those for the eighty meters long DP. Figure 81 shows the bending mode shape of the DC at the spin speed of $89rpm$. Nodes O, A and B represent the top of the DP, the top end of the DC and the drill bit (or bottom end of the DC), respectively. The drill bit displacements and velocities obtained from the drillstring model with an eighty meters long DP and a forty meters long DP are shown in Figure 82 and Figure 83, respectively. It can be seen by comparing Figure 82 with Figure 83 that the drill bit lateral whirl motions are similar for the two different DP lengths, indicating that the eighty meters long DP is enough long and will not have great influences on the investigation of lateral vibrations of the drill bit. It is understandable that the longer DP does not affect much drill bit motions since the DP is much slender and thereby much more flexible than the DC in terms of bending.

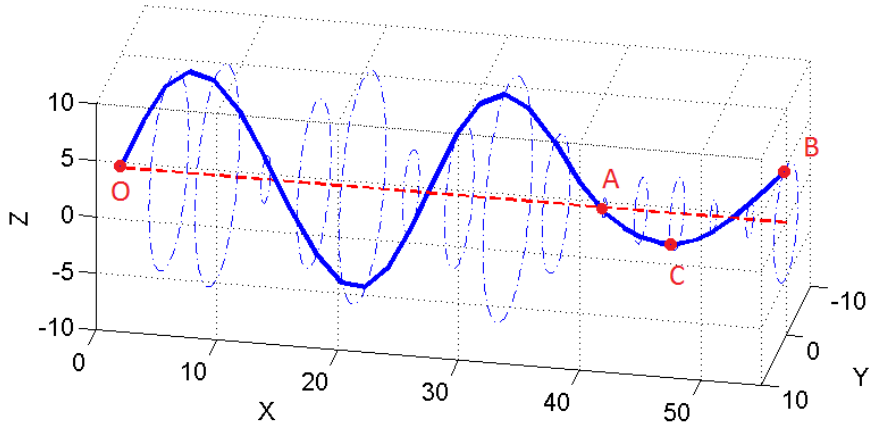

Figure 81. Mode shape of the drillstring with a forty meters long DP at the bending critical speed of $\boldsymbol{\Omega = 89\ rpm}$.

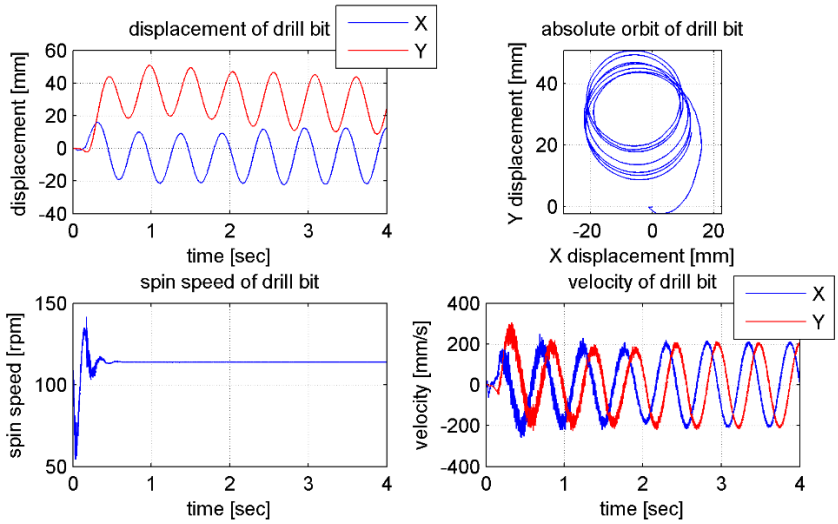

Figure 82. Displacement and velocity of the DC at point B with an eighty meters long DP in the ROB condition at the critical speed of $\boldsymbol{\Omega = 89\ rpm}$.

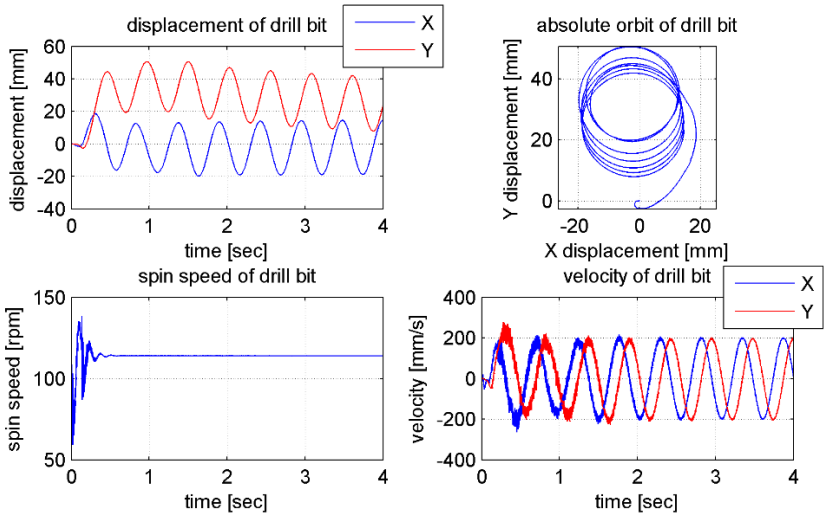

Figure 83. Displacement and velocity of the DC at point B with a forty meters long DP in the ROB condition at the critical speed of $\boldsymbol{\Omega = 89\ rpm}$.

7.2. Drilling Conditions

In general, there are two major drilling conditions, namely rotating-off-bottom (ROB) and drilling-ahead (DA). The former indicates that the DB of the drillstring is not contacting the rocks at the bottom of the well, and thus is rotating without drilling torque on the DB. The latter denotes the drilling status in which the DB is pressing and cutting the rocks at the bottom of the well.

7.2.1. Rotating-off-bottom (ROB)

The drillstring while rotating off bottom can be modeled by setting both pinned points A and B in Figure 20 free, analogous to a pendulum with the top end O pinned. The boundary conditions may be written as $x_O = y_O = z_O = 0$ and $\omega_O = const.$, where the subscript O denotes the top end of the DP near the hoist/rotary table, and the spin speed of the top drive ω_O is constant. It is assumed that the DC mass is eccentric, and no

drilling torque acts on the DB. The drillstring carries the tensile axial load resulting from the weight of the DP, DC, impactors and torsional damper.

7.2.2. Drilling-ahead (DA)

With regard to the DA condition, both ends (A and B) of the DC shown in Figure 20 are pinned, and the drilling torque acting on the DB is included. Hence, the boundary conditions may be written as $x_O = y_O = z_O = 0$, $\omega_O = const.$, and $y_A = z_A = y_B = z_B = 0$. In the axial direction, the hoist pulls the DP, and the bottom of the borehole supports the DC weight. That is to say, the DP is in tension, and the DC is under compressive load. The unbalanced forces caused by the eccentric DC mass are loaded in the middle of the DC.

7.3. Simulation for ROB

The drillstring operating in the ROB condition has been simulated, and the results are demonstrated in Figure 84 through Figure 91. As Figure 84 shows, the largest lateral deflections of the DC in the whirl mode at the bending critical speed of $\Omega = 119rpm$ are located at two bending peaks, i.e. point C ($4.5m$ away from point A) and point B (the bottom of the DC).

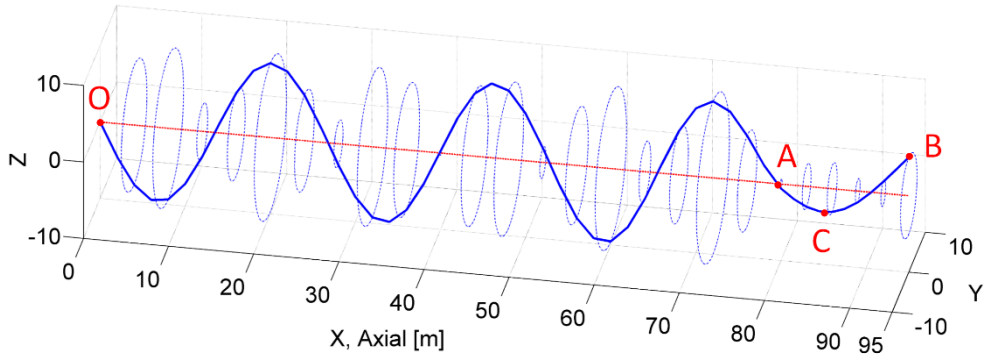

Figure 84. Mode shape of the drillstring at the bending critical speed of $\Omega = 119\ rpm$. Reprinted from Ref. [1].

The impactors are installed in the DC in such a way that the mass of nine impactors are equally distributed ($31.8kg$ per element, $286kg$ in total) with a clearance of $d = 10mm$ between the impactor and DC. As a result, the vibration amplitudes of points B and C at $\Omega = 119rpm$ are reduced from $22mm$ and $12mm$ to $14mm$ and $8mm$, respectively, which can be seen from Figure 85 and Figure 86. This suppression effects on the vibration amplitudes are attributed to the impacting between the DC and impactors that may dissipate the kinetic energy of the drillstring. If we reduce the mass of the impactors from $286kg$ (18% of the mass of the DC) to $143kg$ (9% of the mass of the DC), in which case the mode shape of the drillstring is the same as that shown in Figure 84, the vibration amplitudes at B and C increase from $14mm$ and $8mm$ to $16mm$ and $9mm$, respectively, which is displayed in Figure 85 to Figure 87. This increase can be understood by looking into either the impacting model with the COR or the one with a Hertzian contact force and a nonlinear viscous damping force.

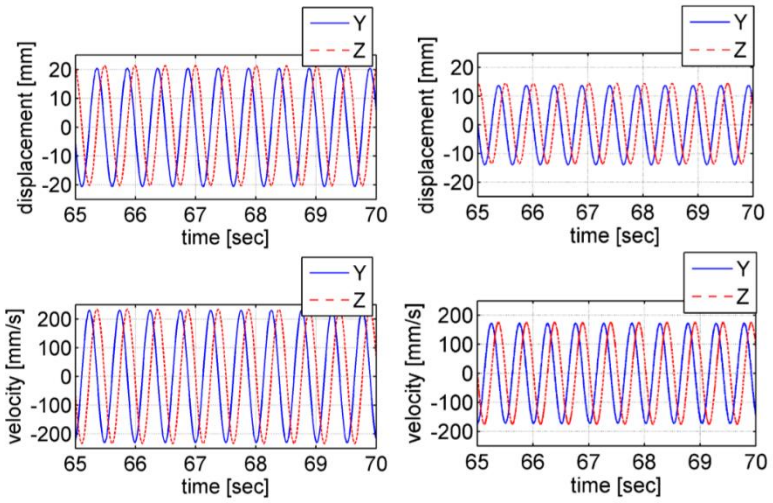

Figure 85. Displacement and velocity of the DC at point B without (left) or with (right) impactors with $d = 10\ mm$ and the total impactor mass of $286\ kg$ in the ROB condition at the critical speed of $\Omega = 119\ rpm$. Reprinted from Ref. [1].

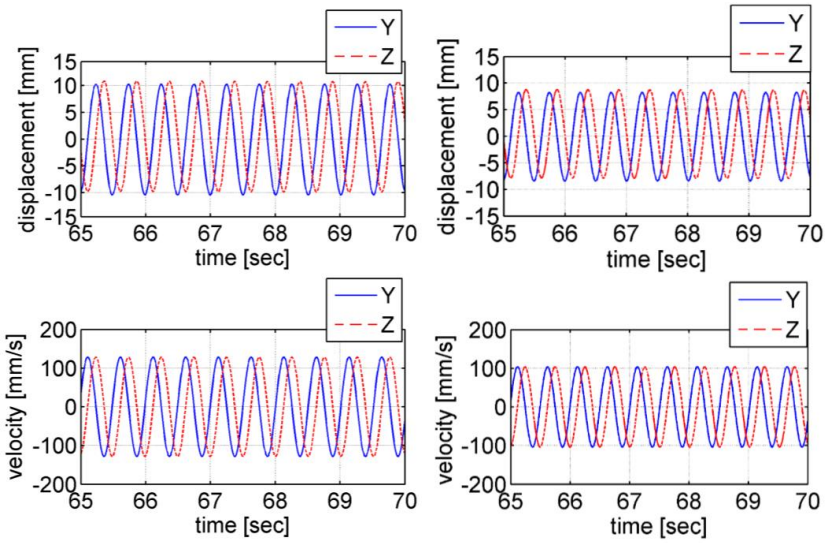

Figure 86. Displacement and velocity of the DC at point C without (left) or with (right) impactors with $d = 10\ mm$ and the total impactor mass of $286\ kg$ in the ROB condition at the critical speed of $\Omega = 119\ rpm$. Reprinted from Ref. [1].

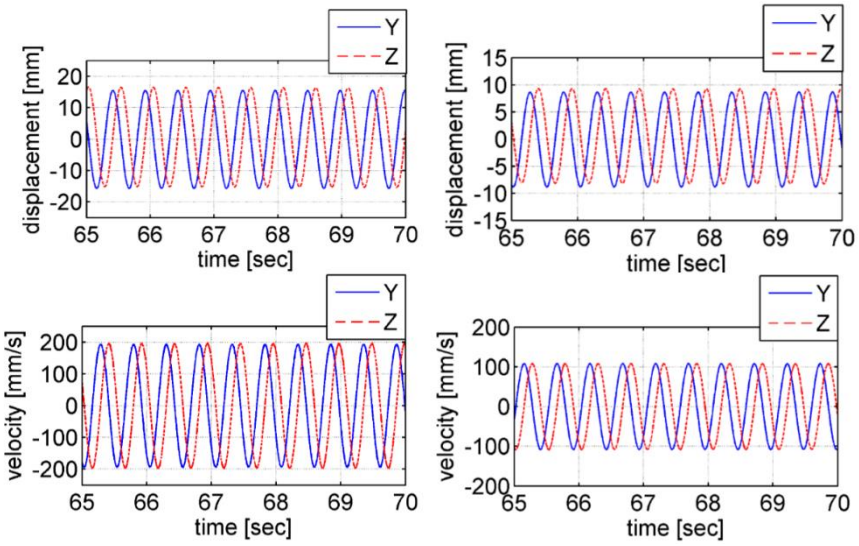

Figure 87. Displacement and velocity of the DC at point B (left) and point C (right) with $d = 10\ mm$ and the total impactor mass of $143\ kg$ under impacting in the ROB condition at the critical speed of $\Omega = 117\ rpm$. Reprinted from Ref. [1].

As far as the impacting model with the COR is concerned, the velocity of the DC after inelastic collision can be described by,

$$\dot{x}_D^+ = \frac{1}{1+\eta}[\eta(1+e_{COR})\dot{x}_I^- + (1-\eta e_{COR})\dot{x}_D^-] \tag{143}$$

where $\dot{x}_D$ represents the velocity of the DC, $\dot{x}_I$ the velocity of the impactor, η the mass ratio of the impactor to the DC, and the superscripts $+$ and $-$ denote the velocity after and before collision, respectively. If we assume that e_{COR} is constant (if η does not change too much) and $\dot{x}_I^- = 0$, it can be derived from Eq. (143) that $\dot{x}_D^+$ drops when η rises, which implies that after collision, the kinetic energy of the DC containing the impactors with larger mass is less than with smaller mass. In other words, more kinetic energy is dissipated by the impactor with larger mass than with smaller mass, indicating that the lateral vibration is attenuated to a larger extent. This conclusion is verified by

the simulation results presented in Figure 85 to Figure 87 that after the mass of the impactors increases, the lateral velocities of point B and point C in impacting decrease from $200mm/s$ and $115mm/s$ to $180mm/s$ and $105mm/s$, respectively.

Regarding the impacting model with a Hertzian contact restoring force and a nonlinear viscous contact damping force, the enhancement of the vibration suppression is attributed to the larger inertia of the impactors, which renders less change of the velocities of the impactors. In other words, the impactor does not follow the motion of the DC under contact forces, implying that the relative velocity between the impactor and the DC may increase (this conclusion does not apply to the impactor with much smaller mass than the DC). According to Eq. (113), an increase in the relative input velocity v_i yields a smaller COR, thereby dissipating more kinetic energy of the DC. As demonstrated in Figure 87, the velocity of the impactor with respect to point C under the total impactor mass of $286kg$ is a little larger than under the total impactor mass of $143kg$. In addition to v_i, the coefficient α usually increases with the mass of the impactor according to the measured data presented in Ref. [63]. Hence, it can be clearly seen that a larger impactor mass renders an increase in both v_i and α, thereby causing the COR to decline and leading to more dissipation of kinetic energy of the DC.

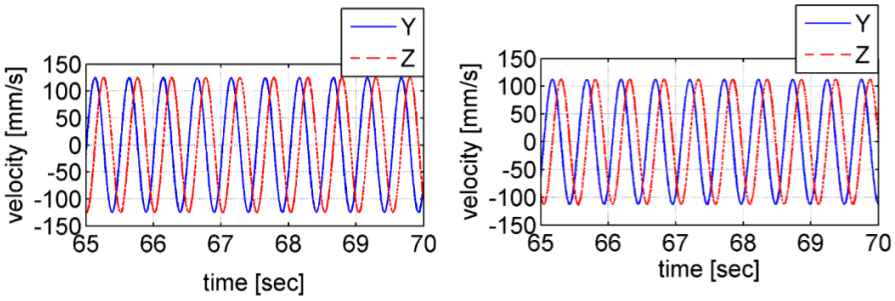

Figure 88. Velocity of the impactor with respect to the DC at point C with $d = 10$ mm and the total impactor mass of 286 kg (left) at the critical speed of $\Omega = 119$ rpm or 143 kg (right) at the critical speed of $\Omega = 117$ rpm under impacting in the ROB condition. Reprinted from Ref. [1].

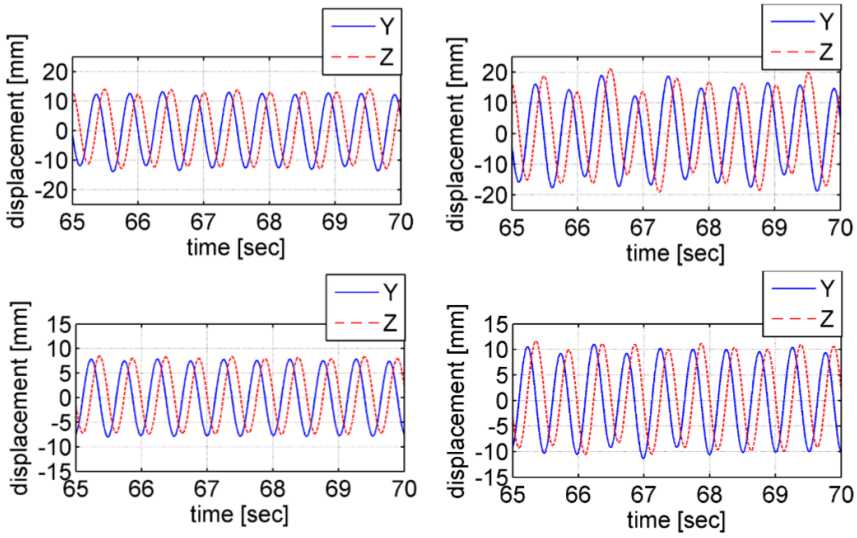

Figure 89. Displacement of the DC at point B (top) and point C (bottom) with $d = 20$ mm (left) or $d = 30$ mm (right) and the total impactor mass of 286 kg under impacting in the ROB condition at the critical speed of $\Omega = 119$ rpm. Reprinted from Ref. [1].

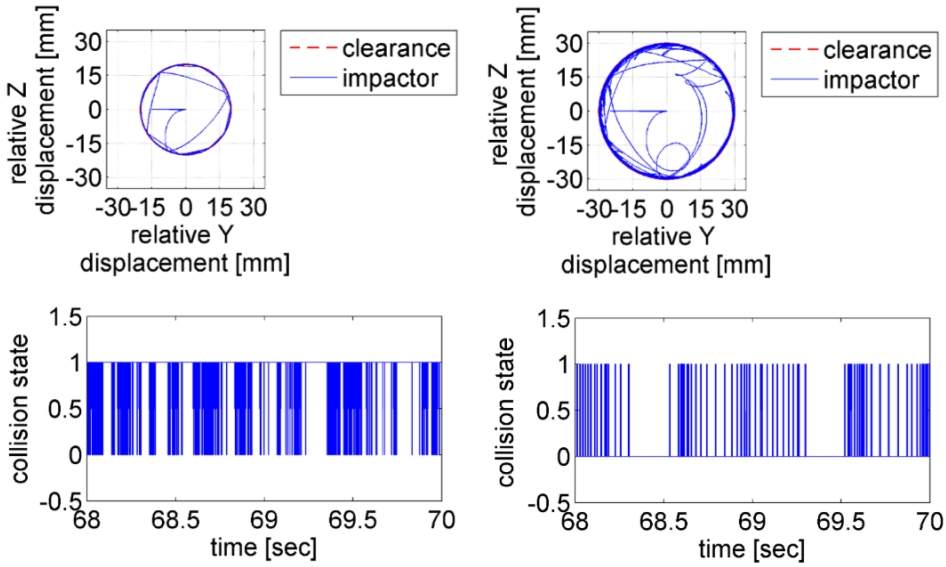

Figure 90. Orbit of the relative displacement of the impactor with respect to the DC (top) and collision state (1 represents collision, 0 no collision) between the impactor and the DC (bottom) at point C with $d = 20\ mm$ (left) or $d = 30\ mm$ (right). Reprinted from Ref. [1].

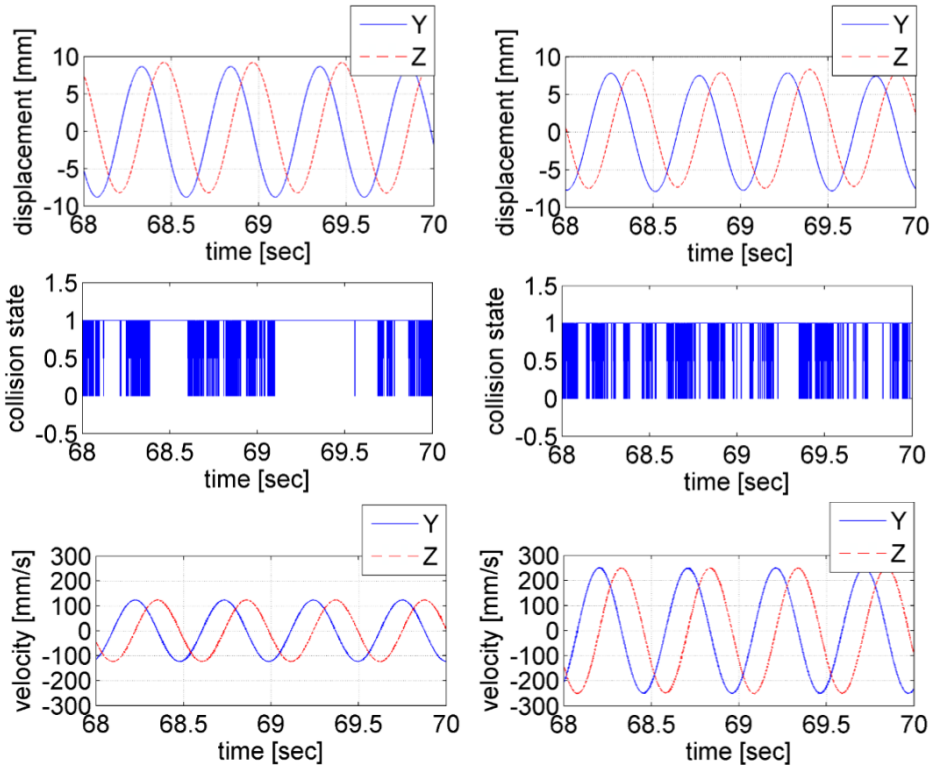

Figure 91. Displacement of the DC (top), collision state (1 represents collision, 0 no collision) between the impactor and DC (middle), and velocity of the impactor with respect to the DC (bottom) at point C with $d = 10\ mm$ (left) or $d = 20\ mm$ (right) and the total impactor mass of $286\ kg$ in the ROB condition at the critical speed of $\Omega = 119\ rpm$. Reprinted from Ref. [1].

Moreover, the clearance between the impactor and DC also has an effect on the suppression of lateral vibrations. As can be seen from Figure 89, the vibration reduction is greater with $d = 20mm$ than with $d = 30mm$. The collision state shown in Figure 90 corresponds to a total impactor mass of $286kg$ in the ROB condition at $\Omega = 119rpm$. This plot indicates that the impactor collides with the DC more frequently with $d = 20mm$ than with$d = 30mm$. Thus, the greater vibration reduction may be plausibly explained by the smaller clearance instigating more frequent impacting, which leads to increased dissipation of kinetic energy.

The energy dissipation mechanism is more complex though since a smaller clearance is likely to cause a decrease in the relative impact velocity as the impact damper may closely follow the DC with a small clearance. This conclusion is verified by analyzing the orbits of the impactor, which is presented as the relative displacements of the impactor with respect to the DC in Figure 90. It can be seen from these orbits that the impactor follows the DC more closely under $d = 20mm$ than under $d = 30mm$. According to Eq. (113), the COR will increase when the input impact velocity drops. Hence, the frequent impacting caused by a small clearance may not necessarily increase the total amount of dissipated kinetic energy. This is illustrated in Figure 91, which shows that the impactor collides with the DC more frequently with $d = 10mm$ than with $d = 20mm$, but the impacting velocity, i.e. the velocity of the impactor with respect to the DC, is smaller under $d = 10mm$ than under $d = 20mm$. Due to this, the vibration amplitudes of the DC at point C with $d = 10mm$ are larger than that with $d = 20mm$.

7.4. Simulation for DA

The drillstring may undergo both lateral whirl and torsional stick-slip vibrations while drilling ahead. As shown in Figure 92, the DC mode that corresponds to the bending critical speed of $\Omega = 91rpm$ is the first bending mode with the largest deflection (point D) appearing in the middle of the DC. The simulation results of the drillstring vibration utilizing the Coulomb torque model with $T_{sld} = 0.8T_{stt}$ are demonstrated in Figure 93. Like in the ROB condition, the weight of the impactors and torsional damper in the DA condition is included regardless of impacting, and the total mass of the impactors is $286kg$ (18% of the mass of the DC). It can be seen from Figure

93 that the largest vibration amplitude approaches $14mm$ without the impactors and torsional damper and drops to $7mm$ in impacting, and the stick-slip vibrations dampened out owing to the torsional damper. For the case presented in Figure 93, nine impactors are installed in an even mass distribution in the DC ($31.8kg$ per element of the DC). The mass and the moment of inertia of the torsional damper are $226kg$ (14% of the mass of the DC) and $0.4kg \cdot m^2$, respectively.

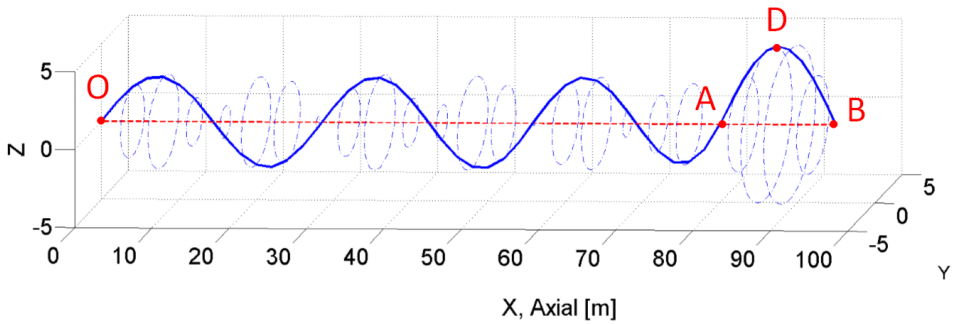

Figure 92. Mode shape of the drillstring at the bending critical speed of $\Omega = 91$ rpm. Reprinted from Ref. [1].

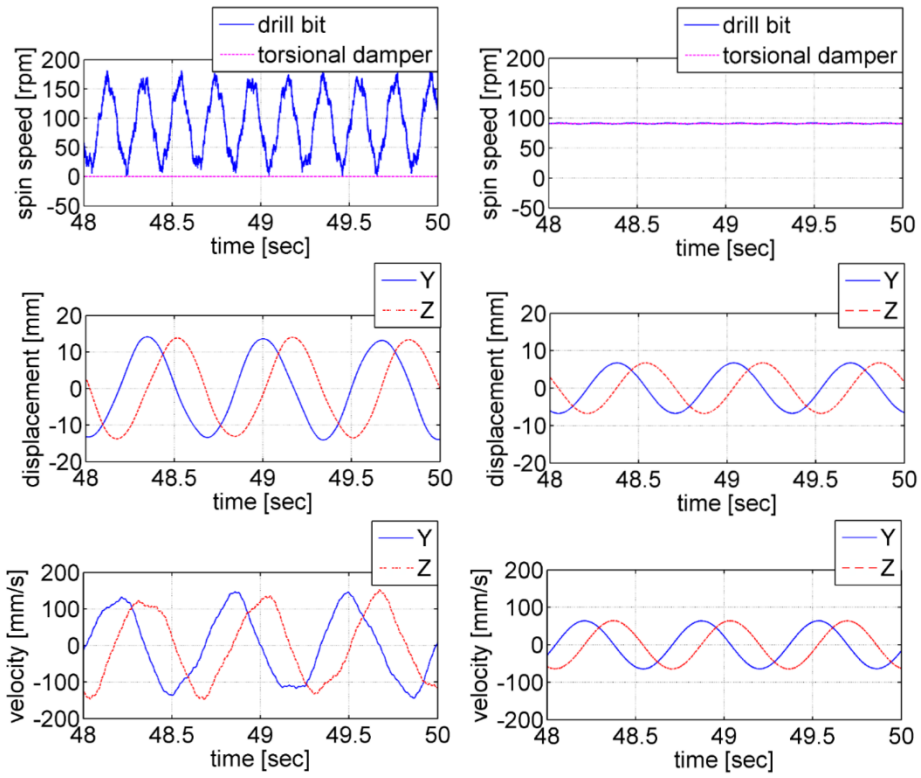

Figure 93. Rotary speed of the DB, lateral displacement and velocity of the DC at point D utilizing the Coulomb torque model without (left) or with (right) the impactors and torsional damper under $d = 10\ mm$ and the even mass distribution of the impactors in the DA condition at the critical speed of $\Omega = 91\ rpm$. Reprinted from Ref. [1].

In addition, the mass distribution of the impactors may have influences on the suppression effects. The mass of the impactors in the DA condition is distributed as (15.9,15.9, 31.8, 47.7, 63.6, 47.7, 31.8, 15.9, and 15.9) kg, which is proportional to the displacement distribution of the DC in the first bending mode (Figure 92), for the nine impactors instead of $31.8kg$ for each impactor. For simplicity, we call it the mode-oriented mass distribution. These two ways of mass distribution are compared in Figure 93 and Figure 94. The simulation results show that a larger mass distributed at point D (the location of the largest displacement in the bending mode) leads to a larger reduction

of the vibration amplitude, which is further reduced from $7mm$ (Figure 93) to $4mm$ (Figure 94). The reason for this larger reduction is partially the same as what has been clarified in the ROB condition, i.e. that the impactor with a larger mass ($63.6kg$) is able to dissipate more kinetic energy of the DC than with a smaller mass ($31.8kg$). The difference lies in that the total mass of the impactors utilizing the mode-oriented distribution remains constant ($286kg$), compared to increasing the mass of the impactors in the ROB case. That is to say, the mode-oriented mass distribution is able to enhance the suppression effects on the lateral vibrations of the DC without changing the total mass of the impactors.

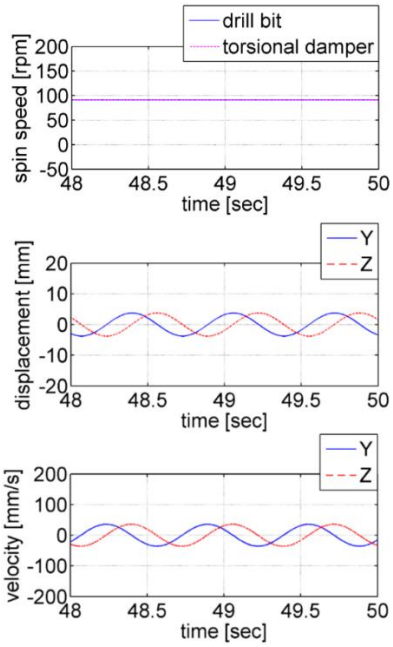

Figure 94. Rotary speed of the DB, lateral displacement and velocity of the DC at point D utilizing the Coulomb torque model with the impactors and torsional damper under $d = 10\ mm$ and the mode-oriented mass distribution of the impactors in the DA condition at the critical speed of $\Omega = 91\ rpm$. Reprinted from Ref. [1].

The stick-slip could appear at a wide range of rotary speeds. As displayed in Figure 93, the peak rotary speed of the DB in the stick-slip vibration may reach twice the rotary speed of the top drive, thereby aggravating the whirl vibration of the DC. Ideally, a torsional damper is installed inside the DC to mitigate the stick-slip vibration of the drillstring, and the torsional damper with a larger moment of inertia is more effective than with a smaller moment of inertia. In practice, however, the torsional damper may be less effective due to the sliding friction torque between the torsional damper and the inner base of the DC that supports the weight of the torsional damper. For the simulation results demonstrated in Figure 93 and Figure 94, the coefficients of sliding friction between the torsional damper and inner base of the DC are both set as $\mu_A = 0.002$, which is close to the coefficient of rolling friction for an angular contact thrust ball bearing. Similar to the drillstring utilizing the Coulomb torque model, the stick-slip vibration induced by the Stribeck torque model can be completely attenuated by the torsional damper under a small coefficient of friction like $\mu_A = 0.002$, which is demonstrated in Figure 95.

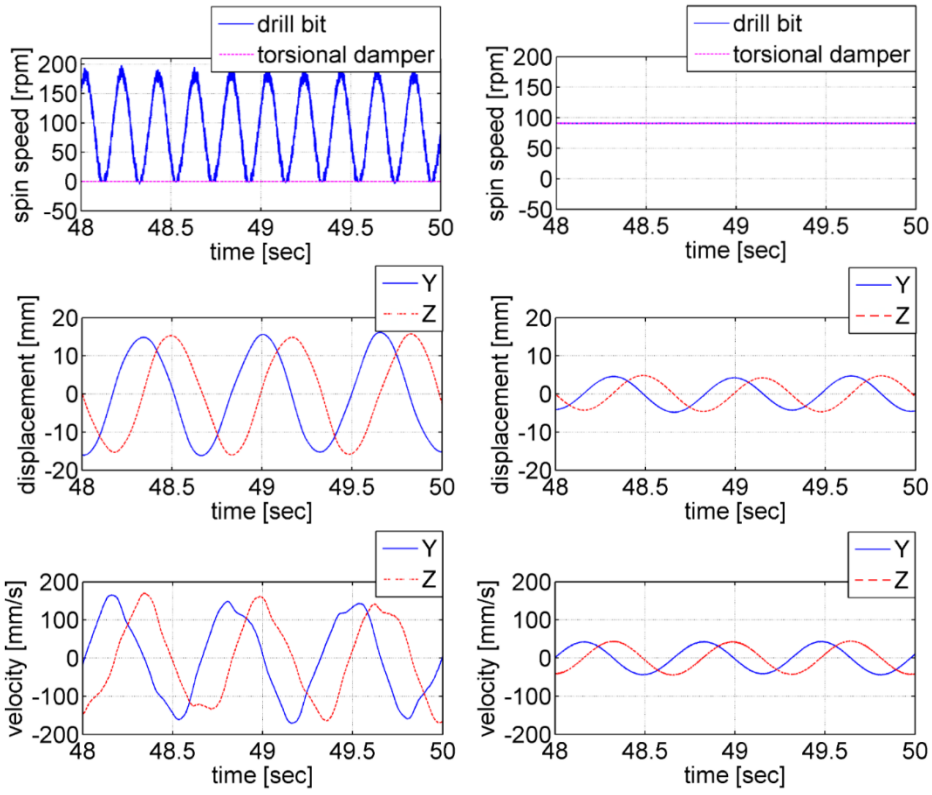

Figure 95. Rotary speed of the DB, lateral displacement and velocity of the DC at point D utilizing the Stribeck torque model without (left) or with (right) the impactors and torsional damper under $d = 20\ mm$ and the mode-oriented mass distribution of the impactors in the DA condition at the critical speed of $\Omega = 91\ rpm$. Reprinted from Ref. [1].

It would be simpler for assembly if the torsional damper is installed directly on the inner base of the DC. In this condition, the friction between the torsional damper and DC base may be treated as the sliding friction between two metal surfaces. Normally, the coefficient of dry sliding friction μ_A is close to 0.35, and μ_A may decrease with the mud fluid lubricating the inner base of the DC. As can be seen from Figure 96, for the Coulomb torque model, an increase in the friction torque between the torsional damper and inner base of the DC results only in a very minor reduction in stick-slip vibration

mitigation. On the contrary, as shown in Figure 97, the torsional vibration of the drillstring that utilizes the Stribeck torque model with $\lambda = 0.02$ may result in limit cycles with the amplitudes oscillating between $77rpm$ and $105rpm$ under a large coefficient of friction of $\mu_A = 0.35$. The limit cycles may dampen out under either a small μ_A or a moderately declining torque curve with $\lambda < 0.02$. This is because a large friction torque, which is attributed to a large μ_A, makes the torsional damper closely chase, or drive the rotating DC. In other words, the relative rotating speed between the torsional damper and DC approaches zero, resulting in less dissipation of kinetic energy. Therefore, any support structure with a low friction torque, such as an angular contact thrust ball bearing, is useful in enhancing the mitigation effects on torsional vibrations. The Stribeck torque model has the characteristic that torque decreases with increased rotary speed, which induces a negative damping and may cause severe torsional vibrations. A moderately declining torque curve, which implies a small λ, leads to a small negative damping. In accordance with Ref. [56], the torque curve usually declines mildly in practice, indicating that $\lambda < 0.025$ is adequate for the real DA case. Note that the Stribeck friction torque will cause torsional instability if the drillstring has no torsional damping.

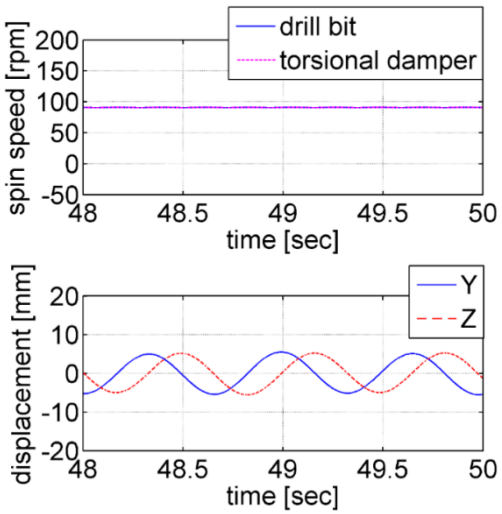

Figure 96. Rotary speed of the DB and lateral displacement of the DC at point *D* utilizing the Coulomb torque model with the impactors and torsional damper under $d = 10\ mm$, $\mu_A = 0.35$, and the even mass distribution of the impactors in the DA condition at the critical speed of $\Omega = 91\ rpm$. Reprinted from Ref. [1].

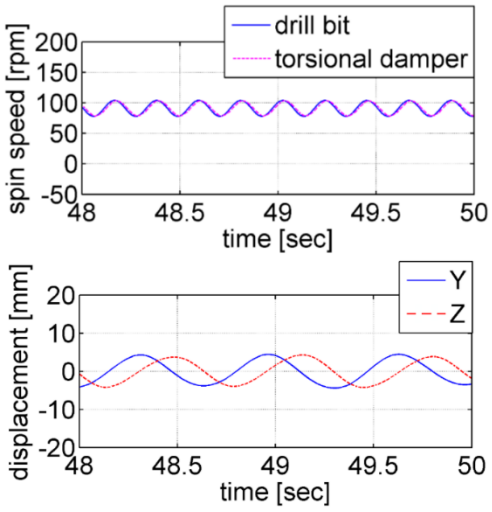

Figure 97. Rotary speed of the DB and lateral displacement of the DC at point *D* utilizing the Stribeck torque model with the impactors and torsional damper under $d = 20\ mm$, $\mu_A = 0.35$, and the mode-oriented mass distribution of the impactors in the DA condition at the critical speed of $\Omega = 91\ rpm$. Reprinted from Ref. [1].

In comparison with the higher-frequency stick-slips shown in Figure 93 and Figure 95, oscillations at the first torsional mode of the full drillstring with a period of $2-10$ seconds are usually more damaging. To model these lower natural frequencies, the length of the DP is extended to $1.2km$, and the DC to $30m$. Additionally, the external torsional damping caused by mud and drilling fluid is set to zero in order to exclude its influence on the mitigation of stick-slip vibrations. Zero torsional damping may result in severe speed oscillation. The speed oscillation will increase as WOB increases so the parametric study starts at zero WOB. The simulation results are presented in Figure 98 and Figure 99. For the Coulomb torque model, as is shown in Figure 98, the torsional vibration of the DB under the extended $30kN$ WOB is suppressed by the torsional damper in the simple speed oscillation period. In contrast, the highest WOB to extend for the Stribeck torque model (Figure 99) is $3kN$.

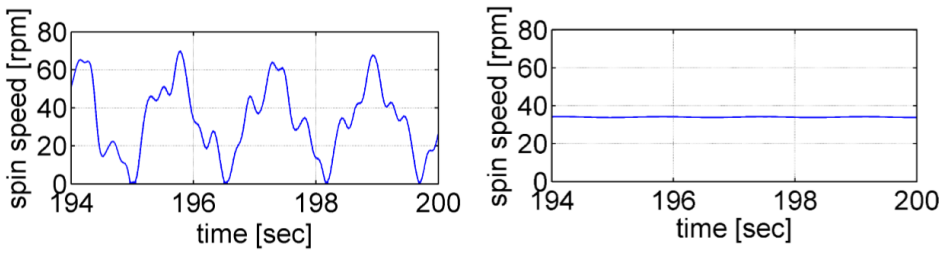

Figure 98. Rotary speed of the DB utilizing the Coulomb torque model without (left) or with (right) the impactors and torsional damper in the DA condition in the first torsional mode of the drillstring under $30\ kN$ WOB in the first torsional mode at the critical speed of $\Omega = 34\ rpm$. Reprinted from Ref. [1].

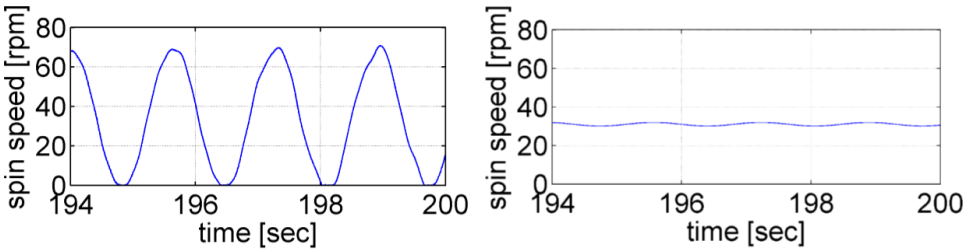

Figure 99. Rotary speed of the DB utilizing the Stribeck torque model without (left) or with (right) the impactors and torsional damper in the DA condition in the first torsional mode of the drillstring under 3 kN WOB in the first torsional mode at the critical speed of $\Omega = 34\ rpm$. Reprinted from Ref. [1].

Besides the stick-slip, the DC and DB may be destabilized by mud or drilling fluid. As pointed out in Ref. [37, 90], this type of destabilizing force may be explained as the presence of cross-coupled stiffness in the form of $\begin{bmatrix} 0 & K_{XY} \\ -K_{XY} & 0 \end{bmatrix}$ at the DC and DB. The simulation results from the drillstring model with $K_{XY} = 7000N/m$ are demonstrated in Figure 100 and Figure 101. The eigenvalue of the drillstring system for the first bending mode of the DC is $0.46 + j9.78$, indicating a negative damping ratio of $\xi = -0.05$. As can be seen from Figure 100, the DC without the impactors and torsional damper is unstable, and the amplitudes of lateral vibration reach $400mm$ in 10 s, which far exceed the clearance between the DC and the borehole. A short time period of $t = 8 - 10s$ is selected to clearly present the stick-slip vibration of the DB. When the impactor dampers and torsional damper are installed in the DC, the drillstring becomes stable, and the vibration amplitudes of the DC are attenuated to $12mm$. Furthermore, the stick-slip vibration is completely suppressed. It is similar with the drillstring utilizing the Stribeck torque model that the impact dampers are able to stabilize the drillstring (Figure

101). Owing to the impactors, the accumulative kinetic energy resulting from the negative damping is dissipated through impacting.

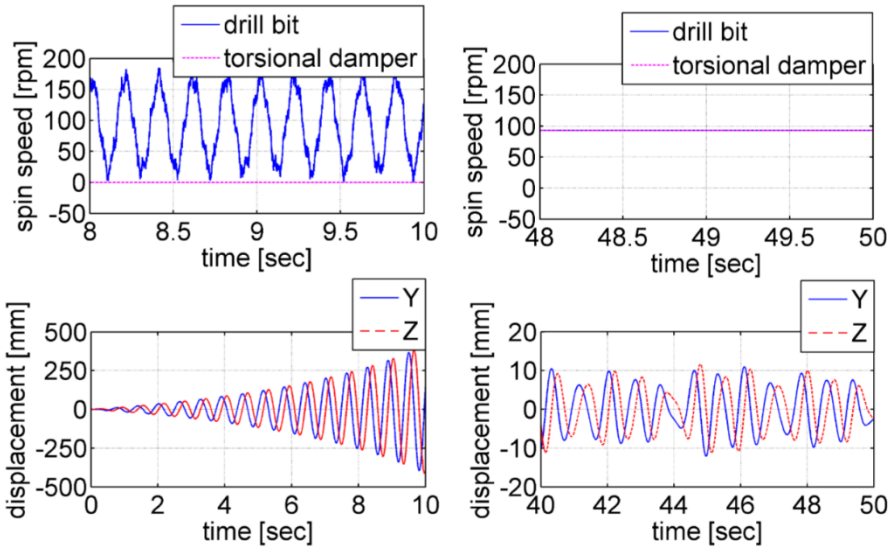

Figure 100. Rotary speed of the DB and lateral displacement of the DC at point D utilizing the Coulomb torque model without (left) or with (right) the impactors and torsional damper, with cross-coupled stiffness, $d = 20\ mm$ and the mode-oriented mass distribution of the impactors in the DA condition at the critical speed of $\Omega = 93\ rpm$. Reprinted from Ref. [1].

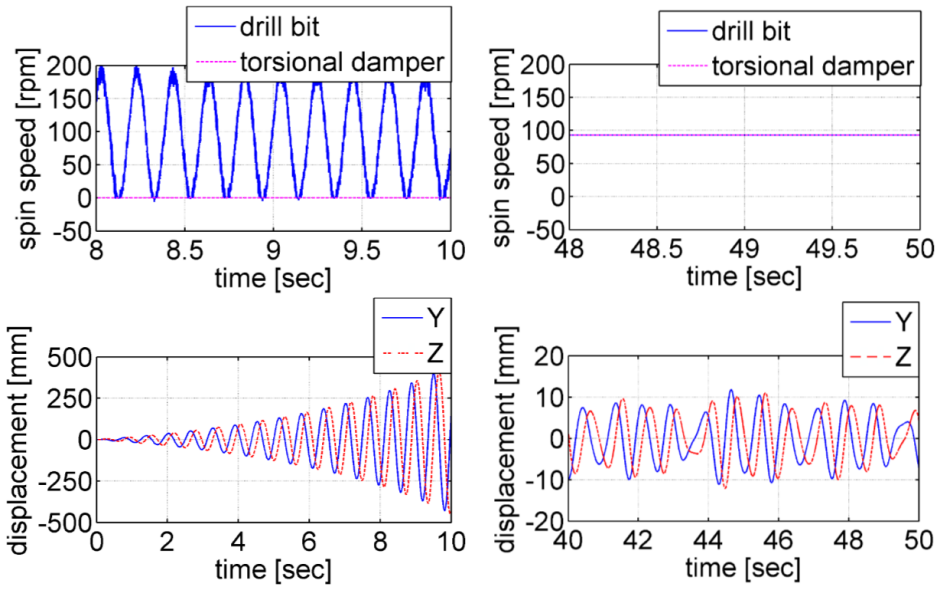

Figure 101. Rotary speed of the DB and lateral displacement of the DC at point D utilizing the Stribeck torque model without (left) or with (right) the impactors and torsional damper, with cross-coupled stiffness, $d = 20\ mm$ and the mode-oriented mass distribution of the impactors in the DA condition at the critical speed of $\Omega = 93\ rpm$. Reprinted from Ref. [1].

7.5. Summary

This chapter analyzed a complete drillstring system that is comprised of a DP, a DC, a DB, and several impact and torsional dampers that are installed in the DC. Coulomb and Stribeck torque models were separately included in the simulation of drillstring vibrations. By using the vibro-impact model and drillgstring FE model developed in Chapter 3, the mitigation effects of the impact and torsional dampers on the drillstring vibration in the working conditions like ROB and DA were investigated. Both of the translational collision between the DC and impactor and the tangential friction in between were considered. The destabilizing forces induced by drilling fluid or mud were also introduced to study the stabilizing effects of the impact damper on the drillstring.

Finally, various design parameters of the impact damper and torsional damper were investigated for the purpose of acquiring stronger suppression effects on drillstring vibration.

8. CONCLUSIONS AND FUTURE WORK

8.1. Summary and Conclusions

The present work (1) improves the rotor dynamic modeling of rotating machinery by developing axisymmetric FE formulations of the stress-stiffening and spin-softening effects, (2) improves the beam FE modeling of a rotor under support motion by integrating a 2D FE hydrodynamic fluid film bearing model, (3) enhances simulation speed and reduces computer recource usage for numerical analysis of a rotor system with flexible support structures by developing a MIMO transfer function modeling approach for support structures, and (4) develops novel impact dampers for suppressing vibrations of low-speed rotating machines (drillstrings).

In regard to the first contribution, the axisymmetric FE formulation of the centrifugal stress-stiffening effects is extended from a stationary structure solid element model in the Cartesian coordinate system to a rotor axisymmetric solid element model in the cylindrical coordinate system. The axisymmetric FE formulation of the spin-softening effects is developed to account for a decrease in radial stiffness of rotating blades and disks. Both axisymmetric FE formulations have been used in the development of rotor dynamic software algorithms.

In addition to the formulation, the improved axisymmetric FE rotor model is used for comparison of solid element and beam element rotor models. It can be concluded from the simulation results that the centrifugal stress-stiffening effects will increase the axial bending stiffness of shafts and disks. The spin-softening effects will reduce the

radial stiffness of shafts and disks. Guidelines for when and how to use the improved axisymmetric FE model for design and analysis of thin-walled rotors and flexible disks are provided.

Regarding the second contribution, a preceding Timoshenko beam element model of a rotor under support motion is improved by correcting the beam FE formulation and replacing the linear eight-coefficient and short journal bearing models with a hydrodynamic fluid film bearing 2D FE model. In comparison with the preceding methods, the support motion is not simply imposed on the rotor, but transferred to rotor via bearing fluid film forces. The conclusions drawn from the simulation results are that support pitch may cause rotor instability. The preload and offset, which increase the eccentricity, help stabilize the rotor under large support motion. Therefore, the offset-half bearing with preload and offset may be a remedy for the instability of a rotor with the four-axial groove bearing (may be extended to any fixed-pad journal bearing) support.

With regard to the third contribution, a MIMO transfer function support structure model is improved by combining the axisymmetric FE rotor and solid element support structure models and transforming into a state-space representation. The simulation results show that the simulation time is substantially reduced (down to 25%). The stability of the rotor system can be predicted from the state-space rotor system model. This MIMO transfer function model is beneficial for designers to do quick revisions of the rotor and support structure combo.

Finally, the novelty of the present work includes the development of centralized impact dampers and torsional dampers to suppress the lateral and torsional vibrations of a drillstring. According to the numerical analysis, the properly arranged (mode-oriented mass distribution) dampers are able to attenuate lateral vibration of the drillstring that operates close to the bending critical speeds and the stick-slip torsional vibration within the operating speed range.

8.2. Future Work

The followings need improvements in the future.

(a) 3D solid element rotor model may be demanded for investigation of non-symmetric rotors such as electric generator and gas turbine blades.

(b) As the shaft wall gets thinner, the axisymmetric FE mesh model needs refinement, which may require more computer resources. In this case, a shell element model could be a better choice in terms of computation efficiency. Thus, a thorough comparison of the axisymmetric FE model with the shell FE model should be conducted in order to understand the merits and demerits of these two rotor modeling approaches.

(c) The high-fidelity models of the Tilting-pad bearings, ball bearings, and squeeze film dampers may be implemented into the present beam FE rotor model with support motion.

(d) LuGre friction model may be applicable to the friction of the drill bit in the contact. This model is based on the elasticity of the contacting solids and can be used to check the attenuation performance of the impact dampers.

REFERENCES

[1] Hu, L., Palazzolo, A., and Karkoub, M., 2016, "Suppression of Lateral and Torsional Stick–Slip Vibrations of Drillstrings With Impact and Torsional Dampers," Journal of Vibration and Acoustics, 138(5), 051013.

[2] Myklestad, N., 1944, "A New Method for Calculating Natural Modes of Uncoupled Bending Vibrations of Airplane Wings and Other Types of Beams," Journal of Aeronautical Science, 11, pp. 153-162.

[3] Pestel, E., and Leckie, F., 1963, Matrix Methods in Elastomechanics, McGraw-Hill, New York.

[4] Nelson, H. D., and McVaugh, J. M., 1976, "The Dynamics of Rotor-Bearing Systems Using Finite Elements," Journal of Engineeering for Industry, 98(2), pp. 593-600.

[5] Nelson, H. D., 1980, "A Finite Rotating Shaft Element Using Timoshenko Beam Theory," Journal of Mechanical Design, 102(4), pp. 793-803.

[6] Thomas, D. L., Wilson, J. M., and Wilson, R. R., 1973, "Timoshenko Beam Finite Elements," Journal of Sound and Vibration, 31(3), pp. 315-330.

[7] Rouch, K. E., and Kao, J.S., 1979, "A Tapered Beam Finite Element for Rotor Dynamics Analysis," Journal of Sound and Vibration, 66(1), pp. 119-140.

[8] Greenhill, L. M., Bickford, W. B., and Nelson, H. D., 1985, "A Conical Beam Finite Element for Rotor Dynamics Analysis," Journal of Vibration, Stress, and Reliability in Design, 107(4), pp. 421-430.

[9] Stephenson, R. W., Rouch, K.E., and Arora, R., 1989, "Modelling of Rotors with Axisymmetric Solid Harmonic Elements," Journal of Sound and Vibration, 131(3), pp. 431-443.

[10] Vest, T. A., and Darlow, M. S., 1990, "A Modified Conical Beam Element Based on Finite Element Analysis: Experimental Correlations," Journal of Vibration and Acousics, 112(3), pp. 350-354.

[11] Stephenson , R. W., and Rouch, K. E., 1993, "Modeling Rotating Shafts Using Axisymmetric Solid Finite Elements with Matrix Reduction," Journal of Vibration and Acoustics, 115(4), pp. 484-489.

[12] Cook, R. D., Malkus, D. S., Plesha , M. E., and Witt, R. J., 2001, Concepts and Applications of Finite Element Analysis, John Wiley & Sons, Inc.

[13] Geradin, M., and Kill, N., 1984, "A New Approach to Finite Element Modelling of Flexible Rotors," Engineering Computations, 1(1), pp. 52-64.

[14] Greenhill, L. M., and Lease, V.J., "Additional Investigations Into the Natural Frequencies and Critical Speeds of a Rotating, Flexible Shaft-Disk System," Proc. ASME Turbo Expo 2007: Power for Land, Sea and Air, pp. 995-1003.

[15] Combescure, D., and Lazarus, A., 2008, "Refined finite element modelling for the vibration analysis of large rotating machines: Application to the gas turbine modular helium reactor power conversion unit," Journal of Sound and Vibration, 318(4-5), pp. 1262-1280.

[16] Guyan, R. J., 1965, "Reduction of Stiffness and Mass Matrices," AIAA Journal, 3(2), pp. 380-380.

[17] Chaudhry, J. A., 2011, "3-D Finite Element Analysis of Rotors in Gas Turbines, Steam Turbines, and Axial Pumps including Blade Vibrations," PhD Dissertation, University of Virginia.

[18] Vollan, A., and Komzsik, L., 2012, Computational Techniques of Rotor Dynamics with the Finite Element Method, CRC Press

[19] Nandi, A., and Neogy, S., 2001, "Modelling of rotors with three-dimensional solid finite elements," The Journal of Strain Analysis for Engineering Design, 36(4), pp. 359-371.

[20] ANSYS, 1989, "ANSYS Engineering Analysis System Theoretical Manual," Swanson Analysis System, INC., Houston, Pennsylvania.

[21] Kirk , R. G., and Gunter, E. J., 1972, "The Effect of Support Flexibility and Damping on the Synchronous Response of a Single-Mass Flexible Rotor," Journal of Engineering for Industry, 94(1), pp. 221-232.

[22] Barrett, L. E., Gunter, E. J., and Allaire, P. E., 1978, "Optimum Bearing and Support Damping for Unbalance Response and Stability of Rotating Machinery," Journal of Engineering for Power, 100(1), pp. 89-94.

[23] Power, R. B., and Wood, D. E., 1984, "2000-hp Motor Support Structure Vibration Sensitivity: Tests, Finite Element Analysis, and Suggested Strategies for Prevention," Journal of Vibration, Acoustics, Stress, and Reliability in Design, 106(1), pp. 113-121.

[24] Iwata, Y., Sato, H., and Tamura, A., 1988, "A Special Case of Critical Speed of Rigid Rotors With Anisotropic Supports," Journal of Sound and Vibration, 121(1), pp. 161-168.

[25] Palazzolo, A., 2016, Vibration Theory and Applications with Finite Elements and Active Vibration Control, John Wiley & Sons, Ltd, United Kingdom.

[26] Stephenson, R. W., and Rouch, K. E., 1992, "Generating Matrices of the Foundation Structure of a Rotor System From Test Data," Journal of Sound and Vibration, 154(3), pp. 467-484.

[27] Vázquez, J. A., and Barrett, L. E., "Transfer Function Representation of Flexible Supports and Casings of Rotating Machinery," Proc. Proc., 17th International Modal Analysis Conference, pp. 1328-1334.

[28] Vázquez, J. A., Barrett, L. E., and Flack, R. D., 2000, "A Flexible Rotor on Flexible Bearing Supports: Stability and Unbalance Response," Journal of Vibration and Acoustics, 123(2), pp. 137-144.

[29] Vázquez, J. A., Barrett, L. E., and Flack, R. D., 2002, "Flexible Bearing Supports, Using Experimental Data," Journal of Engineering for Gas Turbines and Power, 124(2), pp. 369-374.

[30] Moore, J. J., Vannini, G., Camatti, M., and Bianchi, P., 2010, "Rotordynamic Analysis of a Large Industrial Turbocompressor Including Finite Element Substructure Modeling," Journal of Engineering for Gas Turbines and Power, 132(8), p. 082401.

[31] De Santiago, O., and Abraham, E., "Rotordynamic Analysis of a Power Turbine Including Support Flexibility Effects," Proc. Proceedings of ASME Turbo Expo 2008, pp. No. GT2008-50900.

[32] Lin, F., and Meng, G., 2003, "Study on the Dynamics of a Rotor in a Maneuvering Aircraft," Journal of Vibration and Acoustics, 125(3), pp. 324-327.

[33] Driot, N., Lamarque, C. H., and Berlioz, A., 2006, "Theoretical and Experimental Analysis of a Base-Excited Rotor," Journal of Computational and Nonlinear Dynamics, 1(3), p. 257.

[34] Duchemin, M., Berlioz, A., and Ferraris, G., 2006, "Dynamic Behavior and Stability of a Rotor Under Base Excitation," Journal of Vibration and Acoustics, 128(5), pp. 576-585.

[35] Wang, R., Guo, X., and Wang, Y., 2015, "Nonlinear analysis of rotor system supported by oil lubricated bearings subjected to base movements," Proceedings of the Institution of Mechanical Engineers, Part C: Journal of Mechanical Engineering Science, 230(4), pp. 543-558.

[36] Zhang, G., Liu, S., Ma, R., and Liu, Z., 2015, "Nonlinear Dynamic Characteristics of Journal Bearing-Rotor System Considering the Pitching and Rolling Motion for Marine Turbo Machinery," Proceedings of the Institution of Mechanical Engineers Part M: Journal of Engineering for the Maritime Environment, 229(1), pp. 95-107.

[37] Childs, D., 1993, Turbomachinery Rotordynamics: Phenomena, Modeling, and Analysis, John Wiley & Sons, Inc., New York, USA.

[38] Childs, D., 2013, Turbomachinery Rotordynamics with Case Studies, Minter Spring, Wellborn Texas.

[39] Das, A. S., Dutt, J. K., and Ray, K., 2010, "Active Vibration Control of Unbalanced Flexible Rotor–Shaft Systems Parametrically Excited Due to Base Motion," Applied Mathematical Modelling, 34(9), pp. 2353-2369.

[40] Das, A. S., Dutt, J. K., and Ray, K., 2010, "Active Vibration Control of Flexible Rotors on Maneuvering Vehicles," AIAA Journal, 48(2), pp. 340-353.

[41] Dakel, M., Baguet, S., and Dufour, R., 2013, "Steady-State Dynamic Behavior of an On-Board Rotor Under Combined Base Motions," Journal of Vibration and Control, 20(15), pp. 2254-2287.

[42] Dakel, M., Baguet, S., and Dufour, R., 2014, "Nonlinear Dynamics of a Support-Excited Flexible Rotor with Hydrodynamic Journal Bearings," Journal of Sound and Vibration, 333(10), pp. 2774-2799.

[43] Han, Q., and Chu, F., 2015, "Parametric Instability of Flexible Rotor-Bearing System under Time-Periodic Base Angular Motions," Applied Mathematical Modelling, 39(15), pp. 4511-4522.

[44] Frene, J., Nicolas, D., Degueurce, B., Berthe, D., and Godet, M., 1997, Hydrodynamic Lubrication: Bearings and Thrust Bearings, Elsevier Science, Amsterdam.

[45] Adiletta, G., Guido, A. R., and Rossi, C., 1996, "Chaotic Motions of a Rigid Rotor in Short Journal Bearings," Nonlinear Dynamics, 10(3), pp. 251-269.

[46] Buckholz, R. H. a. H., B., 1986, "The Accuracy of Short Bearing Theory for Newtonian Lubricants," Journal of Tribology, 108(1), pp. 73-79.

[47] Rezvani, M. A. a. H., E. J., 1993, "Limitations of the Short Bearing Approximation in Dynamically Loaded Narrow Hydrodynamic Bearings," Journal of Tribology, 115(3), pp. 544-549.

[48] Szeri, A., 1980, Tribology: Friction, Lubrication, and Wear, Mcgraw-Hill.

[49] Earles, L. L. P., A., and Armentrout, R. W., 1990, "A Finite Element Approach to Pad Flexibility Effects in Tilt Pad Journal Bearings: Part I - Single Pad Analysis," Journal of Tribology, 112(2), pp. 169-176.

[50] Jansen, J. D., and van den Steen, L., 1995, "Active Damping of Self-excited Torsional Vibrations in Oil Well Drillstrings," Journal of Sound and Vibration, 179, pp. 647-668.

[51] Sowers, S. F., Dupriest, F. E., Bailey, J. R., and Wang, L., "Roller Reamers Improve Drilling Performance in Wells Limited by Bit and Bottomhole Assembly Vibrations," Proc. SPE/IADC Drilling Conference and Exhibition, pp. 405-412.

[52] Kyllingstad, A., and Halsey, G. W., 1988, "A Study of Slip/Stick Motion of the Bit," SPE Drilling Engineering, 3, pp. 369-373.

[53] Liao, C.-M., Balachandran, B., Karkoub, M., and Abdel-Magid, Y. L., 2011, "Drill-String Dynamics: Reduced-Order Models and Experimental Studies," Journal of Vibration and Acoustics, 133(4), p. 041008.

[54] Vlajic, N., Liao, C.-M., Karki, H., and Balachandran, B., 2013, "Draft: Stick-Slip Motions of a Rotor-Stator System," Journal of Vibration and Acoustics, 136(2), p. 021005.

[55] Dawson, R., Lin, Y. Q., and Spanos, P. D., "Drill String Stick-Slip Oscillations," Proc. Proceedings of the 1987 SEM Spring Conference on Experimental Mechanics, pp. 590-595.

[56] Brett, J. F., 1992, "The Genesis of Bit-Induced Torsional Drillstring Vibrations," SPE Drilling Engineering, 7(03), pp. 168-174.

[57] Leine, R. I., van Campen, D. H., and Keultjes, W. J. G., 2002, "Stick-slip Whirl Interaction in Drillstring Dynamics," Journal of Vibration and Acoustics, 124(2), pp. 209-220.

[58] Jansen, J. D., 1991, "Non-linear Rotor Dynamics as Applied to Oilwell Drillstring Vibrations," Journal of Sound and Vibration, 147, pp. 115-135.

[59] Bailey, J. R. D., F. E., et al., "Development and Application of a BHA Vibrations Model," Proc. International Petroleum Technology Conference, p. IPTC 12737.

[60] Bailey, J. R., Elsborg, C. C., James, R. W., Pastusek, P., Prim, M. T., and Watson, W. W., 2013, "Design Evolution of Drilling Tools to Mitigate Vibrations," SPE Drilling & Completion, 28, pp. 350-369.

[61] Moore, J. J., Palazzolo, A. B., Gadangi, R., Nale, T. A., Klusman, S. A., Brown, G. V., and Kascak, A. F., 1995, "A Forced Response Analysis and Application of Impact Dampers to Rotordynamic Vibration Suppression in a Cryogenic Environment," Journal of Vibration and Acousics, 117(3A), pp. 300-310.

[62] McElhaney, J. M., Palazzolo, A., and Kascak, A., 1997, "Modeling and Simulation Methods for MDOF Structures and Rotating Machinery With Impact Dampers," Journal of Engineering for Gas Turbines and Power, 119(2), pp. 436-446.

[63] Goldsmith, W., 1960, Impact: The Theory and Physical Behaviour of Colliding Solids, Edward Arnold Ltd., London, UK.

[64] Johnson, K. L., 1985, Contact Mechanics, Cambridge University Press, Cambridge, UK.

[65] Hunt, K. H., and Crossley, F. R. E., 1975, "Coefficient of Restitution Interpreted as Damping in Vibroimpact," Journal of Applied Mechanics, 42(2), pp. 440-445.

[66] Rao, J. S., 2011, History of Rotating Machinery Dynamics, Springer Netherlands.

[67] Zienkiewicz, O. C., Taylor, R. L., and Zhu, J. Z. , 2005, The Finite Element Method: Its Basis and Fundamentals, Elsevier Butterworth-Heinemann, Boston.

[68] Petyt, M., 2010, Introduction to Finite Element Vibration Analysis, Cambridge University Press.

[69] Hu, L., and Palazzolo, A., 2018, "An Enhanced Axisymmetric Solid Element for Rotor Dynamic Model Improvement," Journal of Vibration and Acoustics, under review (Permission to use the work will be requested after publication. Access to the dissertation is restricted until after permission is granted).

[70] Engwirda, D., 2017, "MESH2D - Delaunay-based unstructured mesh-generation."

[71] Suh, J., and Palazzolo, A., 2014, "Three-Dimensional Thermohydrodynamic Morton Effect Simulation—Part I: Theoretical Model," Journal of Tribology, 136(3), p. 031706.

[72] Suh, J., and Palazzolo, A., 2014, "Three-Dimensional Thermohydrodynamic Morton Effect Analysis—Part II: Parametric Studies," Journal of Tribology, 136(3), p. 031707.

[73] Stephenson, R. W., 1990, "Rotor system analysis: a coupled rotor-foundation matrix approach,"Dissertation.

[74] Ocvirk, F. W., 1952, "Short-bearing approximation for full journal bearings," No. NACA TN 2808.

[75] Szeri, A. Z., 2010, Fluid Film Lubrication, Cambridge University Press.

[76] Hamrock, B. J. S., S. R.; and Jacobson, B. O., 2004, Fundamentals of Fluid Film Lubrication, CRC Press.

[77] Palazzolo, A., 2011, "Dynamics of Rotating Machinery, Lecture Notes 18," Department of Mechanical Engineering, Texas A&M University.

[78] Kardestuncer, H., 1987, Finite Element Handbook, Mcgraw-Hill.

[79] Yu, J., Craggs, A., and Mioduchowski, A., 1999, "Modelling of Shaft Orbiting with 3-D Solid Finite Elements," International Journal of Rotating Machinery, 5(1), pp. 53-65.

[80] Hu, L., and Palazzolo, A., 2016, "Solid Element Rotordynamic Modeling of a Rotor on a Flexible Support Structure Utilizing Multiple-Input and Multiple-Output Support Transfer Functions," Journal of Engineering for Gas Turbines and Power, 139(1), 012503.

[81] Levy, E. C., 1959, "Complex-Curve Fitting," IRE Transactions on Automatic Control, AC-4, pp. 37-44.

[82] Rosenbrock, H. H., 1970, State-Space and Multivariable Theory, Wiley, New York.

[83] Pace, I. S. B., S., 1974, "Efficient algorithms for linear system calculations Part II Minimal realization," International Journal of Systems Science, 5, pp. 413-424.

[84] Van Dooren, P., 1981, "The Generalized Eigenstructure on Linear System Theory," IEEE Transactions on Automatic Control.

[85] Franklin, G. F., Powell, J. D., and Emami-Naeini, A., 2005, Feedback Control of Dynamics Systems, Prentice Hall, Upper Saddle River, New Jersey.

[86] Vance, J. M. M., B.T.; Tripp, H. A., 1987, "Critical Speeds of Turbomachinery: Computer Predictions vs. Experimental Measurements—Part I: The Rotor Mass-Elastic Model," Journal of vibration, Acoustics, Stress, and Reliability in Design.

[87] Vance, J. M. M., B.T.; Tripp, H. A., 1987, "Critical Speeds of Turbomachinery: Computer Predictions vs. Experimental Measurements—Part II: Effect of Tilt-Pad Bearings and Foundation Dynamics," Journal of vibration, Acoustics, Stress, and Reliability in Design.

[88] Someya, T., 1989, Journal-Bearing Databook, Springer-Verlag Berlin Heidelberg.

[89] Faltinsen, O., 1993, Sea Loads on Ships and Offshore Structures, Cambridge University Press.

[90] Vance, J. M., 1988, Rotordynamics of Turbomachinery, Wiley-Interscience.

[91] Cowper, G. R., 1973, "Gaussian Quadrature Formulas for Triangles," International Journal for Numerical Methods in Engineering, 7(3), pp. 405-408.

[92] Logan, D. L., 2002, A First Course in the Finite Element Method, Brooks/Cole Publishing Co.

[93] Reddy, J. N., 2005, An Introduction to the Finite Element Method, McGraw-Hill.

APPENDIX A

AXISYMMETRIC SOLID HARMONIC FINITE ELEMENT FORMULATION FOR ROTOR SYSTEM

The rotor displacement $\{U_R\}$ of Eq. (6) shown in Chapter 2 can be expanded by using the shape functions and node displacements from certain harmonic modes. Not all the modes are needed because higher-order modes have much less influences on lateral vibrations of the rotor than lower-order modes (particularly zeroth and first order modes). In regard to the centrifugal stress-stiffening and spin-softening effects, both zeroth order and first order modes are effective modes, which can be seen from the derivation presented in Sections 2.3 to 2.4.

In regard to Eq. (5), u_R^e is composed of all harmonics and may be expressed as,

$$\{\mathrm{U_R^e}\} = \sum_{m=0}^{N} \{\mathrm{u_m^e}\} \tag{A 1}$$

with

$$\{\mathrm{u_m^e}\} = [\mathrm{N_m}]\{\mathrm{q_m^e}\} \tag{A 2}$$

The shape function shown in Eq. (5) can be expanded as,

$$[\mathrm{N}] = [N_0 \quad \cdots \quad N_N] \tag{A 3}$$

where the shape function at harmonics = m, $[N_m]$, is composed of the symmetric and antisymmetric components as follows.

$$[\mathrm{N_m}] = [N_{mS} \quad N_{mA}] \tag{A 4}$$

The symmetric components may be written as,

$$\left[\mathrm{N_{mS}}\right]=\left[\begin{array}{ccc:c:ccc} N_{m1}\cos(m\theta) & 0 & 0 & \cdots & N_{m3}\cos(m\theta) & 0 & 0 \\ 0 & N_{m1}\cos(m\theta) & 0 & & 0 & N_{m3}\cos(m\theta) & 0 \\ 0 & 0 & N_{m1}\sin(m\theta) & & 0 & 0 & N_{m3}\sin(m\theta) \end{array}\right] \tag{A 5}$$

The antisymmetric components can be expressed as,

$$\left[\mathrm{N_{mA}}\right]=\left[\begin{array}{ccc:c:ccc} N_{m1}\sin(m\theta) & 0 & 0 & \cdots & N_{m3}\sin(m\theta) & 0 & 0 \\ 0 & N_{m1}\sin(m\theta) & 0 & & 0 & N_{m3}\sin(m\theta) & 0 \\ 0 & 0 & -N_{m1}\cos(m\theta) & & 0 & 0 & -N_{m3}\cos(m\theta) \end{array}\right] \tag{A 6}$$

To facilitate the integral operation of the axisymmetric element for the circumferential angles $\theta \in [0,2\pi]$, $[N_{mS}]$ and $[N_{mA}]$ may be transformed into,

$$[N_{mS}] = \left[N_{m,cos}\right] cos(m\theta) + \left[N_{m,sin}\right] sin(m\theta) \tag{A 7}$$

$$[N_{mA}] = -\left[N_{m,sin}\right] cos(m\theta) + \left[N_{m,cos}\right] sin(m\theta) \tag{A 8}$$

where

$$\left[N_{\mathrm{m,cos}}\right] = \begin{bmatrix} N_{m1} & 0 & 0 & & N_{m3} & 0 & 0 \\ 0 & N_{m1} & 0 & \cdots & 0 & N_{m3} & 0 \\ 0 & 0 & 0 & & 0 & 0 & 0 \end{bmatrix} \tag{A 9}$$

$$\left[N_{\mathrm{m,sin}}\right] = \begin{bmatrix} 0 & 0 & 0 & & 0 & 0 & 0 \\ 0 & 0 & 0 & \cdots & 0 & 0 & 0 \\ 0 & 0 & N_{m1} & & 0 & 0 & N_{m3} \end{bmatrix} \tag{A 10}$$

Substituting Eqs. (A 1)-(A 6) and Eq. (5) into Eq. (6) yields the equations of motion for each element at *m*th order harmonics as,

$$[M_m^e]\{\ddot{q}_m^e\} + [C_m^e]\{\dot{q}_m^e\} + [K_m^e]\{q_m^e\} = \{f_m^e\} \tag{A 11}$$

where $[M_m^e]$, $[C_m^e]$ and $[K_m^e]$ represent mass, damping and stiffness matrix, respectively, $\{q_m^e\}$ is displacement vector, $\{f_m^e\}$ is external force vector, and the superscripts e and $\cdot$ indicate element and derivative of time, respectively.

The element displacement vector $\{q^e\}$ has the following form,

$$\begin{aligned}\{q^e\} = [\quad & u_{0rS1},\ u_{0zS1},\ u_{0\theta S1},\ \dots,\ u_{0rSN_e},\ u_{0zSN_e},\ u_{0\theta SN_e},\\ & u_{0rA1},\ u_{0zA1},\ u_{0\theta A1},\ \dots,\ u_{0rAN_e},\ u_{0zAN_e},\ u_{0\theta AN_e},\\ & \cdots\\ & u_{NrS1},\ u_{NzS1},\ u_{N\theta S1},\ \dots,\ u_{NrSN_e},\ u_{NzSN_e},\ u_{N\theta SN_e},\\ & u_{NrA1},\ u_{NzS1},\ u_{N\theta A1},\ \dots,\ u_{NrAN_e},\ u_{NzAN_e},\ u_{N\theta AN_e}\quad]^T\end{aligned} \tag{A 12}$$

where u are the displacements, the subscripts N and N_e are the number of nodes within an axisymmetric element and number of harmonics, respectively. S and A represent the symmetric and antisymmetric components. As shown in Eq. (4), $u_{0\theta Si}$, u_{0rAi} and u_{0zAi} can be eliminated due to $sin(0) = 0$. As a result, $\{q^e\}$ may be reduced to,

$$\begin{aligned}\{q^e\} = [\quad & u_{0rS1},\ u_{0zS1},\ u_{0\theta A1},\ \dots,\ u_{0rSN_e},\ u_{0zSN_e},\ u_{0\theta AN_e}\\ & \cdots\\ & u_{NrS1},\ u_{NzS1},\ u_{N\theta S1},\ \dots,\ u_{NrSN_e},\ u_{NzSN_e},\ u_{N\theta SN_e}\\ & u_{NrA1},\ u_{NzS1},\ u_{N\theta A1},\ \dots,\ u_{NrAN_e},\ u_{NzAN_e},\ u_{N\theta AN_e}\quad]^T\end{aligned} \tag{A 13}$$

$\{q^e\}$ at the *m*th mode are obtain from Eqs. (A 12) and (A 13) by selecting the items with the first subscript equal to *m*. The matrices and vectors for the rotor FE model can be obtained by assembling all the elemental matrices and vectors.

As shown in Chapters 2 and 3, the integral operation is required to obtain the final FE matrices and vectors. There are generally two ways for numerical analysis in the computer program. One is to apply the Gaussian quadrature numerical integration [91-93]. The other is to use the approximate integration formula, as is shown in [68].

Regarding the Gaussian quadrature method, Table 8 illustrates the weights and evaluation points for integration on a three-node triangle element.

Table 8. Weights and evaluation points for integration on a triangle element.

Point number j	**Weights H_j**	**Evaluation point ξ_j**	**Evaluation point η_j**	**Evaluation point ζ_j**
1	0.10995174	0.81684757	0.09157621	0.09157621
2	0.10995174	0.09157621	0.81684757	0.09157621
3	0.10995174	0.09157621	0.09157621	0.81684757
4	0.22338159	0.10810302	0.44594849	0.44594849
5	0.22338159	0.44594849	0.10810302	0.44594849
6	0.22338159	0.44594849	0.44594849	0.10810302

The approximate integration formula is expressed as,

$$\int_{A^e} L_1^m L_2^n L_3^p dA = \frac{m!n!p!}{(m+n+p+2)!} \cdot 2A^e \quad \text{(A 14)}$$

In this work, linear triangle elements are employed to model the axisymmetric semi-section of the rotor. Therefore, the component of the shape function shown in Eq. (A 5) can be expressed as,

$$N_{mi} = L_i \quad \text{(A 15)}$$

with the evaluation points ξ_j, η_j, and ζ_j representing L_i.

$$\tilde{A}_i = r_j z_k - r_k z_j \quad \text{(A 16)}$$

$$a_i = z_j - z_k \quad \text{(A 17)}$$

$$b_i = r_k - r_j \quad \text{(A 18)}$$

$$L_i = \frac{1}{2A^e}\left(\tilde{A}_i + a_i r + b_i z\right) \quad \text{(A 19)}$$

where i, j, k = 1, 2, 3. The element area A_e is derived from,

$$A^e = \frac{1}{2}(a_1 b_2 - a_2 b_1) \quad \text{(A 20)}$$

The effective centroid of the element is,

$$r = \sum_{i=1}^{3} r_i L_i \quad \text{(A 21)}$$

The constitutive matrix representing the stress-strain relationship in Eq. (27) is given as follows,

$$[D] = \frac{E}{(1+\upsilon)(1-2\upsilon)}\begin{bmatrix} 1-\upsilon & \upsilon & \upsilon & 0 & 0 & 0 \\ \upsilon & 1-\upsilon & \upsilon & 0 & 0 & 0 \\ \upsilon & \upsilon & 1-\upsilon & 0 & 0 & 0 \\ 0 & 0 & 0 & \frac{1}{2}-\upsilon & 0 & 0 \\ 0 & 0 & 0 & 0 & \frac{1}{2}-\upsilon & 0 \\ 0 & 0 & 0 & 0 & 0 & \frac{1}{2}-\upsilon \end{bmatrix} \quad \text{(A 22)}$$

where E and υ are modulus of elasticity and Poisson's ratio, respectively.

Recall that the strain is derived from,

$$\{\varepsilon_m^e\} = [\partial]\{u_m^e\} = [\partial][N_m]\{q_m^e\} \quad \text{(A 23)}$$

$[\partial]$ indicates the partial derivatives of the displacements as shown below,

$$[\partial] = \begin{bmatrix} \frac{\partial}{\partial r} & 0 & 0 \\ 0 & \frac{\partial}{\partial z} & 0 \\ \frac{1}{r} & 0 & \frac{1}{r}\frac{\partial}{\partial \theta} \\ \frac{\partial}{\partial z} & \frac{\partial}{\partial r} & 0 \\ 0 & \frac{1}{r}\frac{\partial}{\partial \theta} & \frac{\partial}{\partial z} \\ \frac{1}{r}\frac{\partial}{\partial \theta} & 0 & \left(\frac{\partial}{\partial r} - \frac{1}{r}\right) \end{bmatrix} \quad \text{(A 24)}$$

Using $[B_m]$ to represent $[\partial][N_m]$ yields,

$$[\partial][N_m] = [B_m] = [[B_{mS}] \quad [B_{mA}]] \tag{A 25}$$

An understanding should be reached that the two harmonics sets, m = 0 and m = 1, 2, … will lead to totally different representations of $[B_m]$. This difference is not specified in any of the aforementioned literatures as the harmonics m = 0 are generally not used in the analysis of lateral vibrations. First, m = 0 leads to the following representation of $[B_m]$,

$$[B_{0S}]_{6\times9} = \begin{bmatrix} \frac{\partial N_{01}}{\partial r} & 0 & 0 & & \frac{\partial N_{03}}{\partial r} & 0 & 0 \\ 0 & \frac{\partial N_{01}}{\partial z} & 0 & \cdots & 0 & \frac{\partial N_{03}}{\partial z} & 0 \\ \frac{N_{01}}{r} & 0 & 0 & & \frac{N_{03}}{r} & 0 & 0 \\ \frac{\partial N_{01}}{\partial z} & \frac{\partial N_{01}}{\partial r} & 0 & & \frac{\partial N_{03}}{\partial z} & \frac{\partial N_{03}}{\partial r} & 0 \\ 0 & 0 & 0 & \cdots & 0 & 0 & 0 \\ 0 & 0 & 0 & & 0 & 0 & 0 \end{bmatrix} \tag{A 26}$$

$$[B_{0A}]_{6\times9} = \begin{bmatrix} 0 & 0 & 0 & & 0 & 0 & 0 \\ 0 & 0 & 0 & \cdots & 0 & 0 & 0 \\ 0 & 0 & 0 & & 0 & 0 & 0 \\ 0 & 0 & 0 & & 0 & 0 & 0 \\ 0 & 0 & -\frac{\partial N_{01}}{\partial z} & \cdots & 0 & 0 & -\frac{\partial N_{03}}{\partial z} \\ 0 & 0 & \left(\frac{N_{01}}{r} - \frac{\partial N_{01}}{\partial r}\right) & & 0 & 0 & \left(\frac{N_{03}}{r} - \frac{\partial N_{03}}{\partial r}\right) \end{bmatrix} \tag{A 27}$$

Secondly, $[B_{mS}]$ and $[B_{mA}]$ with m = 1, 2, … can be obtained from,

$$[B_{mS}] = [B_{m1}]\, sin(m\theta) + [B_{m2}]\, cos(m\theta) \tag{A 28}$$

$$[B_{mA}] = -[B_{m1}]\, cos(m\theta) + [B_{m2}]\, sin(m\theta) \tag{A 29}$$

where

$$[B_{m1}]_{6\times9} = \begin{bmatrix} 0 & 0 & 0 & & \\ 0 & 0 & 0 & & \\ 0 & 0 & 0 & & \\ 0 & 0 & 0 & \cdots & \cdots \\ 0 & -m\frac{N_{m1}}{r} & \frac{\partial N_{m1}}{\partial z} & & \\ -m\frac{N_{m1}}{r} & 0 & \left(\frac{\partial N_{m1}}{\partial r} - \frac{N_{m1}}{r}\right) & & \end{bmatrix} \quad \text{(A 30)}$$

$$[B_{m2}]_{6\times9} = \begin{bmatrix} \frac{\partial N_{m1}}{\partial r} & 0 & 0 & & \\ 0 & \frac{\partial N_{m1}}{\partial z} & 0 & & \\ \frac{N_{m1}}{r} & 0 & m\frac{N_{m1}}{r} & \cdots & \cdots \\ \frac{\partial N_{m1}}{\partial z} & \frac{\partial N_{m1}}{\partial r} & 0 & & \\ 0 & 0 & 0 & & \\ 0 & 0 & 0 & & \end{bmatrix} \quad \text{(A 31)}$$

As show in Eq. (A 11), the damping and stiffness matrices for an element can be further expressed as,

$$[C_m^e] = [G_m^e] + [C_{Vm}^e] \quad \text{(A 32)}$$

$$[K_m^e] = [K_{Sm}^e] + [K_{\sigma m}^e] - [K_{\Omega m}^e] \quad \text{(A 33)}$$

where the subscript m represents the mth mode, $[G^e]$ represents the gyroscopics, $[C_V^e]$ the structural damping (neglectable for most rotating machinery), $[K_S^e]$ the structural stiffness due to structure elasticity, $[K_\sigma^e]$ the centrifugal stress-stiffening effect, and $[K_\Omega^e]$ the spin-softening effect.

For harmonics m = 1, 2, …, the mass and stiffness matrices have been provided in [14]. When m = 0, the symmetric and antisymmetric components of the element mass and stiffness matrices are different. The elemental mass matrix can be defined as,

$$[M_0^e] = \begin{bmatrix} [M_{0SS}^e] & [0] \\ [0] & [M_{0AA}^e] \end{bmatrix} \quad \text{(A 34)}$$

where $[M_{0SS}^e]$ and $[M_{0AA}^e]$ are given by,

$$[M_{0SS}^e] = 2\pi \int_{A^e} \rho \begin{bmatrix} L_1L_1 & 0 & 0 & L_1L_2 & 0 & 0 & L_1L_3 & 0 & 0 \\ 0 & L_1L_1 & 0 & 0 & L_1L_2 & 0 & 0 & L_1L_3 & 0 \\ 0 & 0 & 0 & 0 & 0 & 0 & 0 & 0 & 0 \\ L_2L_1 & 0 & 0 & L_2L_2 & 0 & 0 & L_2L_3 & 0 & 0 \\ 0 & L_2L_1 & 0 & 0 & L_2L_2 & 0 & 0 & L_2L_3 & 0 \\ 0 & 0 & 0 & 0 & 0 & 0 & 0 & 0 & 0 \\ L_3L_1 & 0 & 0 & L_3L_2 & 0 & 0 & L_3L_3 & 0 & 0 \\ 0 & L_3L_1 & 0 & 0 & L_3L_2 & 0 & 0 & L_3L_3 & 0 \\ 0 & 0 & 0 & 0 & 0 & 0 & 0 & 0 & 0 \end{bmatrix} rdA \quad \text{(A 35)}$$

$$[M_{0AA}^e] = 2\pi \int_{A^e} \rho \begin{bmatrix} 0 & 0 & 0 & 0 & 0 & 0 & 0 & 0 & 0 \\ 0 & 0 & 0 & 0 & 0 & 0 & 0 & 0 & 0 \\ 0 & 0 & L_1L_1 & 0 & 0 & L_1L_2 & 0 & 0 & L_1L_3 \\ 0 & 0 & 0 & 0 & 0 & 0 & 0 & 0 & 0 \\ 0 & 0 & 0 & 0 & 0 & 0 & 0 & 0 & 0 \\ 0 & 0 & L_2L_1 & 0 & 0 & L_2L_2 & 0 & 0 & L_2L_3 \\ 0 & 0 & 0 & 0 & 0 & 0 & 0 & 0 & 0 \\ 0 & 0 & 0 & 0 & 0 & 0 & 0 & 0 & 0 \\ 0 & 0 & L_3L_1 & 0 & 0 & L_3L_2 & 0 & 0 & L_3L_3 \end{bmatrix} rdA \quad \text{(A 36)}$$

The elemental stiffness matrix can be written as,

$$[K_0^e] = \begin{bmatrix} 2\pi \int_{A^e} [B_{0S}]^T [D][B_{0S}] rdrdz & [0] \\ [0] & 2\pi \int_{A^e} [B_{0A}]^T [D][B_{0A}] rdrdz \end{bmatrix} \quad \text{(A 37)}$$

where the definitions of $[D]$, $[B_{0S}]$ and $[B_{0A}]$ can be found in [12], and the integrals in Eq. (A 37) are obtained by using Gaussian quadrature. Although the FE model is developed based on three-node triangular elements, the derived matrices can be expanded to other types of elements.

Regarding the strain energy due to centrifugal forces, the expanded strain vector $\{\delta_\sigma^e\}$ shown in Eq. (28) may be as,

$$\{\delta_\sigma^e\} = \left[\frac{\partial u_r}{\partial r},\ \frac{\partial u_r}{\partial z},\ \frac{1}{r}\left(\frac{\partial u_r}{\partial \theta} - u_\theta\right),\ \frac{\partial u_z}{\partial r},\ \frac{\partial u_z}{\partial z},\ \frac{1}{r}\frac{\partial u_z}{\partial \theta},\ \frac{\partial u_\theta}{\partial r},\ \frac{\partial u_\theta}{\partial z},\ \frac{1}{r}\left(u_r + \frac{\partial u_\theta}{\partial \theta}\right)\right]^T \quad \text{(A 38)}$$

With regard to Eq. (32), $[G_{\sigma m}^e]$, may be represented as,

$$[G_{\sigma m}^e] = [G_{\sigma mc}^e]\, cos(m\theta) + [G_{\sigma ms}^e]\, sin(m\theta) \quad \text{(A 39)}$$

where m = 0, 1, 2, ….

Substituting Eq. (A 39) in Eq. (32) yields,

$$[K^e_{\sigma m}] = \pi \int_{A^e} ([G^e_{\sigma mc}]^T [S^e_{\sigma 0}][G^e_{\sigma mc}] + [G^e_{\sigma ms}]^T [S^e_{\sigma 0}][G^e_{\sigma ms}]) r dr dz \qquad \text{(A 40)}$$

where

$$[S^e_\sigma] = \begin{bmatrix} [\sigma^e_0] & [0] & [0] \\ [0] & [\sigma^e_0] & [0] \\ [0] & [0] & [\sigma^e_0] \end{bmatrix} \qquad \text{(A 41)}$$

$$[G^e_{\sigma mc}]_{9\times 18} = \begin{bmatrix} 0 & 0 & 0 & & & 0 & 0 & 0 & & \\ \frac{\partial N_{m1}}{\partial z} & 0 & 0 & \cdots & \cdots & 0 & 0 & 0 & \cdots & \cdots \\ 0 & 0 & 0 & & & \frac{mN_{m1}}{r} & 0 & \frac{N_{m1}}{r} & & \\ 0 & \frac{\partial N_{m1}}{\partial r} & 0 & & & 0 & 0 & 0 & & \\ 0 & 0 & 0 & 2* & 3* & 0 & 0 & 0 & 2* & 3* \\ 0 & 0 & 0 & & & 0 & \frac{mN_{m1}}{r} & 0 & & \\ 0 & 0 & 0 & & & 0 & 0 & -\frac{\partial N_{m1}}{\partial r} & & \\ 0 & 0 & 0 & \cdots & \cdots & 0 & 0 & -\frac{\partial N_{m1}}{\partial z} & \cdots & \cdots \\ 0 & 0 & 0 & & & 0 & 0 & 0 & & \end{bmatrix} \qquad \text{(A 42)}$$

$$[G^e_{\sigma ms}]_{9\times 18} = \begin{bmatrix} 0 & 0 & 0 & & & 0 & 0 & 0 & & \\ 0 & 0 & 0 & \cdots & \cdots & \frac{\partial N_{m1}}{\partial z} & 0 & 0 & \cdots & \cdots \\ -\frac{mN_{m1}}{r} & 0 & -\frac{N_{m1}}{r} & & & 0 & 0 & 0 & & \\ 0 & 0 & 0 & & & 0 & \frac{\partial N_{m1}}{\partial r} & 0 & & \\ 0 & 0 & 0 & 2* & 3* & 0 & 0 & 0 & 2* & 3* \\ 0 & -\frac{mN_{m1}}{r} & 0 & & & 0 & 0 & 0 & & \\ 0 & 0 & \frac{\partial N_{m1}}{\partial r} & & & 0 & 0 & 0 & & \\ 0 & 0 & \frac{\partial N_{m1}}{\partial z} & \cdots & \cdots & 0 & 0 & 0 & \cdots & \cdots \\ 0 & 0 & 0 & & & 0 & 0 & 0 & & \end{bmatrix} \qquad \text{(A 43)}$$

where $2*$ indicates that these three columns have the same form as the left three columns next to them except that the shape function terms N_{m1} are replaced by N_{m2}, and a similar convention for $3*$.

Applying the numerical integration to Eq. (A 40) yields,

$$[K^e_{\sigma m}] = \pi A_e \sum_{j=1}^{N} H_j r_j \left(\left[G^e_{\sigma mc}(\xi_j,\ \eta_j,\ \zeta_j) \right]^T [S^e_{\sigma 0}] \left[\left[G^e_{\sigma mc}(\xi_j,\ \eta_j,\ \zeta_j) \right] + [G^e_{\sigma ms}]^T [S^e_{\sigma 0}][G^e_{\sigma ms}] \right) \quad \text{(A 44)}$$

where H_j, r_j, ξ_j, η_j, and ζ_j are given in Table 8.

As shown in Eq. (36), the elemental spin-softening matrix for the mth harmonics ($m \neq 0$) may be re-arranged as,

$$\underset{18\times18}{[K^e_{\Omega m}]} = \begin{bmatrix} \underset{9\times9}{[K_{\Omega mS}]} & \underset{9\times9}{[0]} \\ \underset{9\times9}{[0]} & \underset{9\times9}{[K_{\Omega mS}]} \end{bmatrix} \quad \text{(A 45)}$$

where

$$\underset{9\times9}{[K^e_{\Omega mS}]} = \Omega^2 \rho \int_{A_e} \begin{bmatrix} N_{m1}N_{mj} & 0 & 0 \\ 0 & 0 & 0 \\ 0 & 0 & N_{m1}N_{mj} \\ N_{m2}N_{mj} & 0 & 0 \\ 0 & 0 & 0 \\ 0 & 0 & N_{m2}N_{mj} \\ N_{m3}N_{mj} & 0 & 0 \\ 0 & 0 & 0 \\ 0 & 0 & N_{m3}N_{mj} \end{bmatrix} \begin{matrix} \\ \\ \\ \\ \\ \\ \\ \\ \\ \end{matrix} \begin{matrix} j=2 & j=3 \end{matrix} r dr dz \quad \text{(A 46)}$$

where $j = 2$ indicates that the three columns have the same form as the left three columns next to them except that the shape function terms N_{m1} are replaced by N_{m2}, and a similar convention for $j = 3$.

$[K^e_{\Omega m}]$ for the zeroth harmonics is different than Eqs. (A 45) and (A 46). When m = 0, $[K^e_{\Omega m}]$ may be written as,

$$[K^e_{\Omega 0}]_{18\times18} = \begin{bmatrix} [K_{\Omega 0S}]_{9\times9} & [0]_{9\times9} \\ [0]_{9\times9} & [K_{\Omega 0A}]_{9\times9} \end{bmatrix} \tag{A 47}$$

where

$$[K^e_{\Omega 0S}]_{9\times9} = \Omega^2\rho \int_{A_e} \begin{bmatrix} N_{01}N_{0j} & 0 & 0 \\ 0 & 0 & 0 \\ 0 & 0 & 0 \\ N_{02}N_{0j} & 0 & 0 \\ 0 & 0 & 0 \\ 0 & 0 & 0 \\ N_{03}N_{0j} & 0 & 0 \\ 0 & 0 & 0 \\ 0 & 0 & 0 \end{bmatrix} \quad j = 2 \quad j = 3 \; rdrdz \tag{A 48}$$

$$[K^e_{\Omega 0A}]_{9\times9} = \Omega^2\rho \int_{A_e} \begin{bmatrix} 0 & 0 & 0 \\ 0 & 0 & 0 \\ 0 & 0 & N_{01}N_{0j} \\ 0 & 0 & 0 \\ 0 & 0 & 0 \\ 0 & 0 & N_{02}N_{0j} \\ 0 & 0 & 0 \\ 0 & 0 & 0 \\ 0 & 0 & N_{03}N_{0j} \end{bmatrix} \quad j = 2 \quad j = 3 \; rdrdz \tag{A 49}$$

where the convention for $j = 2,\ 3$ is similar to Eq. (A 46).

Regarding Eq. (13), the generalized bearing force acting on the circle of node P can be expressed as,

(a) when the DOF, q_j, corresponds to U^P_{nrS} shown in Eq. (4) with n = 0, 1, 2, …,

$$Q_j^P = -\left\{ K_{yy} \sum_{m=0}^{N} u_{mrS}^P + K_{yz} \left[\sum_{m=0,2,\cdots}^{N} u_{mrS}^P \cdot (-1)^{\frac{m}{2}} + \sum_{m=1,3,\cdots}^{N} u_{mrA}^P \cdot (-1)^{\frac{m-1}{2}} \right] \right\}$$

$$-\left\{ K_{zz} \left[\sum_{m=0,2,\cdots}^{N} u_{mrS}^P \cdot (-1)^{\frac{m}{2}} + \sum_{m=1,3,\cdots}^{N} u_{mrA}^P \cdot (-1)^{\frac{m-1}{2}} \right] + K_{zy} \sum_{m=0}^{N} u_{mrS}^P \right\} \cdot \begin{cases} 0, \textit{ if n is odd} \\ (-1)^{\frac{n}{2}}, \textit{ if n is even} \end{cases} \quad \text{(A 50)}$$

(b) when the DOF, q_j, corresponds to U_{nrA}^P shown in Eq. (4) with $n = 0,1,2\cdots$,

$$Q_j^P = -\left\{ K_{zz} \left[\sum_{m=0,2,\cdots}^{N} u_{mrS}^P \cdot (-1)^{\frac{m}{2}} + \sum_{m=1,3,\cdots}^{N} u_{mrA}^P \cdot (-1)^{\frac{m-1}{2}} \right] + K_{zy} \sum_{m=0}^{N} u_{mrS}^P \right\} \cdot \begin{cases} 0, \textit{ if n is odd} \\ (-1)^{\frac{n-1}{2}}, \textit{ if n is odd} \end{cases} \quad \text{(A 51)}$$

The above equations are applicable even if the harmonics number, m, exceeds 2.

In regard to the beam FE formulation of a spinning rotor under support motion in Section 2.8, the kinetic energy for a rigid disk T_d and a shaft segment T_s can be expressed as,

$$T_d = \frac{1}{2} m_d \left(\dot{x}_F + \omega_{Fy} z_F + \omega_{Fy} z_R - \omega_{Fz} y_F - \omega_{Fz} y_R \right)^2$$

$$+ \frac{1}{2} m_d (\dot{y}_F + \dot{y}_R - \omega_{Fx} z_F - \omega_{Fx} z_R + \omega_{Fz} x_F + \omega_{Fz} x_R)^2$$

$$+ \frac{1}{2} m_d \left(\dot{z}_F + \dot{z}_R + \omega_{Fx} y_F + \omega_{Fx} y_R - \omega_{Fy} x_F - \omega_{Fy} x_R \right)^2$$

$$+ \frac{1}{2} I_{pd} \left[\dot{\alpha}_R - \dot{\gamma}_R \beta_R + \omega_{Fx} \left(1 - \frac{1}{2} \beta_R^2 \right) \left(1 - \frac{1}{2} \gamma_R^2 \right) + \omega_{Fy} \left(1 - \frac{1}{2} \beta_R^2 \right) \gamma_R - \omega_{Fz} \beta_R \right]^2$$

$$+ \frac{1}{2} I_{td} \cdot$$

$$\left[\begin{array}{c} \dot{\beta}_R \cos \alpha_R + \dot{\gamma}_R \sin \alpha_R \left(1 - \frac{1}{2} \beta_R^2 \right) + \omega_{Fx} \sin \alpha_R \cdot \beta_R \left(1 - \frac{1}{2} \gamma_R^2 \right) - \omega_{Fx} \cos \alpha_R \cdot \gamma_R \\ + \omega_{Fy} \sin \alpha_R \cdot \beta_R \cdot \gamma_R + \omega_{Fy} \cos \alpha_R \left(1 - \frac{1}{2} \gamma_R^2 \right) + \omega_{Fz} \sin \alpha_R \left(1 - \frac{1}{2} \beta_R^2 \right) \end{array} \right]^2$$

$$+\frac{1}{2}I_{td}\begin{bmatrix} -\dot{\beta}_R \sin\alpha_R + \dot{\gamma}_R \cos\alpha_R\left(1-\frac{1}{2}\beta_R^2\right) + \omega_{Fx}\cos\alpha_R\cdot\beta_R\left(1-\frac{1}{2}\gamma_R^2\right) + \\ \omega_{Fx}\sin\alpha_R\cdot\gamma_R + \\ \omega_{Fy}\cos\alpha_R\cdot\beta_R\cdot\gamma_R - \omega_{Fy}\sin\alpha_R\left(1-\frac{1}{2}\gamma_R^2\right) + \omega_{Fz}\cos\alpha_R\left(1-\frac{1}{2}\beta_R^2\right) \end{bmatrix}^2$$

(A 52)

$$T_s = \frac{1}{2}\int_0^L \left[\rho_s A_s(\dot{y}_S^2 + \dot{z}_S^2) + I_{ts}\left(\dot{\beta}_S^2 + \dot{\gamma}_S^2\right)\right] dx$$

$$+\omega_{Fx}\int_0^L \left[\rho_s A_s(y_S\dot{z}_S - \dot{y}_S z_S) + I_{ts}\left(\beta_S\dot{\gamma}_S - \dot{\beta}_S\gamma_S\right)\right] dx$$

$$-(\Omega+\omega_{Fx})\int_0^L I_{ps}\beta_S\dot{\gamma}_S dx + \frac{1}{2}\int_0^L \rho_s A_s\left[\omega_{Fx}^2(y_S^2+z_S^2) + \omega_{Fz}^2 y_S^2 + \omega_{Fy}^2 z_S^2\right] dx$$

$$+\frac{1}{2}\int_0^L \left[I_{ts}\omega_{Fx}^2(\beta_S^2+\gamma_S^2) + I_{ps}\left(\omega_{Fz}^2\beta_S^2 + \omega_{Fy}^2\gamma_S^2\right)\right] dx$$

$$+\int_0^L \rho_s A_s \begin{bmatrix} x_S\left(\omega_{Fz}\dot{y}_S - \omega_{Fy}\dot{z}_S - \omega_{Fx}\omega_{Fy}y_S - \omega_{Fx}\omega_{Fz}z_S\right) + T_1\dot{y}_S \\ +T_2\dot{z}_S + T_3 y_S + T_4 z_S - \omega_{Fy}\omega_{Fz}\beta_S\gamma_S \end{bmatrix} dx$$

$$+\int_0^L \begin{bmatrix} I_{ts}\left(\omega_{Fz}\dot{\gamma}_S + \omega_{Fy}\dot{\beta}_S - \omega_{Fx}\omega_{Fy}z_S + \omega_{Fx}\omega_{Fz}y_S + \omega_{Fy}\omega_{Fz}\beta_S\gamma_S\right) \\ +I_{ps}\left(\omega_{Fx}\omega_{Fy}z_S + \Omega\omega_{Fy}\gamma_S - \omega_{Fx}\omega_{Fz}\beta_S - \Omega\omega_{Fz}\beta_S - \omega_{Fy}\omega_{Fz}\beta_S\gamma_S\right) \end{bmatrix} dx$$

$$+\frac{1}{2}\int_0^L \left[\rho_s A_s x_S T_5 + \rho_s A_s T_6 + \rho_s A_s x_S^2\left(\omega_{Fy}^2+\omega_{Fz}^2\right) + I_{ts}\left(\omega_{Fy}^2+\omega_{Fz}^2\right)\right.$$

$$\left. + I_{ps}(\Omega+\omega_{Fx})^2\right] dx -$$

$$\frac{1}{2}\int_0^L \left[I_{ps}\omega_{Fx}^2(\beta_S^2+\gamma_S^2) + I_{ps}\Omega\omega_{Fx}(\beta_S^2+\gamma_S^2) + I_{ts}\left(\omega_{Fz}^2\beta_S^2 + \omega_{Fy}^2\gamma_S^2\right)\right] dx \quad \text{(A 53)}$$

where

$$T_1 = \dot{y}_F + \omega_{Fz}x_F - \omega_{Fx}z_F \quad \text{(A 54)}$$

$$T_2 = \dot{z}_F + \omega_{Fx}y_F - \omega_{Fy}x_F \quad \text{(A 55)}$$

$$T_3 = \omega_{Fx}\left(\dot{z}_F + \omega_{Fx}y_F - \omega_{Fy}x_F\right) - \omega_{Fz}\left(\dot{x}_F - \omega_{Fz}y_F + \omega_{Fy}z_F\right) \quad \text{(A 56)}$$

$$T_4 = \omega_{Fy}\left(\dot{x}_F - \omega_{Fz}y_F + \omega_{Fy}z_F\right) - \omega_{Fx}(\dot{y}_F + \omega_{Fz}x_F - \omega_{Fx}z_F) \quad \text{(A 57)}$$

$$T_5 = \omega_{Fz}\dot{y}_F - \omega_{Fy}\dot{z}_F + \omega_{Fy}^2 x_F + \omega_{Fz}^2 x_F - \omega_{Fx}\omega_{Fy}y_F - \omega_{Fx}\omega_{Fz}z_F \quad \text{(A 58)}$$

$$\begin{aligned} T_6 = {} & \dot{x}_F^2 + \dot{y}_F^2 + \dot{z}_F^2 + \omega_{Fx}^2(y_F^2 + z_F^2) + \omega_{Fy}^2(x_F^2 + z_F^2) + \omega_{Fz}^2(x_F^2 + y_F^2) \\ & + 2\omega_{Fx}(y_F\dot{z}_F - \dot{y}_F z_F) + 2\omega_{Fy}(\dot{x}_F z_F - x_F\dot{z}_F) + 2\omega_{Fz}(x_F\dot{y}_F - \dot{x}_F y_F) \\ & - 2\left(\omega_{Fx}\omega_{Fy}x_F y_F + \omega_{Fx}\omega_{Fz}x_F z_F + \omega_{Fy}\omega_{Fz}y_F z_F\right) \end{aligned} \quad \text{(A 59)}$$

where L represents the length of the shaft segment.

APPENDIX B

STATE-SPACE FORMULATION FOR ROTOR-BEARING-SUPPORT SYSTEMS

The variables in the state-space model of the rotor and support are defined as follows.

$$\{q_R\} = \begin{bmatrix} \{\dot{U}_R\} \\ \{U_R\} \end{bmatrix} \tag{B 1}$$

$$[A_R] = \begin{bmatrix} -[M_R]^{-1}[C_R] & -[M_R]^{-1}[K_R] \\ [I] & [0] \end{bmatrix} \tag{B 2}$$

$$[B_{\mathrm{RB}}] = \begin{bmatrix} [M_R]^{-1}[B_{\mathrm{RB1}}] \\ [0] \end{bmatrix} \tag{B 3}$$

$$[B_{\mathrm{RB1}}] = \begin{bmatrix} \vdots & & & \\ 1 & 1 & 0 & 0 \\ \vdots & & & \\ 0 & 0 & 1 & 1 \\ \vdots & & & \\ 1 & 0 & 0 & 0 \\ \vdots & & & \\ 0 & 0 & 1 & 0 \\ \vdots & & & \\ 0 & 1 & 0 & 0 \\ \vdots & & & \\ 0 & 0 & 0 & 1 \\ \vdots & & & \end{bmatrix} \text{ corresponding to } \begin{bmatrix} \vdots \\ U_{0rS}^{A_1} \\ \vdots \\ U_{0rS}^{A_2} \\ \vdots \\ U_{1rS}^{A_1} \\ \vdots \\ U_{1rS}^{A_2} \\ \vdots \\ U_{1rA}^{A_1} \\ \vdots \\ U_{1rA}^{A_2} \\ \vdots \end{bmatrix} \tag{B 4}$$

$$\{f_B\} = \begin{bmatrix} F_{BY1} \\ F_{BZ1} \\ F_{BY2} \\ F_{BZ2} \end{bmatrix} \tag{B 5}$$

$$[B_{\mathrm{RU}}] = \begin{bmatrix} [M_R]^{-1}[B_{\mathrm{RU1}}] \\ [0] \end{bmatrix} \tag{B 6}$$

$$[B_{\mathrm{RU1}}] = \begin{bmatrix} \vdots & \\ 1 & 1 \\ \vdots & \\ 1 & 0 \\ \vdots & \\ 0 & 1 \\ \vdots & \end{bmatrix} \text{ corresponding to } \begin{bmatrix} \vdots \\ U^B_{0rS} \\ \vdots \\ U^B_{1rS} \\ \vdots \\ U^B_{1rA} \\ \vdots \end{bmatrix} \tag{B 7}$$

$$\{f_U\} = \begin{bmatrix} F^B_{UX} \\ F^B_{UY} \end{bmatrix} \tag{B 8}$$

$$[C_R] = [[0] \quad [C_{\mathrm{R2}}]] \tag{B 9}$$

$$[C_{\mathrm{R2}}] = \begin{bmatrix} & \vdots & & \\ 1 & 1 & 0 & 0 \\ & \vdots & & \\ 0 & 0 & 1 & 1 \\ & \vdots & & \\ 1 & 0 & 0 & 0 \\ & \vdots & & \\ 0 & 0 & 1 & 0 \\ & \vdots & & \\ 0 & 1 & 0 & 0 \\ & \vdots & & \\ 0 & 0 & 0 & 1 \\ & \vdots & & \end{bmatrix}^T \text{ corresponding to } \begin{bmatrix} \vdots \\ U^{A_1}_{0rS} \\ \vdots \\ U^{A_2}_{0rS} \\ \vdots \\ U^{A_1}_{1rS} \\ \vdots \\ U^{A_2}_{1rS} \\ \vdots \\ U^{A_1}_{1rA} \\ \vdots \\ U^{A_2}_{1rA} \\ \vdots \end{bmatrix}^T \tag{B 10}$$

In the state-space support model, $[A_S]$, $[B_S]$ and $[C_S]$ are the minimal realization of the corresponding state-space matrices $\left[\tilde{A}_S\right]$, $[\tilde{B}_S]$ and $\left[\tilde{C}_S\right]$, which may be expressed as,

$$\left[\tilde{A}_S\right] = \begin{bmatrix} [A_{\mathrm{AiY1}}] & [0] & [0] & [0] \\ [0] & [A_{\mathrm{AiZ1}}] & [0] & [0] \\ [0] & [0] & [A_{\mathrm{AiY2}}] & [0] \\ [0] & [0] & [0] & [A_{\mathrm{AiZ2}}] \end{bmatrix} \tag{B 11}$$

$$[A_{\mathrm{AiBj}}] = \begin{bmatrix} [A_{\mathrm{Y1Bj}}] & [0] & [0] & [0] \\ [0] & [A_{\mathrm{Z1Bj}}] & [0] & [0] \\ [0] & [0] & [A_{\mathrm{Y2Bj}}] & [0] \\ [0] & [0] & [0] & [A_{\mathrm{Z2Bj}}] \end{bmatrix} \tag{B 12}$$

$$[\tilde{B}_S] = \begin{bmatrix} [B_{\mathrm{AiY1}}] & [0] & [0] & [0] \\ [0] & [B_{\mathrm{AiZ1}}] & [0] & [0] \\ [0] & [0] & [B_{\mathrm{AiY2}}] & [0] \\ [0] & [0] & [0] & [B_{\mathrm{AiZ2}}] \end{bmatrix} \tag{B 13}$$

$$[B_{\mathrm{AiBj}}] = \begin{bmatrix} [B_{\mathrm{Y1Bj}}] \\ [B_{\mathrm{Z1Bj}}] \\ [B_{\mathrm{Y2Bj}}] \\ [B_{\mathrm{Z2Bj}}] \end{bmatrix} \tag{B 14}$$

$$[\tilde{C}_S] = [[C_{\mathrm{AiY1}}] \quad [C_{\mathrm{AiZ1}}] \quad [C_{\mathrm{AiY2}}] \quad [C_{\mathrm{AiZ2}}]] \tag{B 15}$$

$$[C_{\mathrm{AiBj}}] = \begin{bmatrix} [C_{\mathrm{Y1Bj}}] & [0] & [0] & [0] \\ [0] & [C_{\mathrm{Z1Bj}}] & [0] & [0] \\ [0] & [0] & [C_{\mathrm{Y2Bj}}] & [0] \\ [0] & [0] & [0] & [C_{\mathrm{Z2Bj}}] \end{bmatrix} \tag{B 16}$$

where the subscripts A, B indicate Y or Z, and i, j =1 or 2. The entries of the state-space matrices shown in Eqs. (B 12), (B 14), and (B 16) are derived from the TFs $G_{AiBk}(s)$ individually.

Suppose that there are two bearings involved (can be extended to any number), then the damping and stiffness matrices of the bearings are defined as,

$$[C_B] = \begin{bmatrix} c_{YY1} & c_{YZ1} & 0 & 0 \\ c_{ZY1} & c_{ZZ1} & 0 & 0 \\ 0 & 0 & c_{YY2} & c_{YZ2} \\ 0 & 0 & c_{ZY2} & c_{ZZ2} \end{bmatrix} \tag{B 17}$$

$$[K_B] = \begin{bmatrix} k_{YY1} & k_{YZ1} & 0 & 0 \\ k_{ZY1} & k_{ZZ1} & 0 & 0 \\ 0 & 0 & k_{YY2} & k_{YZ2} \\ 0 & 0 & k_{ZY2} & k_{ZZ2} \end{bmatrix} \tag{B 18}$$

$$\{y_R\} = \begin{bmatrix} U_{RY1} \\ U_{RZ1} \\ U_{RY2} \\ U_{RZ2} \end{bmatrix} \tag{B 19}$$

$$\{y_S\} = \begin{bmatrix} U_{SY1} \\ U_{SZ1} \\ U_{SY2} \\ U_{SZ2} \end{bmatrix} \tag{B 20}$$

$$[A_T] = \begin{bmatrix} [I] + [B_{\mathrm{RB}}][C_B][C_R] & -[B_{\mathrm{RB}}][C_B][C_S] \\ -[B_S][C_B][C_R] & [I] + [B_S][C_B][C_S] \end{bmatrix} \tag{B 21}$$

$$[B_T] = \begin{bmatrix} [A_R] - [B_{\mathrm{RB}}][K_B][C_R] & [B_{\mathrm{RB}}][K_B][C_S] \\ [B_S][K_B][C_R] & [A_S] - [B_S][K_B][C_S] \end{bmatrix} \tag{B 22}$$

$$[B_{\mathrm{UT}}] = \begin{bmatrix} [B_{\mathrm{RU}}] \\ [0] \end{bmatrix} \tag{B 23}$$

$$\{q\} = \begin{bmatrix} \{q_R\} \\ \{q_S\} \end{bmatrix} \tag{B 24}$$

where the state variable vector of the support structure $\{q_S\}$ accompanies the generation of the matrices $[A_T]$ and $[B_T]$ and has no physical meanings.

APPENDIX C

PARAMETERS FOR FORCE-INTERFERENCE RELATIONS IN THE IMPACT MODEL

By referring to Ref. [63], the parameter k in the formula for the force-interference relations can be expressed as,

$$k = \frac{4}{3} \cdot \frac{q_k}{(\delta_1+\delta_2)\sqrt{A+B}} \tag{C 1}$$

where

$$\delta_1 = \frac{1-\nu_1^2}{E_1\pi} \tag{C 2}$$

$$\delta_2 = \frac{1-\nu_2^2}{E_2\pi} \tag{C 3}$$

ν and E denote the Poisson's ratio and modulus of elasticity, respectively, and the subscripts 1 and 2 refer to the sphere and cylindrical cup, respectively. For contact between a sphere and a cylindrical cup, A and B can be obtained from,

$$A = \frac{1}{2}\left(\frac{1}{R_1} - \frac{1}{R_2}\right) \tag{C 4}$$

$$B = \frac{1}{2R_1} \tag{C 5}$$

where R_1 and R_2 represent the radius of sphere and cylindrical cup, respectively. q_k is dependent upon A and B and can be looked up in Ref. [63].